INFORMATION TO USERS

This manuscript has been reproduced from the microfilm master. UMI films the text directly from the original or copy submitted. Thus, some thesis and dissertation copies are in typewriter face, while others may be from any type of computer printer.

The quality of this reproduction is dependent upon the quality of the copy submitted. Broken or indistinct print, colored or poor quality illustrations and photographs, print bleedthrough, substandard margins, and improper alignment can adversely affect reproduction.

In the unlikely event that the author did not send UMI a complete manuscript and there are missing pages, these will be noted. Also, if unauthorized copyright material had to be removed, a note will indicate the deletion.

Oversize materials (e.g., maps, drawings, charts) are reproduced by sectioning the original, beginning at the upper left-hand corner and continuing from left to right in equal sections with small overlaps. Each original is also photographed in one exposure and is included in reduced form at the back of the book.

Photographs included in the original manuscript have been reproduced xerographically in this copy. Higher quality 6" x 9" black and white photographic prints are available for any photographs or illustrations appearing in this copy for an additional charge. Contact UMI directly to order.

UMI

A Bell & Howell Information Company
300 North Zeeb Road, Ann Arbor MI 48106-1346 USA
313/761-4700 800/521-0600

UNIVERSITY OF CALIFORNIA

Santa Barbara

Alternating Molecular Beam Epitaxy and Characterization of InGaAs Quantum Dots and Quantum Dot Lasers

A Dissertation submitted in partial satisfaction of the requirements for the degree of

Doctor of Philosophy

in

Electrical and Computer Engineering

by

Richard Paul Mirin

Committee in charge:

Professor John Bowers, Chairperson

Professor Arthur Gossard

Professor Evelyn Hu

Professor James Speck

December, 1996

UMI Number: 9718607

UMI Microform 9718607
Copyright 1997, by UMI Company. All rights reserved.

This microform edition is protected against unauthorized
copying under Title 17, United States Code.

UMI
300 North Zeeb Road
Ann Arbor, MI 48103

The dissertation of Richard Paul Mirin
is approved:

Professor Arthur C. Gossard

Professor Evelyn L. Hu

Professor James S. Speck

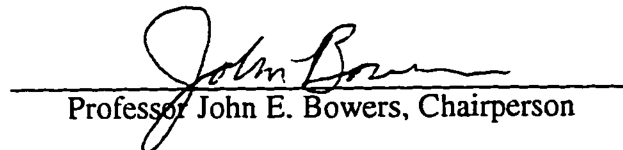

Professor John E. Bowers, Chairperson

December 1996

Alternating Molecular Beam Epitaxy and Characterization of InGaAs Quantum Dots and Quantum Dot Lasers

Copyright © by
Richard Paul Mirin
1996

Acknowledgements

I would like to thank my committee for all of their assistance in preparing this dissertation. My committee chairman, Prof. John Bowers, gave me the freedom to work on whatever projects I chose (as long as the rest of his group had enough MBE material). Prof. Art Gossard has been my unofficial co-advisor since I arrived in Santa Barbara. His insight has caused me to think much more carefully about many problems than I otherwise would have. Prof. Evelyn Hu has also been almost a co-advisor since I arrived in Santa Barbara, and I thank her for all the support she has given me over the years. Prof. Jim Speck has provided many valuable discussions about materials characterization of quantum dots

I could write paragraphs about all the help John English has given me over the years, but instead I will just say that all of this would not have been possible without his assistance in the MBE lab and the pool halls. In addition to keeping all things running smoothly in the Bowers lab, Tom Reynolds has kept my car running with all his advice over the years.

James Ibbetson took all of the TEM images that appear in this dissertation. Eric Tarsa performed the X-ray measurements. I'd like to thank these two for participating in numerous crazy experiments over the years. Extensive conversations with Dubravko Babic about lasers, fabrication, C programming, and life in general have kept the past six years very interesting.

I learned a lot about MBE and lasers by working with Mark Mondry, Tim Strand, Brian Thibeault, and Bruce Young. Dan Cohen and Dan Tauber taught me about the physics and measurements of semiconductor lasers. I had many helpful

discussions with Naggi Asmar, John Cerne, and Andrea Markelz about PL. Gil Chinn and Paul Haskell are both masters of the C programming language, and I thank them for helping me with debugging code, as well as their friendship over the years. Kenichi Nishi has been very helpful in sharing discussions about quantum dots, and I thank him for also being a good friend.

I would like to thank the National Science Foundation and the Center for Quantized Electronic Structures (QUEST) for financial support.

Finally, to the rest of my friends and colleagues over the past six years, thanks for everything!

Dedicated to my parents

VITA

January 29, 1967: Born in Brooklyn, New York

May, 1990: B.S, Electrical Engineering and Computer Science/Materials Science and Engineering, University of California, Berkeley

April, 1992: M.S., Electrical and Computer Engineering, University of California, Santa Barbara

Dec., 1996: Ph.D., Electrical and Computer Engineering, University of California, Santa Barbara

Publications

1. "Systematic Observation of Strain-Induced Lateral Confinement of Excitons in GaAs/AlGaAs Quantum Well by Chemical Dry Etching," I-H. Tan, D. Lishan, R. Mirin, V. Jayaraman, T. Yasuda, E. L. Hu, and J. Bowers, *Appl. Phys. Lett.*, **59**(15), 1875-1877, October (1991).
2. "Strain-induced Lateral Confinement of Excitons in GaAs/AlGaAs Quantum Well by Chemical Dry Etching," I. H. Tan, D. Lishan, R. Mirin, V. Jayaraman, T. Yasuda, E. Hu, and J. Bowers, *J. Vac. Sci. Tech. B*, **9**(6), 3498-3501, November/December (1991).
3. "Mode-locked GaAs Vertical Cavity Surface Emitting Lasers," W. B. Jiang, R. Mirin, and J. E. Bowers, *Appl. Phys. Lett.*, **60**(6), 677-679, February (1992).
4. "Photoluminescence Study of Strain-Induced Quantum Well Dots by Wet Etching Technique," I-H. Tan, R. Mirin, V. Jayaraman, S. Stone, E. L. Hu, J. E. Bowers, and J. Merz, *Appl. Phys. Lett.*, **61**(3), 300-302, July (1992).
5. "Optical Study of Strained Quantum Well Wires," I-H. Tan, T. Yasuda, M. Y. He, R. Mirin, D. Lishan, E. L. Hu, J. E. Bowers, J. Merz, and A. Evans, *J. Vac. Sci. Tech.* A, **10**(4), 664-668, July/August (1992).
6. "InGaAs Quantum Well Wires Grown on Patterned GaAs Substrates," R. Mirin, I-H. Tan, H. Weman, M. Leonard, T. Yasuda, J. E. Bowers, and E. L. Hu, *J. Vac. Sci. Tech. A*, **10**(4), 697-700, July/August (1992).
7. "Study of Partial Strain Release and Surface States Formed on the Side Wall of InGaAs Quantum Well Wires," I-H. Tan, R. Mirin, T. Yasuda, M. Y. He, E. Hu, J. E. Bowers, P. Hansma, and A. Evans, *J. Vac, Sci Tech. B*, **10**(4), 1971-1974, July/August (1992).
8. "Effect of the Confinement Layer Composition on the Internal Quantum Efficiency and Modulation Response of Quantum Well Lasers," R. Nagarajan, R. P. Mirin, T. E. Reynolds, and J. E. Bowers, *Photon. Tech. Lett.*, **4**(8), 832-834, August (1992).
9. "Evaluation of the Etch Depth Dependence of Three Dimensional Confinement in Strain-Induced Quantum Well Dots," I. H. Tan, Y. L. Chang, S. Shi, R. Mirin, E. Hu, J. Merz, and J. Bowers, *J. Vac. Sci. Tech. B*, **10**(6), 2851-2854, November/December (1992).
10. "144°C Operation of 1.3 μm InGaAsP Vertical Cavity Lasers on GaAs Substrates," J. J. Dudley, M. Ishikawa, D. I. Babić, B. I. Miller, R. Mirin, W. B. Jiang, J. E. Bowers, and E. L. Hu, *Appl. Phys. Lett.*, **61**(26), 3095-3097, December (1992).
11. "Femtosecond Periodic Gain Veritcal-Cavity Lasers," W. B. Jiang, M. Shimizu, R. P. Mirin, T. E. Reynolds, and J. E. Bowers, *Photon. Tech. Lett.*, **5**(1), 23-24, January (1993).
12. "Morphology and Optical Properties of Strained InGaAs Quantum Well Wires," R. Mirin, M. Krishanmurthy, I. H. Tan, J. Bowers, A. C. Gossard, and E. Hu, *J. of Crystal Growth*, **127**, 881-886, February (1993).
13. "Observation of quasi-periodic facet formation during high temperature growth of AlAs and AlAs/GaAs superlattices", R.P. Mirin, M. Krishnamurthy, J.P. Ibbetson, J.H. English, and A.C. Gossard*J. Cryst. Growth*, **127**, 908-912 February (1993).
14. "Observation of Quantum Confinement in Strain-Induced Quantum Wires/Dots," I-H. Tan, T. Yasuda, R. Mirin, D. Lishan, E. Hu, J. Bowers, and J. Merz, Quantum-Effect Physics, Electronics and Applications, Institute of Publishing, London, (1993).
15. "Electrically Pumped Mode-Locked Vertical-Cavity Semiconductor Lasers," W. Jiang, M. Shimizu, R. P. Mirin, T. E. Reynolds, and J. E. Bowers, *Opt. Lett.*, **18**, November (1994).
16. "Experimental Evidence for Hole Transport Limited Intensity Modulation Response in Quantum Well Lasers," R. Nagarajan, R. P. Mirin, T. E. Reynolds, and J. E. Bowers, *Electronics Letters*, **29**(19), 1688-1690, September (1993).

17. "Temperature-dependent quasi-periodic facetting of AlAs grown by MBE on (100) GaAs substrates", R.P. Mirin, M. Krishnamurthy, J.P. Ibbetson, A.C. Gossard, J.H. English, and P. Petroff, *Mat. Res. Soc. Symp. Proc.*, Vol. 312, 273-277 (1993).
18. "Femtosecond periodic gain vertical cavity lasers", W. Jiang, M. Shimizu, R.P. Mirin, T.E. Reynolds, and J.E. Bowers, *OSA Proc. Ultrafast Electronics and Optoelectronics*, Vol. 14, 2 (1993).
19. "Effects of As_4 flux on RHEED oscillations during growth of GaAs at low temperatures", J.P. Ibbetson, R.P.Mirin, U.K. Mishra, and A.C. Gossard, *J. Vac. Sci. Tech. B* , Vol. 12, No. 2, pp. 1050-1053 (1994).
20. "Low Threshold, Wafer Fused Long Wavelength Vertical Cavity Lasers," J. J. Dudley, D. I. Babić, R. Mirin, L. Yang, B.I. Miller, R. J. Ram, T. Reynolds, E. L. Hu, and J. E. Bowers, *Applied Physics Letters*, **64**(12), 1463-1465, March (1994).
21. "Optically pumped all-epitaxial wafer-fused 1.52 μm vertical-cavity lasers", D. I. Babić, J.J. Dudley, K. Streubel, R.P. Mirin, E.L. Hu, J.E. Bowers, *Electronics Letters*, **30**(9), 704-706 (1994).
22. "Low temperature limits to molecular beam epitaxy of GaAs", R.P. Mirin, J.P. Ibbetson, U.K. Mishra, and A.C. Gossard, , *Applied Physics Letters*, **65**(18), 2335-2337, October (1994).
23. "Double-fused 1.52 μm vertical-cavity lasers", D. I. Babić, J.J. Dudley, K. Streubel, R.P. Mirin, E.L. Hu, J.E. Bowers, *Applied Physics Letters* , **66**(9), 1030-1032, February (1995).
24. "Traveling-Wave Photodetectors with 172 GHz Bandwidth and 76 GHz Bandwidth-Efficiency Product," K. S. Giboney, R. L. Nagarajan, T. E. Reynolds, S. T. Allen, R. P. Mirin, M. J. Rodwell, and J. E. Bowers, *IEEE Photonics Technology Letters*, **7**(4), April (1995).
25. "Transverse-mode and polarisation characteristics of double-fused 1.52-μm vertical-cavity lasers," D. I. Babic, K. Streubel, R. P. Mirin, N. M. Margalit, J. E. Bowers, and E. L. Hu, *Electronics Letters*, **31** (8), 653-654, April 13 (1995).
26. "Room-temperature continuous-wave operation of 1.54 μm vertical-cavity lasers," D. I. Babic, K. Streubel, R. P. Mirin, N. M. Margalit, J. E. Bowers, E. L. Hu, *Photonics Technology Letters*, **7** (11), 1225-1227, November (1995).
27. "1.3 μm room temperature photoluminescence from InGaAs quantum dots on GaAs", R.P. Mirin, J. Ibbetson, K. Nishi, A. Gossard, and J. Bowers, *Applied Physics Letters*, **67** (23), 3795-3797, December (1995).
28. "Characterization of metal mirrors on GaAs," D. I. Babic, R. P. Mirin, E. L. Hu, J. E. Bowers, *Electronics Letters* , **32** (4), 319-320, February (1996).
29. "Fabrication and characteristics of double-fused vertical-cavity lasers," D.I. Babic, K. Streubel, R.P. Mirin, N. M. Margalit, M.G. Peters, E.L. Hu, J.E. Bowers,*Optical and Quantum Electronics*, **28** (5), 475-485, May (1996).
30. "Laterally oxidized long wavelength cw vertical-cavity lasers," N.M. Margalit, D.I. Babic, K. Streubel, R.P. Mirin, D.E. Mars, J.E. Bowers, and E.L. Hu, *Applied Physics Letters*, **69** (4), 471-472, July (1996).32.
31. "Submilliamp long-wavelength vertical cavity lasers," N.M. Margalit, D.I. Babic, K. Streubel, R.P. Mirin, R.L. Naone, J.E. Bowers, and E.L. Hu, *Electronics Letters*, **32** (18), 1675-1677, August 29 (1996).
32. "Room temperature lasing from InGaAs quantum dots," R. Mirin, A. Gossard, and J. Bowers, *Electrronics Letters*, **32** (18), 1732-1734, August 29 (1996).
33. "Overgrowth of InGaAs Quantum Dots formed by Alternating Molecular Beam Epitaxy," R.P. Mirin, J.P. Ibbetson, J.E. Bowers, and A.C. Gossard, accepted for publication in *Journal of Crystal Growth.*

Conference Presentations

1. I-H. Tan, D. Lishan, R. Mirin, V. Jayaraman, T. Yasuda, E. Hu and J. Bowers, "Strain Induced Lateral Confinement of Excitons in GaAs/AlGaAs Quantum Well by Chemical Dry Etching," Electron, Ion and Photon Beams Conference (EIPB), Session D2, Seattle, WA, May 29-31 (1991).
2. I-H. Tan, T. Yasuda, R. Mirin, D. Lishan, V. Jayaraman, C. Prater, E. L. Hu, J. E. Bowers, and J. Merz, "The Formation of Strain-Induced Quantum Well Wires by Low Damage Chemical Dry Etching," LEOS Summer Topical Meeting-Microfabrication for Photonics and Optoelectronics, Newport Beach, CA July 29-Aug. 1 (1991).
3. W. B. Jiang, R. Mirin, and J. E. Bowers "Mode-Locked GaAs Vertical Cavity Surface Emitting Lasers," LEOS 1991 Annual Meeting, paper PD2, San Jose, CA, Nov. (1991).
4. I-H. Tan, T. Yasuda, M. Y. He, R. Mirin, D. Lishan, E. Hu, J. Bowers, J. Merz, and A. Evans, "Optical Study of Strained Quantum Well Wires," American Vacuum Society Annual Symposium, Seattle, WA, Nov. 11-15 (1991).
5. R. Mirin, I. H. Tan, R. Yasuda, J. Bowers, and E. Hu, "InGaAs Quantum Well Wires Grown on Patterned GaAs Substrates," American Vacuum Society Annual Symposium, Seattle, WA, Nov. 11-15 (1991).
6. I-H. Tan, T. Yasuda, R. Mirin, D. Lishan, E. Hu, J. Bowers, and J. Merz, "Observation of Quantum Confinement in Strained Quantum Wires/Dots," Int. Workshop on Quantum Effect Physics, Electronics, and Applications, Luxor, Egypt, Jan. 6-10, (1992).
7. I-H. Tan, R. Mirin, T. Yasuda, M. Y. He, E. Hu, J. Bowers, P. Hansma, and A. Evans, "Study of Partial Strain Release and Surface States Formed on the Side Wall of InGaAs Quantum Well Wires," Physics and Chemistry of Semiconductor Interfaces Conference (PCSI), Death Valley, CA, Jan. 28-30 (1992).
8. I-H. Tan, S. Shi, R. Mirin, E.L. Hu, J. Merz, and J. E. Bowers, "Study of the Surface Cleaning Effects to the InGaAs Quantum Well Wires by Atomic Force Microscopy and Photoluminescence Spectroscopy," Spring Conference of Material Research Society (MRS), San Francisco, CA, Apr. 27-May 1 (1992).
9. I-H. Tan, T. Yasuda, R. Mirin, D. Lishan, E.H. Hu, J. E. Bowers and J. Merz, "Excitons in Strain-Induced Quantum Well Wires/Dots," Quantum Electronics and Laser Science Conference(CLEO), INVITED PAPER, Anaheim, CA May 10-15 (1992).
10. W. B. Jiang, D. Derickson, R. Mirin, and J. E. Bowers, "Importance of Laser Cavity Length Detuning in Mode-Locked Vertical-Cavity Surface-Emitting Lasers," Quantum Electronics and Laser Science Conference (CLEO), paper JThE2, Anaheim, CA, May 10-15 (1992).
11. I-H. Tan, Y. L. Chang, S. Shi, R. Mirin, E. Hu, J. Merz and J. Bowers, "Evaluation of the Etch Depth Dependence of Three Dimensional Confinement in Strain-Induced Quantum Well Dots," Electron, Ion, and Photon Beams Conference (EIPB), Orlando, FL, May 26-29 (1992).
12. R. Mirin, I. H. Tan, M. Krishanmurthy, J. Bowers, A. C. Gossard, and E. Hu, "Morphology and Optical Properties of Strained InGaAs Quantum Well Wires," 7th International Conference on Molecular Beam Epitaxy, Schwabisch Gmund, Germany, Aug. (1992).
13. R.P. Mirin, M. Krishnamurthy, J.P. Ibbetson, J.H. English, and A.C. Gossard, "Observation of quasi-periodic facet formation during high temperature growth of AlAs and AlAs/GaAs superlattices", 7th International Conference on Molecular Beam Epitaxy, Schwabisch Gmund, Germany, Aug. (1992).

14. J. J. Dudley, M. Ishikawa, B. I. Miller, D. I. Babić, R. Mirin, W. B. Jiang, M. Shimizu, J. E. Bowers, and E. L. Hu, "InGaAsP (1.3 μm) Vertical Cavity Lasers Using GaAs/AlAs Mirrors," 1992 Optical Society of America Annual Meeting, paper FKK7, Albuquerque, NM, Sep. 20-25 (1992).
15. R. Nagarajan, R. P. Mirin, T. E. Reynolds, and J. E. Bowers, "Carrier Confinement and its Effect on the Internal Quantum Efficiency and Modulation Response of Quantum Well Lasers," 13th International Semiconductor Laser Conference, Takamatsu, Japan, Sep. (1992).
16. J. J. Dudley, M. Ishikawa, D. I. Babić, B. I. Miller, R. Mirin, W. B. Jiang, J. E. Bowers, and E. L. Hu, "144° C Lasing of 1.3 μm InGaAsP VCSELs Utilizing GaAs/AlAs Mirrors," 13th International Semiconductor Laser Conference, Postdeadline paper, Takamatsu, Japan, Sep. (1992).
17. I-H. Tan, R. Mirin, V. Jayaraman, S. Shi, E. Hu, J. Bowers, and J Merz, "Strain-Induced Quantum Well Wires and Dots Utilizing an InGaAs Stressor," Second Int. Symposium on New Phenomena in Mesoscopic Structures, Kauai, HI, Dec. 7-11 (1992).
18. J. J. Dudley, D. I. Babić, H. Wada, M. Shimizu, R. Mirin, J. E. Bowers, and E. Hu, "InGaAsP Vertical Cavity Lasers," SPIE OE/LASE 1993, #1850-10, Los Angeles, CA, Jan. 18 - 20 (1993).
19. W. B. Jiang, M. Shimizu, R. Mirin, T. Reynolds, and J. E. Bowers, "Femtosecond Periodic Gain Vertical-Cavity Surface-Emitting Lasers," Ultrafast Electronic & Optoelectronics Conference, San Francisco, CA, Jan. 25-27 (1993).
20. R.P. Mirin, M. Krishnamurthy, J.P. Ibbetson, A.C. Gossard, J.H. English, and P. Petroff, "Temperature-dependent quasi-periodic facetting of AlAs grown by MBE on (100) GaAs substrates", Spring Meeting of the Materials Research Society, Symposium P, (1993).
21. J. J. Dudley, D. I. Babić, R. Mirin, L. Yang, B. I. Miller, R. J. Ram, T. Reynolds, E. L. Hu, and J. E. Bowers, "Low Threshold, Electrically Injected InGaAsP (1.3 μm) Vertical Cavity Lasers on GaAs Substrates," postdeadline paper, IEEE 51st Device Research Conference, Santa Barbara, CA, June 21 - 23 (1993).
22. M. Shimizu, W. Jiang, R. P. Mirin, T. E. Reynolds, and J. E. Bowers, "Electrically Pumped Mode-Locked Vertical-Cavity Semiconductor Lasers," Japanese Applied Physics Annual Meeting, Hokaido, Japan, September (1993).
23. J.P. Ibbetson, R.P.Mirin, U.K. Mishra, and A.C. Gossard, "Effects of As4 flux on RHEED oscillations during growth of GaAs at low temperatures", North American Workshop on Molecular Beam Epitaxy, Stanford, CA, September (1993).
24. M. Shimizu, W. Jiang, R. P. Mirin, T. E. Reynolds, and J. E. Bowers, "External-Cavity Mode-Locked Surface-Emitting Lasers," Photonic Switching Systems and Devices, Tokyo, Japan, October 22 (1993).
25. J. J. Dudley, D. I. Babić, L. Yang, R. Mirin, B. I. Miller, R. J. Ram, T. Reynolds, E. L. Hu, and J. E. Bowers, "Wafer Fused Long Wavelength Vertical Cavity Lasers," IEEE Lasers and Electro-optics Society Annual Meeting, paper SCL4.1, San Jose, CA, November 15-18 (1993).
26. J.J. Dudley, D. I. Babić, R. Mirin, L. Yang, B. I. Miller, E. L. Hu, and J. E. Bowers, "Wafer Fused, Low Threshold, Long Wavelength Vertical Cavity Lasers on GaAs Substrates," AFCEA Conference, McLean, VA, March 22-24 (1994).
27. D. I. Babić, J. J. Dudley, K. Streubel, R. P. Mirin, E. L. Hu, and J. E. Bowers, "Optically Pumped All-Epitaxial Wafer-Fused 1.52-μm Vertical Cavity Lasers," Indium Phosphide and Related Materials Conference, paper WA4, Santa Barbara, CA, March 28-30 (1994).
28. J. J. Dudley, D. I. Babić, R. Mirin, L. Yang, B. I. Miller, E. L. Hu, and J. E. Bowers, "Temperature and Transverse Mode Characteristics of InGaAsP (1.3 μm) Vertical Cavity Lasers on GaAs Substrates," Indium Phosphide and Related Materials Conference, paper WA3, Santa Barbara, CA, March 28-30 (1994).

29. J.E. Bowers, D.I. Babić, J.J. Dudley, R.P. Mirin, R.J. Ram, and E.L. Hu, "Long-wavelength vertical-cavity lasers," paper 14D3-1, Fifth Optoelectronics Conference, Makuhari, Chiba, Japan, July 12-15 (1995) **(Invited)**.
30. D. I. Babić, J. J. Dudley, K. Streubel, R. P. Mirin, N.M. Margalit, E. L. Hu, and J. E. Bowers, "Double-fused 1.52-μm Vertical Cavity Lasers," 1994 IEEE Laser and Electro-Optics Annual Mtg., paper PD1.3, Boston, MA, Oct. 31-Nov. 4 (1994).
31. D. I. Babić, J. J. Dudley, R. P. Mirin, J. E. Bowers, and E.L. Hu, "Long-wavelength Vertical Cavity Lasers," 1994 International Electron Devices Mtg., paper 31.1, San Francisco, CA, Dec. 11-14 (1994) **(Invited)**.
32. D. I. Babic, J. J. Dudley, R. J. Ram, R. P. Mirin, J. E. Bowers, and E. L. Hu, "Long Wavelength Vertical Cavity Surface Emitting Lasers," Integrated Photonics Research Topical Meeting, Paper IFA1, Dana Point, CA, February 23-25 (1995) **(Invited)**.
33. R. Mirin, J. Ibbetson, K. Nishi, A. Gossard, and J. Bowers, "1.32 μm room temperature photoluminescence from InGaAs quantum dots on GaAs," Quantum Optoelectronics, paper QThC3, March 15-17, 1995.
34. K. Nishi, R. Mirin, D. Leonard, G.M. Ribeiro, P. Petroff, and A. Gossard, "InAs/InGaAs Self-assembled Quantum Dots Grown on (311)B GaAs by molecular beam epitaxy," 7th International Conference on InP and Related Materials, Sapporo, Hokkaido, Japan, May 9-13 (1995).
35. D. I. Babic, J. J. Dudley, K. Streubel, R. P. Mirin, N. Margalit, J. E. Bowers and E. L. Hu, "Transverse Mode and Polarization Characteristics of Double-fused 1.52μm Vertical-cavity Lasers," 7th International Conference on InP and Related Materials, Sapporo, Hokkaido, Japan, Paper SB1-2, May 9-13 (1995).
36. D. I. Babić, I-H. Tan, R. P. Mirin, J. E. Bowers, and E.L. Hu, "Wafer fusion for optical communication applications," 1995 Conference on Lasers and Electro-optics, paper CWB7, Baltimore, MD, May 22-26 (1995). **(Invited)**
37. R.P. Mirin, J.P. Ibbetson, J.E. Bowers, and A.C. Gossard, "Room Temperature Photoluminescence at 1.32 μm from InGaAs Quantum Dots on GaAs Substrates," 37th Electronic Materials Conference, Charlottesville, VA, June 21-23, 1995.
38. D. I. Babic, K. Streubel, R. P. Mirin, N. M. Margalit, J. E. Bowers, E. L. Hu, D. E. Mars, L. Yang, and K. Carey, "Room-temperature continuous-wave operation of 1.54 μm vertical-cavity lasers," IOOC-95 Conference, Hong Kong, June 26-30 (1995).
39. N.M. Margalit, D.I. Babic, K. Streubel, R.P. Mirin, J.E. Bowers, and E.L. Hu, "Laterally oxidized long-wavelength cw vertical cavity lasers," OFC '96. Optical Fiber Communication. Vol.2. 1996 Technical Digest, February 25-March 1, 1996. San Jose, CA.
40. R. Mirin, A. Gossard, and J. Bowers, "Room temperature lasing from excited states of InGaAs quantum dots," paper 2.4, International Conference on Quantum Devices and Circuits, Alexandria, Egypt, June 4-8, 1996.
41. D. I. Babic, K. Streubel, R. P. Mirin, J. Piprek, N. M. Margalit, J. E. Bowers, E. L. Hu, D. E. Mars, L. Yang, K. Carey, "Room-temperature performance of double-fused 1.54 um vertical-cavity lasers," submitted to 8th Int. Conf. on Indium Phosphide and Related Materials, Schwabish Gemund, Germany, 1996. **(Invited)**
42. R.P. Mirin, A.C. Gossard, and J.E. Bowers, "Room-temperature lasing from excited states of InGaAs quantum dots," 1996 Electronic Materials Conference, Santa Barbara, CA, June 26-28, 1996.
43. R.P. Mirin, J.E. Bowers, and A.C. Gossard, "Alternating MBE formation of multiple layers of InGaAs quantum dots and application to quantum dot lasers," 9th International Conference on Molecular Beam Epitaxy (MBE IX), paper 3.2, Malibu, CA, August 5-9, 1996.

44. N.M. Margalit, D.I. Babic, K. Streubel, R.P. Mirin, R.L. Naone, J.E. Bowers, and E.L. Hu, "Submilliamp long-wavelength vertical cavity lasers," 15th IEEE International Semiconductor Laser Conference, paper M3.5, October 13-18, 1996, Haifa, Israel.

Abstract

Alternating molecular beam epitaxy is used to grow quantum dots of InGaAs on GaAs via the Stranski-Krastanow growth transition. These quantum dots can emit light at wavelengths as long as 1320 nm at room temperature. Quantum dot lasers have been grown and fabricated using methods that are practically identical to those used to form quantum well lasers. The quantum dot lasers exhibit very strong state-filling. At room temperature, state-filling leads to lasers whose lasing wavelength depends strongly on the threshold current density; shorter lasers require larger threshold current densities and thus have more state-filling and a correspondingly longer wavelength emission than longer lasers. These state-filling effects are less pronounced as the laser is cooled and the threshold current density decreases. This leads to a compensation of the bandgap increase with decreasing temperature, yielding lasers that have a very stable lasing wavelength over the temperature range of 80-300 K.

Table of Contents

Chapter 1: Introduction....1
- 1.1 Molecular Beam Epitaxy....2
- 1.2 MBE Growth Modes....3
- 1.3 Other Quantum Dot Fabrication Methods....6
- 1.4 Density of States....7
- 1.5 Quantum Dot Lasers....8
- 1.6 Dissertation Outline....9

Chapter 2: Alternating Molecular Beam Epitaxy of InGaAs and Photoluminescence: I....11
- 2.1 Introduction....11
- 2.2 Intial Alternating Molecular Beam Epitaxy Developments....12
- 2.3 Multilayer Samples....18
- 2.4 Single InGaAs Epilayers....23
- 2.5 Summary....32

Chapter 3 Photoluminescence II: Temperature-dependence and Intensity-dependence....35
- 3.1 Introduction....35
- 3.2 Temperature-dependent PL....36
- 3.3 Intensity-dependent PL....53
- 3.4 Summary....65

Chapter 4 Morphological and Structural Characterization of InGaAs Islands....67
- 4.1 Introduction....67
- 4.2 Reflection High Energy Electron Diffraction....68
- 4.3 Atomic Force Microscopy....72
- 4.4 X-ray Diffraction....97
- 4.5 Transmission Electron Microscopy....109
- 4.6 Summary....113

Chapter 5 AMBE Issues and Optimization: Overgrowth and Multiple Layers....115
- 5.1 Introduction....115
- 5.2 Overgrowth Optimization....116
- 5.3 Barrier Thickness Effects on Multiple Layer Samples....126
- 5.4 Optimization of Growth Temperature....131
- 5.5 Smaller Dots and Multiple Layers of Smaller Dots....138
- 5.6 Summary....148

Chapter 6 Quantum Dot Lasers....151
- 6.1 Introduction....151
- 6.2 Experimental Procedures....153
- 6.3 Rayleigh Scattering Limits on Quantum Dot Lasers....169
- 6.4 Summary....173

Chapter 7 Conclusions..........175
7.1 Introduction..........175
7.2 Future Work..........176
7.3 Summary..........179

Appendix A: .Growth Log..........181
A.1 Introduction..........181
A.2 Photoluminescence Samples..........182
A.3 Photoluminescence Reference Samples..........185
A.4 Overgrowth Samples..........186
A.5 Smaller Dots..........187
A.6 Growth Temperature Optimization Samples..........189
A.7 X-ray Samples..........190
A.8 Atomic Force Microscopy Samples..........192

Appendix B: AFM Analysis..........193

Bibliography..........215

Chapter 1: Introduction

One of the first problems that students of quantum mechanics solve is that of the "particle-in-a-box." This problem involves calculating the distribution of allowed energy states of a particle confined inside a three-dimensional box with infinitely high barriers. This problem is quite easily solvable in closed form, and it points out the discrete nature of allowed states in quantum-confined systems. But until recently, the idea of actually making a particle-in-a-box was not a possibility.

The one-dimensional version of the particle-in-a-box problem is called a quantum well. The particle is constrained by barriers in one dimension, but is free in the two orthogonal dimensions. This problem has also been around for many years (see Weisbuch and Vinter, 1991 for a review of the properties of quantum wells), but the question of how to make a quantum well has only been solved in the last twenty years. The basic idea is to sandwich a thin film of semiconductor (the quantum well) between barriers consisting of semiconductors with larger bandgaps. The first demonstrations of quantum effects were at Bell Laboratories in 1974 by Dingle (Dingle, Wiegmann, and Henry, 1974) and at IBM in 1974 by Esaki and Chang (Esaki and Chang, 1974). However, it was several more years before the particle-in-a-box, or **quantum dot**, was realized.

In this dissertation I will describe the fabrication and characterization of quantum dots and quantum dot lasers. These quantum dots are formed *in situ* by using alternating molecular beam epitaxy to deposit strained InGaAs on GaAs. They can emit light at room temperature at wavelengths as long as 1300 nm, which is a much larger wavelength then can be obtained with a InGaAs quantum well on GaAs.

Careful control of the overgrowth and burial of these quantum dots has led to the development of quantum dot lasers. These lasers exhibit very stable wavelength operation over a wide temperature range because of a compensation between state-filling and bandgap change. The strong state-filling effects also lead to quantum dot lasers whose emission wavelength varies strongly with the laser length, due to the variation in mirror loss.

1.1 Molecular Beam Epitaxy

Atomic-level control of epitaxial layers was first achieved using the technique which is designated **molecular beam epitaxy** (MBE). This technique was first developed by John Arthur at Bell Laboratories in 1967, and large advances were made by Al Cho at Bell Laboratories in the late 1960's and early 1970's to bring MBE to the forefront of epitaxial growth technologies. Arthur's work (Arthur, 1967) shows that a three-temperature, ultrahigh vacuum scheme can be used to deposit homoepitaxial layers of GaAs. This has been developed for all III-V semiconductors, as well as IV-VI semiconductors, metal-on-metal epitaxy, II-VI semiconductors, and just about every combination of the above. There is substantial literature on the subject (Parker, 1985, Tsao, 1993, Cho, 1994) of MBE, but a brief description of III-V MBE will facilitate reading of this dissertation for those unfamiliar with the topic.

The basic idea of MBE is that by working in an ultrahigh vacuum (UHV) environment, an epitaxial film can be extremely pure since there are very few residual impurity gases such as H_2O or O_2 which can contribute impurity atoms to the epitaxial film. Atoms or molecules can be evaporated onto a substrate without

encountering impurity atoms or molecules, or even other evaporated atoms. Thus comes the name **molecular beam.** High quality III-V semiconductor films are often limited by impurities in the evaporated source materials, rather than by residual impurities in the vacuum chamber.

III-V semiconductors, in particular GaAs, were the first materials deposited by MBE. Arthur found that no As_4 molecules stuck to a heated GaAs surface unless there was some Ga already deposited on the GaAs surface. Conversely, all the Ga atoms stuck to the GaAs surface except at very high temperatures. So, by co-depositing Ga and As_4, he was able to demonstrate epitaxial growth of GaAs at temperatures very far from the near-equilibrium temperatures used in liquid phase epitaxy (LPE), which was the dominant technique for depositing epitaxial films at that time. More importantly, though, was the demonstration that MBE could be used to get precise control of the epitaxial film thickness, down to monolayer precision. This was the first big step to obtaining precision control over epitaxial film thicknesses, heteroepitaxial interfaces, and dopant positioning. This has led to commercialization of several devices, such as semiconductor lasers for use in compact disc players and laser printers and transistors for use in cellular phones. Many other applications have already been demonstrated and undoubtedly many more will follow.

1.2 MBE Growth Modes

One of the main advantages of MBE over other epitaxial growth techniques is the ability to obtain atomically-smooth layers and interfaces between layers. A materials scientist would say that the films grow in the Frank-van der Merwe mode (see Figure 1-1 (a)). This is a layer-by-layer growth mode that is generally favored

by crystal growers since it minimizes interface roughness, which is a major cause of inhomogeneous broadening in quantum wells (particularly narrow quantum wells) and scattering of electrons in two-dimensional electron gases.

Homoepitaxial films usually grow in a layer-by-layer manner unless unusual conditions, such as high impurity level concentrations, exist. Heteroepitaxial films may also grow in a layer-by-layer manner, but they can also grow in one of two **island** growth modes. The first one is known as the Volmer-Weber growth mode (see Figure 1-1 (b)). In this mode, not even a single monolayer of the deposited material will cover the surface of the substrate. Instead, islands of material immediately form.

In the Stranski-Krastanow growth mode (layer-plus-island), the first monolayer of deposited material uniformly covers the surface (it **wets** the surface), but the subsequent layers form islands (see Figure 1-1 (c)). It is often desirable to grow heteroepitaxial films which are not lattice-matched, such as $In_xGa_{1-x}As/GaAs$ or Ge/Si. Despite the lattice-mismatch, the growing film will remain **pseudomorphic** as long as the thickness is below some so-called "critical thickness." The critical thickness does **not** imply anything about dislocation formation. In cases of large lattice-mismatch, the mechanism for strain-release is the formation of three-dimensional islands on the surface. The islands partially relieve the strain in the film because each atomic plane is no longer constrained to line up with the underlying substrate; instead, some bowing is allowed, especially near the edges of the islands. Thus, the driving force for island formation is the reduction of strain energy.

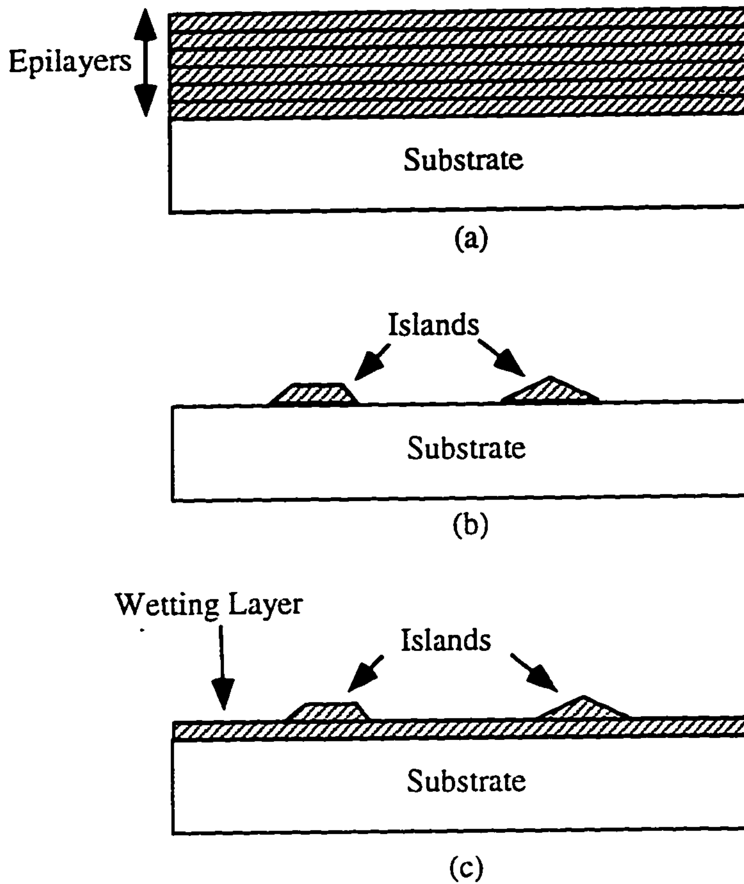

Figure 1-1 (a) Frank-van der Merwe (layer-by-layer) growth,
(b) Volmer-Weber (island) growth
(c) Stranski-Krastanow (layer-plus-island) growth

The Stranski-Krastanow growth of InGaAs on GaAs is the method that is used for the fabrication of the quantum dots described in this dissertation. This technique was originally proposed as a method of forming reduced dimensional structures (quantum dots) by Goldstein *et al.*, 1985. However, it was only in 1993 (Leonard *et al.*, 1993, Moison *et al.*, 1994) that this method became popular and the real evidence for three-dimensional confinement began to arise.

1.3 Other Quantum Dot Fabrication Methods

Several different methods have been used for fabrication of quantum dot arrays. For II-VI semiconductors, precipitation from solution is widely used (Rodden, Sotomayor-Torres, and Ironside, 1995). However, this is not readily compatible with standard device fabrication methods since the glass matrix that surrounds the quantum dots in electrically insulating.

Most other quantum dot fabrication methods involve starting with a quantum well and then modifying the potential with lateral patterning. These methods include etch-and-regrowth (Hirayama *et al.*, 1994), patterned stressors (Kash *et al.*, 1992), and patterned gates (Wharam *et al.*, 1994). The etch-and regrowth method is the best technique for integration of quantum dots into real devices such as lasers. However, there are several drawbacks to this technique, including difficulty in forming large, uniform arrays because of the e-beam lithography required, as well as damage induced by the etching. The difficulties in fabrication have hampered research in the area of quantum dot devices. However, using the Stranski-Krastanow growth mode described earlier, researchers are beginning to understand the physics and fabrication of quantum dots at unprecedented levels.

The Stranski-Krastanow growth technique has many advantages over other methods of fabricating quantum dots since the Stranski-Krastanow dots are formed *in situ*, during crystal growth. First, these Stranski-Krastanow quantum dots are extremely easy to fabricate since they involve no external processing. Second, the interfaces are buried without ever being exposed to air. And third, it is possible to make extremely small quantum dots by careful control of the growth conditions.

1.4 Density of States

The interest in fabricating quantum structures, such as quantum wells, quantum wires, and quantum dots, comes from the modification of the **density of states** (DOS) (see Figure 1-2) that arises due to the quantization. For a bulk semiconductor, the DOS is given by the expression

$$\rho(E)dE = \frac{\sqrt{E}}{2\pi^2}\left[\frac{2m^*}{\hbar^2}\right]^{3/2} . \tag{1-1}$$

For a quantum well with thickness L_Z, the DOS is given by

$$\rho(E)dE = \frac{m^*}{\pi\hbar^2 L_z}. \tag{1-2}$$

For a quantum wire with thickness L_Z and lateral dimension L_X, the DOS is given by

$$\rho(E)dE = \frac{2}{\pi L_x L_z \sqrt{E}}\left[\frac{2m^*}{\hbar^2}\right]^{1/2} . \tag{1-3}$$

Finally, for the case of a single quantum dot, the DOS is simply a delta function, with the height of the delta function equal to the degeneracy of the given state. For an ideal array of quantum dots, the degeneracy is also multiplied by the dot density.

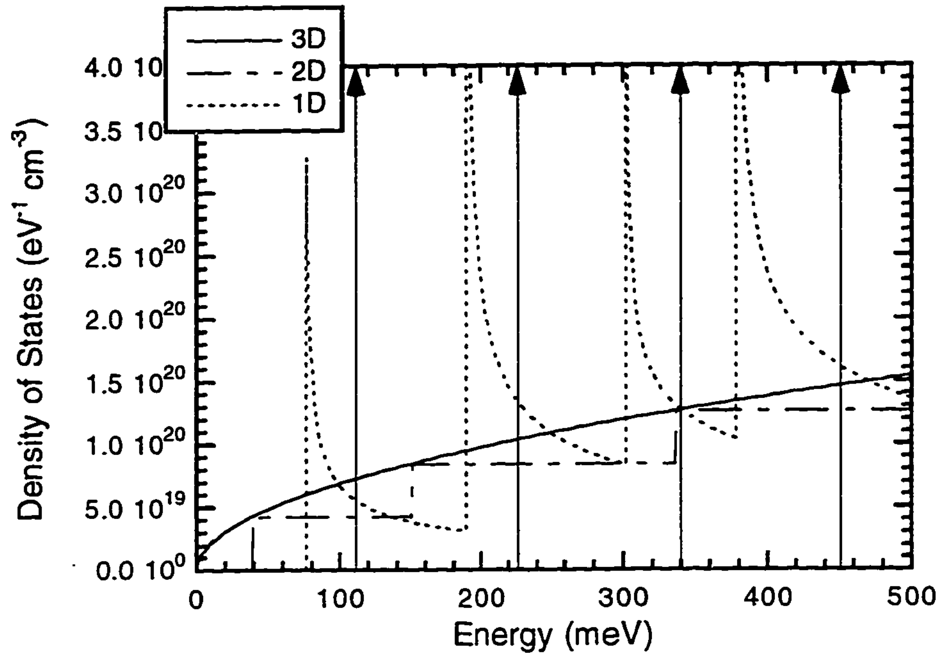

Figure 1-2 Density of states for bulk, quantum well, quantum wire and quantum dot. The height of the quantum dot delta function is determined by the degeneracy of the state.

The important thing to notice in the above equations is the energy-dependence of the DOS. This energy dependence, convoluted with the Fermi-Dirac distribution function, determines how the electrons and holes are distributed as the number of carriers increases. This in turn will determine the gain in a semiconductor laser; further details will be discussed in Chapter 6.

1.5 Quantum Dot Lasers

The modification of the DOS in a quantum dot has led to many predictions about improved performance of quantum dot lasers compared to bulk and quantum well lasers. The first analysis of a so-called "multidimensional quantum well"

(quantum dot) laser came from Arakawa and Sakaki in 1982. They predicted that a quantum dot laser should have a characteristic temperature, T_0 ($I=I_0\exp(T/T_0)$), that is infinite.

Other predictions about improved performance in quantum dot lasers include high gain coefficients, large differential gain, and low threshold currents (Asada, Miyamoto, and Suematsu, 1986). These predictions of improved performance have provided the incentive for researchers to investigate techniques for fabricating arrays of quantum dots. However, only with the recent advances in Stranski-Krastanow growth of InGaAs on GaAs have researchers begun to investigate the properties of quantum dot lasers. For further discussions about research in this area, see Chapter 6 of this dissertation.

1.6 Dissertation Outline

Chapter 2 describes the initial experiments on alternating MBE growth of InGaAs quantum dots and the characterization of these quantum dots using photoluminescence (PL). Chapter 3 presents additional PL measurements on some of the samples described in Chapter 2. Both intensity-dependent PL and temperature-dependent PL are used to obtain additional information about the optical properties of the quantum dots. Chapter 4 shows all of the morphological and structural information obtained on these quantum dots. Measurements presented in this chapter include reflection high energy electron diffraction, atomic force microscopy, high resolution X-ray diffraction, and transmission electron microscopy. Chapter 5 discusses additional experiments aimed at optimizing the growth and burial of the quantum dots, as well as experiments on multiple layers of quantum dots. Chapter 6

puts all of the work of the previous chapters together into growth and characterization of quantum dot lasers. Finally, Chapter 7 summarizes the important results in this dissertation and suggests avenues for future work.

Chapter 2: Alternating Molecular Beam Epitaxy of InGaAs and Photoluminescence: I

2.1 Introduction

In this chapter I will describe the initial experiments in which alternating molecular beam epitaxy (MBE) is used to deposit $In_xGa_{1-x}As$ on (100) GaAs substrates. Conventional III-V MBE uses **simultaneous** beams of Group III and Group V elements; a variation of this is called **alternating** MBE (AMBE). In AMBE, the Group V flux (this is always diatomic arsenic, As_2, in these experiments) is modulated, as well as the Group III flux (Ga and In, in these experiments). The advantage of AMBE compared to conventional MBE is that with AMBE the Group III adatoms can diffuse longer distances on the surface before incorporating. This is often called **MEE** (migration-enhanced epitaxy) (Horikoshi, Kawashima, and Yamaguchi, 1988), especially when depositing full monolayers of the Group III element.

I will also discuss photoluminescence (PL) measurements on the samples grown by AMBE. PL describes the process by which an incident light source impinges on a semiconductor, creating electron-hole pairs by exciting electrons from the valence band into the conduction band (Pankove, 1971). The incident light source is usually a laser that excites the electrons high up into the conduction band. The carriers then recombine radiatively or nonradiatively. We are interested in the carriers that recombine radiatively and thus emit photons. The emitted photons are focused onto a spectrometer that has a grating to spatially disperse the light. The

spatially dispersed light is incident on a photodetector that converts this light to an electrical signal.

In the PL measurements described in this section, the light source is an argon ion laser that emits at 488 nm and 514.5 nm. The spectrometer is either a Spex 1404 (0.85 m double-grating) or a McPherson 2051 (single-grating). The photodetector is a North Coast EO-817A Ge photodiode operating at 77 K with a built-in low noise preamplifier. A Stanford Research Systems Model SR540 optical chopper is used to modulate the incident laser beam, and the output signal from the Ge detector is measured with a lock-in amplifier.

In the following sections, the MBE growth sequence that is used to form coherently-strained, quantum-sized islands (dots) of InGaAs is described, including the evolution of the epilayer design used to obtain the first report of 1.3 μm room-temperature PL (RTPL) from InGaAs quantum dots grown by AMBE on (100) GaAs substrates. RTPL measurements used to characterize these samples are also described. Morphological characterization and additional PL measurements on these samples will be described later in this dissertation.

2.2 Initial Alternating Molecular Beam Epitaxy Developments

2.2.1 Background and Preliminary Observations

The first samples grown by AMBE are patterned regrowth samples (Mirin *et al.*, 1992, Mirin *et al.*, 1993). *In situ* Cl_2 etching is used to fabricate InGaAs, V-groove quantum wires on GaAs. A sample of (100) GaAs with SiO_2 as an etch mask

is patterned, leaving 1.2 μm gaps in the SiO_2 so that the Cl_2 could etch the exposed GaAs and form V-grooves. This patterned sample is mounted along with a planar reference sample (also (100) GaAs) on a molybdenum sample holder for etch-and-regrowth experiments. AMBE is used to grow these samples because the Ga and In atoms can diffuse from where they impinge on the surface to the bottom of the V-groove in order to form a quantum wire there. It is well-known that In has a much larger diffusion length than Ga (Kapon, 1994, and references therein). InAs has a much lower melting temperature than GaAs (942°C versus 1238°C), which indicates that the In-As bond strength is weaker than the Ga-As bond strength (Casey and Panish, 1978, Lide, 1990). Thus, it is more difficult for an In adatom to become chemisorbed than for a Ga adatom, and it may thus be possible to obtain higher In mole fraction at the bottom of the V-groove than along the sidewalls.

While growing these quantum wire samples, the reflection high-energy electron diffraction (RHEED) pattern is monitored from both the patterned sample and the planar reference sample. During the growth of the InGaAs layers, the RHEED pattern from the planar sample often changed from streaky, which is indicative of two-dimensional, layer-by-layer growth, to spotty, which is indicative of three-dimensional, island growth (for additional information regarding RHEED patterns, see Chapter 4, Morphological and Structural Characterization of InGaAs Islands, of this dissertation). No steps are taken to prevent this from happening because the main concern is the patterned quantum wire sample. However, In could be segregating to the growth front due to the unusual growth technique used, thus giving a highly strained, In-rich surface that exceeds the critical thickness for layer-by-layer growth. It is well-known that In can segregate to the surface during MBE growth of InGaAs, especially under conditions of high-temperature and/or low arsenic flux

(Ebner and Arthur, 1987, Yamaguchi and Horikoshi, 1989, Yamaguchi and Horikoshi, 1990, Houzay*et al.*, 1989, Brandt *et al.*, 1993, Gerard *et al.*, 1993, Hayakawa *et al.*, 1993, Muraki *et al.*, 1993, Nagle *et al.*, 1993).

2.2.2 First AMBE Experiments

In order to better understand the effects of growing on a Cl_2-etched surface, a control sample (QDPL-01) (see Appendix I for more details on the individual layer structures) is grown on an unetched, thick buffer layer of GaAs. The layer structure is shown in Figure 2-1. The thick buffer layer ensured that the InGaAs

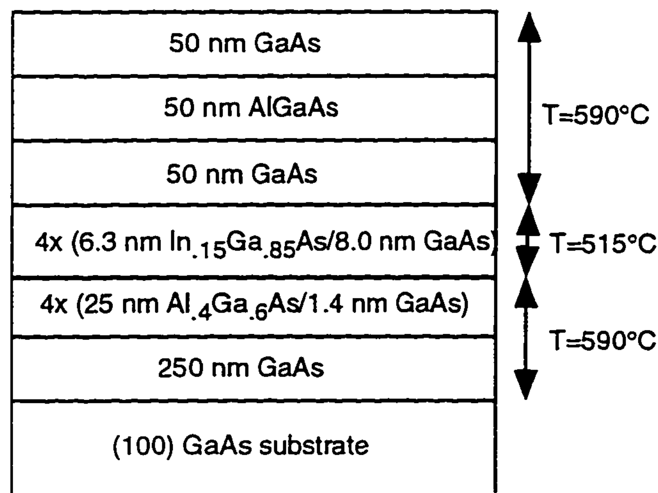

Figure 2-1 Layer diagram for QDPL-01.

epilayer is far removed from any polishing damage on the original substrate or any point defects that are due to contamination of the oxide-desorbed surface. This is standard MBE practice, but it is not possible for the regrowth samples because a thick buffer layer would planarize the V-groove too much, leaving a rounded surface that is unsuitable for quantum wire growth.

Low temperature PL and RTPL spectra from QDPL-01 are shown in Figures 2-2 and 2-3, respectively. One surprising result from these RTPL measurements is that the peak wavelength is much larger than anticipated. Theory predicts a peak at around 950 nm, but instead a peak is observed around 1160 nm. The reason for this long wavelength peak is unclear; however, it is extremely interesting since long wavelength emission is difficult to obtain from InGaAs on GaAs It is particularly important to shift the wavelength out to 1.3 μm, which is technologically important for fiber optic communications.

The other surprising result from this sample is in the measured linewidths. The room temperature full width at half maximum (FWHM) is 62.4 meV, and the FWHM at 1.4 K is 67.5 meV. The intensity is good, so the material quality is not suspect. However, these linewidths are surprisingly large, especially the low temperature linewidth (a good InGaAs QW usually has a low temperature linewidth less than 10 meV). One possible explanation is that the four InGaAs epilayers have somehow become different thicknesses, which would lead to a spread in peak emission wavelengths. This is qualitatively consistent with the RHEED pattern observations during the InGaAs growth: the RHEED pattern during each subsequent InGaAs layer showed the transition to three-dimensional growth more quickly than the previous InGaAs layer.

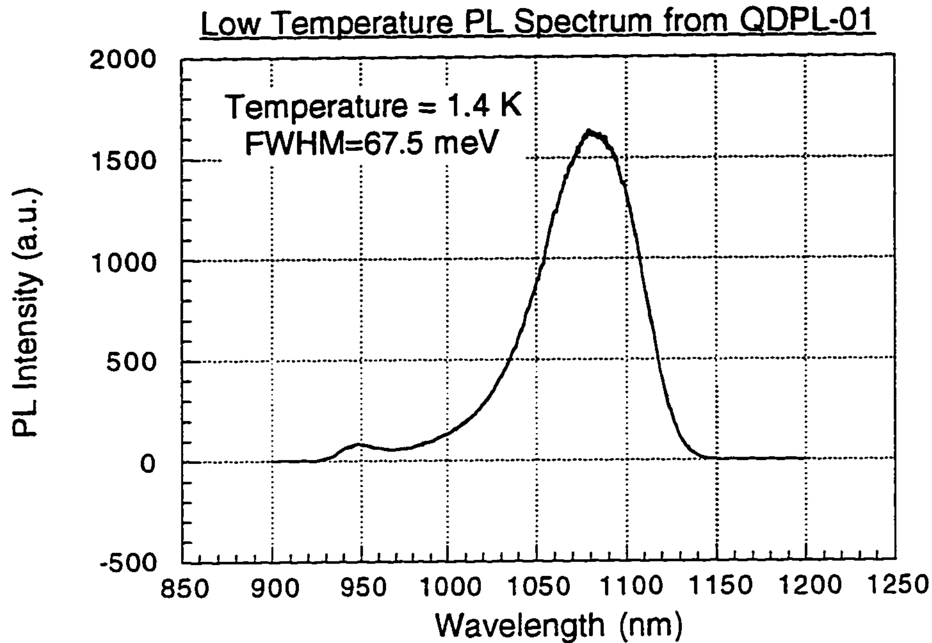

Figure 2-2 PL spectrum at 1.4 K from QDPL-01 exhibits a much broader low temperature linewidth than is typical from a smooth quantum well.

2.2.3 *Three-dimensional Growth from a Single InGaAs Epilayer*

Another sample (QDPL-02) is grown that is similar to the regrowth control sample (QDPL-01). The main difference is that QDPL-02 (Figure 2-4) has only a single 19.6 monolayer (ML) (5.54 nm) $In_{0.17}Ga_{0.83}As$ epilayer, instead of the four InGaAs epilayers used in QDPL-01. The RHEED pattern changes from 2D-to-3D after about 16 MLs (4.53 nm) are grown. This confirms that the reason for the spotty pattern is not a rough initial surface due to the growth of a buffer layer that is too thin to provide a smooth starting surface.

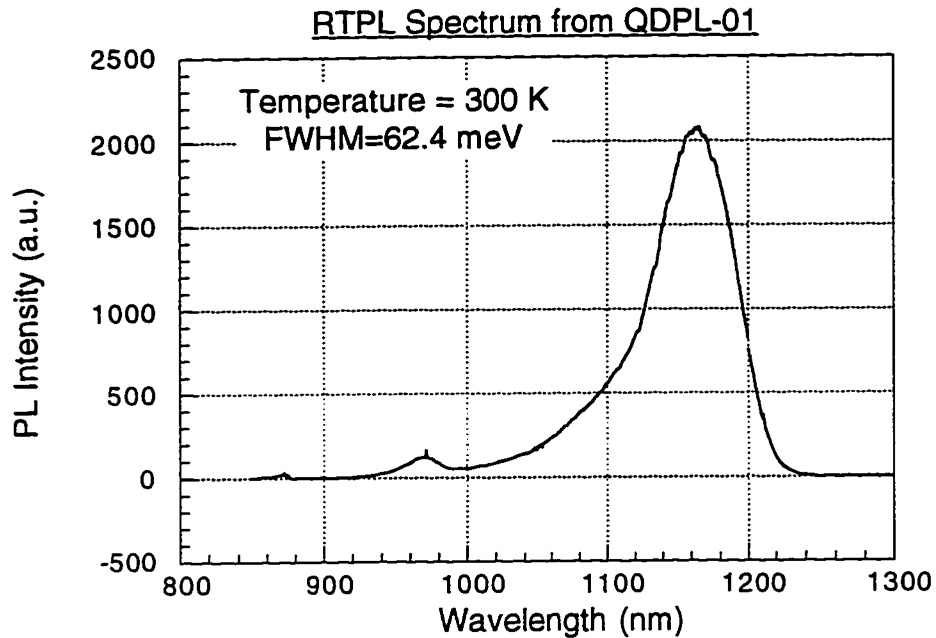

Figure 2-3 RTPL spectrum from QDPL-01 has a peak emission around 1150 nm, despite the fact that the QW was designed for 950 nm at 300 K.

2.2.4 Reduced Substrate Temperature

The observed behavior is now known to be due to the InGaAs; one possible cause of this behavior is that the In is segregating to the surface and causing the surface to become In-rich. This would lead to a lower critical thickness for layer-by-layer growth than expected. The identical structure to QDPL-02 is then grown, except at a reduced temperature (QDPL-03). Lowering the temperature should reduce the amount of In segregating to the surface. This experiment is only a moderate success-the RHEED transition from 2D-to-3D is observed after deposition of 16.9 MLs (4.81 nm), only slightly thicker than the previous sample.

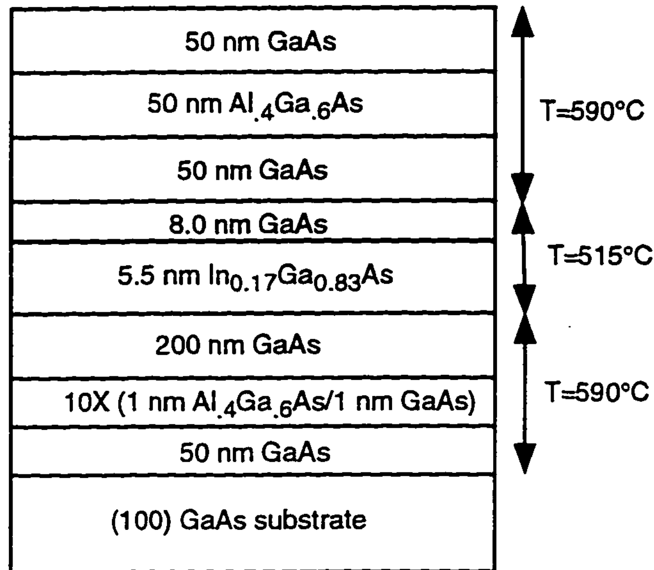

Figure 2-4 Layer diagram for QDPL-02. Note that the same structure is used for QDPL-13 to -20, except for the InGaAs composition and thickness. See Appendix A for detailed descriptions of the InGaAs layers.

2.3 Multilayer Samples

2.3.1 Preliminary Growths

I decided that substrate temperature might be the wrong parameter to investigate now- if a large fraction of the In is segregating, then changing the temperature by 0.04 k_BT would not be enough to change the behavior very much. Since changing the substrate temperature didn't affect the growth very much, I attempted to vary the In content in the QW, and also to try multiple layers of InGaAs, similar to the etch-and-regrowth samples and QDPL-01. The next sample grown, QDPL-04, has two layers of 22.0 monolayers (6.23 nm) of $In_{0.15}Ga_{0.85}As$, separated by 8.0 nm of GaAs. The RHEED pattern remains two-dimensional during the entire growth. Another sample is then grown that is similar to previous samples

(QDPL-01) in which the 2D-to-3D transition is observed. QDPL-05 has an increased In mole fraction (19%) and an increased thickness to 20.0 MLs (5.67 nm). The number of $In_{0.19}Ga_{0.81}As$ epilayers is also increased to three since previous experiments (on etch-and-regrowth samples) showed that the RHEED pattern transition to three-dimensional growth occurred with a smaller deposited thickness for subsequent layers.

The RHEED pattern from this sample displays the expected 2D-3D transition. The first $In_{0.19}Ga_{0.81}As$ epilayer shows signs of three-dimensional growth after about 17.6 MLs (4.98 nm) of the 20.0 ML total thickness have been completed. The second $In_{0.19}Ga_{0.81}As$ epilayer shows signs of 3D growth after 15.6 MLs have been completed. The third $In_{0.19}Ga_{0.81}As$ epilayer is even more dramatic: after only 9.8 MLs have been grown, the RHEED pattern shows signs of three-dimensional growth. Based on these observations of the RHEED pattern transitions, two additional samples are grown, one with two $In_{0.19}Ga_{0.81}As$ epilayers (QDPL-06) and one with five $In_{0.19}Ga_{0.81}As$ epilayers (QDPL-07).

2.3.2 Room temperature PL measurements on Preliminary Growths

RTPL measurements are carried out on these samples, and the spectra are shown in Figures 2-5 to 2-8. The spectrum from QDPL-04 (two QWs, 22.0 monolayers (6.23 nm) of $In_{0.15}Ga_{0.85}As$, no signs of three-dimensional growth) shows one narrow peak (Figure 2-5) at 952 nm with a FWHM of 20.5 meV. The RTPL spectrum from QDPL-06 (two $In_{0.19}Ga_{0.81}As$ epilayers) is shown in Figure 2-6. There are two peaks visible in this spectrum, one at 970 nm (FWHM = 27.0 meV) and a weak, broad peak around 1050 nm. The peak at 970 nm can probably be

attributed to the InGaAs layer that is closest to the substrate because that layer is not very rough compared to the latter InGaAs layer. The broad, double-peak around 1050 nm must then come from the second InGaAs layer.

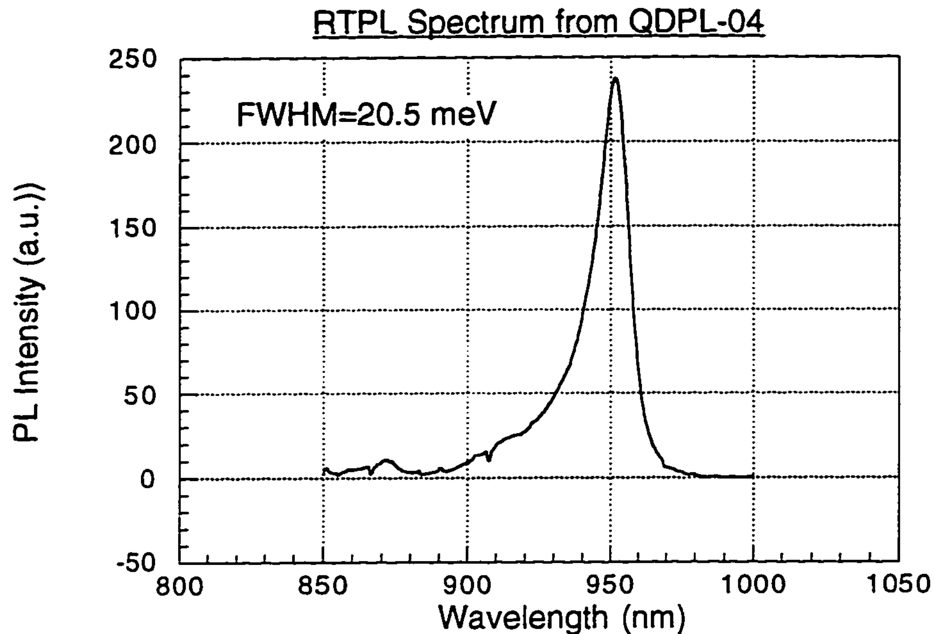

Figure 2-5 RTPL spectrum from QDPL-04 shows the narrow linewidth expected from a smooth QW.

The RTPL spectrum from QDPL-05 exhibits multiple peaks, and the most intense peak is at a much longer wavelength than the peak from the quantum wells of QDPL-04. As seen in Figure 2-7, there are two peaks in the spectrum, one at 1150 nm with a FWHM of 54.4 meV, and another at 970 nm with a FWHM of 30.5 meV. The peak at 970 nm can probably be attributed to the InGaAs layer that is closest to the substrate because that layer is not very rough compared to the latter two InGaAs layers. The peak at 1150 nm is due to emission from the latter two InGaAs layers, with the dominant emission coming from the layer that is closest to the surface. Note that the shoulder that appears around 1100 nm corresponds to the broad peak seen in

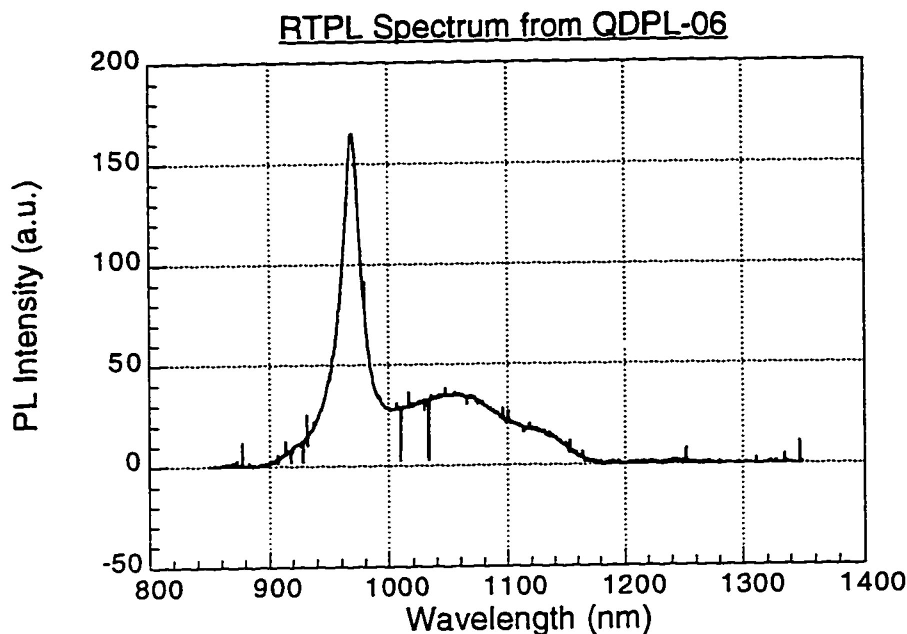

Figure 2-6 RTPL spectrum from QDPL-06 (two InGaAs epilayers). The narrow, low energy peak comes from the InGaAs layer closest to the substrate.

QDPL-06 in Figure 2-6.

The RTPL spectrum from QDPL-07 (five InGaAs layers) has three distinct peaks (Figure 2-8), around 1235 nm, 1190 nm, and 970 nm. As with the previous samples, the longer wavelength peaks can be attributed to the layers closest to the surface. In Figure 2-8, the relative intensities of the two longest wavelength peaks displays unusual behavior as the pump power is changed. As the pump power is increased, the shorter wavelength peak becomes larger than the longer wavelength peak. This is somewhat surprising since the lower energy transition should be more efficient at capturing carriers. This behavior will be investigated in more detail later.

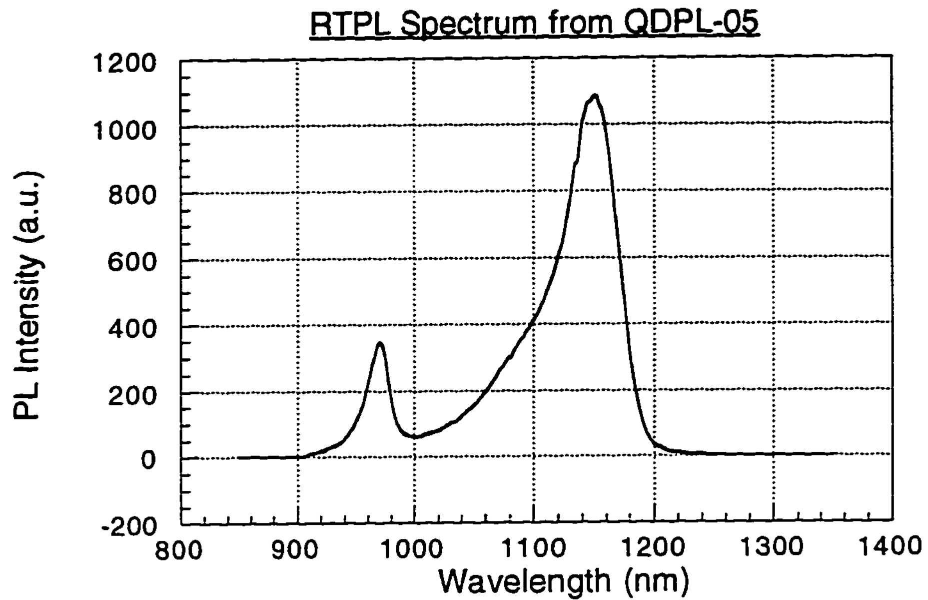

Figure 2-7 RTPL spectrum from QDPL-05 (three InGaAs layers). The higher energy peak is from the InGaAs layer closest to the substrate.

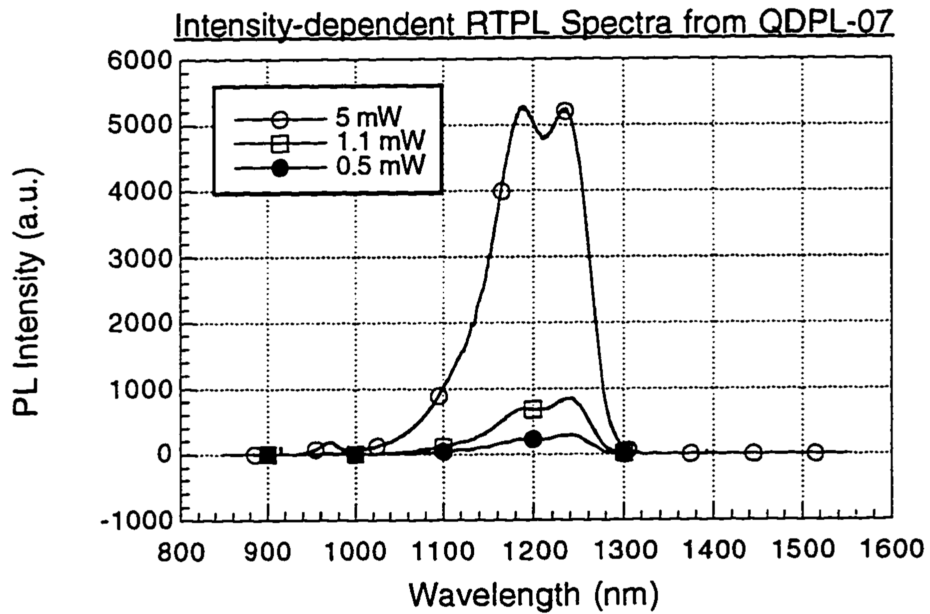

Figure 2-8 RTPL spectra from QDPL-07 (five InGaAs layers) at various pump powers. The maximum wavelength is around 1240 nm.

2.4 Single InGaAs Epilayers

2.4.1 Preliminary Growths: Lower Indium Mole Fraction, Thicker Epilayers

The multilayer samples discussed in the previous section demonstrate that it is possible to shift the wavelength out beyond what is typically possible with an InGaAs QW on GaAs. However, those multilayer samples have very complicated epilayer structures that make it difficult to interpret all the PL spectra. In order to simplify the problem, samples with just a single InGaAs epilayer are grown. These single layer samples have a **thicker** single layer in order to produce the same facetted RHEED pattern as the multilayer samples had produced. The first sample (QDPL-08) has a single 45 monolayer (12.7 nm) $In_{0.15}Ga_{0.85}As$ epilayer (see Figure 2-4). The RHEED pattern of this sample shows signs of three-dimensional growth after about 30 monolayers are grown. It becomes very spotty after about 45 monolayers are grown, which indicates that the surface is nearly covered by three-dimensional features. In order to see the effects of continuing to grow strained material after the surface has facetted, another sample (QDPL-09) with 50 monolayers (14.1 nm) of $In_{0.15}Ga_{0.85}As$ is grown. The RHEED pattern did not change much compared to the previous 45 monolayer sample.

RTPL spectra from these samples are shown in Figures 2-9 and 2-10. The longer wavelength peak from QDPL-08 is at 1045 nm, compared to the 1065 nm peak that is seen from QDPL-09. This confirms that a thicker layer is needed to obtain longer wavelength emission, which verifies that the samples still show the effects of quantum confinement. Both samples show very broad emission spectra, as well as a strong dependence of the shorter wavelength peak on the pump power.

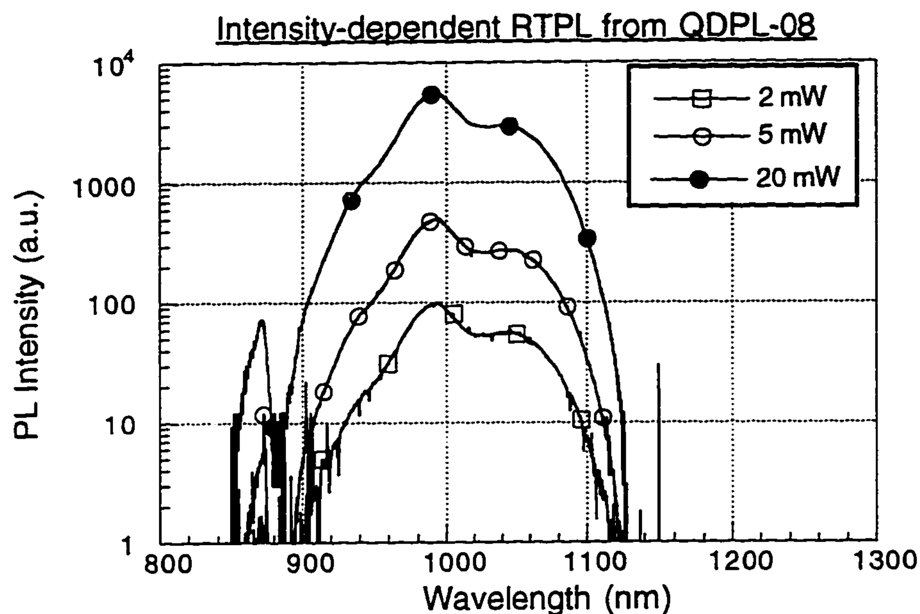

Figure 2-9 RTPL spectra from QDPL-08 (12.7 nm $In_{0.15}Ga_{0.85}As$).

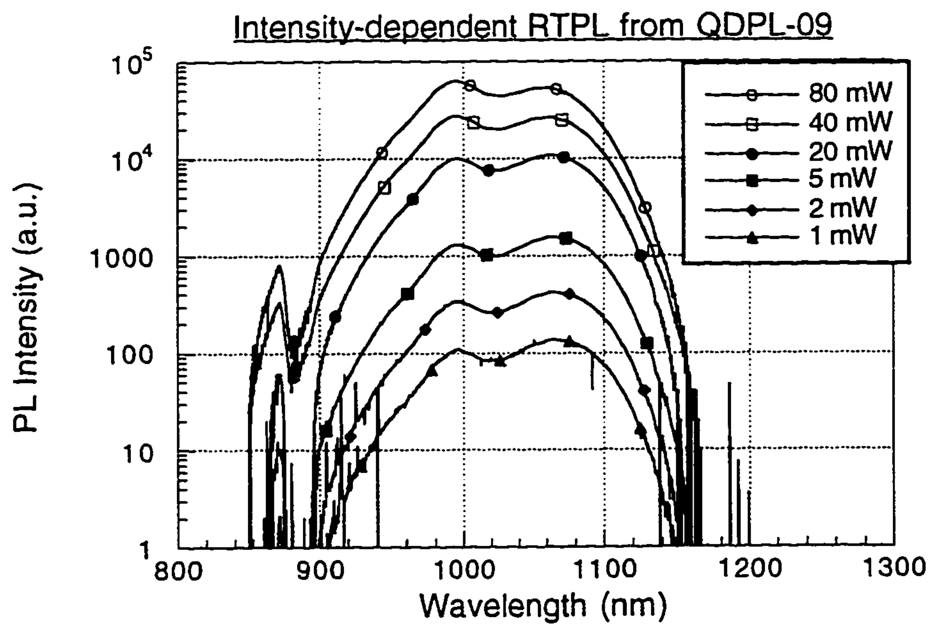

Figure 2-10 RTPL spectra from QDPL-09 (14.1 nm $In_{0.15}Ga_{0.85}As$).

Higher pump powers lead to stronger short wavelength emission, which is consistent with a higher density of states at the shorter wavelength. No saturation effects are observed over the range of pump powers used for this experiment.

2.4.2 Longer Wavelength Emission from Thicker Epilayers

Despite the fact that the RHEED pattern indicates three-dimensional growth, which is usually associated with poor optical quality material, the emission wavelength continues to increase as the thickness of the InGaAs epilayer increases. Samples QDPL-10, -11, and -12 are grown having 60, 70, and 80 monolayers of $In_{0.15}Ga_{0.85}As$, respectively (see Figure 2-4). The RTPL spectra (Figure 2-11) from these three samples continues to show the same trend as previous samples: thicker epilayers correspond to longer wavelength emission, with no decrease in emission intensity. In fact, the sample with the thickest epilayer shows the brightest emission, which indicates that defects are not a problem, despite having a three-dimensional surface. The peak RTPL emission wavelength from the three samples is 1071 nm, 1085 nm, and 1112 nm, respectively. QDPL-12 also has the most well-defined single peak, with a broad FWHM of 78 meV. QDPL-11 and QDPL-12 are both double-peaked, which leads to a very large FWHM. It is noteworthy that the peak position of the higher energy peak does not change as the thickness is increased, which suggests that the origin of this peak is not associated with the three-dimensional layer.

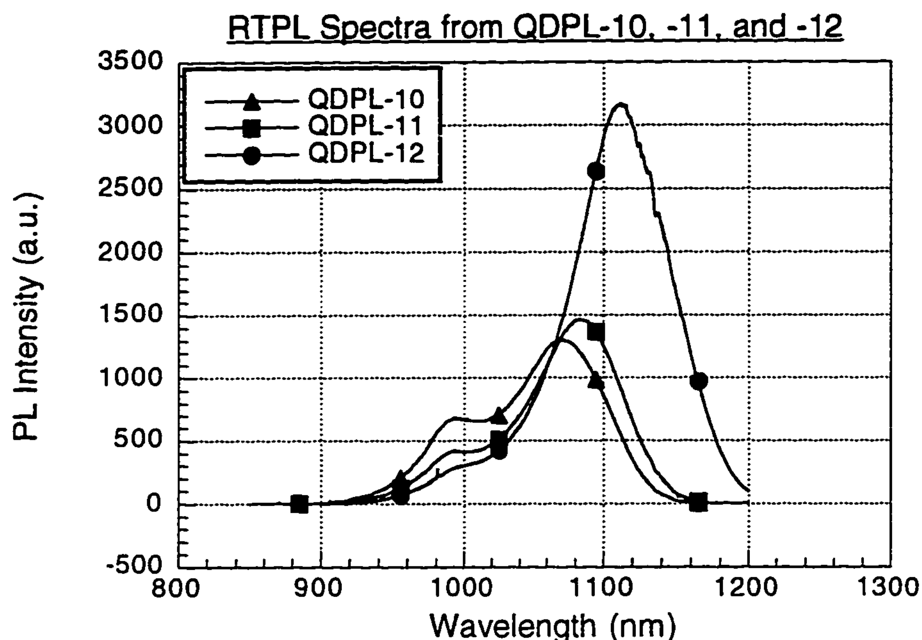

Figure 2-11 RTPL spectra from QDPL-10, -11, and -12 (17.0, 19.8, and 22.6 nm of $In_{0.15}Ga_{0.85}As$, respectively).

2.4.3 Increased Indium Mole Fraction

In order to investigate the effect of changing the In content, a sample (QDPL-13) with 41 monolayers of $In_{0.19}Ga_{0.81}As$ (see Figure 2-4) is grown. After deposition of 19.1 monolayers, the RHEED pattern becomes spotty (with 15% In mole fraction, it took 30.0 monolayers). This demonstrates the importance of the indium mole fraction in determining the morphological properties of these epilayers. The observed behavior is consistent with my In segregation hypothesis: a higher In mole fraction leads to a more rapid buildup of In at the surface, and consequently a transition to three-dimensional growth with a thinner epilayer.

Intensity-dependent RTPL spectra from QDPL-13 are shown in Figure 2-12.

The peak emission wavelength is at 1213 nm at low pump power and decreases to about 1189 nm at high pump power. This peak emission wavelength is about 100 nm longer than any previous single layer sample. This long wavelength is obtained despite the fact that the total thickness is around half that of the thickest $In_{0.15}Ga_{0.85}As$ sample. As a comparison, 45 monolayers of $In_{0.15}Ga_{0.85}As$ has a peak wavelength of only 1045 nm. The FWHM from QDPL-13 is still quite broad, ranging from 99.6 meV at low pump power to 120 meV at high pump power.

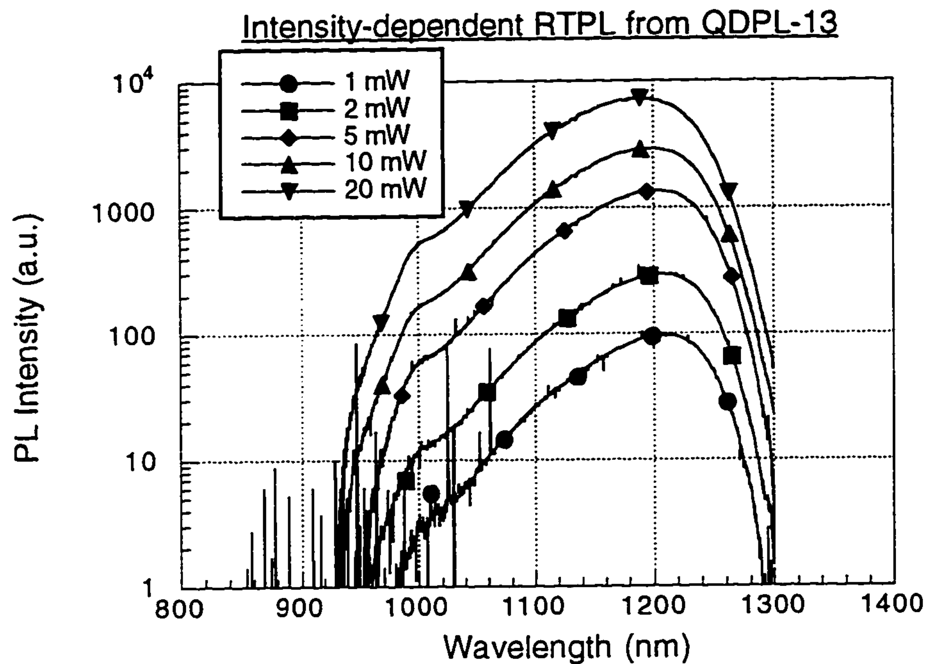

Figure 2-12 RTPL spectra from QDPL-13 (11.6 nm of $In_{0.19}Ga_{0.81}As$).

2.4.4 Thicker Layers with Higher Indium Mole Fraction

The next two samples (QDPL-14 and -15) maintain the same 19% In mole fraction as QDPL-13, and the thickness is increased to 50 and 59 monolayers, respectively. One additional sample (QDPL-16) is grown, which increases the In

mole fraction to 22%; the epilayer thickness is 42.8 monolayers (see Figure 2-4). The RHEED pattern indicates three-dimensional growth after deposition of only about 12.4 monolayers, compared to 19.1 monolayers for the 19% In mole fraction and 30 monolayers for the 15% In mole fraction.

RTPL spectra from these three samples are shown in Figure 2-13. QDPL-14 has a peak emission wavelength of 1191 nm and a FWHM of 131 meV. QDPL-15 has a peak emission wavelength of 1259 nm and a FWHM of 134 meV. And QDPL-16 has a peak emission wavelength of 1309 nm and a FWHM of 80 meV. However, there is one problem with this sample: the RTPL intensity is poor. It has decreased by almost an order of magnitude from the best previous samples. Note that QDPL-15 also shows poor RTPL intensity compared to QDPL-14. Poor intensity can be due to many different reasons, but the obvious one in this case is that the material quality is degraded due to the introduction of nonradiative defects caused by the large amount of strain. It is not unexpected that there would be a limit to the thickness of these strained layers, even if the three-dimensional growth allows partial strain relief.

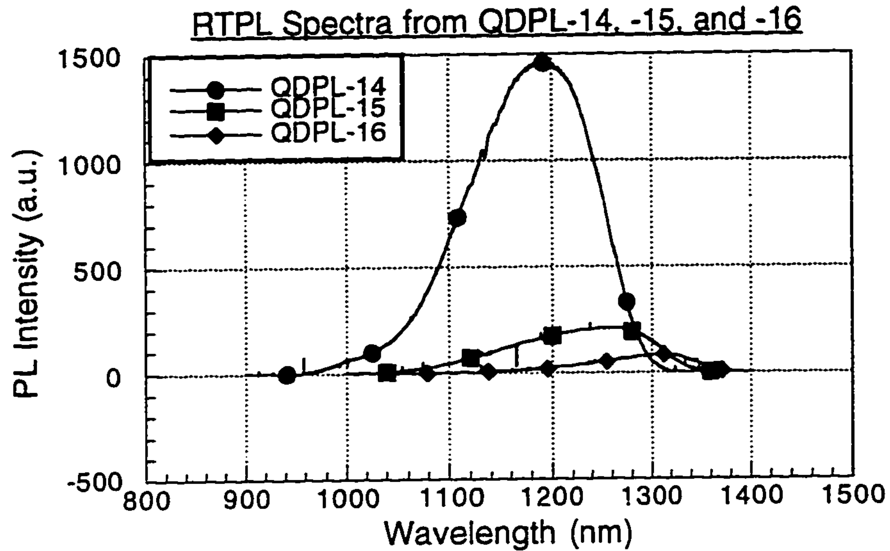

Figure 2-13 RTPL spectra from QDPL-14, -15, and -16. Note the drop in intensity for QDPL-15 and -16.

2.4.5 Long Wavelength Emission from Thinner InGaAs Epilayers

Two additional samples (QDPL-17 and -18) of $In_{0.22}Ga_{0.78}As$ with 38 and 33.2 monolayers, respectively, are grown to investigate whether the previous samples have too much strain . The RTPL emission peaks (Figure 2-14) are at about 1296 nm and 1270 nm, respectively, and the FWHMs are 80.2 meV and 84.2 meV, respectively. The intensity is somewhat improved over that of QDPL-16. It is worth noting here that the wavelength barely changes when the number of monolayers is decreased from 42.8 to 38.0. However, the PL intensity increases when the thickness is decreased. This is a strong indication that defects are responsible for the decreased PL intensity. There are also no signs of higher energy peaks in the spectra from these two samples.

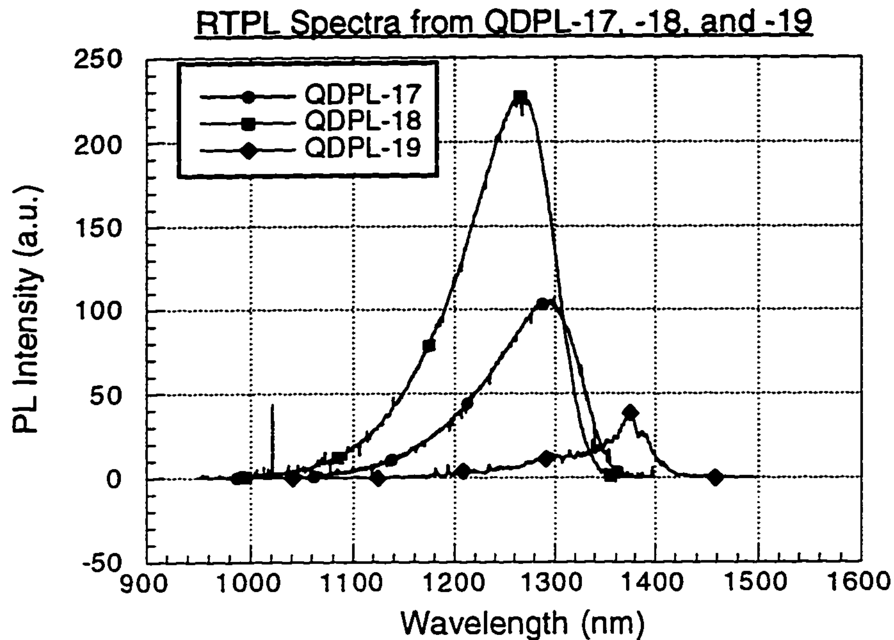

Figure 2-14 RTPL spectra from QDPL-17, -18, and -19. QDPL-19 has a linewidth of only 29.6 meV, but it also has a relatively weak intensity.

2.4.6 Narrow Linewidth at Long Wavelength: Even Higher Indium Mole Fraction

In order to see the effect of continuing to increase the In content, an additional sample (QDPL-19) is grown with a composition of $In_{0.30}Ga_{0.70}As$ and a thickness of 31 monolayers. The RHEED pattern changes from 2D-to-3D after deposition of about 8 monolayers. The RTPL emission peak (Figure 2-14) from this sample is around 1374 nm, which is the longest wavelength emission ever reported from an InGaAs epilayer grown on GaAs. The FWHM of only 29.6 meV is also very narrow compared to previous samples. Unfortunately, this sample also has relatively poor intensity compared to the other samples.

Since a thinner epilayer could still be used to obtain emission around 1300 nm, another sample (QDPL-20) with 22.1 monolayers of $In_{0.30}Ga_{0.70}As$ is grown. This RTPL emission peak (Figure 2-15) is at 1318 nm, but the most striking thing about the emission is the FWHM : it is only 26.4 meV at low pump power and increases only slightly to 28.2 meV at higher pump powers. This is much narrower than any other samples grown, while still maintaining high brightness.

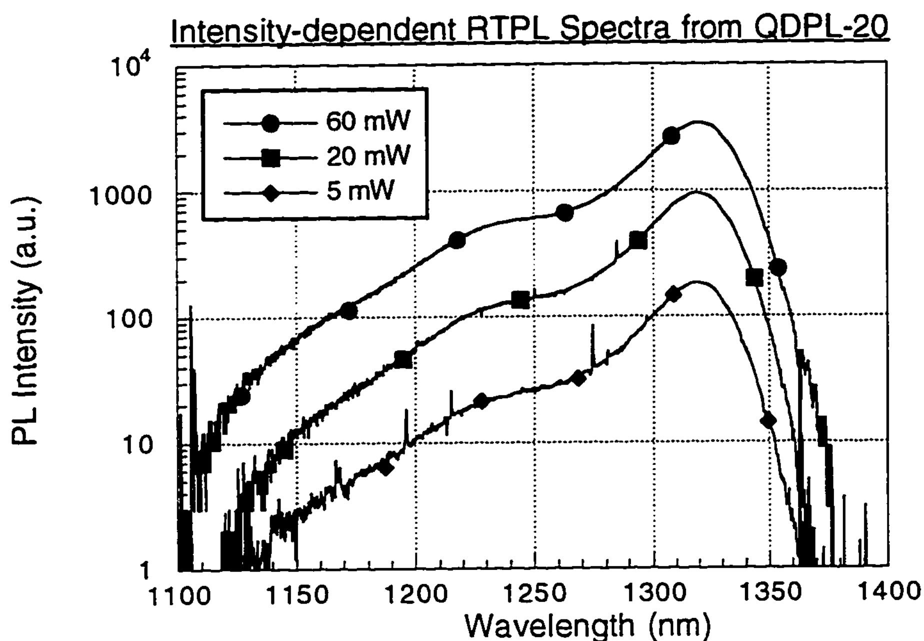

Figure 2-15 RTPL from QDPL-20. The peak emission is at 1318 nm, and the linewidth is 26 meV.

2.4.7 Thinner Samples with 30% Indium Mole Fraction

Additional samples are grown to further characterize the luminescence properties from these InGaAs epilayers. QDPLCTRL-02 has a 9.3 nm, $In_{0.25}Ga_{0.75}As$ epilayer (see Figure 2-4). This sample is used as a reference so that

the overall material quality from the MBE machine can be evaluated. QDPL-21 is a repeat of QDPL-20, with 22.1 MLs of $In_{.3}Ga_{.7}As$. QDPL-22 has the same composition QDPL-21, except the InGaAs epilayer is terminated after 17.7 MLs have been deposited.

RTPL spectra from these three samples are shown in Figure 2-16. The spectrum from QDPLCTRL-02 has a peak emission intensity that is 5 times higher than that of QDPL-22 and 10 times that of QDPL-21. The integrated intensity from QDPL-22 is twice that of QDPL-21, which suggests that QDPL-21 has some defects that cause nonradiative recombination of the photoexcited carriers. The integrated intensity from QDPLCTRL-02 is about 1.35 times that from QDPL-22. The linewidths from QDPL-21 and QDPL-22 are both about 53 meV, about 4.3 times larger than the 12.4 meV linewidth from QDPLCTRL-02. These results indicate that the optical quality of the InGaAs islands is not as good as that of an InGaAs QW. However, the brighter photoluminescence from the thinner layer of InGaAs islands is encouraging, and this is the thickness that is used in fabrication of laser diodes, which will be discussed in Chapter 6 of this dissertation.

2.5 Summary

This chapter summarizes the preliminary AMBE experiments and PL measurements used to obtain the first systematic study of how to obtain 1.3 μm emission from InGaAs on GaAs. The only previously work on this subject that was successful (Roan and Cheng, 1991) used a monolayer-superlattice structure to obtain 1.34 μm emission at room-temperature, although the FWHM was much larger than was obtained in this study (60 meV versus 26 meV). I have shown that indium mole

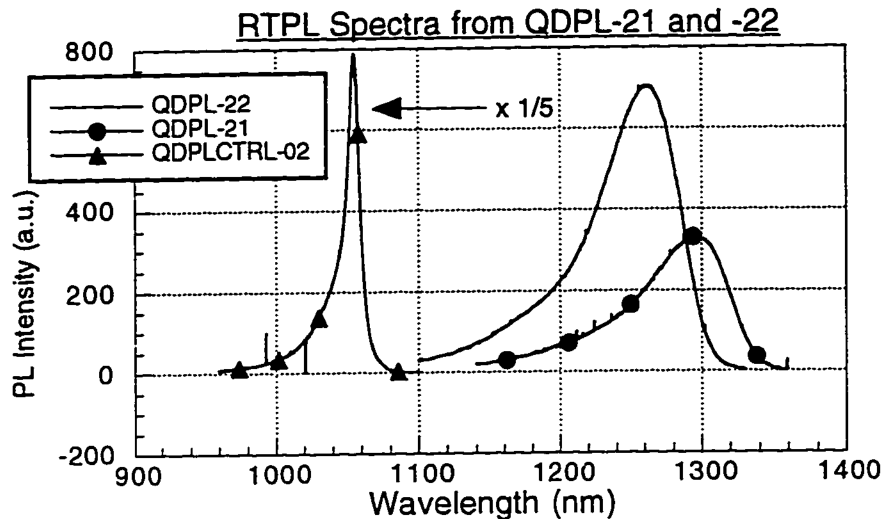

Figure 2-16 The relative intensity from QDPL-21 and -22 indicate that there are defects in QDPL-21 which reduce the radiative efficiency.

fraction is the most important parameter needed in controlling emission wavelength and the linewidth. The emission wavelength from the InGaAs islands can also be controlled somewhat by varying the deposited thickness. The RHEED patterns that are briefly described in this section indicate three-dimensional growth, also known as islanding. Nonetheless, I have shown that despite this island-growth, which is usually something to be avoided when growing strained layers, strong room temperature PL emission can be obtained over a wide spectral range. Further PL measurements will be used to further qualify this statement in Chapter 3, Photoluminescence: II, and Chapter 5: AMBE Optimization, of this dissertation.

Chapter 3: Photoluminescence II-Temperature Dependence and Intensity Dependence

3.1 Introduction

In the previous chapter, I demonstrated that arrays of quantum dots with very narrow (26 meV) full widths at half maximum can be grown using alternating molecular beam epitaxy of $In_{.3}Ga_{.7}As$ on (100) GaAs. The peak emission wavelength from these arrays can be as large as 1320 nm at room temperature. In order to better assess the suitability of these quantum dots for incorporation into a diode laser, additional information from photoluminescence (PL) can be obtained.

In this chapter I will discuss additional PL measurements on some of the samples described in Chapter 2. Temperature-dependent PL measurements are used to investigate the integrated PL intensity, the peak PL intensity, and the linewidth (both full width at half maximum (FWHM) and half width at half maximum (HWHM)) from a quantum dot sample, and these results are compared to a quantum well sample. As the samples are cooled down, k_BT decreases. The consequences of this are that thermal broadening of the linewidth is eliminated, and thermionic emission out of a quantum well decreases, thus leading to an increase in the PL efficiency.

Intensity-dependent PL can provide information about defects in the material and about the density of states. At low pump power, nonradiative recombination can cause low PL efficiency if defects are present. The linewidth is narrowest at low pump powers regardless of whether nonradiative defects are present since the photo-

excited carriers will relax down into the regions of lowest energy (the widest regions of a quantum well, for example) when few carriers are present. At high pump powers, defects are saturated (in good quality material), and the emitted intensity should be linearly proportional to the incident power. The linewidth broadens at high powers as more carriers are present to populate the higher energy regions (the narrowest regions of a quantum well). Since we are interested in using the quantum dots in lasers, it is important to have efficient recombination at the high carrier concentrations needed for lasers.

All of the PL measurements described in this section use the same basic setup. The excitation source is an Ar^+ laser that is modulated by a Stanford Research Systems Model SR540 chopper, and the incident power is measured with a photodetector. The incident laser light is focused onto the sample. The emitted light from the sample is focused onto the input slit of a Spex 1404 (0.85 meter, double-grating) monochromator. The signal is measured by a North Coast EO-817A Ge photodiode operating at 77 K. The output from the Ge detector is acquired by a lock-in amplifier and a computer.

3.2 Temperature-dependent Photoluminescence

3.2.1 Introduction

Temperature-dependent PL can provide important information about the optical quality of quantum structures, as well as information about the nonradiative processes that occur in these structures. The two most important optical properties that are examined here are emission intensity (both peak and integrated) and linewidth

(both FWHM and HWHM) . I will first give some background discussion on what is expected from ideal quantum wells and quantum dots, and then discuss other experimental results on quantum wells and quantum dots. I will then present experimental data comparing a quantum well sample with a quantum dot sample.

The temperature-dependent PL properties of quantum wells have been extremely well studied over the past 15-20 years (Miller *et al.*, 1980, Bacher *et al.*, 1991, Michler *et al.*, 1992, Bacher *et al.*, 1993, Vening, Dunstan, and Homewood, 1993). The most important results are summarized as follows: (i) integrated PL intensity increases as the QWs are cooled, (ii) peak emission intensity increases as the QWs are cooled, and (iii) FWHM decreases as the QWs are cooled. There has been little reported on the temperature-dependence of the linewidth (Miller *et al.*, 1980).

The temperature-dependence on the emission linewidth can be easily understood by examining the well-known equations for optical transition rates. At a single wavelength, λ_{21}, the emitted intensity I_{21}can be shown (Coldren and Corzine, 1995) to be proportional to the reduced density of states, ρ_r, and the difference in occupation probabilities between the conduction band, f_2, and the valence band, f_1:

$$I_{21} \propto \rho_r (f_2 - f_1), \tag{3-1}$$

where f_1 and f_2 are given by:

$$f_1 = \frac{1}{e^{(E_1 - E_{Fv})/kT} + 1} \tag{3-2}$$

and

$$f_2 = \frac{1}{e^{(E_2 - E_{Fc})/kT} + 1}. \tag{3-3}$$

At high temperatures, states that are higher in energy than the peak of the density of states are thermally populated, leading to a high-energy tail in the spectrum. As the temperature is lowered, the Boltzmann tail, which populates higher energy states, is suppressed, and the spectrum essentially maps out the density of states.

The measured linewidth of a quantum well is determined by both the temperature at which the sample is measured and the interfaces between the quantum well and barrier materials. The theoretical lineshape function of an ideal quantum well (perfect square well with no interface roughness) is a Lorentzian whose linewidth is determined by the intraband scattering time, τ_{in} (Coldren and Corzine, 1995):

$$L(E-E_{21}) = \frac{1}{\pi} \frac{\hbar/\tau_{in}}{(\hbar/\tau_{in})^2 + (E-E_{21})^2}. \tag{3-4}$$

For a real quantum well measured at low temperatures, the lineshape function is a Gaussian or Lorentzian (Herman, Bimberg, and Christen, 1991). The lineshape function is convoluted with the Fermi-Dirac distribution of carriers in both the conduction and valence bands (see Equation 3-1). The bandedge usually determines the HWHM on the low energy side of the peak at all temperatures. The HWHM on the high energy side of the peak is usually determined by the statistical distribution of carriers at high temperatures and by the inhomogeneous broadening due to the interfaces at low temperatures.

An ideal array of quantum dots is essentially an array of artificial atoms. It has a non-interacting, uniform size distribution, and the areal density of states (equivalent to a quantum well) is simply a delta function at one energy with an

amplitude equal to the areal density of quantum dots. The linewidth at all temperatures should be homogeneously broadened (lifetime broadened) since there can be no statistical distribution of carriers due to the delta function density of states. The linewidth should then be essentially unchanged at all temperatures, except for that due to the change in lifetime. The intensity should increase as the temperature decreases since carriers have a smaller probability of tunneling out of the quantum dot states and into the continuum states.

Real arrays of quantum dots such as the ones measured here are not perfectly uniform in size. As will be shown in Chapter 4, there is a distribution of sizes, both in height and lateral dimensions. These fluctuations in size lead to deviations in the linewidth from the Lorentzian that is predicted by Equation 3-4. In Chapter 4, I will present some theory that relates the PL linewidth to size fluctuations in the quantum dots.

3.2.2 Experimental Results

Figure 3-1 shows PL spectra at several different temperatures from QDPLCTRL-01, which is a 9.3 nm $In_{.25}Ga_{.75}As$ quantum well sample (see Appendix A for more details about the layer structure). As the temperature is cooled to 1.4 K, the peak emission intensity rises sharply (Figure 3-2) down to about 80 K. The integrated PL intensity also rises sharply (Figure 3-3) as the sample is cooled. The FWHM monotonically decreases as the temperature decreases (Figure 3-4).

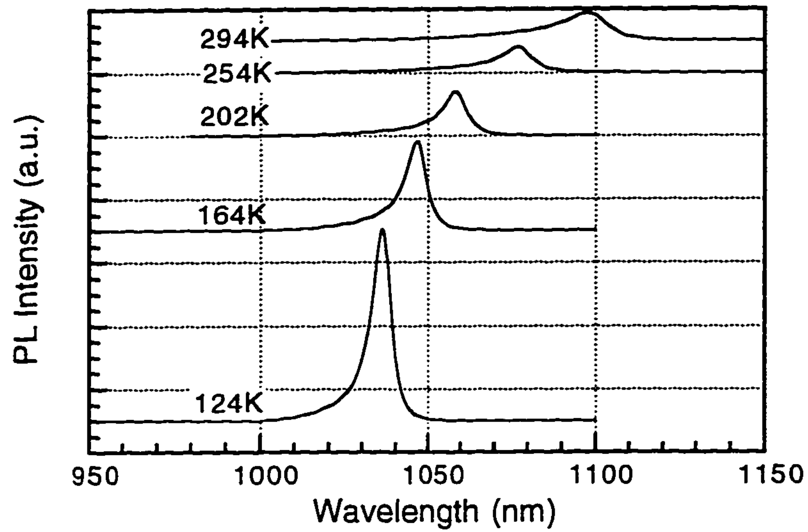

Figure 3-1 Temperature-dependent PL from QDPLCTRL-01 (9.3 nm $In_{.26}Ga_{.74}As$ QW). The linewidth rapidly narrows as the temperature decreases because thermal broadening is eliminated.

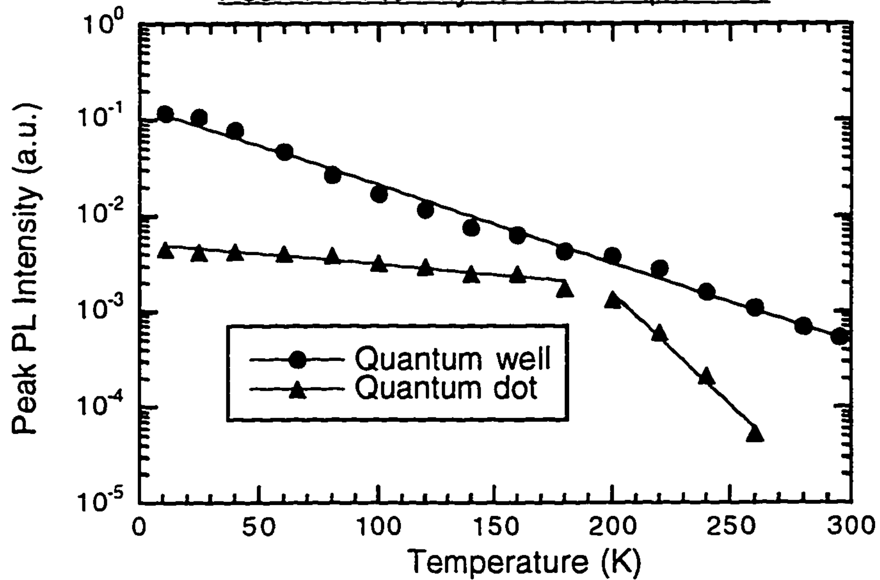

Figure 3-2 Peak PL intensity versus temperature at fixed pump power. The solid lines are curve fits to the data and are given as Equations 3-14, 3-15, and 3-16.

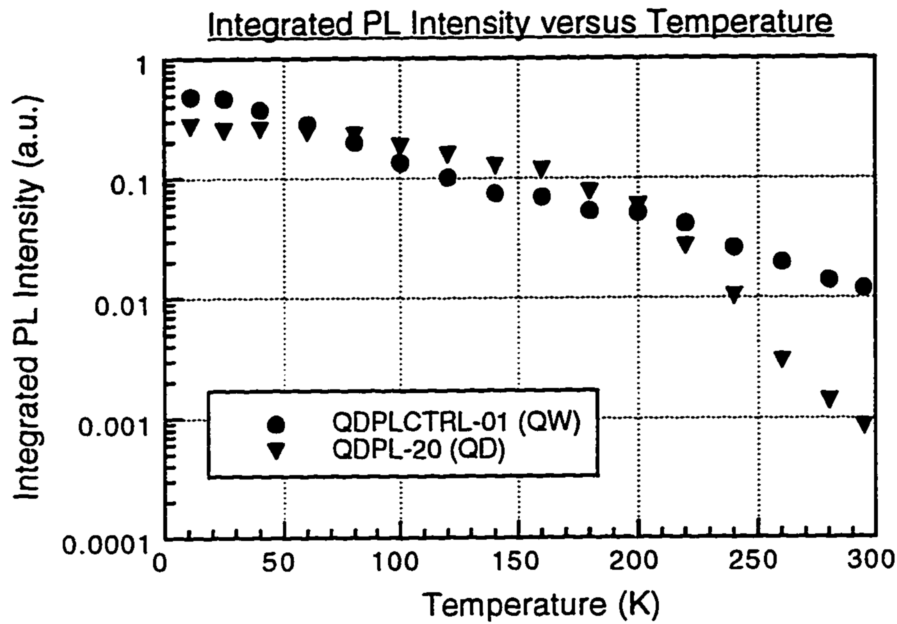

Figure 3-3 Integrated PL intensity versus temperature. The quantum dots are as efficient as the quantum well at temperatures below about 200 K.

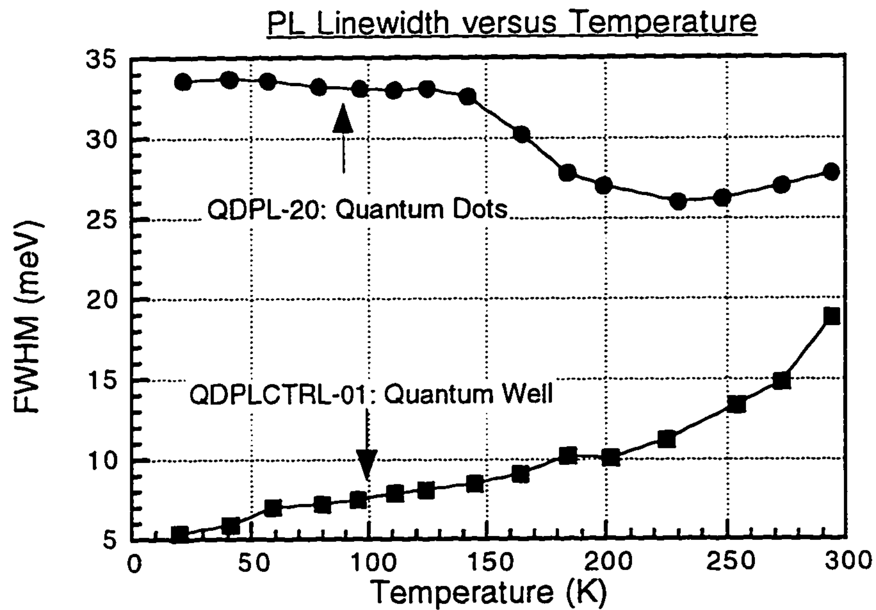

Figure 3-4 FWHM versus temperature at fixed pump power. The lack of linewidth narrowing from the quantum dot sample as the temperature decreases indicates that the linewidth is dominated by inhomogeneous broadening.

Figure 3-5 shows the temperature-dependent PL from QDPL-20, which is the 22.1 ML $In_{.3}Ga_{.7}As$ quantum dot sample discussed in Chapter 2 (see Appendix A for a complete layer structure). As with the quantum well sample, the peak emission intensity (Figure 3-2) and the integrated PL intensity (Figure 3-3) rise rapidly as the temperature decreases. However, the peak emission intensity stops rising at about 200 K. Also, the FWHM (Figure 3-4) from QDPL-20 does not decrease like the FWHM from QDPLCTRL-01.

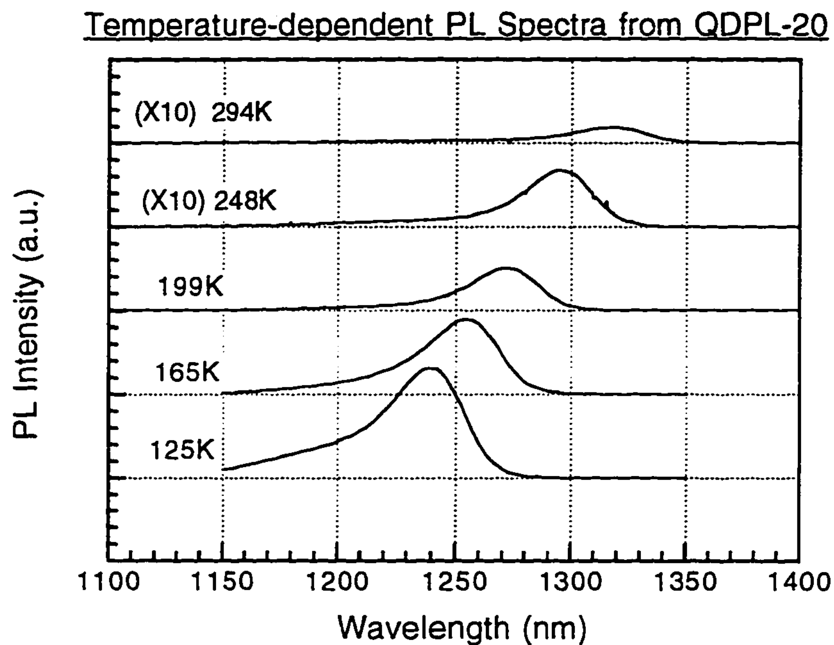

Figure 3-5 Temperature-dependent PL from QDPL-20 at constant pump power. Note the high energy shoulder that becomes pronounced as the sample is cooled.

3.2.3 Comparison and Discussion

Figure 3-3 shows that as the sample is cooled from room temperature to about

200 K, the integrated PL intensity rises much more rapidly in the quantum dot sample than in the quantum well sample. Below about 200 K, the integrated PL intensity from the two samples is comparable. This is a good indication that the quantum dots are effectively capturing carriers, and the carriers are recombining radiatively. The integrated PL intensity from the QD sample is slightly better than from the QW sample at 200 K, but the rate of increase in the QW sample is higher, and the integrated PL intensity from the QW sample surpasses that of the QD sample around 60 K.

Figure 3-6 (a) shows the integrated PL intensity on an Arrhenius plot. The data can be fit to an equation that has a form similar to a Fermi-Dirac function. This equation can be derived starting from a rate equation for excitons as follows (Bacher *et al.*, 1991):

$$\frac{\partial c}{\partial t} = -\frac{c}{\tau} - \frac{c e^{-E_A / kT}}{\tau_0} + g, \qquad (3\text{-}5)$$

where c is the exciton concentration, τ is the excitonic lifetime, E_A is the activation energy for some thermally-excited, nonradiative recombination process, τ_0 is the time constant for this nonradiative recombination process, and g is the generation rate of excitons by the pump laser light. At steady-state, which is the condition of CW excitation that is used in these experiments, we have:

$$\frac{\partial c}{\partial t} = 0 \qquad (3\text{-}6)$$

and

$$g = \frac{c_0}{\tau}. \qquad (3\text{-}7)$$

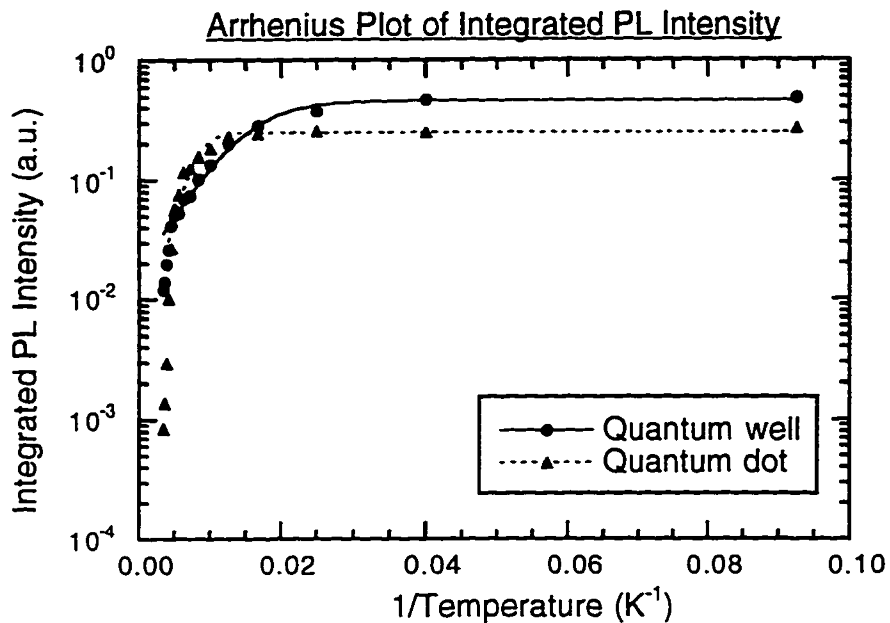

Figure 3-6 (a) Arrhenius plot of the integrated PL intensity. The lines are least-squares fit of the data.

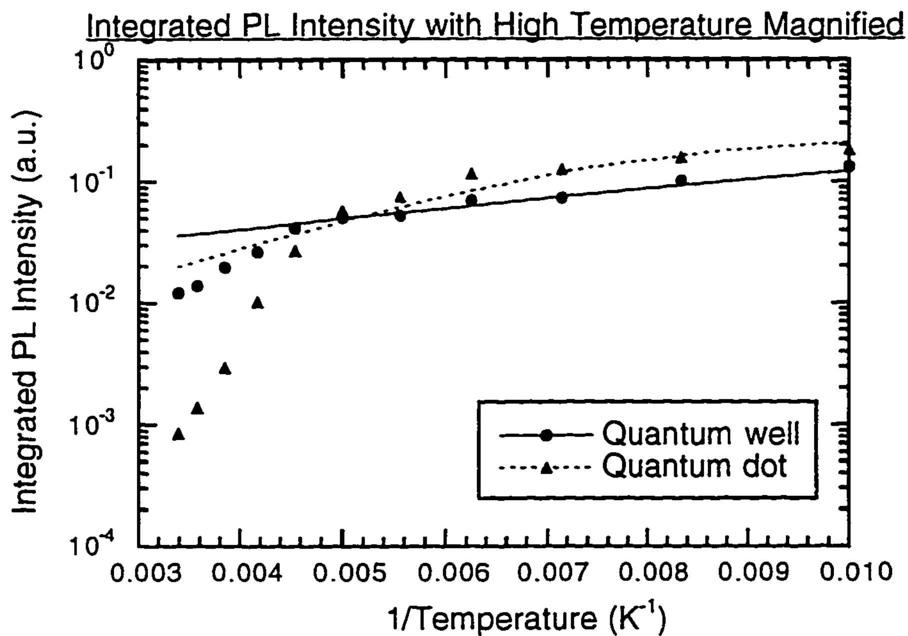

Figure 3-6 (b) Magnification of the high-temperature portion of the Arrhenius plot of the integrated PL intensity. The fit is poor at high temperature.

Solving this yields

$$c(T) = \frac{c_0}{1+(\tau/\tau_0)e^{-E_A/kT}}. \qquad (3\text{-}8)$$

Now, we make the assumption that the excitonic lifetime, τ, is equal to the radiative recombination lifetime, and thus the first term in Equation 3-5 ($-c/\tau$) corresponds to photon emission. Then, we can substitute W_λ for c, and we finally obtain:

$$W_\lambda(T) = \frac{W_{\lambda 0}}{1+(\tau/\tau_0)\exp(-E_A/kT)} \qquad (3\text{-}9)$$

where $W_\lambda(T)$ is the temperature-dependent integrated PL intensity and $W_{\lambda 0}$ is the limiting value of integrated PL intensity at low temperature.

A least-squares fit of the data for the QW sample to Equation 3-9 yields

$$W_\lambda(T) = \frac{0.464}{1+25.15e^{-0.0190eV/kT}}, \qquad (3\text{-}10)$$

and

$$W_\lambda(T) = \frac{0.251}{1+96.04e^{-0.0536eV/kT}} \qquad (3\text{-}11)$$

for the quantum dot sample.

However, careful examination of these fits (Figure 3-6 (b)) show that they give much better agreement at temperatures below 200 K than at higher temperatures. The data presented here suggests that it is better to fit the data from 10 K to 200 K by

the above Fermi-Dirac-style equation, and the data above 200 K by an exponential decay with a different activation energy than the activation energy in the exponential part of the Fermi-Dirac-style equation. The reason for the difference in activation energies is a second decay mechanism that becomes more pronounced at higher temperatures. Since it has been shown in the literature (Bacher *et al.*, 1991, Michler *et al.*, 1992, Vening, Dunstan, and Homewood, 1993) that the activation energy in the Fermi-Dirac-style equation corresponds to thermionic emission of carriers and/or excitons from the quantum well, the high temperature mechanism is probably due to defects in the QW cladding layers. As the temperature is increased, excitons are more likely to be thermally ionized, and single charge carriers are more likely to find a defect to recombine nonradiatively.

The same data shown in Figure 3-6 (a) and (b) is shown again in Figures 3-7 (a) and (b), except now an additional nonradiative recombination mechanism, with a different activation energy and scattering time is added in order to fit the data over the entire temperature range. For the quantum well, the least-squares fit to the data is

$$W_\lambda(T) = \frac{0.491}{1 + 4.1e^{-0.00920eV/kT} + 73.3e^{-0.0366eV/kT}} \cdot \qquad (3\text{-}12)$$

For the quantum dot sample, the least-squares fit to the data gives

$$W_\lambda(T) = \frac{0.260}{1 + 10.9e^{-0.0290eV/kT} + 2.13x10^{6}e^{-0.241eV/kT}} \cdot \qquad (3\text{-}13)$$

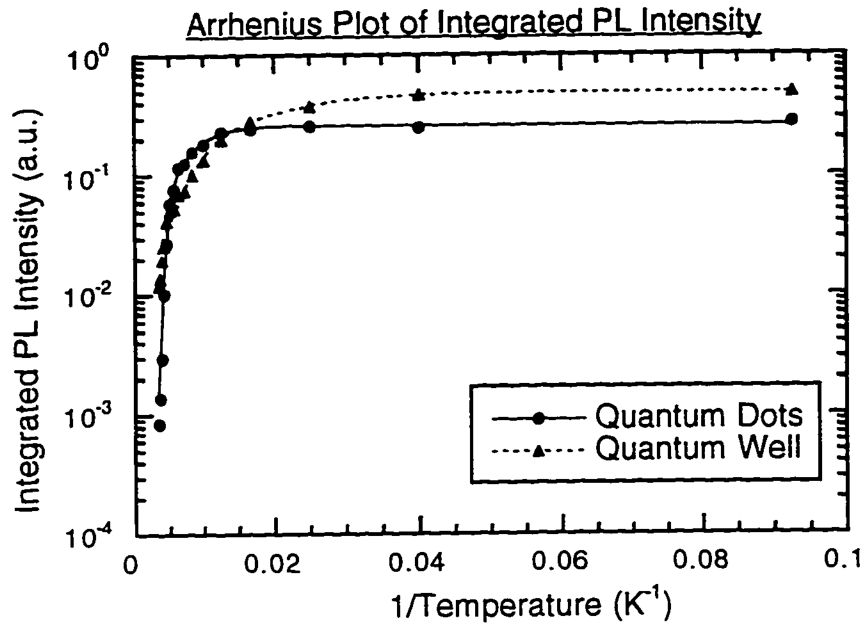

Figure 3-7 (a) Arrhenius plot of integrated PL intensity with two nonradiative mechanisms.

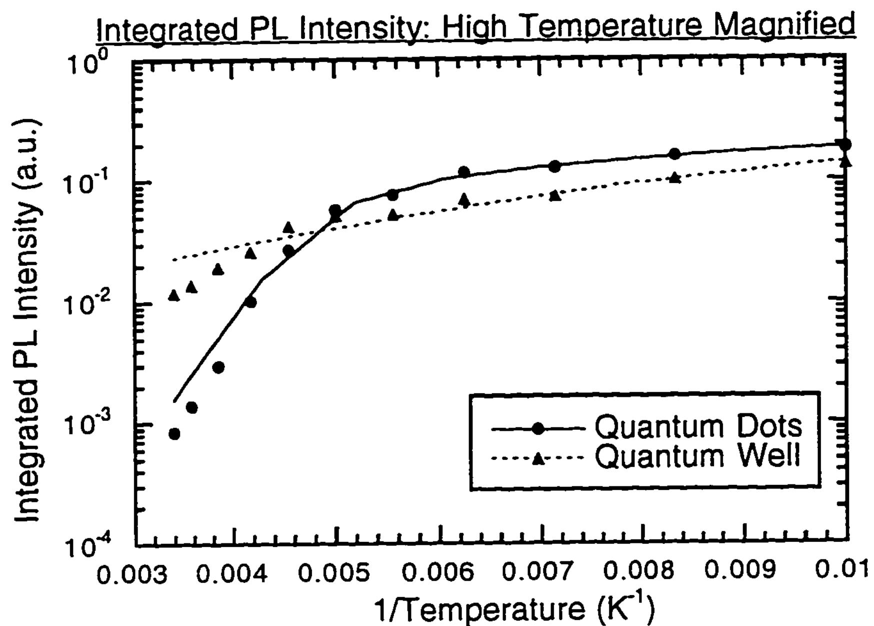

Figure 3-7 (b) High temperature region of Arrhenius plot with two nonradiative mechanisms shows much better agreement with the data than one nonradiative mechanism (Figure 3-6 (b)).

Comparing Equations 3-12 and 3-13, I find that the activation energy for thermionic emission from the quantum dot sample is 29.0 meV compared to 9.2 meV for the quantum well sample. The higher activation energy in the quantum dot sample is consistent with a higher barrier between the ground state in the quantum dots and the continuum states in the barrier. This is as expected since the quantum dot sample has the same barrier material as the quantum well sample, but the quantum dot sample has a longer emission wavelength and thus less quantization energy for the ground state as compared to the quantum well sample. The exponential prefactors are similar for the two samples (10.9 for the quantum dot sample compared to 4.1 for the quantum well sample), which means that the ratio of excitonic lifetime, τ, to scattering time out of the quantum well or quantum dot, τ_0, differ by a factor of about 2. This is consistent with a reduced density of phonons in a quantum dot (Benisty, Sotomayor-Torres, and Weisbuch, 1991) although by means conclusive evidence of a phonon bottleneck in quantum dots.

The second activation energy for the quantum dot sample is 241 meV versus 36.6 meV for the quantum well sample. The consequence of this is a much more rapid thermal quenching of the luminescence in the quantum dot sample at high temperature. Although there is some uncertainty about the cause of the rapid loss of PL intensity in the quantum dot sample, I believe that there are some defects formed due to the growth far beyond the 2D-3D growth transition. As shown in Figure 2-16, a sample identical to the quantum dot sample measured here (22.1 MLs of $In_{.3}Ga_{.7}As$) shows decreased RTPL intensity compared to a sample that only has 17.7 MLs of $In_{.3}Ga_{.7}As$. Furthermore, Figure 2-14 shows that increasing the thickness to 31 MLs leads to a very weak PL intensity at room temperature. This implies that not all the strain is relieved by the islands, and nonradiative defects can

form.

In the two samples compared here, the peak emission intensity at room temperature from the QD sample is much lower (about 1/50) than that of the QW sample (see Figure 3-2). However, the peak emission intensity from the QD sample rises much more rapidly from room temperature down to about 200 K than does the peak intensity from the QW sample. Below 200 K, the peak emission intensity from the QD sample increases very slowly, while that of the QW sample continues to increase at about the same rate. Note that the QW peak emission intensity remains higher than that of the QD sample over the entire temperature range.

The rapid increase in the peak emission intensity of the QD sample slows down as the efficiency improves; as seen in Figure 3-3, the integrated PL intensity becomes comparable to that of the QW sample at 200 K, which is the same temperature where the rate of increase of peak emission intensity decreases. At 160 K, where the QD peak emission intensity begins to saturate, excited state luminescence becomes more pronounced in the PL spectra (see Figure 3-5).

The peak emission intensity data for the QW sample has exponential behavior over the entire temperature range. The equation that best fits this data is

$$W_{\lambda}(T) = 0.1375e^{-0.0188eV/kT}. \tag{3-14}$$

The peak PL intensity data for the QD sample is best fit by two different exponential equations. The high temperature data ($\geq$ 200 K) follows

$$W_{\lambda}(T) = 70.25e^{-0.0536eV/kT}, \tag{3-15}$$

whereas the low temperature data (≤ 180 K) is given by

$$W_{\lambda}(T) = 0.00518e^{-0.00508eV/kT}. \quad (3\text{-}16)$$

The difference in behavior between the integrated PL intensity and the peak PL intensity is due to the fact that the integrated PL intensity data includes all radiative recombination in the QW or QD layer, including the thermally distributed carriers. The peak PL intensity essentially maps out the peak in the density of states (see Equation 3-1).

The FWHM of the QW sample monotonically decreases as the sample is cooled (Figure 3-4), as expected due to the narrower thermal distribution of carriers. Note that as the radiative efficiency increases at low temperature, the effective carrier density in the quantum well increases and thus the linewidth observed may not be the minimum obtainable linewidth for this sample. Nonetheless, this experiment clearly illustrates the central results of the earlier discussion about the linewidth narrowing in quantum wells at low temperatures.

The FWHM from the QD sample is only 28 meV at room temperature, which is the best linewidth reported to date for arrays of Stranski-Krastanow quantum dots (note that *single quantum dots* show sub-meV linewidths (Marzin *et al.*, 1994)). The linewidth decreases slightly to 26 meV at about 200 K, but then increases to about 33 meV and then saturates there. Theoretically, only a weak temperature dependence is expected from an ideal array of **uniform** quantum dots; the lifetime should get a bit shorter due to larger overlap of the electron and hole wavefunctions (and thus a larger transition matrix element) and therefore the linewidth should **monotonically** increase slightly. The linewidth is not a monotonically increasing function in this

case.

Careful examination of the spectra in Figure 3-5 show that the broadening at low temperatures is due to an increase in the high energy tail, which is unexpected in the case of an ideal array of quantum dots. It was noted earlier that for the quantum well sample the linewidth might not be the minimum obtainable linewidth at a given temperature because the efficiency increases as the sample is cooled and the carrier density increases, thus leading to some band-filling. This band-filling, or **state-filling** in the case of quantum dots, is almost certainly what is causing the broadening of the linewidth for the quantum dot sample. Note also that the peak emission intensity (Figure 3-3), which reflects the density of states, is saturated at about the same temperature where excited state luminescence becomes more pronounced. Further evidence of state-filling will be given in the next section on intensity-dependent PL, but remember that despite the high density of quantum dots ($2\text{-}3 \times 10^{10}$ cm^{-2}), the reduced density of states in a quantum well with a reduced effective mass of $0.026m_0$ (the case of InAs) is 1×10^{14} $eV^{-1} \cdot cm^{-2}$, which is about four orders of magnitude higher than the areal density of quantum dots.

Figure 3-8 shows the HWHM on the low energy side of the peak. Since this value stays approximately constant over the entire temperature range, I assert that the linewidth for the quantum dot sample is due to inhomogeneous broadening. This inhomogeneous broadening is due to the size distribution of this less-than-ideal array of quantum dots. Further evidence of this will be presented in Chapter 4, Morphological and Structural Characterization.

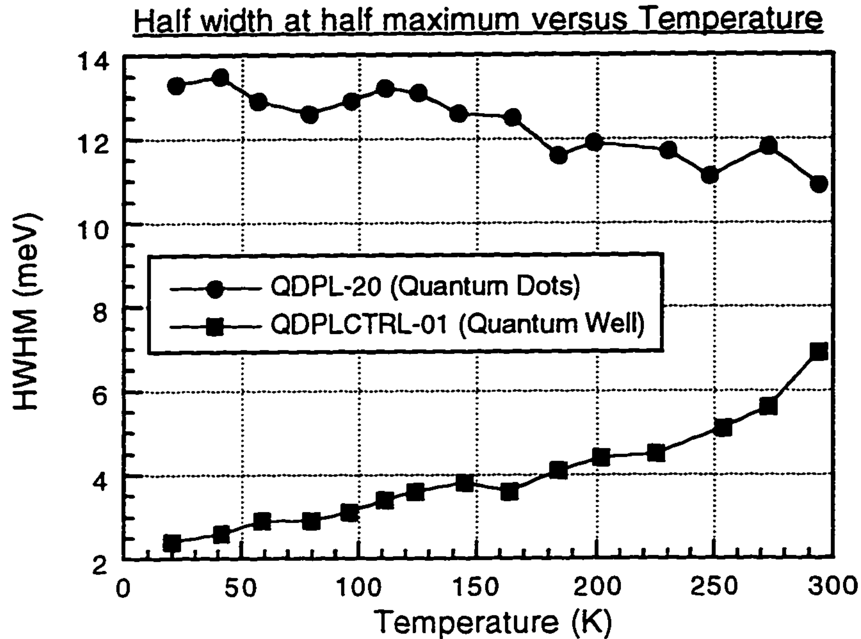

Figure 3-8 HWHM versus temperature for QDPL-20 and QDPLCTRL-01. The HWHM of the QD sample remains approximately constant, which suggests inhomogeneous broadening.

3.2.4 Summary

Temperature-dependent PL with a constant pump power is used to compare a QD sample with a QW sample. The intensity, both peak and integrated, and the linewidth, both FWHM and HWHM, are measured from room temperature to 1.4 K. The QW sample behaves as expected: the peak and integrated intensity both increase as the temperature is decreased as the thermally-excited, nonradiative processes become less efficient. The linewidth monotonically decreases as the sample is cooled since the thermal distribution of carriers becomes narrower.

The QD sample has very different behavior. At high temperatures, the intensity from the QD sample increases much more rapidly as the temperature is

lowered than the intensity from the QW sample. This is probably due to the suppression of defect-related nonradiative recombination. The integrated PL intensity from the QD sample is comparable to that of the QW sample below about 200 K. However, the peak emission intensity from the QW sample remains higher than that of the QD sample. This indicates efficient recombination from excited states in the QDs, as shown in Figure 3-5. The linewidth of the QD sample is inhomogeneously broadened as indicated by the lack of narrowing as the temperature is cooled. Nonetheless, the room temperature linewidth of 28 meV is still the best ever reported for an array of Stranski-Krastanow quantum dots. The differences seen between the QW and the QD samples accurately reflect the density of states available in each sample. For the QD sample, the PL linewidth indicates that this array of quantum dots is less than ideal. AFM images will be shown in Chapter 4 that reveal that the size distribution of the QDs is the cause of the broad linewidth at low temperatures.

3.3 Intensity-Dependent Photoluminescence

3.3.1 Introduction

The PL spectrum of a given sample depends strongly on the intensity of the exciting source, which is an Ar^+ laser for these experiments. To get a rough idea of the expected carrier densities, assume a 100 μm spot size (this is a realistically achievable spot size if a good focusing lens is used). A typical value of pump power used for low intensity pumping is around 0.1-1 mW. Thus, a reasonable value for low intensity pumping is around 1-10 W/cm^2. Assuming each incident photon is absorbed and creates one electron-hole pair with a lifetime of 500 nsec, a carrier sheet

density of $5x10^{10}$ - $5x10^{11}cm^{-2}$ with 100 % collection efficiency in the quantum well. This is somewhat of an ideal case; in reality, about 30% of the incoming light is reflected off the sample, and lens aberrations make it difficult to focus to less than 150 μm. Thus, a more typical value is around $1x10^{10}$ cm^{-2}.

Quantum well materials have been studied extensively with intensity-dependent photoluminescence (IDPL) (Miller *et al.*, 1980, Cingolani and Ploog, 1991). In high quality material, the integrated PL intensity is proportional to the incident pump power since each incident photon creates one electron-hole pair to be captured in the quantum well. The general result is that as the intensity increases, the PL linewidth also increases slowly due to band-filling effects. At very high pump intensities, such as are obtained in QW laser diodes, the band-filling effects are partly offset by bandgap renormalization. It takes extremely high pump intensities to saturate the ground state transition in a QW since the density of states is very high.

Quantum dots have also been studied with IDPL. Castrillo *et al.*, 1995 have studied state-filling in semiconductor dots grown by OMVPE. The dots are InP with InGaP barriers, and the dot density is approximately 10^8 cm^{-2}. They see significant state-filling at a power density of about 40 W/cm^2, compared to about 8000 W/cm^2 for a GaAs QW with GaInP barriers. They attribute this to efficient carrier collection by the InP dots; the state-filling is observed at 200 times lower excitation intensity than in the QW, which is comparable to the carrier collection area/actual dot area (500 times). Although there is probably *some* effect due to efficient carrier collection in the dots, this is not enough evidence to show that the observed state-filling is due to carrier capture by the dots. A much simpler explanation is simply that the areal density of states is lower in the dot sample compared to the QW sample. If the observed state-filling is due to carrier capture in the quantum dots, then the integrated

PL intensity would higher in the dot than in the QW at low excitation intensities, which is when the state-filling effect is unimportant. This is not observed. Furthermore, even at the lowest excitation intensity presented, there is significant luminescence from higher energy states such as other dots (the sample described in this paper has a bimodal distribution), the SK wetting layer, and the GaInP barriers. This is evidence that the carrier capture in the dots is not very efficient, and the lower areal density of states in the dot sample compared to the QW sample is the real cause for the observed state filling in the QDs.

3.3.2 Experimental Results-Room Temperature

Figure 3-9 shows RTPL spectra from QDPLCTRL-03, which is a single 6.5 nm $In_{.2}Ga_{.8}As$ QW (the layer diagram is given in Appendix A). The pump power is varied over two and a half orders of magnitude, as indicated in this figure. The peak emission wavelength increases from 991 nm at the lowest pump power to 997 nm at the highest pump power. The peak intensity monotonically increases as the pump power is increased. No excited state luminescence is observed in this QW sample.

Figure 3-10 shows RTPL spectra from QDPL-23, which is a 17.7 ML $In_{.3}Ga_{.7}As$ QD sample (the layer diagram is given in Appendix A). As the pump power is varied over three orders of magnitude, the emitted intensity from the ground state of the QDs becomes saturated and the linewidth broadens dramatically as excited state luminescence becomes more pronounced. At high pump powers, the excited state luminescence intensity is larger than the ground state luminescence intensity for the QD sample. This is not observed in the QW sample.

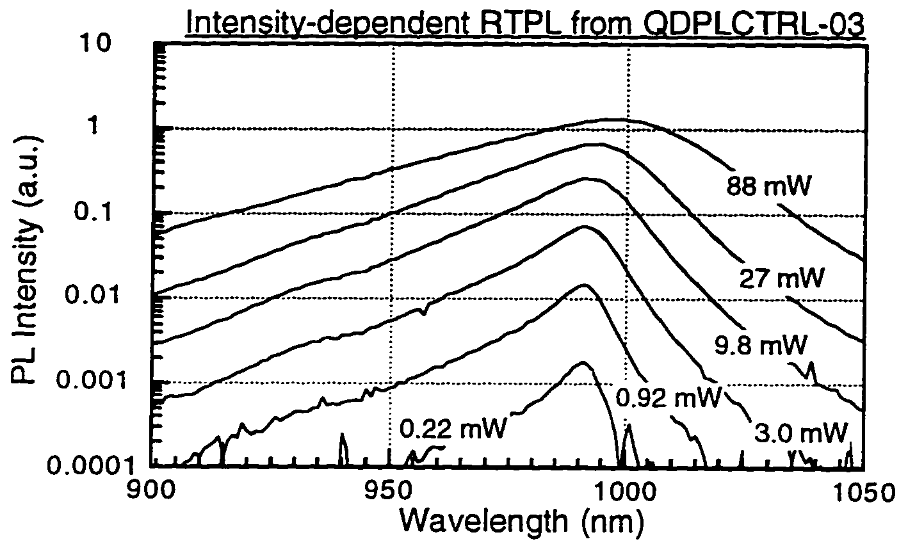

Figure 3-9 Intensity-dependent RTPL spectra from QDPLCTRL-03. The pump intensity is varied over two and a half orders of magnitude.

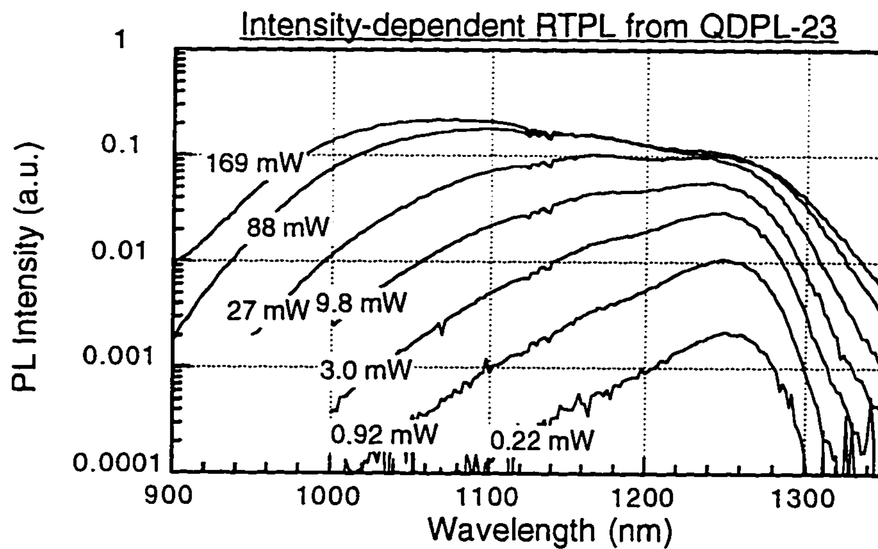

Figure 3-10 Intensity-dependent PL spectra from QDPL-23. The pump intensity is varied over about three orders of magnitude.

3.3.3 Comparison and Discussion of Intensity-Dependent Room Temperature PL

The reason for the differences seen between Figures 3-9 and 3-10 is the density of states available in the two different structures. In the QW sample, the density of states is about 1 x 10^{14} $eV^{-1}\cdot cm^{-2}$ (this assumes a parabolic band structure and uses the effective mass of InAs, which gives the lowest possible value); in the QD sample, there is only one electron allowed per dot ground state. Thus, the areal density of states is equal to the number of quantum dots, which is 2-3 x 10^{10} cm^{-2} (see the AFM images in Chapter 4). This means that as the number of electron-hole pairs is increased by the increased pump power, the QDs can all have carriers in their ground states. When this happens, any additional carriers must occupy excited states in the QDs. This accounts for the saturation of the ground state emission intensity and the increase of the excited state luminescence at high pump powers.

Figure 3-11 shows the integrated PL intensity versus pump power for the QD and QW samples. At low pump powers, the QD sample has a higher intensity than does the QW sample, but this is reversed at higher pump powers. The integrated PL intensity from the QW sample is linear at intermediate-to-high pump powers (9-88 mW), and increases superlinearly below that. If all the carriers created are recombining radiatively, then an increase in pump power corresponds to a linearly proportional change in the integrated PL intensity, since the number of electron-hole pairs generated is linearly proportional to the pump power. This suggests that some nonradiative mechanism is present in the QW sample, but this nonradiative mechanism becomes saturated at higher pump powers.

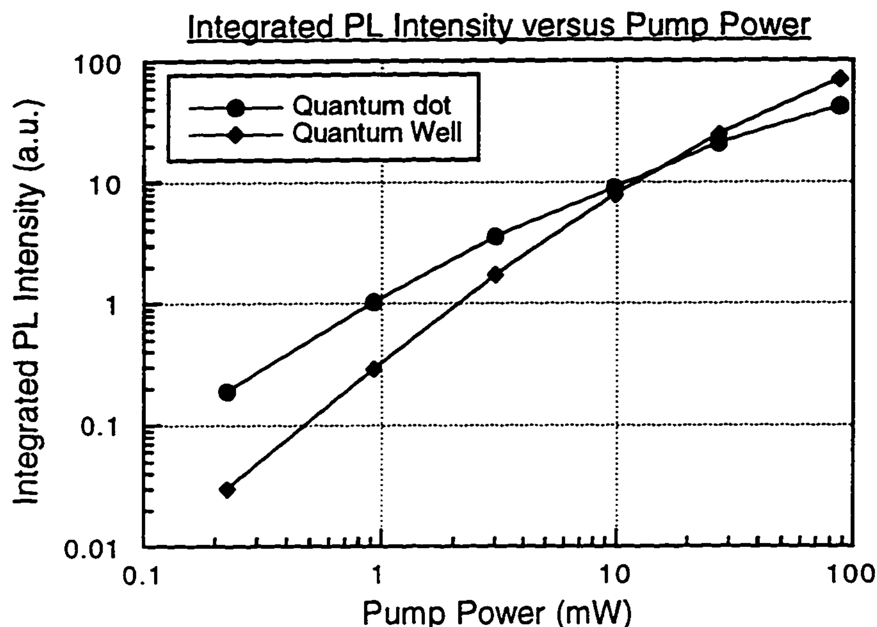

Figure 3-11 Integrated PL intensity versus pump power for the QD sample and the QW sample, over two and a half orders of magnitude variation in pump intensity.

The integrated PL intensity from the QD sample increases superlinearly at low pump powers, but above about 3 mW of pump power it increases sublinearly. This change from superlinear to sublinear behavior indicates a change in the nonradiative mechanism. Since the sublinear behavior occurs in the regime where excited state luminescence begins to dominate the spectrum, this suggests that carriers may be escaping from the QDs as the barrier is decreased and then finding some nonradiative recombination sites.

Figure 3-12 shows the FWHM and HWHM as a function of pump power for the two samples discussed above. The FWHM for QDPL-23 is about 50 meV at low pump power. It increases rapidly as the pump power is increased due to the excited

state luminescence caused by state-filling. The HWHM on the low energy side of the peak stays relatively unchanged as the pump power is increased since the lower energy states are usually filled quite easily. Beyond about 10 mW of pump power, the linewidth is not plotted since the excited state emission intensity is larger than that of the ground state.

For comparison, the FWHM and HWHM of the QW sample is shown. Both the FWHM and the HWHM of the QW sample increase as the pump power is increased. However, the FWHM for the QW sample does not increase as rapidly as does that of the QD sample since the density of states is much higher in the QW sample.

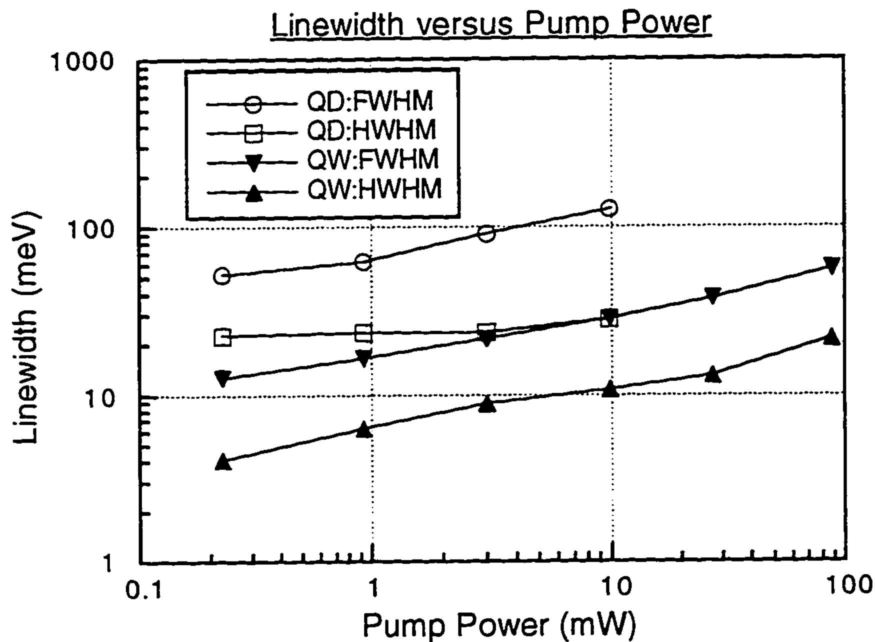

Figure 3-12 The FWHM and HWHM as a function of pump power both reflect that the density of states in the QW sample is higher than that of the QD sample.

3.3.4 Experimental Results-77 K

IDPL is also measured on these two samples at 77 K. Figures 3-13 and 3-14 show IDPL for QDPL-23 and QDPLCTRL-03, respectively. The pump power is varied over two and half orders of magnitude. Note that the lowest pump power used is an order of magnitude lower than is used for RT-IDPL experiments because the radiative efficiency is higher at low temperature.

The peak emission wavelength for the QW sample is at 934 nm for all pump powers. There is no excited state emission visible in the region over which this sample has been measured. Note that the flat region at the center of the peak at the highest pump power used in Figure 3-14 is due to saturation of the lock-in amplifier used to measure the output voltage from the Ge detector; this is the reason that higher excitation intensities are not used to further measure these samples.

The peak emission wavelength for the QD is at about 1150 nm for all pump powers. Excited state luminescence is visible as the broadening of the peak occurs at high pump powers. The peak emission wavelength has not saturated despite the two and half orders of magnitude increase in pump power used in this experiment.

3.3.5 Comparison and Discussion of Intensity-dependent, 77 K Photoluminescence

Figure 3-15 shows the integrated PL intensity versus pump power for the two samples. The QD sample has a higher integrated PL intensity than does the QW sample over the entire range of pump powers used in this experiment. This is a good indication of efficient recombination of excited carriers in the QD sample. In the previous section on temperature-dependent PL, it was shown for similar

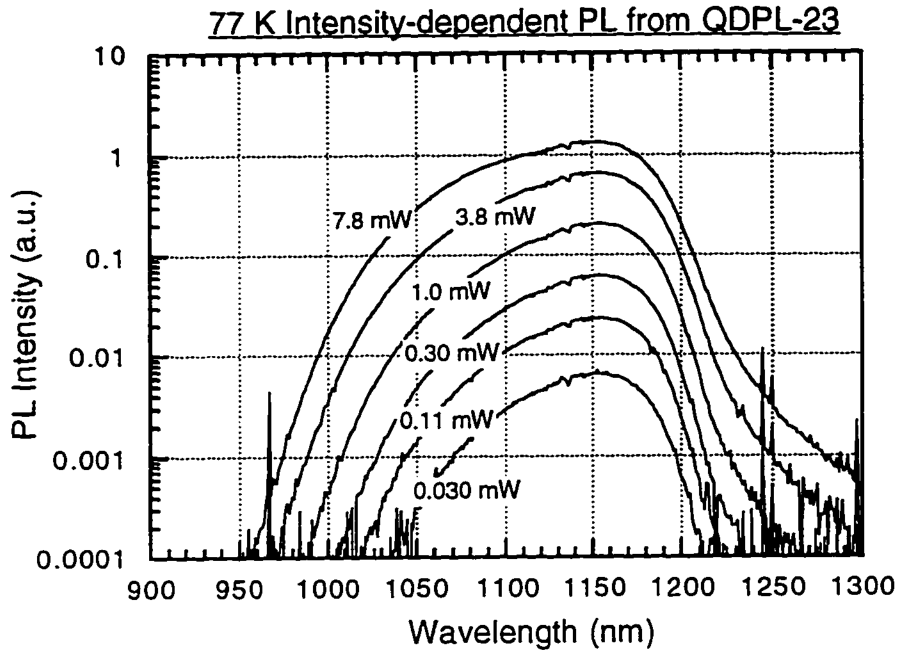

Figure 3-13 77 K, intensity-dependent PL from QDPL-23.

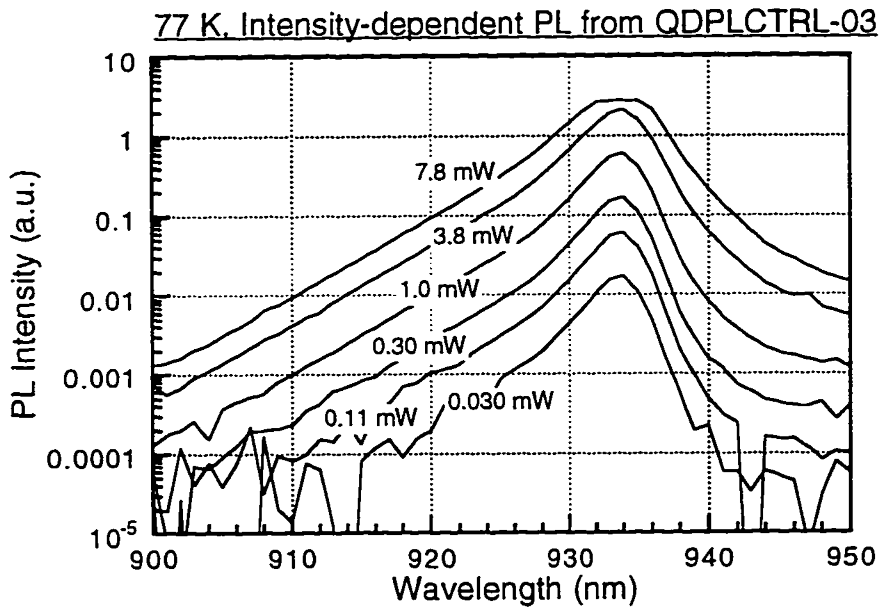

Figure 3-14 77 K, intensity-dependent PL from QDPLCTRL-03. Note that the flat region at the peak is due to saturation of the lock-in amplifier used to measure the output from the cooled Ge detector.

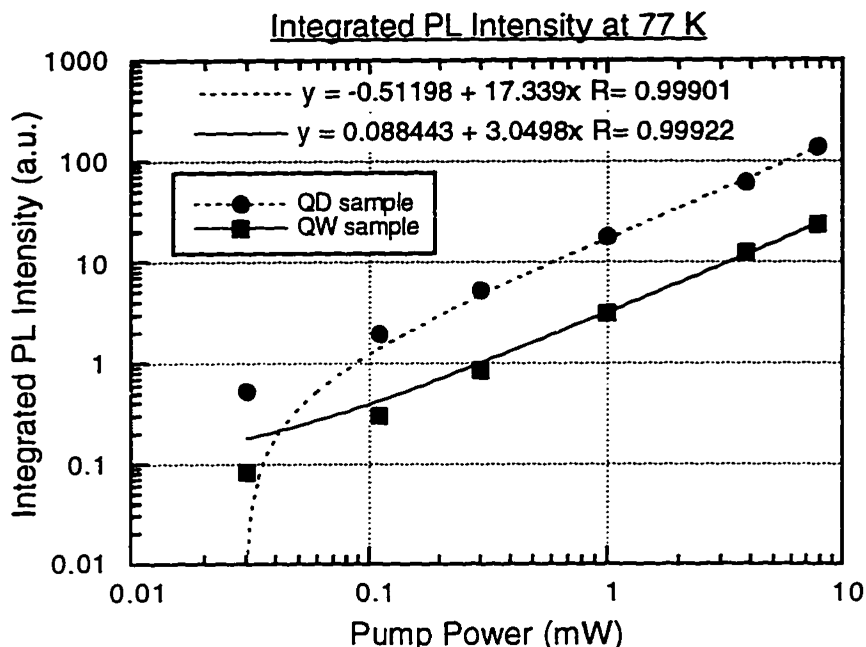

Figure 3-15 Intensity-dependent PL at 77 K. The lines are curve fits to a linear function.

samples that the QD efficiency is comparable to that of a QW at temperatures below about 200 K. For the samples compared in this intensity-dependent measurement, the barrier for electrons in the QD is larger than the barrier seen by electrons in the QW. Thus, it is expected that thermal excitation of carriers in the QW sample will lead to lower efficiency than in the QD sample.

Figure 3-16 shows the peak intensity versus pump power at 77 K for these two samples. The QW sample has a higher peak intensity than does the QD sample at all pump powers, despite the fact that the integrated PL intensity is higher for the QD sample. The reason for this is the higher density of states available in the QW sample.

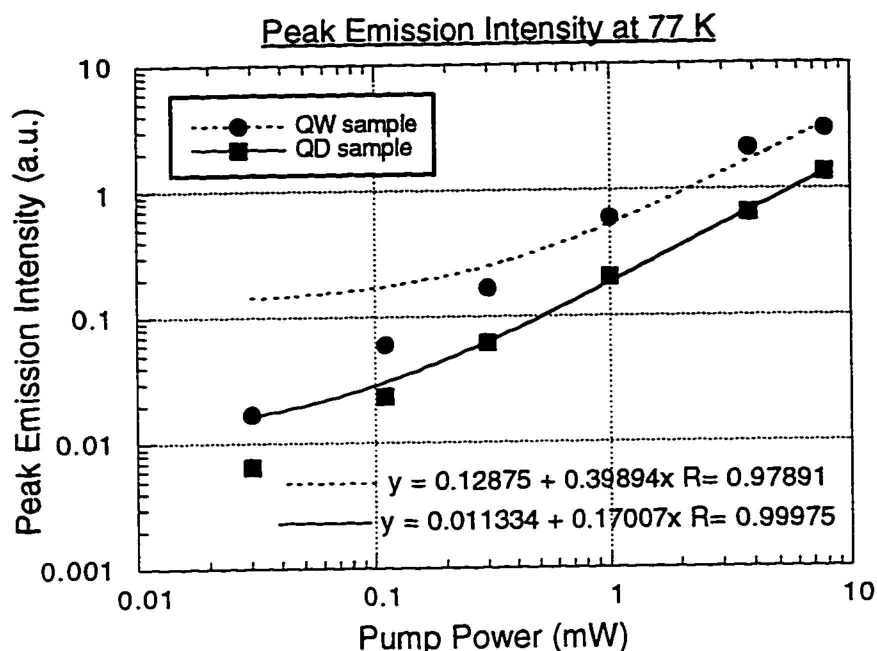

Figure 3-16 Peak emssion intensity at various pump powers at 77 K. The lines are curve fits to a linear function.

Figure 3-17 shows the FWHM and the HWHM of both the QD and the QW samples. The linewidth from the QD sample is larger than at room temperature (see Figure 3-12). The reason for this is the increased radiative efficiency at low temperatures, leading to excited state emission that causes the observed broadening. The FWHM begins to increase dramatically at the highest pump powers used in this experiments. The shoulder corresponding to excited state luminescence becomes comparable in intensity to the ground state peak. The HWHM remains approximately constant as the pump power increases since the lower energy states are more easily filled. This confirms that excited state luminescence is responsible for the broadening at higher pump powers.

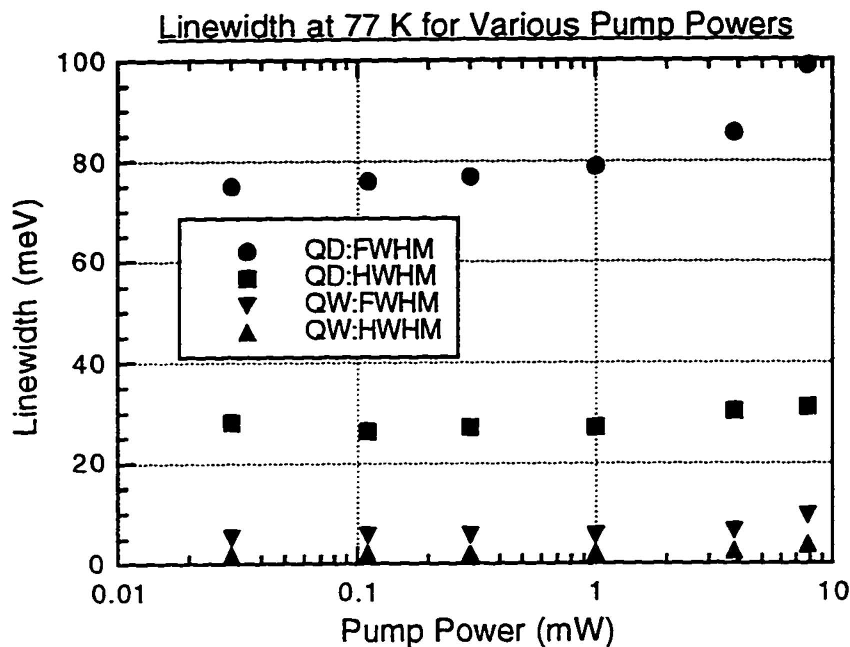

Figure 3-17 Linewidth versus pump power at 77 K for QDPL-23 and QDPLCTRL-03.

The QW sample has a much narrower FWHM (< 6 meV) than it has at room temperature due to the suppression of thermal broadening. Neither the FWHM nor the HWHM increases much as the pump power is increased because of the high density of states in the quantum well. This is similar to the behavior observed from the QW sample at room temperature.

3.3.6 Summary

Intensity-dependent PL at room temperature and 77 K has been used to compare the behavior of a QD sample with that of a QW sample. At room temperature, the peak emission from the ground state of the QD sample can be

saturated by intense excitation from an incident laser pump beam. Excited state emission becomes more intense than the ground state emission at high pump powers due to the higher density of states. The excited state emission is very efficient as indicated by the linear increase in integrated PL intensity at high pump powers. The FWHM increase seen at high pump powers can be attributed to the excited state emission since the HWHM on the low energy side of the peak increases more slowly than the FWHM.

3.4 Summary

Temperature-dependent PL and intensity-dependent PL have been used to compare the behavior of a QD sample with a QW sample. The temperature-dependent PL demonstrates that the QD sample can have very efficient radiative recombination, including efficient recombination from excited states when the ground state has been saturated. This suggests that the so-called "phonon bottleneck" (Benisty, Sotomayor-Torres, and Weisbuch, 1991) is not important in these samples. The temperature-dependent PL also indicates that the PL linewidth is dominated by inhomogeneous broadening even at room temperature since the linewidth does not narrow when the sample is cooled. Since thermal broadening is not dominating the low temperature spectra, inhomogeneous broadening due to the size distribution of QDs must be limiting the linewidth at low temperatures. Further evidence to support this statement will be presented in Chapter 4, Morphological and Structural Characterization. The lineshape reflects the density of states, which in this case is simply a distribution of delta functions.

The temperature-dependence of the integrated PL intensity shows that there

are two mechanisms that contribute to the decrease of integrated PL intensity. Thermionic emission out of the QDs causes a slight reduction in the integrated PL intensity at intermediate temperatures. At high temperatures, the rapid decrease in integrated PL intensity indicates some defects as the cause of nonradiative recombination.

Intensity-dependent PL on the QD sample demonstrates that the ground state can be saturated at high pump powers, and excited state luminescence can be more intense than the ground state luminescence at high pump powers. This can be explained by the higher density of states for the excited states compared to the ground state. This will become important in making lasers out of these quantum dots since lasers must have a high carrier concentration in order to achieve inversion. Further evidence of this will be presented in Chapter 6, Fabrication and Characterization of Quantum Dot Lasers.

Chapter 4: Morphological and Structural Characterization of InGaAs Islands

4.1 Introduction

In order to better understand the Stranski-Krastanow growth process by which the InGaAs islands form, and thereby understand and improve the optical properties of these quantum dots, the structural and morphological properties of these islands must be studied. There are several different measurement techniques that can be used. The reflection high-energy electron diffraction (RHEED) pattern from these samples can easily be captured during the growth to give a real-time, *in situ* measurement of the island formation. Atomic force microscopy (AFM) is used for studying the surface morphology and for studying the progression of the island growth. Since the islands are the final layer grown for the AFM samples, the RHEED patterns can be correlated with the AFM images. Transmission electron microscopy (TEM) is a valuable tool for investigating the island density (plan view) and for looking at dislocations and other general structural properties (cross-section). Finally, X-ray diffraction can give a wide variety of information about several parameters such as layer thickness, composition, and In segregation.

The RHEED patterns shown in this section were acquired with a CCD camera and video frame-grabber from k-space Associates. The AFM images were acquired with a Digital Instruments Nanoscope III using either the contact mode or the non-contact "tapping" mode. The X-ray diffractometer is a Philips MRD equipped with a rotating anode source and a low noise detector.

4.2 Reflection High-Energy Electron Diffraction

4.2.1 Introduction

RHEED is a valuable tool for studying the island formation because it is a real-time, *in situ* measurement technique. Because of the glancing angle of incidence, the RHEED beam only samples the top few monolayers of the surface. The Bragg condition normal to the surface is thus relaxed, and a typical RHEED pattern during the growth of flat GaAs appears "streaky". This is indicative of a two-dimensional surface.

During the growth of InGaAs islands using the Stranski-Krastanow growth mode, the surface morphology changes from two-dimensional to three-dimensional. The corresponding RHEED pattern is then dominated by transmission effects and appears "spotty". The RHEED pattern transition from streaky to spotty is used as an indicator that the InGaAs layer has formed islands.

4.2.2 RHEED Observations

The samples used for RHEED measurements are grown under similar conditions to those used for all other sample growths, except that the substrate is not rotated for the RHEED measurements. The growth rates are measured using RHEED oscillations and are: GaAs = 0.425 monolayers/second (MLs/s) and InAs = 0.248 MLs/s. The arsenic species is As_2, and the As_2 beam-equivalent-pressure (BEP) is 9.0×10^{-6} Torr, which is approximately equal to 2.0 MLs/s as measured using As-uptake oscillations (Neave, Joyce, and Dobson, 1984). After oxide desorption at

about 620°C in an As_2 flux, a GaAs buffer layer is grown around 600°C, and then the sample is cooled in an As_2 flux while the substrate temperature is decreased to 515°C for the growth of the InGaAs islands. When the temperature has reached 515°C, the $In_{.3}Ga_{.7}As$ is deposited. The following layer sequence is repeated 25 times, giving a nominal deposited thickness of 22.1 monolayers (about 6.3 nm): 0.265 MLs of In, 2.0 MLs of As, 0.62 MLs of Ga, 3 second delay with no incident flux, and 6.0 MLs of As. Note that the amount of deposited As is actually achieved by leaving the As_2 shutter open for the requisite time, and any excess As desorbs from the surface.

The RHEED pattern from GaAs at 515°C (the growth temperature for the InGaAs islands) under an incident As flux is a *c*(4x4) (not shown). If there is no As flux incident on the surface, the RHEED pattern will slowly return (about 15 seconds) to the (2x4) pattern that is observed at higher temperatures (540°C-650°C) with an incident As flux, as shown in Figures 4-1 (a) and 4-2 (a).

Figure 4-1 (a)-(f) shows a series of RHEED images taken along the $[0\bar{1}1]$ azimuth after various amounts of $In_{.3}Ga_{.7}As$ have been deposited. Figure 4-2 (a)-(f) shows the RHEED pattern along the [011] azimuth with the same amount of $In_{.3}Ga_{.7}As$ deposition as in Figure 4-1. The nominal deposited thicknesses are 0, 3.5, 7.1, 8.0, 8.8, and 9.7 MLs of $In_{.3}Ga_{.7}As$. These images show that as the $In_{.3}Ga_{.7}As$ is deposited, the (2x4) surface reconstruction quickly disappears. This is quite common during the growth of strained layers due to surface disorder.

The RHEED pattern undergoes dramatic changes as the thickness is increased from 7.1 MLs (Figures 4-1 (c) and 4-2 (c)) to 8.0 MLs (Figures 4-1 (d) and 4-2 (d)). Along the $[0\bar{1}1]$ azimuth, the pattern changes from just the specular spot (Figure 4-1 (c)) to a mixture of chevrons with the specular streak (Figure 4-1 (d)) This is indicative of the transition from layer-by-layer growth (2D) to island growth (3D).

Figure 4-1 RHEED images along the $[0\bar{1}\bar{1}]$ azimuth after deposition of (a) 0 MLs, (b) 3.5 MLs, (c) 7.1 MLs, (d) 8.0 MLs, (e) 8.8 MLs, and (f) 9.7 MLs of $In_{.3}Ga_{.7}As$ by alternating MBE..

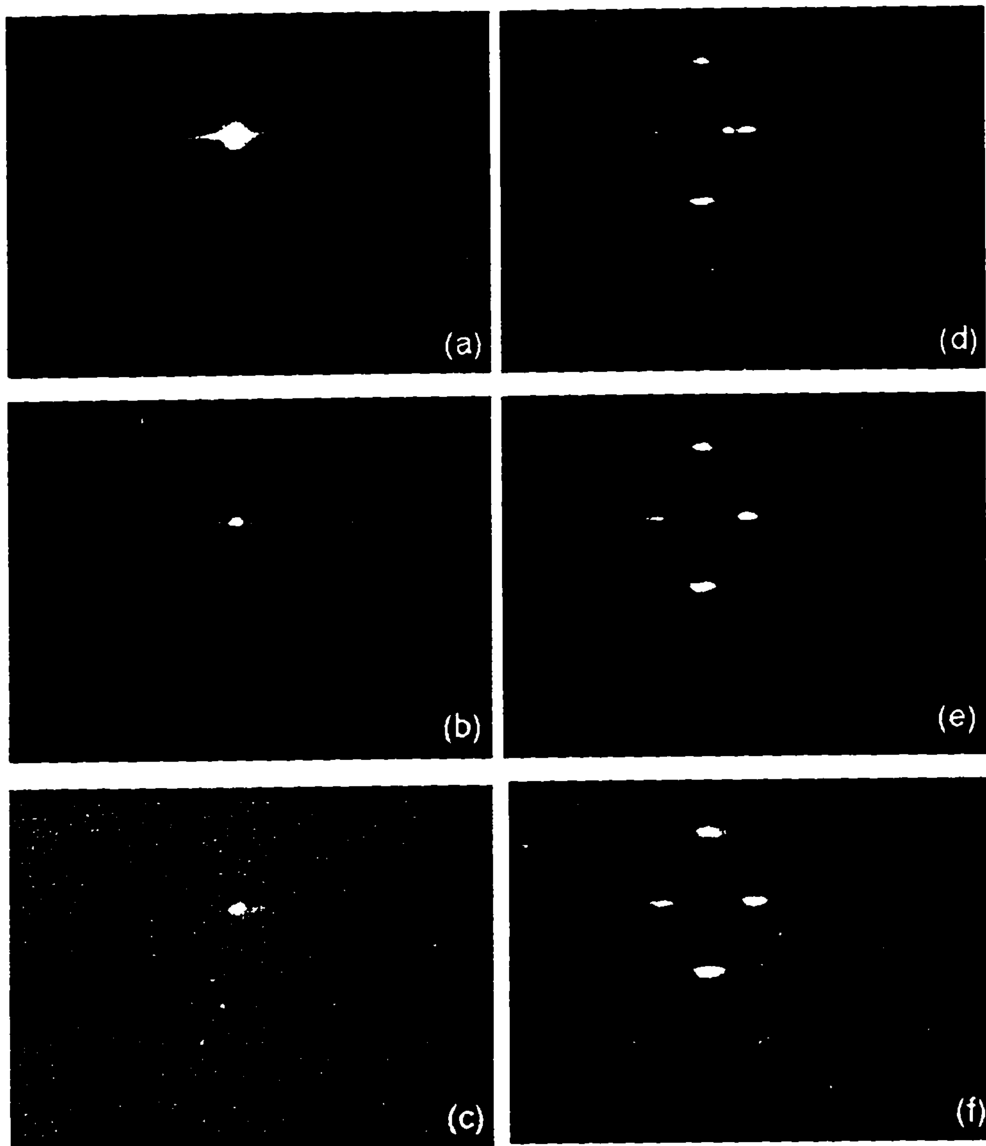

Figure 4-2 RHEED images along the [01 1] azimuth after deposition of (a) 0 MLs, (b) 3.5 MLs, (c) 7.1.0 MLs, (d) 8.0 MLs, (e) 8.8 MLs, and (f) 9.7 MLs of $In_{.3}Ga_{.7}As$ by alternating MBE..

When the $In_{.3}Ga_{.7}As$ thickness is increased further to 8.8 MLs (Figure 4-1 (e)), the chevrons along the $[0\bar{1}1]$ azimuth sharpen and become more pronounced while the specular streak diminishes. Finally, when the thickness is increased even further to 9.7 MLs (Figure 4-1 (f)), the RHEED pattern taken along the $[0\bar{1}1]$ azimuth contains only chevrons; all traces of the specular streak have completely vanished. This chevroned-RHEED pattern remains essentially unchanged until at least 22.1 MLs of $In_{.3}Ga_{.7}As$ have been deposited.

The RHEED pattern along the [011] azimuth undergoes a similar change from a specular streak (7.1 MLs, Figure 4-2 (c)) to a diamond-shaped spot pattern that has a double-spot near the original position of the specular spot (8.0 MLs, Figure 4-2 (d)). As the $In_{.3}Ga_{.7}As$ thickness is increased to 8.8 MLs (Figure 4-2 (e)), the double-spot becomes just a single spot, with the original specular reflection disappearing This pattern remains through at least 22.1 MLs of growth.

4.2.3 Discussion

The chevrons that are observed along the $[0\bar{1}1]$ azimuth are very well-defined. The angle between the streaks that form the chevron is about 50°. The half-angle (25°) is equal to the angle between the (100) plane, which gives the streak that is perpendicular to the shadow-edge in Figures 4-1 (a)-(d), and the plane that gives the chevrons (Simmons, Mitchell, and Lawless, 1967). This is the (311) plane. Since the chevrons are so well-defined (the width of the streaks is about the same as the width of the streaks from the (100) plane), these (311) planes must also be well-defined, with little or no components of other planes mixed in.

These chevrons are not observed along the [011] azimuth. Instead, just a

spotty pattern corresponding to transmission is observed. This means that there are not well-defined sidewalls along this azimuth. Instead, there must be many small facets of different orientations, so that no coherent interference can be observed.

4.2.4 Summary

RHEED is an extremely useful technique for determining when the InGaAs has layer has undergone the transition from two-dimensional, layer-by-layer growth to three-dimensional, island growth. The chevrons that are observed along the $[0\bar{1}1]$ azimuth indicate that the islands have well-defined sidewalls. The sidewalls are {311} as determined by measuring the angle of the chevron. In the next section, I will correlate the changes in the RHEED pattern with the surface morphology as determined using AFM.

4.3 Atomic Force Microscopy

4.3.1 Introduction

In the last five years, Atomic Force Microscopy (AFM) has become a common characterization tool for investigating surface morphology of nanoscale structures. This is probably the most common technique in use for researchers studying Stranski-Krastanow growth of islands (Moison *et al.*, 1994). Unlike TEM, AFM requires little or no preparation of the sample after growth. The fast sample turnaround and ease of use make AFM an excellent method for investigating the surface morphology of Stranski-Krastanow islands.

4.3.2 Experimental Results-Preliminary Sample Growth

The first sample grown for AFM characterization is QDAFM-01. This sample is identical to QDPL-21 (see Chapter 2 and Appendix A for more details), except the growth is terminated immediately after the InGaAs layer is completed; no GaAs capping layer is deposited. The growth consists of (see Figure 4-3 and Appendix A for a layer diagram) a 50 nm buffer layer of GaAs, a 10 period superlattice of $Al_{0.4}Ga_{0.6}As$/GaAs (1 nm/1 nm, 20 nm total), and a 200 nm GaAs layer, all grown at a substrate temperature of about 600°C. Next, the substrate temperature is lowered to 515°C in an As_2 flux to deposit the $In_{.3}Ga_{.7}As$ layer. The $In_{.3}Ga_{.7}As$ layer is 22.1 MLs thick and is deposited using the alternating MBE sequence described earlier. After deposition is completed, the sample is cooled down in an As_2 flux. The sample is kept in vacuum until just before it is measured to minimize the surface contamination and/or oxidation.

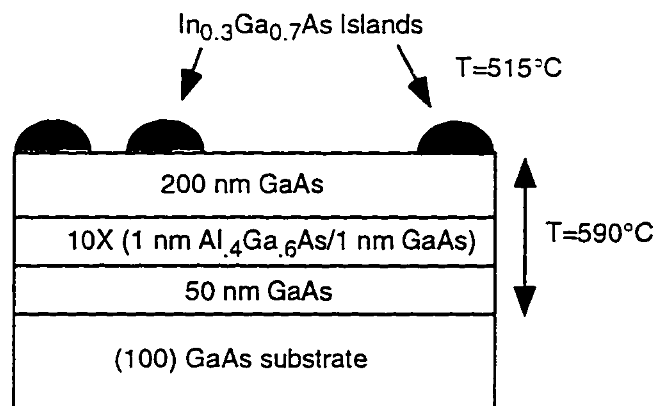

Figure 4-3 Layer diagram for QDAFM-01 through -08. The $In_{.3}Ga_{.7}As$ layer is deposited by AMBE, and the nominal thicknesses are given in Appendix A.

4.3.3 AFM Measurements and Analysis on QDAFM-01

AFM images at different magnifications are shown in Figures 4-4 (a) and (b). The images show that practically the entire surface is covered with islands. The larger image (Figure 4-4 (a)) has two anomalously large islands that appear as very bright in this image. These islands have probably partially relaxed (Leonard, Pond, and Petroff, 1994). Higher resolution AFM images of these areas (not shown) do not reveal any more details about these defects.

The image in Figure 4-4 (b) is analyzed using the software in Appendix B. The island density is 2-3 x 10^{10} cm^{-2}. Histograms of the peak height (the height at the center of the island), the major axis length, and the minor axis length are shown in Figures 4-5 (a)-(c). The mean height is 23.5 nm with a standard deviation of 3.6 nm. The mean length of the major axis is 54.1 nm with a standard deviation of 7.3 nm. The mean length of the minor axis is 36.1 nm with a standard deviation of 6.4 nm. The height resolution is determined by the parameters set during use of the microscope, and in this case it is better than 1.0 Å. The in-plane resolution is determined by the size of the area imaged and the number of pixels per image (128x128, 256x256, or 512x512): Figure 4-4 (b) is a 1 μm x 1 μm image with 512 x 512 pixels, thus giving a pixel size of 1.95 nm x 1.95 nm. Thus, the standard deviation in lateral dimension is only slightly larger then the uncertainty due to the quantization noise of the microscope.

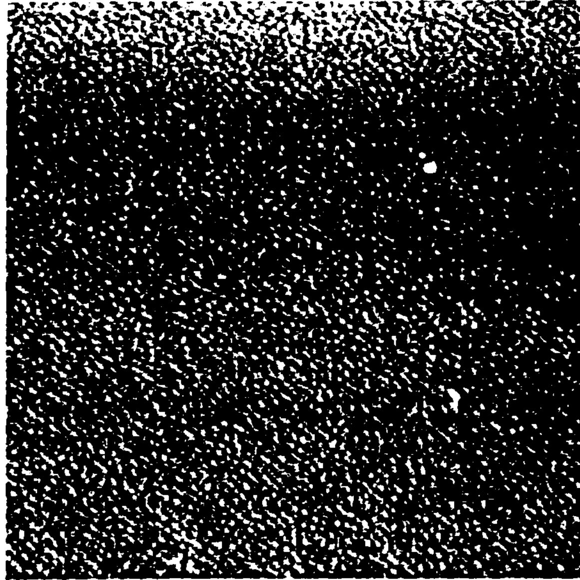

Figure 4-4 (a) 3 μm x 3 μm x 30 nm AFM image of QDAFM-01, which has 22.1 MLs of $In_{.3}Ga_{.7}As$ deposited by AMBE.

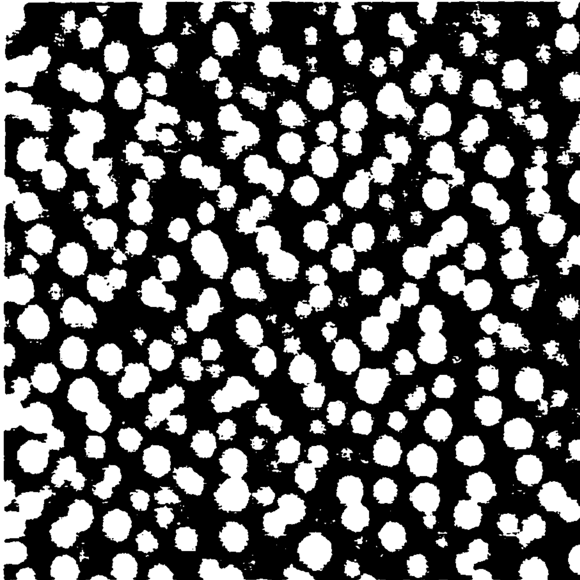

Figure 4-4 (b) 1 μm x 1 μm x 30 nm AFM image of QDAFM-01.

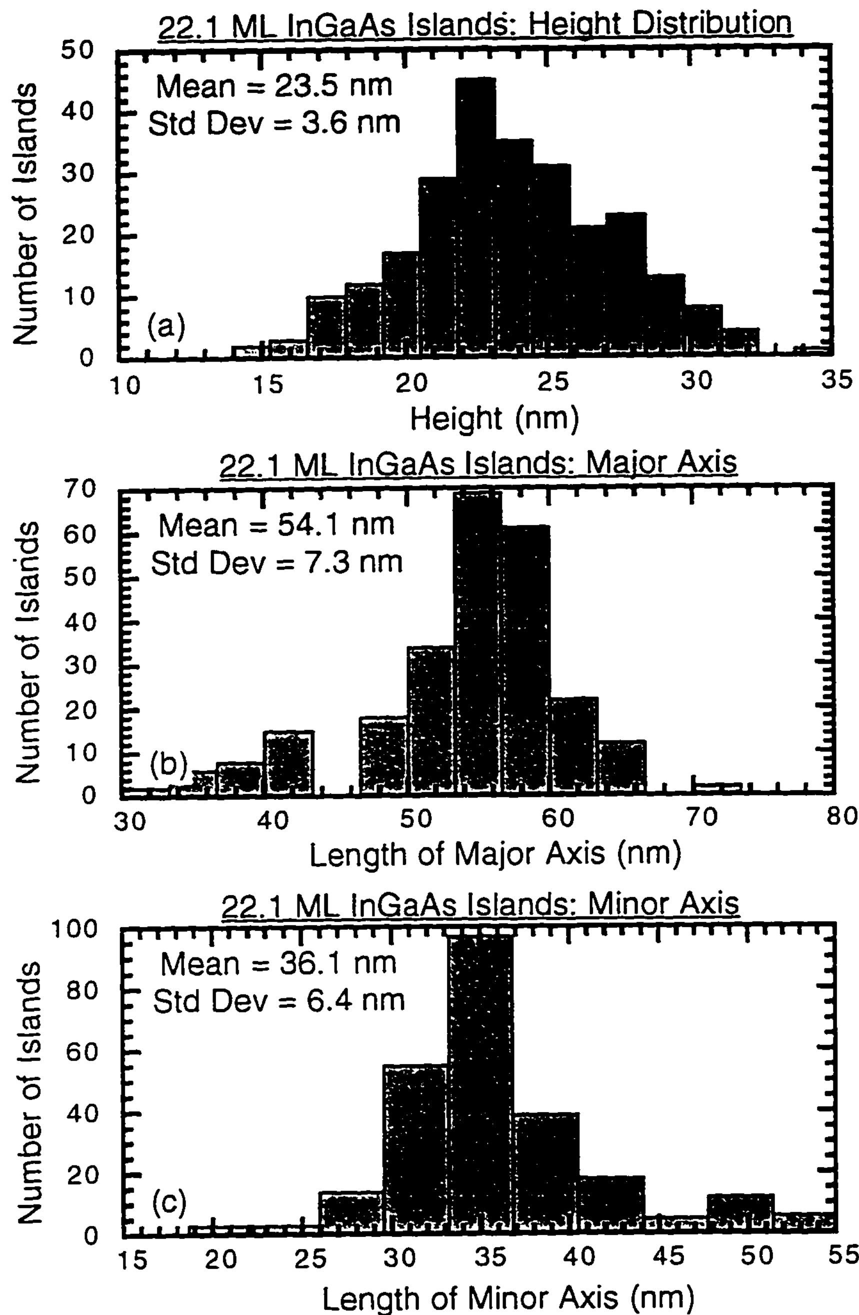

Figure 4-5 For 22.1 ML InGaAs islands (QDAFM-01), the size distribution of (a) height, (b) length of the major axis, and (c) length of the minor axis.

An identical sample (QDPL-21, see Chapter 2 and Appendix A) to QDAFM-01 was grown consecutively, except that QDPL-21 had a cap layer so that photoluminescence (PL) measurements can be made. Room temperature PL measurements on QDPL-21 are shown in Figure 2-16. For the case of a quantum well, the linewidth of the emission spectrum can be related to the fluctuations in the well width (Herman, Bimberg, and Christen, 1991). The transition energy in a quantum well is given by

$$E_{tr} = E_{gap} + \frac{\pi^2\hbar^2}{2m_eL^2} + \frac{\pi^2\hbar^2}{2m_hL^2} \tag{4-1}$$

where E_{gap} is the bandgap of the island material, m_e is the effective mass of the electron, m_h is the effective mass of the hole, and L is the quantum well thickness. This equation assumes a square quantum well with infinite barriers. We can apply this same equation to the quantum dots by taking L to be the height of the quantum dot and adding a term due to the lateral quantization:

$$E_{tr} = E_{gap} + \frac{\pi^2\hbar^2}{2m_eL^2} + \frac{\pi^2\hbar^2}{2m_hL^2} + E_{lat}(L_{lat}). \tag{4-2}$$

This equation can be written in terms of the reduced exciton mass, m_r, where

$$m_r = \frac{m_em_h}{m_e+m_h} \tag{4-3}$$

so that

$$E_{tr} = E_{gap} + \frac{\pi^2\hbar^2}{2m_rL^2} + E_{lat}(L_{lat}). \tag{4-4}$$

Differentiating Equation 4-4 yields

$$\frac{dE}{dL} = -\frac{\pi^2 \hbar^2}{m_r L^3} + \frac{dE_{lat}}{dL_{lat}}. \tag{4-5}$$

Now, since the lateral dimensions of the quantum dots are much larger than the height of the quantum dots, the lateral quantization energy is much smaller than the quantization energy due to the height. Furthermore, the fluctuations in the lateral dimensions will cause only small fluctuations in the energy. Therefore, we can neglect the change in energy due to lateral quantization, and Equation (4-5) then becomes

$$\frac{dE}{dL} = -\frac{\pi^2 \hbar^2}{m_r L^3}. \tag{4-6}$$

Thus, the fluctuations in energy are related to the fluctuations in island height by

$$\Delta E = \frac{\pi^2 \hbar^2}{m_r L^3} \Delta L. \tag{4-7}$$

Assuming a reduced mass that is equal to the effective mass of an electron in InAs (0.026 m_0) and using the histogram values for L and ΔL, Equation 4-7 yields a value of 7.8 meV for ΔE. The measured value of the half width at half maximum from Figure 2-16 is 19.0 meV. This is a reasonable agreement given all the assumptions that are behind the theory. The only fluctuations considered here are those due to the fluctuations in height of the islands; lateral size fluctuations are neglected. For the islands considered in this example, this is probably a good approximation since the lateral dimensions are much larger than the height of the islands. The quantization energy assumes a square well potential with infinite

barriers. This probably overestimates the quantization energy since the island is not square, and the barriers are not infinite. Finally, there is a large uncertainty in the reduced mass. In this example I have assumed that the effective mass of the hole is much larger than that of the electron. This may not be accurate because of the uncertainty of the effects of strain on the valence band structure. For strained InGaAs quantum wells on GaAs, strong mixing of the valence bands due to the strain causes the reduction of the effective mass of the holes near the zone center. A similar effect may be happening in this case. Furthermore, due to the non-hydrostatic strain caused by the three-dimensional growth, even the conduction band mass will be modified by the strain. Given all of the unknown parameters, reasonable agreement between theory and experiment is obtained.

4.3.4 Systematic Growth Study

A series of samples was grown to characterize the surface morphology both before and after island formation. QDAFM-02 was terminated after the GaAs buffer layer was completed. The layer structure was 50 nm of GaAs, a 25 period superlattice of AlAs/GaAs (1 nm/1 nm, 50 nm total), and 200 nm of GaAs (see Figure 4-3 and Appendix A). The substrate temperature was about 590°C, and the growth rates were: GaAs = 0.928 MLs/s, AlAs = 0.712 MLs/s, and As = 2.0 MLs/s. The RHEED pattern (Figures 4-1 (a) and 4-2 (a)) taken after growth was that of a streaky, (2x4) reconstructed surface.

A 3 μm x 3 μm AFM image of the surface is shown in Figure 4-6. Despite the streaky RHEED pattern, it is clear that the surface is not perfectly flat. There are long, narrow terraces aligned along the $[0\bar{1}1]$ direction. Careful examination of the

edges of the terraces shows a dense step-bunching. Figure 4-7 is a section analysis from the software on the Digital Instruments AFM computer. The largest terrace height is 3.367 nm, which is equal to 12 atomic steps of height 0.28 nm. The width of the largest terraces is 200-250 nm. Note that the height-to-width ratio of the AFM distorts the apparent angle of the edge of these terraces; as Figure 4-7 shows in the inset, the slope angle at the terrace-edge is less than 2°.

Figure 4-6 3 μm x 3 μm x 4 nm AFM image of QDAFM-02, which is the GaAs buffer layer on which the InGaAs is grown.

QDAFM-03 has the same buffer layers as QDAFM-02, and then 3.5 monolayers (4 cycles) of $In_{0.3}Ga_{0.7}As$ are deposited at 515°C by using the same alternating MBE technique described above for the growth of QDAFM-01. Figure 4-8 is a 2 μm x 2 μm AFM image of this surface. Figure 4-9 shows a section analysis of this surface. Compared to QDAFM-02 (the GaAs buffer layer), this image still shows the same large-scale, GaAs terraces due to the GaAs step-bunching, and

additionally shows a fine scale roughness that is not seen on just the GaAs buffer layer, which appears relatively smooth in between terraces. This fine scale roughness is on the order of 0.5 nm in height. It is particularly of interest to note that all of the terraces now have a peak in height at the *top edges*. This is in sharp contrast to the GaAs buffer layer, which tends to be single-peaked towards the center of the terrace.

QDAFM-04 has 6.2 monolayers of $In_{0.3}Ga_{0.7}As$ deposited by AMBE on top of the GaAs buffer layer. Figures 4-10 (a) and (b) show 3 µm x 3 µm and 1 µm x 1 µm AFM images, respectively, of the surface. Now the surface roughness is very large and it appears very non-uniform, as though the InGaAs is forming small clusters on the surface instead of uniformly covering the surface.

Figures 4-11 (a) and (b) are 3 µm x 3 µm and 600 nm x 600 nm AFM images of QDAFM-05, which has 7.1 monolayers of $In_{0.3}Ga_{0.7}As$ deposited by AMBE in addition to the same buffer sequence as QDAFM-02. The small clusters that are visible with 6.2 monolayers of deposition are no longer seen on QDAFM-05. Although the RHEED pattern still appears streaked, the AFM images shown in Figure 4-11 shows that a few islands (about 5×10^7 cm^{-2}) have formed. These islands appear at the corners of the elongated GaAs terraces.

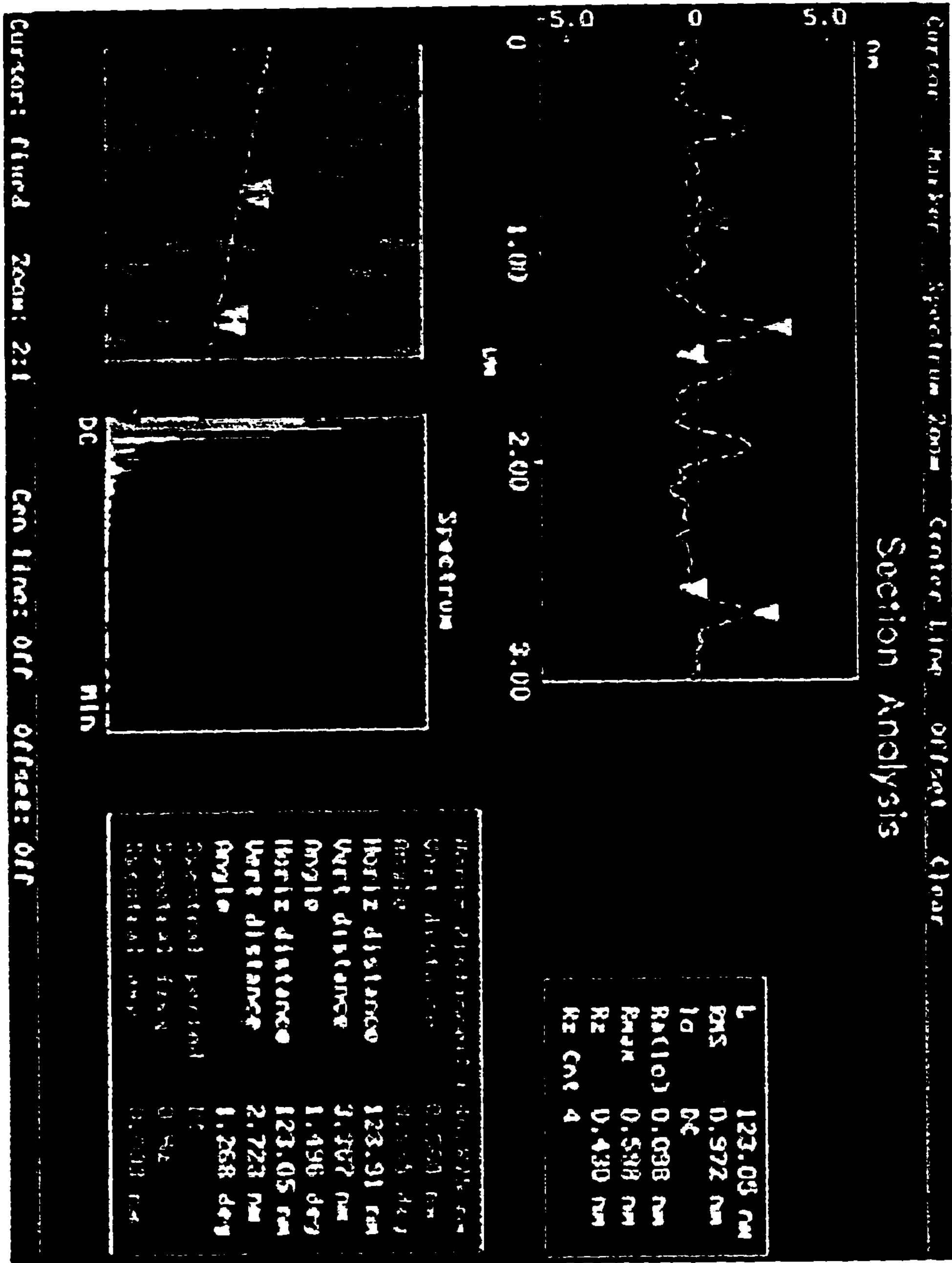

Figure 4-7 AFM sectional analysis shows the atomic steps in the GaAs buffer layer.

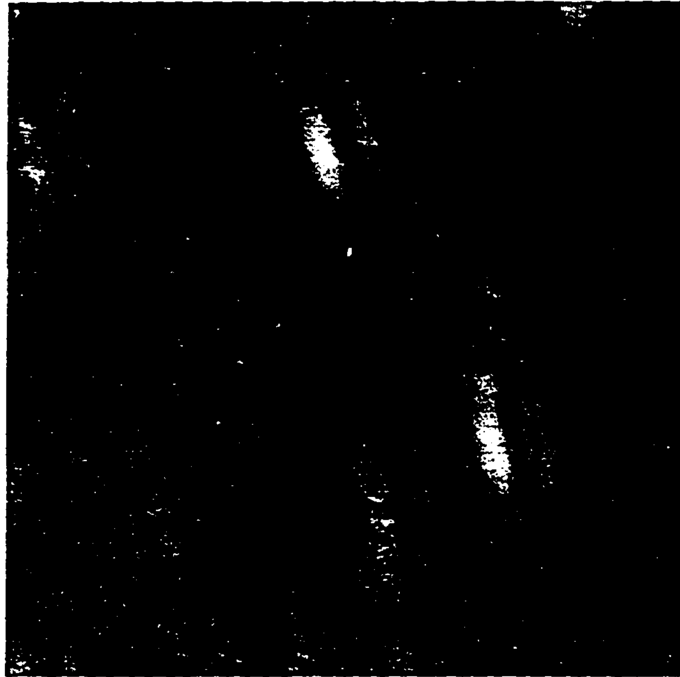

Figure 4-8 2 µm x 2µm x 4 nm AFM image of 3.5 MLs of $In_{.3}Ga_{.7}As$ grown by AMBE.

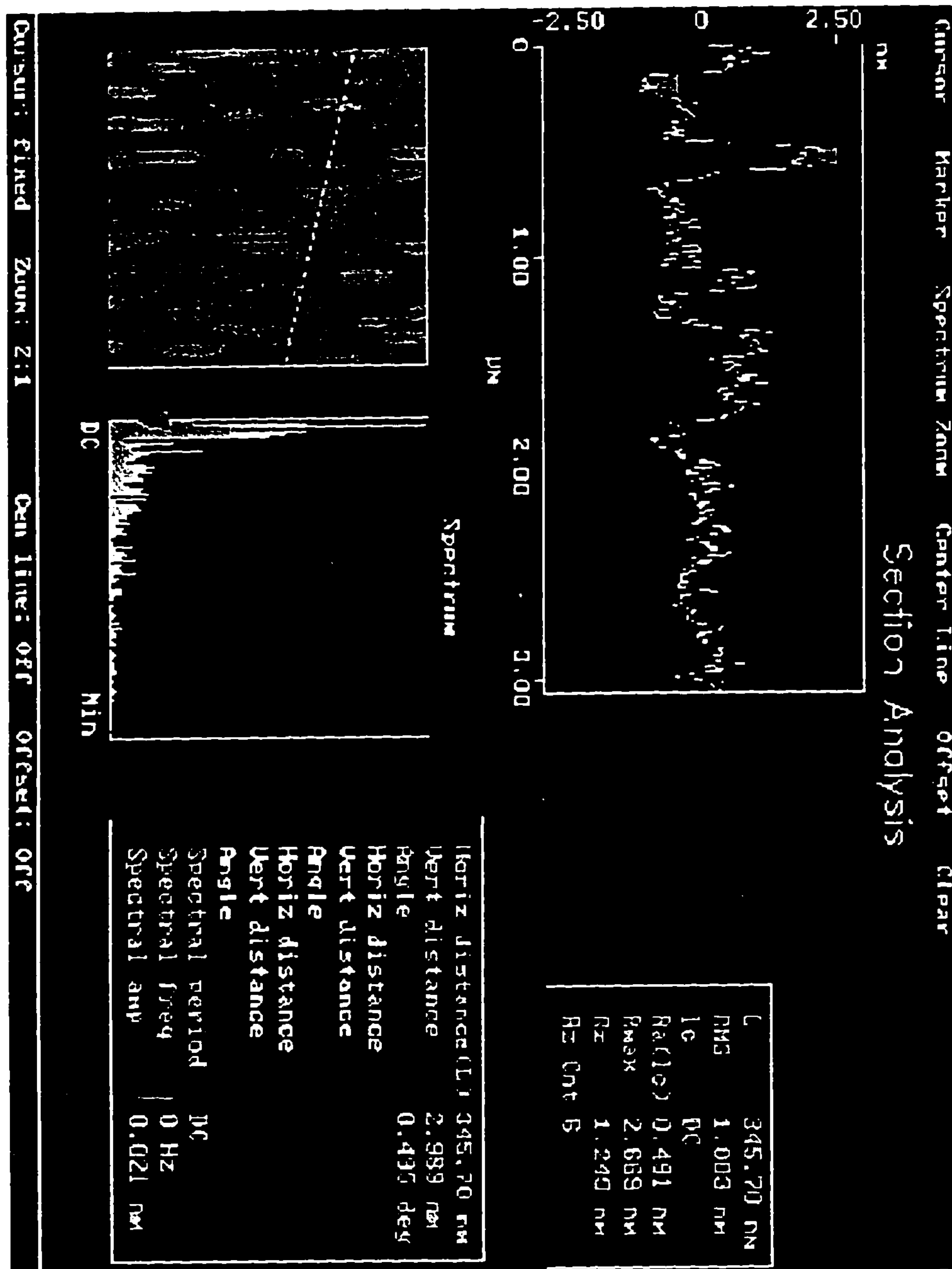

Figure 4-9 Section analysis of QDAFM-03 shows fine scale roughness due to the InGaAs in between the GaAs terraces.

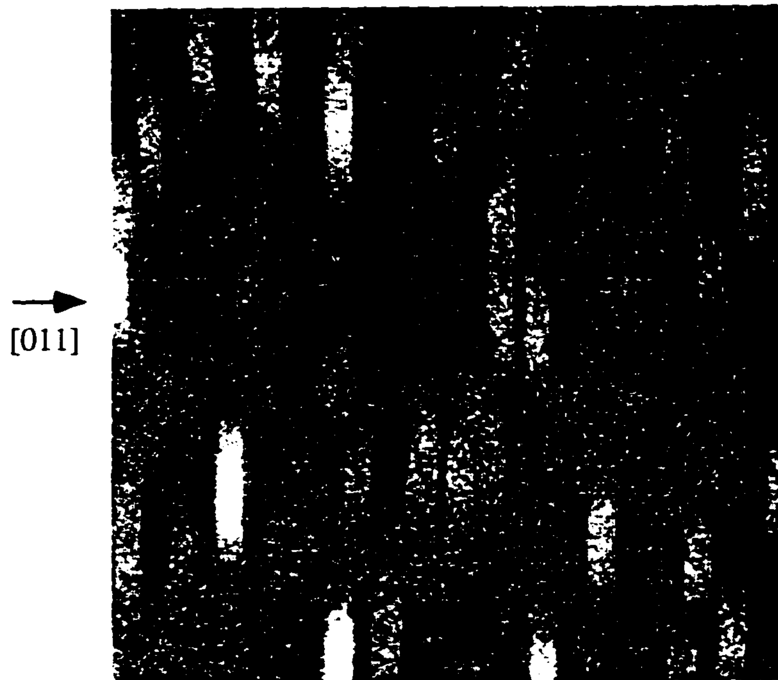

Figure 4-10 (a) 3 μm x 3 μm x 8 nm AFM image of QDAFM-04.

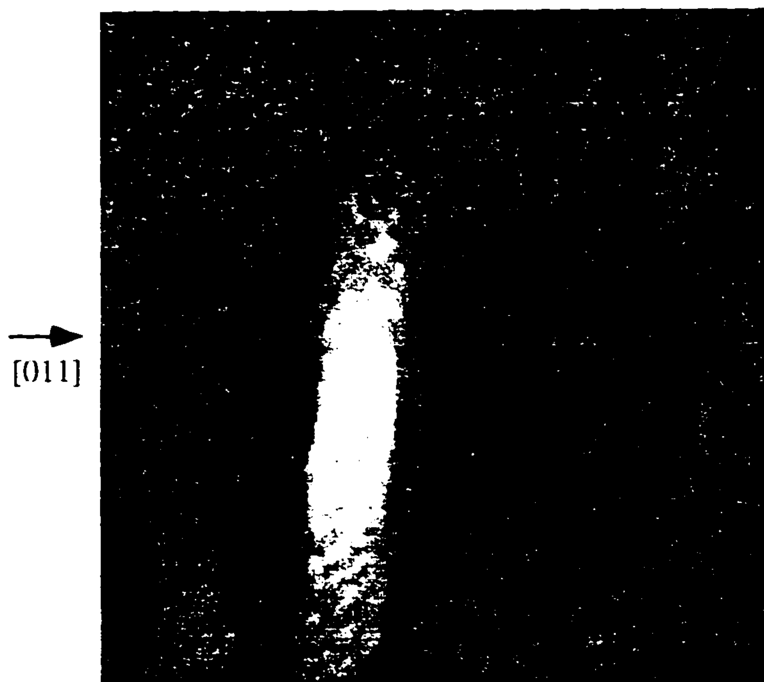

Figure 4-10 (b) 1 μm x 1 μm x 8 nm AFM image of QDAFM-04.

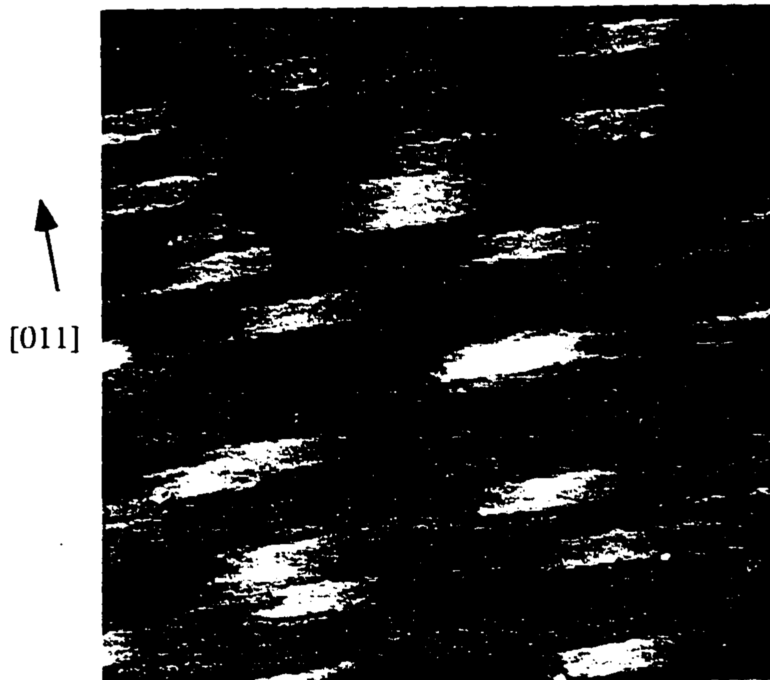

Figure 4-11 (a) 3 μm x 3 μm x 5 nm AFM image of QDAFM-05 shows the first few islands forming on the terrace tops.

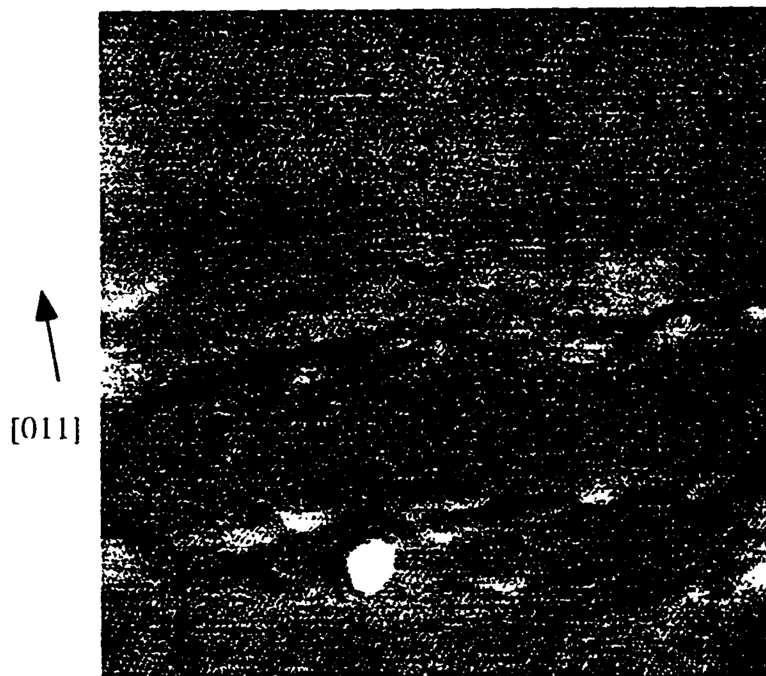

Figure 4-11 (b) 600 nm x 600 nm x 5 nm AFM image of QDAFM-05 shows a closeup of one island on a terrace edge.

QDAFM-06 has the identical buffer layer structure as QDAFM-02, and in addition has 8.0 monolayers of $In_{0.3}Ga_{0.7}As$ deposited by the above shutter sequence. Figures 4-12 (a) and (b) are 5 μm x 5 μm and 1.2 μm x 1.2 μm AFM images of QDAFM-06, respectively. The island density has now increased to about 2-3 x 10^8 cm^{-2}. Note that all of the islands appear *on the top* of the GaAs terraces.

QDAFM-07 has 13.3 monolayers of $In_{0.3}Ga_{0.7}As$ deposition. Figures 4-13 (a) and (b) are AFM images from this sample. The InGaAs islands are now well-formed, and they completely cover the surface. The island density is 4-5 x 10^{10} cm^{-2}. There are long chains of islands formed at the edges of the elongated GaAs terraces. Note that there are always *two* chains of islands formed, one at the top of either terrace-edge.

QDAFM-08 has 17.7 monolayers of InGaAs deposition. The AFM images (see Figures 4-14 (a) and (b)) look very similar to those from QDAFM-07 (13.3 monolayers. Figure 4-13)): chains of islands aligned along terrace-edges can easily be seen, and the island density is still 4-5 x 10^{10} cm^{-2}.

4.3.5 Analysis and Discussion

The AFM samples grown below the 2D-3D transition thickness demonstrate that it is simple for the In adatoms to diffuse to the edges of the GaAs terraces, but it is difficult for these adatoms to move down the terrace edge. This implies that a Schwoebel barrier (Schwoebel and Shipsey, 1966) exists at the terrace edges that prevents the adatoms from moving down the steps. This leads to the formation of InGaAs clusters at the edges of the terraces; these InGaAs clusters are the precursor to the formation of larger islands.

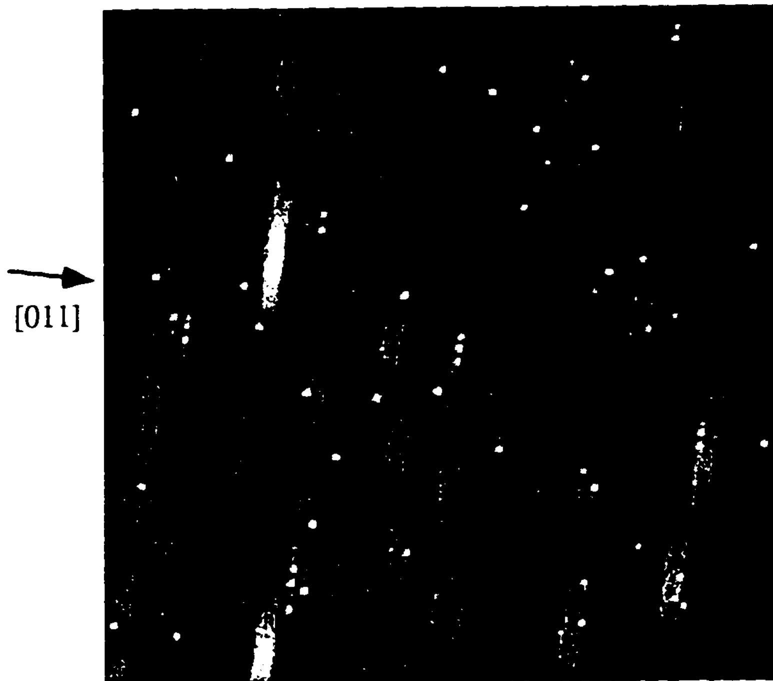

Figure 4-12 (a) 5 μm x 5 μm x 6 nm AFM image of QDAFM-06 shows several islands forming on the terrace tops.

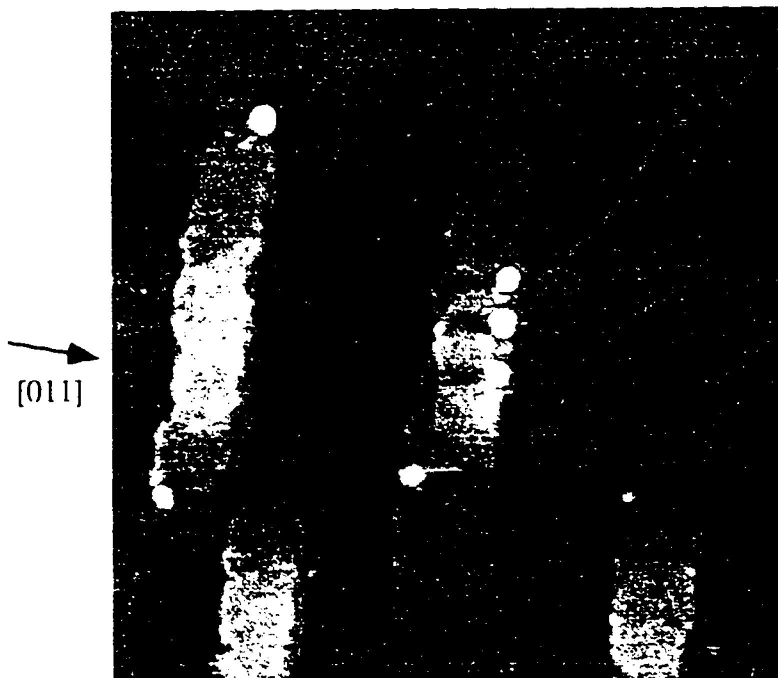

Figure 4-12 (b) 1.2 μm x 1.2 μm x 6 nm AFM image of QDAFM-06 shows a chain of islands forming along a terrace top.

mean

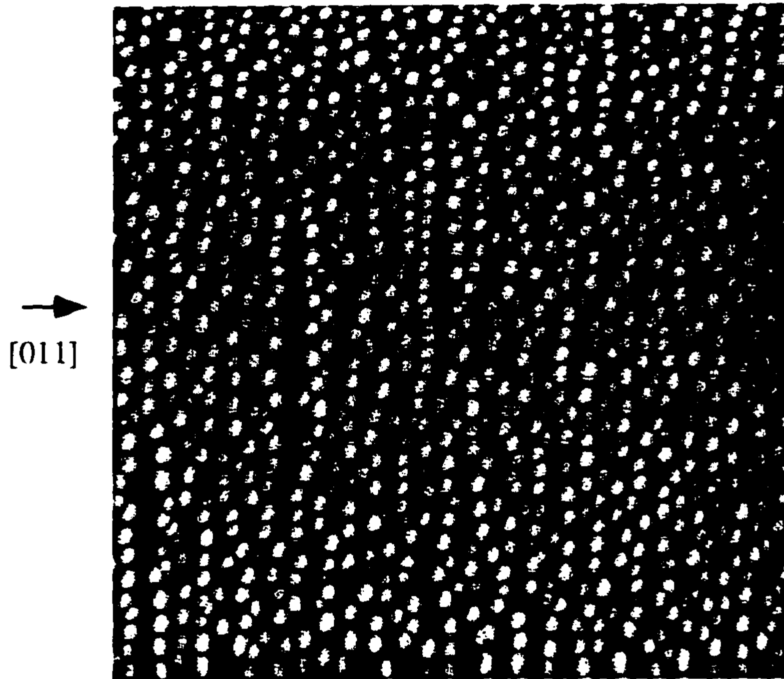

Figure 4-13 (a) 2 μm x 2 μm x 15 nm AFM image of QDAFM-07 shows island chains on terrace tops.

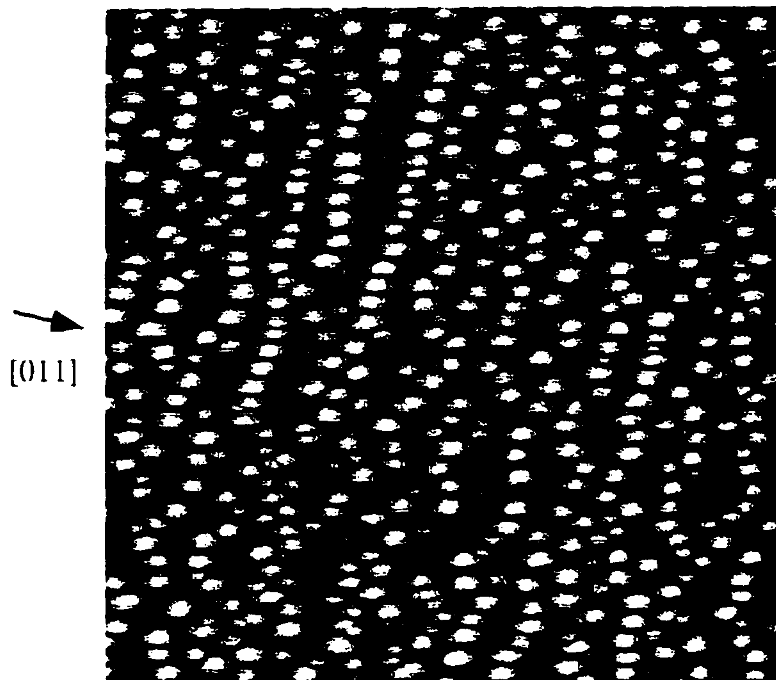

Figure 4-13 (b) 1 μm x 1 μm x 15 nm AFM image of QDAFM-07.

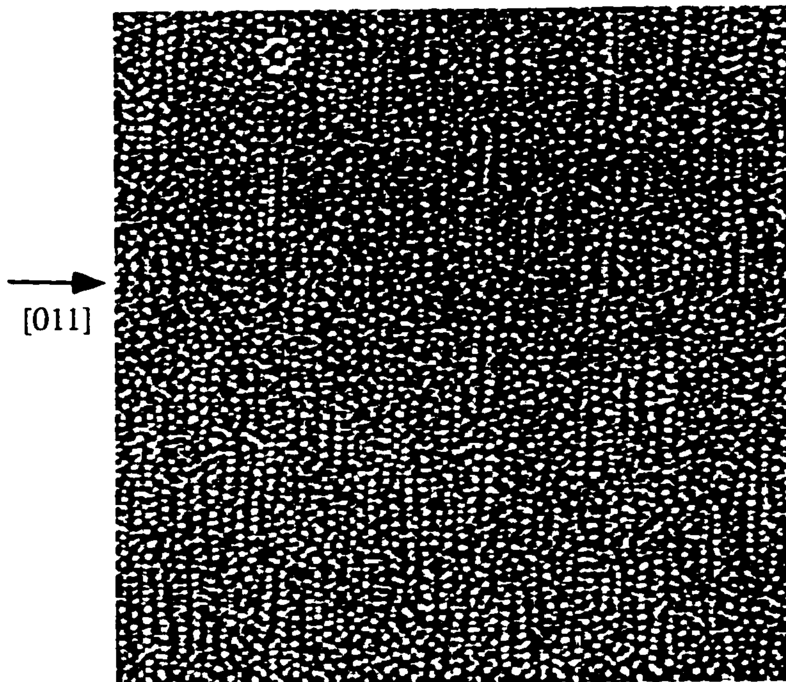

Figure 4-14 (a) 5 μm x 5 μm x 15 nm AFM image of QDAFM-08 shows that the surface is covered with islands, including chains of islands along the terrace tops.

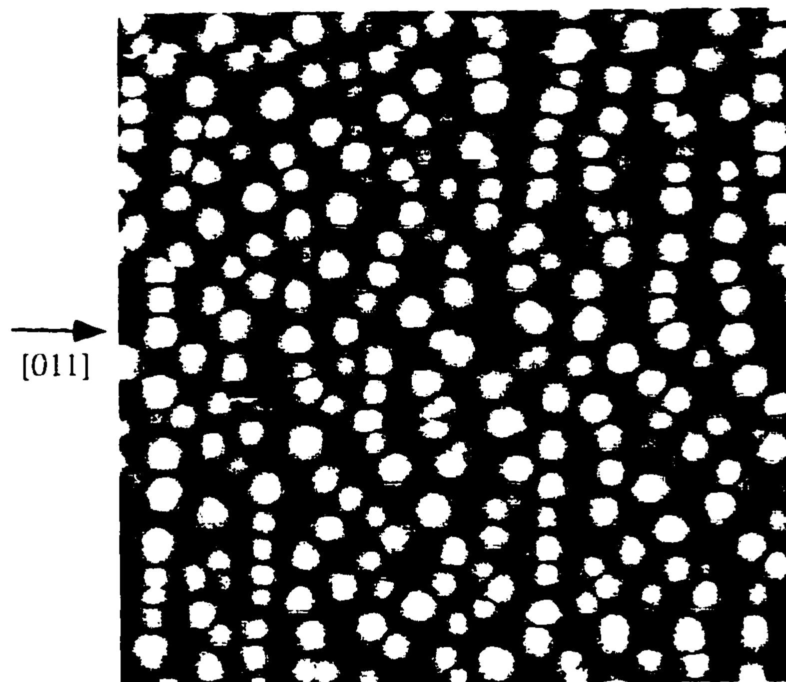

Figure 4-14 (b) 1 μm x 1 μm x 15 nm AFM image of QDAFM-08 in between the terraces.

Histograms from QDAFM-07 (13.3 MLs of $In_{.3}Ga_{.7}As$) are shown in Figure 4-15 (a)-(c). The mean height is 11.9 nm with a standard deviation of 1.9 nm. The length of the $[0\bar{1}1]$-oriented major axis is 29.4 nm with a standard deviation of 5.1 nm, and the mean length of the [011]-oriented minor axis is 19.6 nm with a standard deviation of 4.1 nm.

Histograms from QDAFM-08 (17.7 MLs of $In_{.3}Ga_{.7}As$) are shown in Figure 4-16 (a)-(c). The mean height is 9.2 nm with a standard deviation of 1.7 nm. The mean length of the $[0\bar{1}1]$-oriented major axis is 32.6 nm with a standard deviation of 6.1 nm, and the mean length of the [011]-oriented minor axis is 29.5 nm with a standard deviation of 5.3 nm.

It is surprising to find that the apparent height of the 17.7 ML islands is actually smaller than that of the 13.3 ML islands. This comes about despite the island densities being very similar. The major axis length of both samples is very similar, but the length of the minor axis is much larger for the 17.7 ML islands.

There are several possible explanations for the above discrepancy in height. Part of the reason for the 13.3 ML islands appearing taller than the 17.7 ML islands may be due to the AFM image processing software. In order to obtain good quality images, it is necessary to "flatten " the images. This takes all of the points in a given line and sums them so that each line has the same sum. The effect of this is that wherever there is an island, there appears darker horizontal lines that correspond to the space in between islands. Thus, in order for the sum to be equal, the local minima are reduced even further. This causes an apparently larger island size since the image processing software in Appendix B has to use some average of the local minima to define the zero point. Since the islands in the 17.7 ML sample have larger in-plane dimensions compared to the 13.3 ML sample, the effect of summing along a trace is

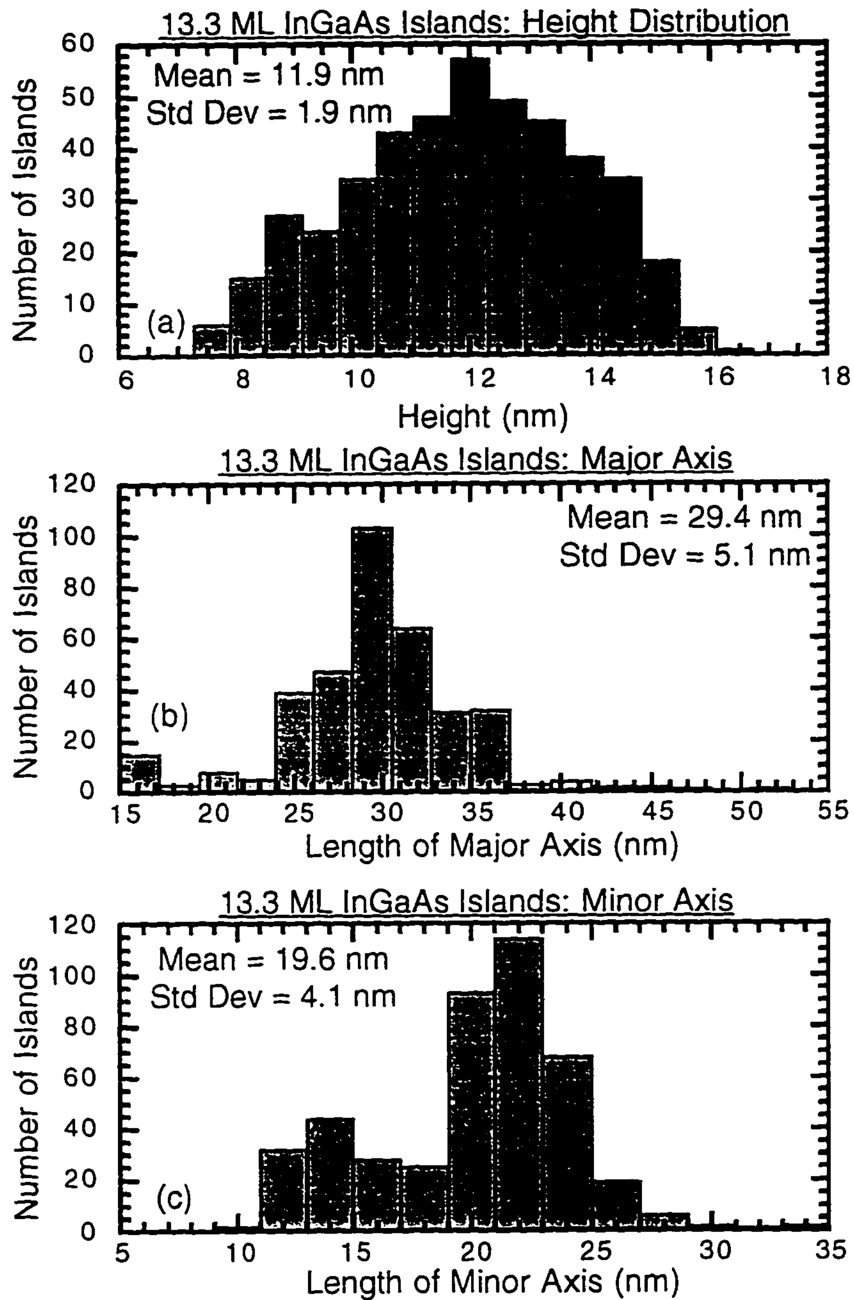

Figure 4-15 For 13.3 ML InGaAs islands (QDAFM-07), the size distribution of (a) height, (b) length of the major axis, and (c) length of the minor axis.

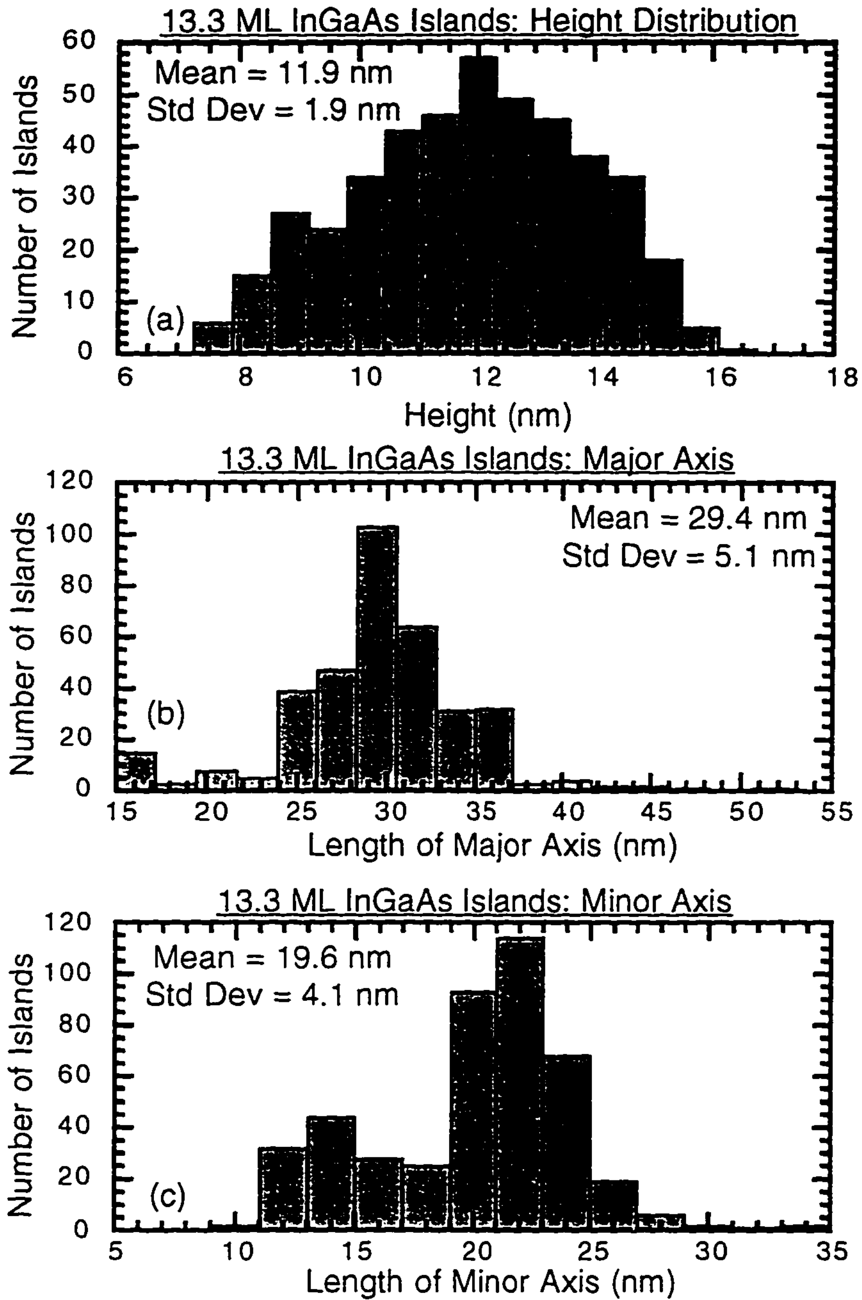

Figure 4-15 For 13.3 ML InGaAs islands (QDAFM-07), the size distribution of (a) height, (b) length of the major axis, and (c) length of the minor axis.

magnified since there is less flat area in the 13.3 ML sample.

Another possible cause for this discrepancy is that the image of QDAFM-07 (13.3 ML islands) contains a large GaAs terrace. Since the islands form on top of the terrace, as noted earlier, they are actually a few nm smaller (the height of the terrace) than the apparent height computed by the histogram software in Appendix B.

From the images shown here, it is possible to conclude that the island density increases rapidly around the 2D-3D transition, but then saturates at about 4-5 x 10^{10} cm^{-2}. Although the images of QDAFM-01 (22.1 ML islands) only have an island density of 2-3 x 10^{10} cm^{-2}, it is ambiguous as to whether the island density later decreases since QDAFM-01 was grown several months apart from the remainder of the samples and does not have the large GaAs terraces to align the islands. Other researchers have found that island coalescence is accompanied by relaxed islands, but there are is only weak evidence for that in these samples.

The major axis length appears to fairly constant above a certain value of deposited thickness, but the minor axis length varies considerably. It is again difficult to draw any strong conclusions by comparing the 13.3 and 17.7 ML samples to the 22.1 ML sample because the island density is lower for the 22.1 ML sample.

4.3.6 Island Shape

By combining the RHEED pattern information with the AFM images, we can determine the real shape of an island. As seen in Figure 4-1, the chevron along the $[0\bar{1}1]$ azimuth has an angle of about 50°, which means that the facet causing diffraction into that chevron is a (311) plane. Also, there is no intensity in the specular streak ((100) plane), which indicates that the islands do not have a flat top as

has been seen with some MOCVD-grown Stranski-Krastanow islands (Georgsson *et al.*, 1995). The AFM images also suggest a sharp peak and not a flat top. The AFM image and the RHEED pattern can be combined to produce the picture of an island as shown in Figure 4-17. The sidewalls of the pyramid along the [011] direction are formed from well-defined (311) planes. The sidewalls along the orthogonal [011] direction are somewhat rounded instead, as indicated by the absence of chevrons in the RHEED pattern.

Nötzel *et al.*, 1991 have experimentally shown (using both RHEED and high-resolution transmission electron microscopy) that (311) GaAs breaks into (311) terraces joined by {331} facets at temperatures ranging from room temperature to about 590°C. This is in agreement with theoretical predictions that the (311) face can lower its surface energy by forming facets (Chadi, 1984). The InGaAs islands grown here very well-defined (311) planes and show no indications of any {331} facets. In order to properly predict which facet planes will bound the islands, it is important to consider the strain energy associated with a given facet, in addition to the energy associated with a free surface of a given facet. Finally, kinetic limitations on facet formation must also be considered since MBE growth is far from an equilibrium growth process.

4.3.7 Summary

AFM images provide a greater deal of information about the growth of InGaAs islands, both before the islands form and the evolution of the islands. The GaAs buffer layer can be used to form laterally-aligned chains of islands. The InGaAs islands form on top of the GaAs terraces. This is caused by a Schwoebel

barrier at the edges of the terraces that prevents the In adatoms from migrating down the step edges. Island densities as high as 5 x 10^{10} cm^{-2} have been measured with a height uniformity of about ± 15%. The in-plane island shape is slightly elliptical with the major axis oriented along the $[0\bar{1}1]$ direction. Finally, the uniformity of the islands has been shown to give good agreement with a simple theory for relating the size fluctuations to the photoluminescence linewidth.

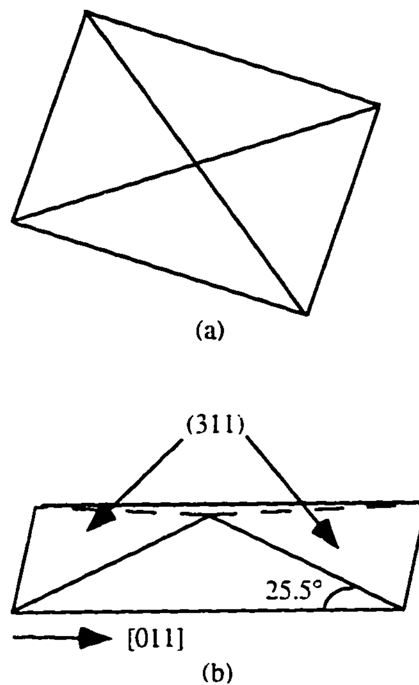

Figure 4-17 Schematic representation of the shape of an InGaAs island.
(a) Plan view, and (b) Side View

4.4 X-ray Diffraction

4.4.1 Introduction

High-resolution X-ray diffraction (HRXRD) is a very powerful tool for

determining the composition and/or thickness of an unknown layer. The experimental results are then compared to simulated results, and discrepancies can be used to tell the crystal grower what he or she *actually* grew. For (100)-oriented III-V semiconductors, the (400) reflection, which is commonly referred to as the symmetric reflection, is the most commonly used reflection.

HRXRD can be used to detect ultrathin (< 1 monolayer) semiconductor layers under the proper conditions (Tapfer, Ospelt, and von Känel, 1990, Holloway, 1990). The ideal structure for detecting ultrathin layers consists of a thick layer (such as a GaAs substrate), the ultrathin layer, which should have a different lattice constant than the substrate (such as InGaAs), and another thin layer that is identical to the thick layer. The important parameter in these structures is the so-called "phase-shift parameter," which is defined to the product of strain and thickness (Wie *et al.*, 1989, Tapfer, Ospelt, and von Känel, 1990). This is analogous to the "optical thickness" used in optics, which is the product of the index of refraction and the layer thickness.

The interference pattern around the main peak is extremely sensitive to the phase-shift parameter. The symmetry of this main peak will periodically repeat, and the period is given by (Holloway, 1990)

$$\Delta t \approx \frac{d/m}{\delta d/d} \tag{4-8}$$

where Δt is the period, d is lattice constant of the substrate and thin cap layer, δd is the difference in unstrained lattice constants between the substrate and the thin strained layer, and m is an integer corresponding to the particular reflection that is used. Thus, by comparison of the symmetry around the main (substrate) peak, the thickness-strain product can be accurately determined if the other growth parameters

are known with a reasonable amount of accuracy.

All of the experimental data that will be presented in this section are taken with a Philips MRD X-ray diffractometer equipped with a low noise detector and a rotating anode source. A double-channel cut (220) Ge crystal is used on the input arm of the diffractometer in order to select only the Cu$K\alpha_1$ line at 1.54056 Å. Approximately 6 orders of magnitude of signal-to-noise are obtained with this configuration. The simulation software is called **R**ocking Curve **A**nalysis by **D**ynamical **S**imulation (RADS) and is available from Bede Scientific Instruments. This software performs dynamical simulations based on the Takagi-Taupin equations.

4.4.2 HRXRD on a Complex Epilayer Structure

An example is seen in Figure 4-18, where the following structure (QDPLCTRL-02) is grown on a (100) GaAs substrate (see Appendix A): superlattice buffer, 200 nm GaAs, 93 Å $In_{0.26}Ga_{0.74}As$, 58 nm GaAs, 50 nm $Al_{.4}Ga_{.6}As$, and 50 nm GaAs. Note that these are the nominal thicknesses and compositions as determined from RHEED oscillations; the actual composition and thicknesses are more accurately determined from the X-ray measurements. The broad peak centered near -4000 arcseconds is due to the $In_{0.26}Ga_{0.74}As$ QW; the simulation shows that the nominal composition of 26% In is very accurately obtained in the experimentally grown sample.

4.4.3 Sample Growth

The above example is used to illustrate that HRXRD experiments and

simulations can be used to very accurately describe complex epitaxial structures. However, there are many different features in the data, and it is not always apparent which features correspond to a particular layer in a multilayer structure. Therefore, a simplified

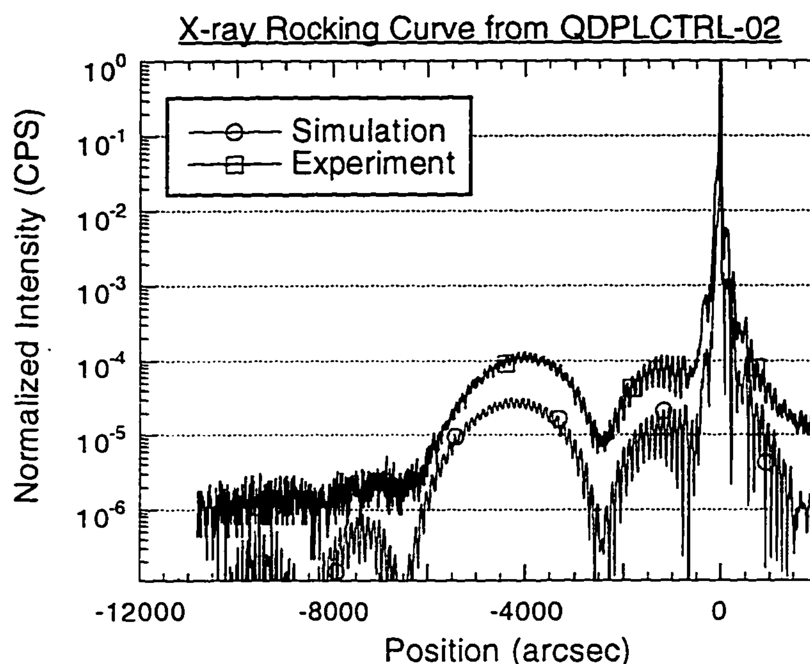

Figure 4-18: Comparison of experimental X-ray rocking curve with a simulation of the same QW structure. Excellent agreement is obtained between the two.

structure, consisting of only a GaAs buffer layer, an $In_xGa_{1-x}As$ layer grown by AMBE, and a GaAs cap layer, was grown. The GaAs buffer layer is indistinguishable from the GaAs substrate. Thus, there are only two layers to distinguish.

Three samples are grown for X-ray characterization. All three consist of a 200 nm GaAs buffer layer, an $In_{0.3}Ga_{0.7}As$ layer, and a 58 nm GaAs cap layer (see Figure 4-19 and Appendix A). QDXRAY-01 has a 7.1 ML (2.01 nm) $In_{0.3}Ga_{0.7}As$

layer; this is equal to the thickness immediately prior to the 2D-3D transition. QDXRAY-02 has a 13.3 ML (3.76 nm) $In_{0.3}Ga_{0.7}As$ layer, and QDXRAY-03 has a 17.7 ML (5.01 nm) $In_{0.3}Ga_{0.7}As$ layer. Both of these latter samples have quantum dots embedded in the GaAs cap layer.

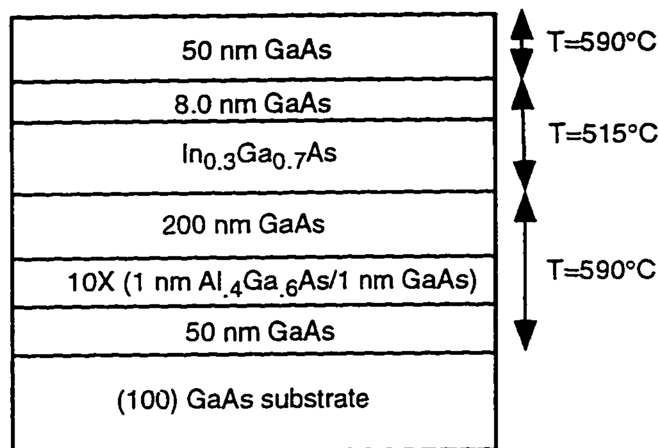

Figure 4-19 Layer diagram for QDXRAY-01, -02, and -03. The $In_{.3}Ga_{.7}As$ layer is deposited by AMBE and is nominally 7.1 MLs, 13.3 MLs, and 17.7 MLs thick for the three samples.

4.4.4 Experiments and Simulations

Figure 4-20 shows the experimental data obtained from QDXRAY-01 superimposed on a simulation. The modulation around the main peak (the substrate peak) is due to the Pendellösung fringes from the nominally 58 nm GaAs cap layer. By measuring the peak-to-peak spacing, the actual GaAs cap layer thickness is 57.8 nm.

In order to investigate the effects of the thin InGaAs epilayer, it is necessary to study the interference around the substrate peak as described earlier in this section. Under the growth conditions used for these samples, In segregation is very

important. The limiting case of In segregation is that all of the deposited In is segregating to the surface. This would lead to an InAs layer that is 2.12 monolayers thick. Assuming that this layer is elastically strained and a Poisson's ratio of 0.3, this corresponds to a thickness in the growth direction of 0.655 nm. The simulation shown in Figure 4-20 uses a 0.655 nm layer of elastically-strained InAs sandwiched between a GaAs substrate and a 58 nm GaAs cap layer. Note that the simulated data is normalized to the experimental data such that the maxima closest to the substrate peak at about -484 arcseconds are of equal intensity.

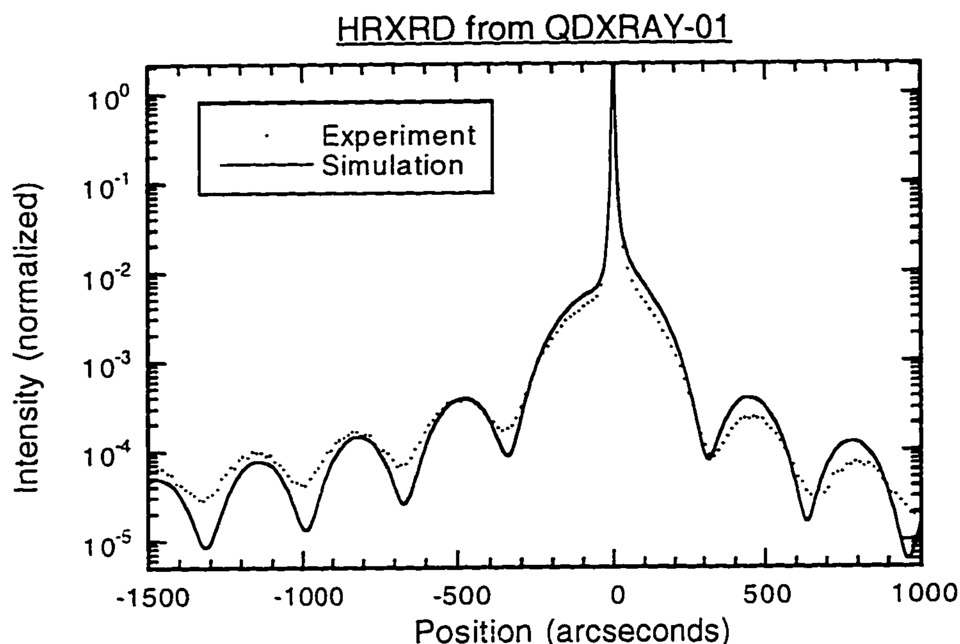

Figure 4-20 HRXRD from QDXRAY-01. The simulated curve is for a 0.655 nm InAs layer, which is the thickness if all of the In segregates and is elastically strained.

Figures 4-21 (a) and (b) show the experimental data for QDXRAY-02 (13.3 MLs $In_{.3}Ga_{.7}As$). The experimental data is shown superimposed on a simulation.

This simulation assumes that all of the In segregates and forms a planar layer of InAs that is 3.98 MLs thick. Figures 4-22 (a) and (b) show the experimental data for QDXRAY-03 (17.7 MLs $In_{.3}Ga_{.7}As$). The simulation again assumes that all of the In deposited in this layer segregates and forms a planar InAs layer that is 5.30 MLs thick.

4.4.5 Discussion

The experimental data for QDXRAY-01 agrees well with the simulation of 2.12 MLs of coherently-strained InAs. Both the experimental and simulated curves are asymmetric until the first minima (both the positive and negative angles), with a skew towards positive values. The positions of all the experimental maxima and minima agree to within about 15 arcseconds of the simulated ones.

The agreement between the experimental data and the simulation suggests that all of the In is segregating to the surface. This confirms experiments in which the substrate temperature is varied during the growth of the InGaAs layer. In these experiments (see Appendix A for a complete description of these samples), which will be presented in Chapter 5, AMBE Optimization, the RHEED pattern shows the transition from 2D-3D growth after the same amount of InGaAs is deposited from substrate temperatures of 460-515°C. Outside of this temperature range, the transition requires more InGaAs deposition. This is due to decreased In segregation at lower temperatures and In evaporation at higher temperatures.

The only caveat of note is that the interference pattern is determined by the *product* of strain and thickness. Thus, one measurement is inadequate for unambiguously determining composition (and thus strain) and thickness. Additional

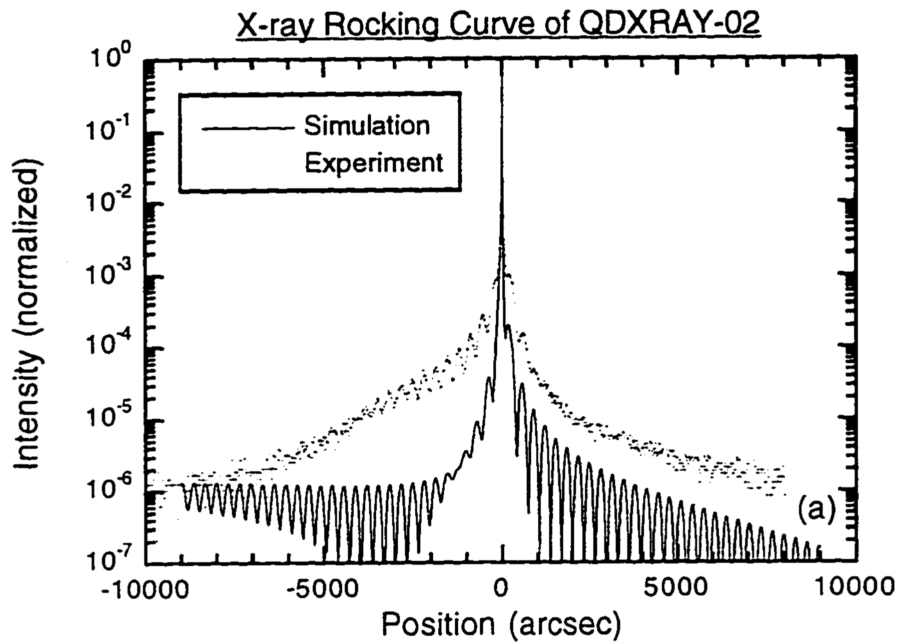

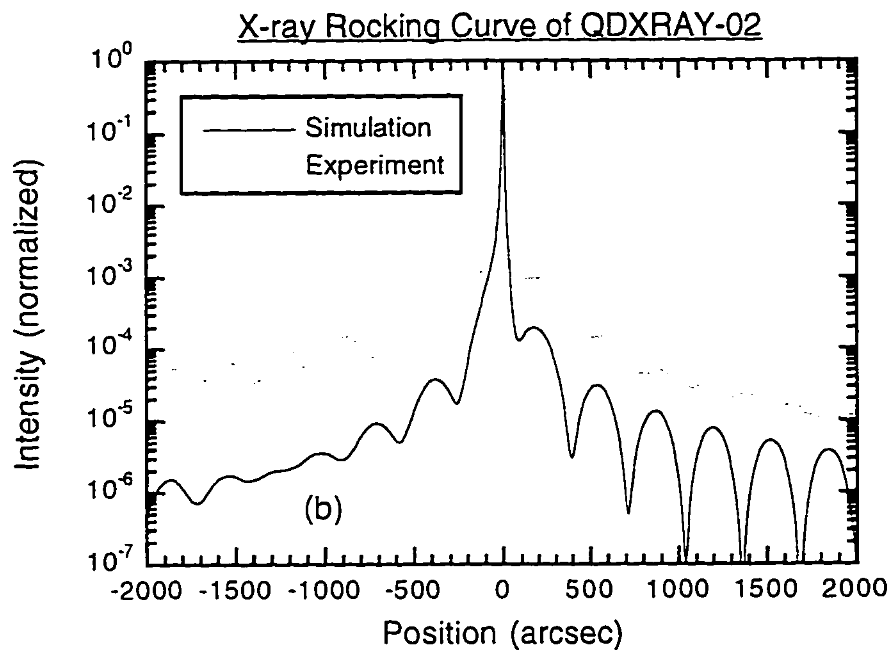

Figure 4-21 Simulation of 3.975 MLs of InAs compared to QDXRAY-02 (13.3 MLs of $In_{.3}Ga_{.7}As$, which contains 3.975 MLs of InAs).

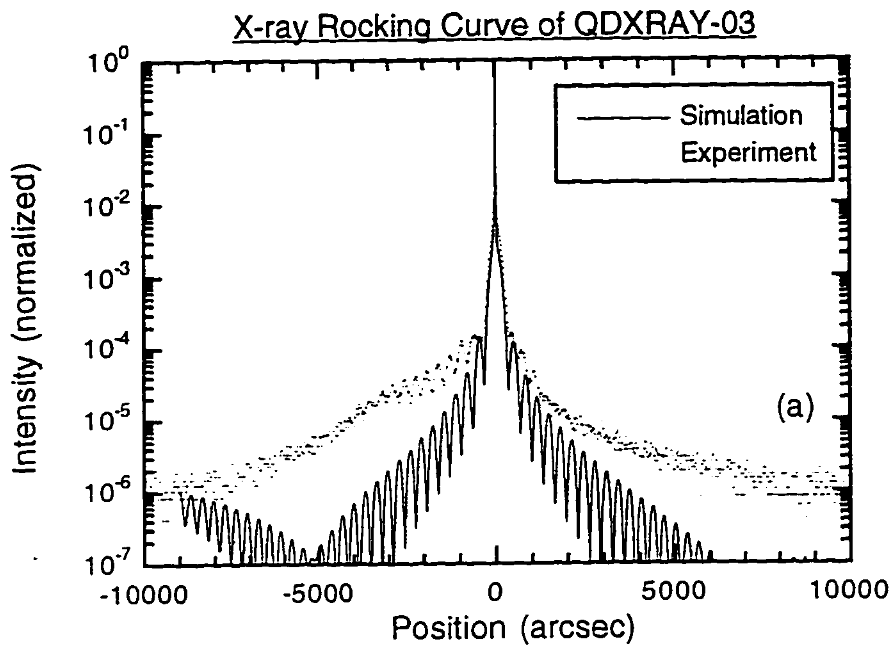

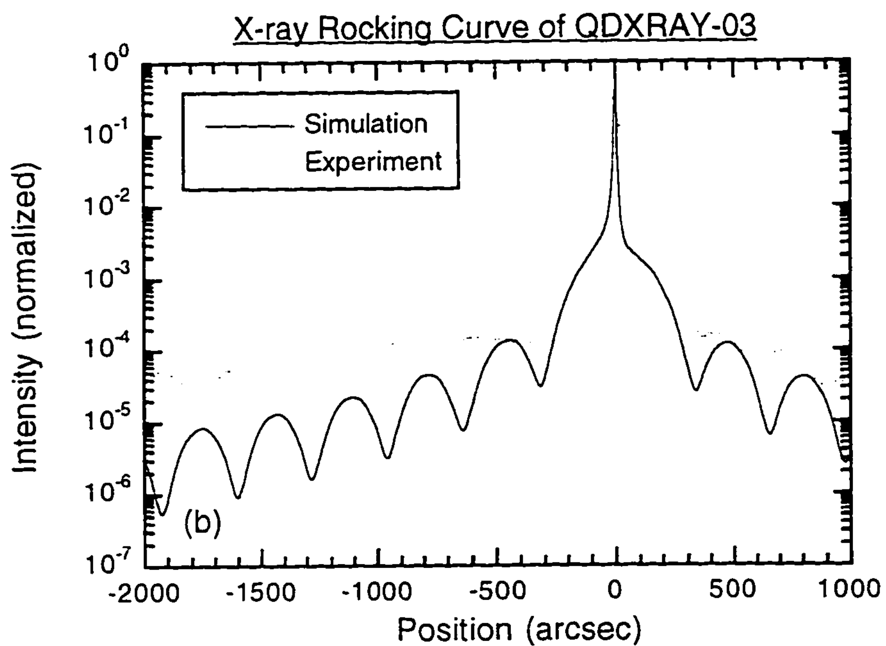

Figure 4-22 Simulation of 5.30 MLs of InAs compared to QDXRAY-03 (17.7 MLs of $In_{.3}Ga_{.7}As$, which contains 5.30 MLs of InAs).

measurements such as asymmetrical reflection would have to be performed in order to unambiguously say that all the In has segregated and formed an InAs layer. Nonetheless, given all the other measurements that have been performed and the excellent match between the simulation and the experiment, it is reasonable to conclude that all of the In is segregating in this sample.

There is poor agreement between the experimental data for the 13.3 and 17.7 ML samples and the simulations that assume all the In segregates into a single layer. Since the RHEED pattern and the AFM images show that neither of these samples is two-dimensional, this is not very surprising. As can be seen in the Figures 4-21 (a) and 4-22 (a), assuming a two-dimensional InAs layer leads to a very broad peak around -9000 arcseconds. The experimental data is buried in the noise at those angles. The experimental data for QDXRAY-03 also shows a shoulder peak around -3000 arcseconds; this does not appear in the simulation. Furthermore, the high-resolution rocking curves shown in Figures 4-21 (b) and 4-22 (b) both show poor agreement of the interference pattern around the substrate peak. Not only is the symmetry in poor agreement, but the peaks are almost 180° out of phase.

These structures that contain InGaAs islands need to be modeled by a more complicated structure in order to obtain better agreement between experiment and simulation. From the AFM images shown in the previous section, we can estimate the height of the islands and their areal coverage. Based on those numbers, we can then approximate the average composition of the layer of islands that is buried in GaAs.

From the experimental data we can extract a few parameters that are useful for determining what compositions and thicknesses to try in the simulations. Both Figures 4-21 (a) and 4-22 (a) have a shoulder-like peak around -3000 arcseconds; this

is more pronounced in 4-21 (a), which implies a thicker epilayer is contributing to this peak in 4-21 (a) than in 4-20 (a). Since 4-21 (a) shows the experimental data from QDXRAY-03, which has 17.7 MLs of $In_{.3}Ga_{.7}As$, versus 4-20 (a), which shows the data from QDXRAY-02, which has only 13.3 MLs of $In_{.3}Ga_{.7}As$, I surmise that this shoulder-like peak is due to the layer of islands. A peak at -3000 arcseconds corresponds to an In mole fraction of about 20%. Since the nominal mole fraction of the islands is 30%, and the areal coverage is 40-60%, the weighted average In mole fraction of the layer containing the islands is 12-18%.

Figure 4-23 shows the experimental data for QDXRAY-02 superimposed with a simulation of 0.63 nm of InAs (the Stranski-Krastanow wetting layer), 10.0 nm of $In_{.15}Ga_{.85}As$, and 58 nm of GaAs (note that the Pendellösung fringe spacing for the samples with InGaAs islands still corresponds to 58 nm, despite the fact that the GaAs is deposited on a nonplanar surface). As seen in Figure 4-23 (b), the symmetry around the substrate peak is approximated very well by this simulation. The positions of the maxima are shifted slightly since the exact thicknesses of the epilayers are not well-known.

Figure 4-24 shows the experimental data for QDXRAY-02 superimposed with a simulation of 0.63 nm of InAs (the Stranski-Krastanow wetting layer), 10.0 nm of $In_{.2}Ga_{.8}As$, and 58 nm of GaAs. The larger In mole fraction corresponds to a higher areal coverage of InGaAs islands. This simulation shows only fair agreement with the experimental data. The symmetry of the main peak agrees well, as does the position of the maxima at positive angles. However, at negative angles, the maxima from the simulation are almost 180° out of phase with the experimental data. Further simulations have yielded no better agreement.

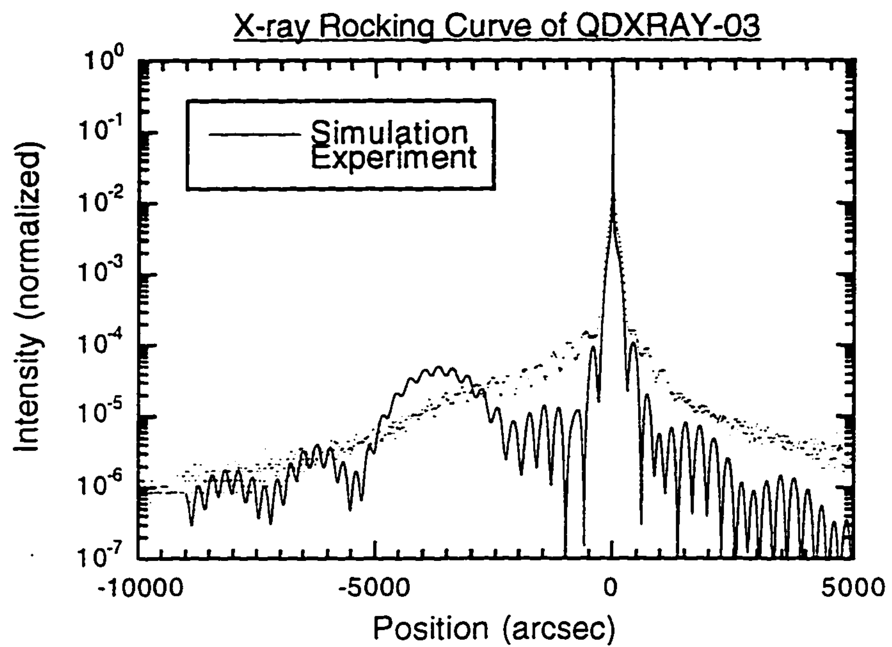

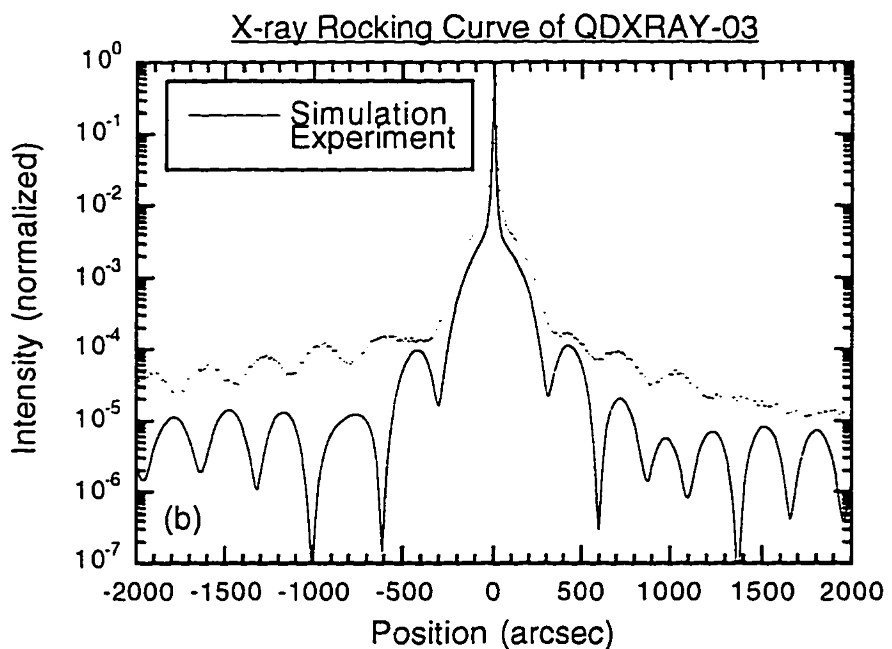

Figure 4-23 Simulation of 6.3 Å InAs, 100 Å $In_{.2}Ga_{.8}As$, and 580 Å GaAs.

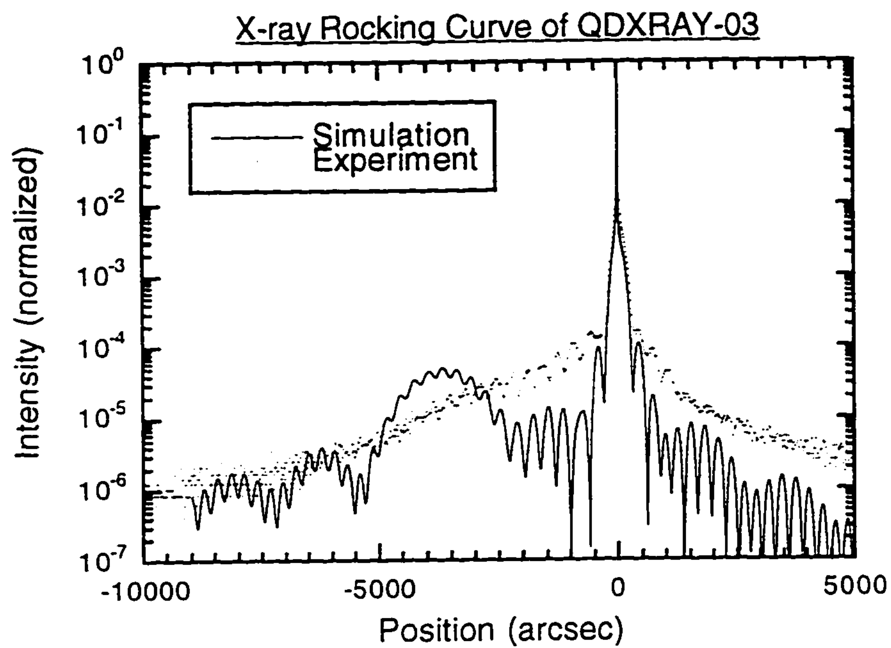

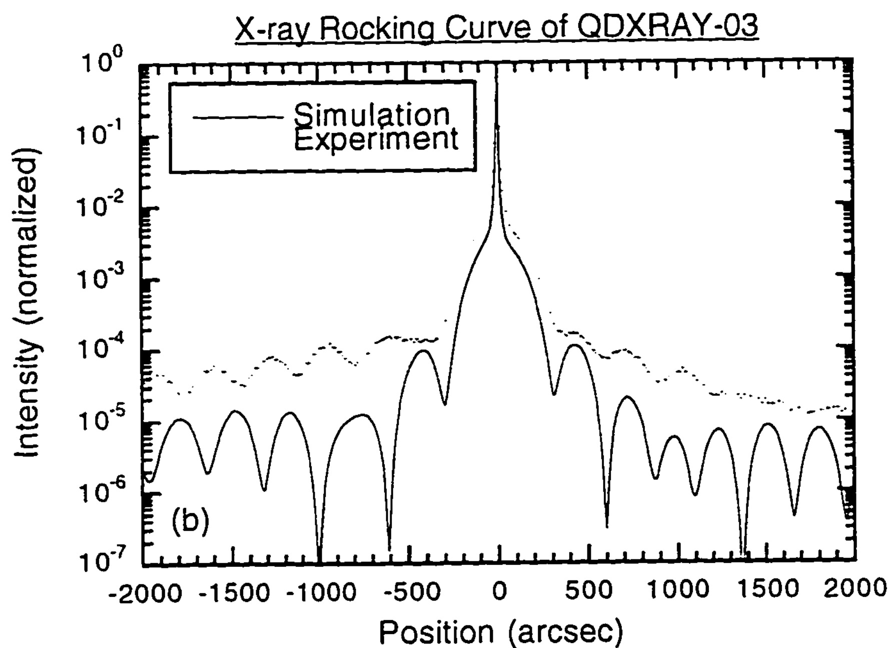

Figure 4-24 Simulation of 6.3 Å InAs, 100 Å $In_{.2}Ga_{.8}As$, and 580 Å GaAs.

4.4.6 Summary

HRXRD is an excellent technique for characterizing ultrathin semiconductor epilayers. It has been used successfully to correlate the In segregation effects in alternating MBE growth of InGaAs. For a two-dimensional strained layer that is just below the thickness that is needed to change to three-dimensional growth, excellent agreement can be obtained between dynamical simulations and experiments. However, when the growth is three-dimensional, the simulations become much more complicated and only qualitative trends can be reproduced by the simulations. The three-dimensional layer that is buried can be approximated by an average composition based on the height and lateral dimensions of the islands. This approximation may be limited since strain relaxation at the edges of islands distorts the lattice parameter along the (400) direction. This relaxation is not uniform and it may be expected to cause a broadening of peaks. Nonetheless, these initial results are encouraging and suggest that a more systematic study of the island formation be carried out. Using islands with pure InAs and lower areal coverage should be beneficial since there are fewer complications due to uncertainty in alloy composition and high areal coverage.

4.5 Transmission Electron Microscopy

4.5.1 Introduction

Transmission electron microscopy (TEM) is useful for obtaining direct images of the samples of interest. For these samples with InGaAs islands, both plan view and cross-sectional TEM can be used. Plan view TEM can be used to estimate the

island density and size. This is similar to the information obtained by AFM, except that samples for plan view TEM can have a cap layer on top of the islands and thus are suitable for other measurements such as photoluminescence. Cross-sectional TEM (XTEM) can be used to look for dislocations and other possible defects. If appropriate marker layers are used, XTEM can also show the efficiency of the GaAs overgrowth at planarizing the islands.

4.5.2 Plan View TEM

Figure 4-25 shows a plan view TEM of QDPL-20, which is a 22.1 ML $In_{.3}Ga_{.7}As$ sample. The photoluminescence from this sample is shown in Figure 2-15, and a detailed layer diagram and growth conditions are given in Appendix A. Figure 4-25 clearly shows the islands as a densely packed array.

Figure 4-25 Plan view TEM from QDPL-20.

4.5.3 Cross-sectional TEM

Figure 4-26 shows a XTEM image of QDPL-20. The image is a (200) dark field image taken under two-beam conditions. This is designed to maximize chemical contrast in this material system. The islands in this sample are practically in contact with one another because the growth has continued well beyond the 2D-3D transition.

Figures 4-27 (a), (b), and (c) show (200) dark field XTEM images from

QDPLS-03, -04, and -05, respectively. These samples have one, three, and five layers of 13.3 ML $In_{.3}Ga_{.7}As$ islands with 25 nm GaAs spacer layers. More details about the sample growth and layer structure can be found in Appendix A, and PL measurements on these samples will be discussed in Chapter 5, AMBE Issues and Optimization.

Figure 4-26 XTEM from QDPL-20. The InGaAs layer is dark and the AlGaAs layer is white.

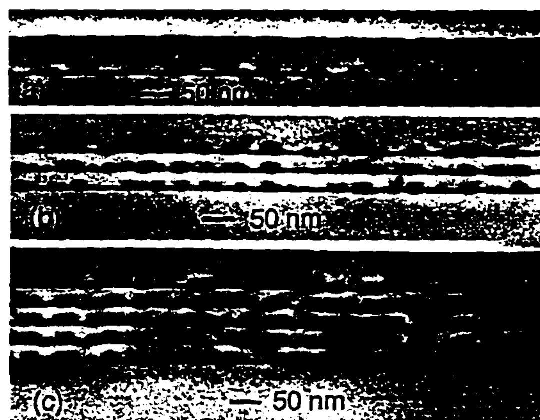

Figure 4-27 XTEM of 1, 3, and 5 layers of 13.3 ML InGaAs islands with 25 nm space layers.

4.5.4 *Discussion*

The TEM image from QDPL-20 (Figure 4-26) has no visible threading dislocations. In addition, the plan view image (Figure 4-25) does not show any Moiré patterns that are visible if two materials with different in-plane lattice constants are overlayed (Lin *et al.*, 1994). This means that any defects that have formed have not relieved any residual strain in the islands.

None of the multilayer samples in Figure 4-27 show any threading dislocations. The multilayer samples show a vertical alignment of the islands, as has been seen by others (Xie *et al.*, 1995, Solomon *et al.*, 1996). It is also clear in Figure 4-27 (b) and (c) that the subsequent layers of islands are larger than the initial layer. This corresponds to the RHEED observations during the growth that the 2D-3D transition occurs for a slightly lower deposited thickness. Since the interfaces at the subsequent layers still appear to be smooth, it is likely that the strain field from the underlying islands is causing the nucleation of the subsequent layers on top of the earlier layers. Finally, I note that there is some type of extra contrast observed in the five layer structure that is not visible in the one and three layer samples. I speculate that this is due to the additional strain of the these multiple layers, and some defects have formed. This will be discussed more in Chapter 5 when PL measurements on these samples are described.

4.6 Summary

Several different morphological and structural characterization experiments on InGaAs islands have been presented in this chapter. Histograms taken from AFM

images show that the islands are uniform in size, and the size distribution can account for the PL linewidth. TEM images do not show any defects such as threading dislocations. Multiple layer samples show vertical alignment of islands despite a thick spacer layer in between layers. Since the interfaces at subsequent layers appears flat, the strain field due to the underlying islands must be causing the islands to align. The subsequent layers of islands are somewhat larger than the initial layer, which agrees with the RHEED observation of earlier 2D-3D transition. X-ray rocking curves from a sample with an InGaAs layer just thinner than what is required to have the 2D-3D transition confirm that all of the In is segregating to the surface due to the alternating molecular beam deposition technique that is used for the growth. Rocking curves from samples with islands show only fair agreement with simulation because of the many uncertainties in composition, thickness, and strain state of the islands.

Chapter 5: AMBE Issues and Optimization: Overgrowth and Multiple Layers

5.1 Introduction

In the previous chapters I have established that alternating molecular beam epitaxy (AMBE) is a very simple technique for growing quantum dots of InGaAs on GaAs. These quantum dots exhibit room temperature photoluminescence, a necessary first step in making laser diodes. However, it is desirable to determine what growth parameters affect the optical properties of the quantum dots so that the best optical properties can be obtained.

In this chapter I will discuss refinements to the AMBE growth of the InGaAs islands, as well as refinements to the growth of the GaAs that is grown immediately on top of the InGaAs islands. I will also discuss the growth of samples with multiple layers of InGaAs islands since the overgrowth is strongly related to the growth of the barrier in between layers of islands. The most important thing to keep in mind during this chapter is that all of these improvements in growth are intended to improve the properties of laser diodes with InGaAs quantum dot active regions. This implies that high PL intensity and narrow linewidth are the two most desirable properties to achieve.

This chapter is organized as follows: in the first section a description of some experiments used to optimize the overgrowth on top of the InGaAs quantum dots is given. First, the differences in the optical properties of two quantum dots samples with different schemes used to grow the GaAs which buries the quantum dots are

examined. The first sample has continuous growth of the GaAs which is used to bury the quantum dots, but the substrate temperature is raised after the quantum dots have been partially buried. The second sample uses a growth pause in order to change the substrate temperature after partial burial of the quantum dots. The remainder of the first section describes the growth and characterization of samples used to optimize the thickness of GaAs which is grown on top of the quantum dots before the growth pause to raise the substrate temperature is implemented. The following section describes the growth and characterization of multilayer samples. Then, the next section describes samples in which the substrate temperature has been varied in order to optimize the optical properties of the quantum dots. Finally, the growth and characterization of smaller quantum dots and multiple layers of smaller quantum dots with optimized growth conditions is described.

5.2 Overgrowth Optimization

5.2.1 Background

An area of Stranski-Krastanow growth that has been overlooked by most researchers is the issue of overgrowth on top of the coherent islands. The previous research in this area has mostly focused on the morphological aspects of the overgrowth (Yao, Andersson, and Dunlop, 1991, Lin *et al.*, 1994). The area of overgrowth is a very important, not only for devices such as lasers and resonant tunnel diodes, but also from a fundamental point of understanding the interface, strain, bandstructure, etc. There has been one report (Xie *et al.*, 1995) on the optical properties of quantum dots in which the overgrowth has been varied. In this case,

low temperature PL was used to characterize quantum dots with MBE-grown and MEE-grown GaAs overlayers. The quantum dots with the MEE-grown overlayers show a somewhat better intensity compared to the MBE-grown overlayers.

There are several things that must be noted: the islands are coherently strained, which means that no dislocations have formed. However, because the islands are three-dimensional, the forces parallel to the plane of the wafer are no longer equal, especially at the edges of the islands. Thus, the atoms near the island edge can "relax" from lining up directly with the underlying atoms. The bonds can be elastically stretched between neighboring atoms; this is a similar concept to the use of InGaAs stressors to form quantum wires and quantum dots (Tan *et al.*, 1991), an idea that has also been extended by using Stranski-Krastanow islands as the stressor (Sopanen, Lipsanen, and Ahopelto, 1995). So, not only is the underlying GaAs strained by the Stranski-Krastanow island, but the GaAs that is deposited that is used to overgrow the islands is also strained, with the opposite sign than that of the InGaAs island.

5.2.2 Introduction

In this section, I will discuss optimization of the overgrowth of the GaAs layer on top of the InGaAs quantum dots. From my perspective, optimization means that I want to optimize the overgrowth with respect to the optical properties of the quantum dots. I would like to have a combination of the highest PL intensity, the narrowest linewidth, and control over the peak emission wavelength. The PL intensity should be highest when the material surrounding the quantum dots is of the highest quality. The substrate temperature during the growth of the InGaAs quantum

dots is typically 515°C. However, the substrate temperature for MBE of high-quality GaAs is typically 570-700°C. Lower substrate temperatures generally lead to higher concentrations of point defects such as antisites and vacancies. These defects are particularly important in optical emitting devices such as lasers where minority carrier lifetimes are important. Therefore, I intend to minimize the amount of GaAs that is deposited on top of the quantum dot at the low growth temperature used for quantum dot formation. This technique has been demonstrated successfully for overgrowth of GaAs on a single monolayer on InAs (Ilg *et al.*, 1993).

One problem that arises when attempting to minimize the thickness of GaAs grown at low temperature is quantum dot evaporation due to incomplete burial of the island by the incoming material. The problem is substantially more complicated than for the case of burying an InGaAs quantum well. For the case of the quantum well, the surface is planar, and the InGaAs is completely buried by the incoming flux since a uniformly thick film is formed by the incident flux. However, the surface that contains quantum dots is nonplanar, as seen in the atomic force microscope images shown in Chapter 4, and Ga migration and incorporation are known to vary with the crystallographic orientation of the different planes (Mirin *et al.*, 1993, Kapon, 1994, and references therein). Therefore, simply depositing a few monolayers of GaAs and then raising the substrate temperature, as is typically done with a QW, is likely to cause the quantum dots to partially evaporate due to the high vapor pressure of InAs relative to GaAs. The effect of the loss of In is a decrease in the peak emission wavelength as the dots shrink and the quantization energy increases.

As a final note, for the growth of multiple layers of quantum dots, it is important to have a nearly identical starting surface for the start of each quantum dot layer so that the layer-to-layer uniformity is good. Therefore, the overgrowth must

also smooth the surface quickly if multiple quantum dot layers are desired in close proximity to one another, as is the case when designing lasers since the optical confinement factor, Γ, depends on having a large overlap between the transverse optical mode in the waveguide and the gain medium (Coldren and Corzine, 1995). This suggests that higher substrate temperatures, which enhance surface migration length, are needed.

5.2.3 Continuous Growth versus Growth Pause

For the preliminary experiment, two samples with identical layer structures are grown. The difference between the two samples is the transition from the quantum dot growth temperature of 515°C to the final temperature of 590°C. In both samples, 17.7 monolayers of $In_{0.3}Ga_{0.7}As$ are grown by alternating MBE at 515°C, followed by 8.0 nm of GaAs grown by conventional MBE (simultaneous beams of Ga and As_2) at 515°C (see Figure 5-1 and Appendix A for additional details). The first sample (QDPLOVG-01) then has the substrate temperature set to about 590°C, and GaAs is continuously deposited by conventional MBE as the substrate temperature increased. The second sample (QDPLOVG-02) has a growth pause after the initial deposition of the 8.0 nm GaAs layer. The substrate temperature is increased with only the As_2 flux incident on the surface. Deposition by conventional MBE continued when the substrate temperature reached 570°C, and continued as the temperature is increased to about 590°C.

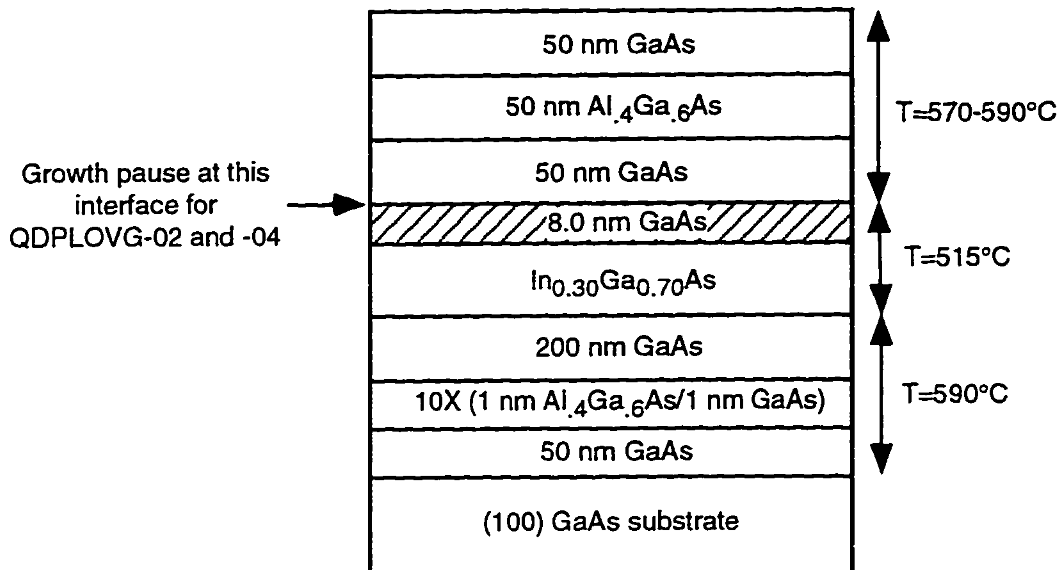

Figure 5-1: Layer diagram for QDPLOVG-01, -02, -03, and -04. The $In_{.3}Ga_{.7}As$ epilayer thickness is 17.7 MLs for -01 and -02, and 22.1 MLs for -03 and -04. Other QDPLOVG samples have similar structures, except for a varying thickness of the 8.0 nm GaAs layer immediately adjacent to the InGaAs. See Appendix A for detailed descriptions of the InGaAs layers.

The results of this experiment are shown in Figure 5-2, which shows RTPL spectra from the two samples described above. QDPLOVG-02 has a peak intensity 3-4 times that of QDPLOVG-01. In addition, the linewidth has narrowed from 60.0 meV (75.2 nm) for QDPLOVG-01 down to 41.5 meV (49.4 nm) for QDPLOVG-02. These improvements can both be attributed to improvements in the quality of the overgrowth on top of the nonplanar coherent islands. In addition, there is a small shift in the PL peak wavelength from 1259 nm (QDPLOVG-01) to 1220 nm (QDPLOVG-02) (≈ 31 meV). This difference is probably due to In segregation to the surface (Ebner and Arthur, 1987, Yamaguchi and Horikoshi, 1989, Yamaguchi and Horikoshi, 1990, Houzay*et al.*, 1989, Brandt *et al.*, 1993, Gerard *et al.*, 1993, Hayakawa *et al.*, 1993, Muraki *et al.*, 1993, Nagle *et al.*, 1993), and/or In re-evaporation from the areas of QDPLOVG-02 that are not buried deeply by the 8.0 nm

of GaAs that are deposited at 515°C. Indium segregation leads to a smearing out of the interface and shallower confinement, and re-evaporation gives thinner, In-poor layers, both of which lead to shorter wavelength emission.

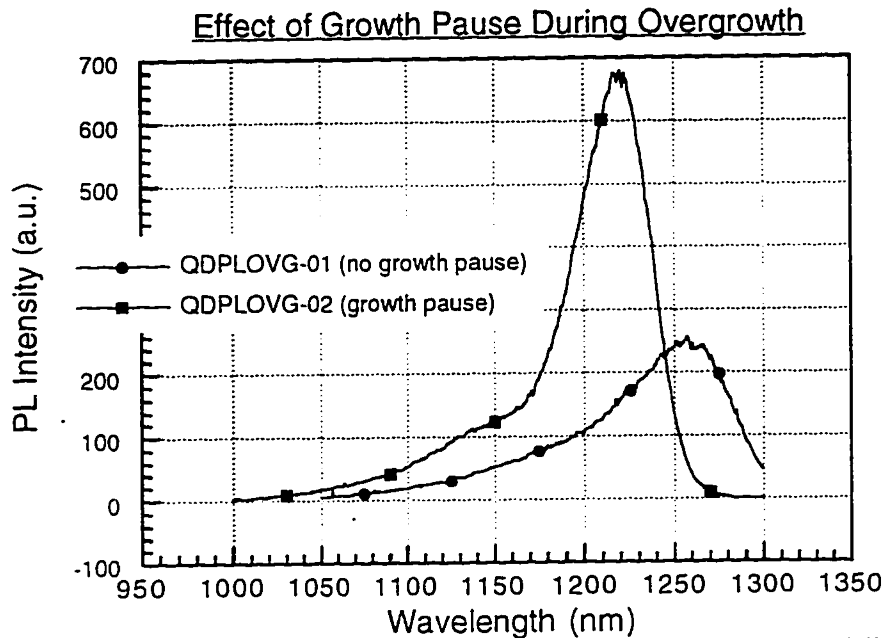

Figure 5-2 RTPL spectra show the benefits of using a growth pause after partially burying the InGaAs islands with GaAs. The substrate temperature is raised after the growth pause, before any additional GaAs is grown.

This overgrowth experiment is repeated on two more samples, QDPLOVG-03 and -04, with QDPLOVG-03 having continuous growth of the capping layer and QDPLOVG-04 having a growth pause after the first 8.0 nm have been deposited (see Figure 5-1). These samples are grown consecutively in order to eliminate the possibility of differences in the condition of the MBE machine causing misleading results. The InGaAs epilayer in these two samples consists of 22.1 MLs of $In_{.3}Ga_{.7}As$, instead of the 17.7 MLs used in QDPLOVG-01 and -02. In addition, a sample (QDPLOVG-05) that has two layers of 22.1 MLs of $In_{.3}Ga_{.7}As$ separated by

a 25.0 nm barrier of GaAs is grown. The first 8.0 nm of the barrier are grown at the InGaAs island growth temperature of 515°C, and then the temperature is raised to 570°C to grow the other 17.0 nm of GaAs. The temperature is then dropped to 515°C to deposit the second layer of InGaAs islands, and then the same capping procedure is applied.

The RTPL spectra from these three samples are shown in Figure 5-3. The results confirm those seen from QDPLOVG-01 and -02. The peak emission wavelength from QDPLOVG-04 is at 1234 nm, which is about 25 nm shorter than the peak emission wavelength from QDPLOVG-03. This is similar to the shift seen between QDPLOVG-01 and -02. The FWHM from QDPLOVG-04 is only 35.6 meV, compared to the 53.2 meV FWHM measured from QDPLOVG-03. Again, this improvement is similar to the improvement seen in the previous experiment. This provides strong evidence that the quality of the overgrowth layer strongly affects the optical quality of the underlying InGaAs islands and establishes that a growth pause in the capping layer improves the optical properties of the islands.

Finally, the two layer sample, QDPLOVG-05 has lower intensity than either of the single layer samples. This is probably due to defects in the second InGaAs layer caused by excessive strain. Since it is already established (Chapter 2) that just a single layer of 22.1 MLs of InGaAs gives a somewhat decreased PL efficiency compared to 17.7 MLs of InGaAs (Figure 2-16), it is not entirely surprising that adding a second layer would decrease the efficiency even further since additional strain is added. Further discussion about multilayer samples will be presented later in this chapter.

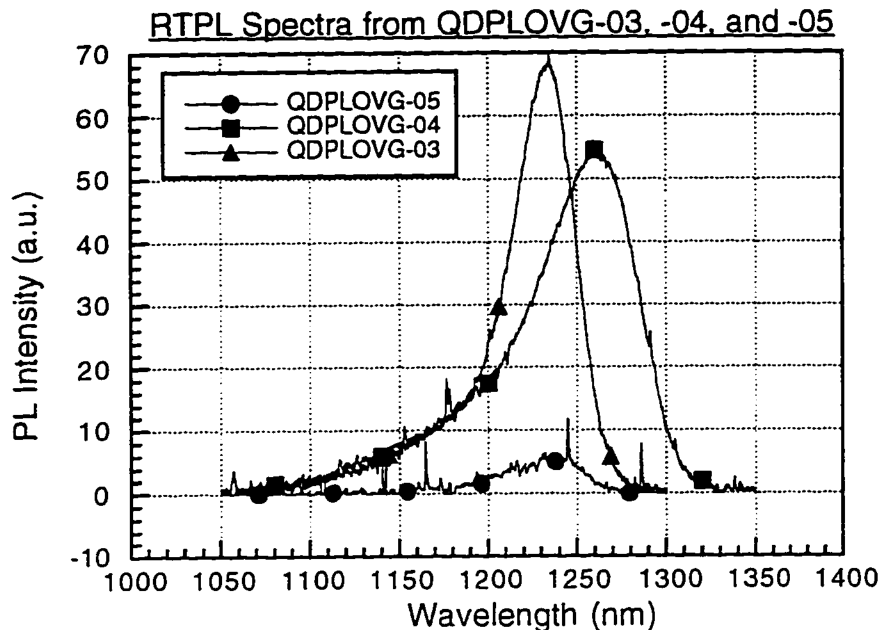

Figure 5-3 The RTPL spectra from QDPLOVG-03 and -04 show that a narrower linewidth can be obtained by using a growth pause during the GaAs overgrowth layer.

5.2.4 Optimization of Low Temperature Overgrowth Thickness

It is now established that it is preferable to include a growth pause in order to raise the substrate temperature during the growth of the GaAs overlayer rather than growing the GaAs overlayer continuously while raising the temperature. The next important parameter to optimize is the thickness of GaAs grown at the low substrate temperature of 515°C (Ilg *et al.*, 1993). A series of three samples (QDPLOVG-06, -07, -08) is grown in which the thickness of GaAs grown at 515°C is varied. QDPLOVG-06 has 12.0 nm, QDPLOVG-07 has 6.0 nm, and QDPLOVG-08 has 3.0 nm of GaAs grown at 515°C (see Figure 5-1). The total thickness of GaAs grown remains constant at 58.0 nm.

The results of this experiment are seen in Figure 5-4, which shows RTPL spectra from these three samples. The 3.0 nm overgrowth (QDPLOVG-08) is clearly inadequate for maintaining the desired wavelength. Its peak wavelength is 1126 nm, about 100 nm shorter than QDPLOVG-06 (1233 nm) and QDPLOVG-07 (1215 nm). QDPLOVG-07 has both higher intensity and narrower linewidth (41.5 meV versus 60.3 meV) than QDPLOVG-06. The wavelength shift between QDPLOVG-06 and QDPLOVG-07 is 18 nm, which indicates some In segregation and/or In re-evaporation in QDPLOVG-06. However, this is a fairly small shift in wavelength, and the benefits of the improved intensity and linewidth probably outweigh the wavelength shift.

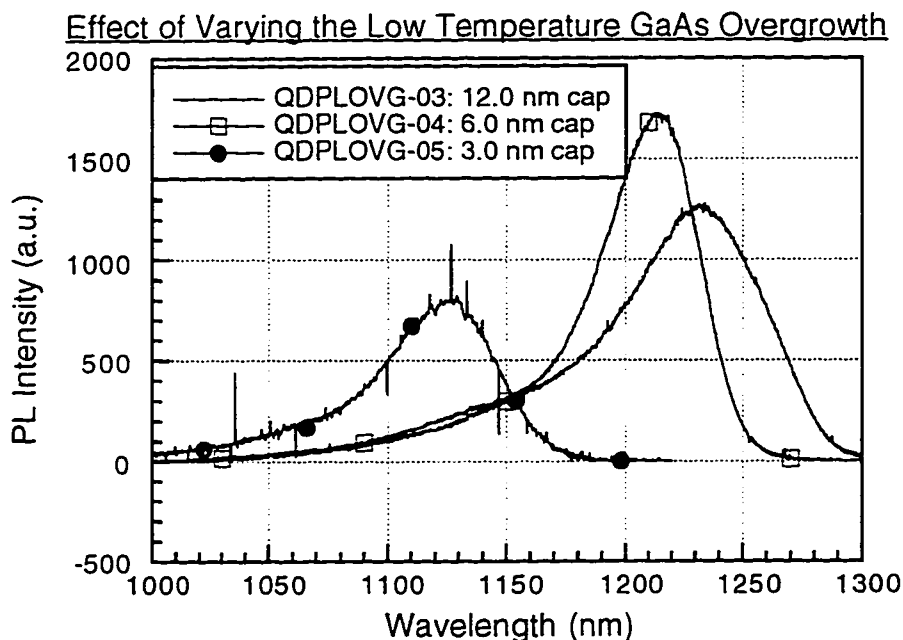

Figure 5-4 RTPL spectra show the importance of controlling the overgrowth thickness deposited at low growth temperature.

An additional set of samples are grown to see if further refinement of the overgrowth thickness is possible. Samples QDPLOVG-09, -10, -11, and -12 have low temperature overgrowth layer thicknesses of 4.5 nm, 6.0 nm, 7.5 nm, and 9.0 nm, respectively (see Figure 5-1) .

RTPL spectra are seen in Figure 5-5. QDPLOVG-12, with the 9.0 nm overgrowth at 515°C, has a much higher peak intensity and narrower linewidth than any of the other three samples. Furthermore, the wavelength shift from QDPLOVG-09, -10, and -11 is at least 40 nm compared to QDPLOVG-12, which indicates insufficient burial by the low temperature GaAs. Thus, 9.0 nm is the optimum overgrowth thickness for these quantum dots.

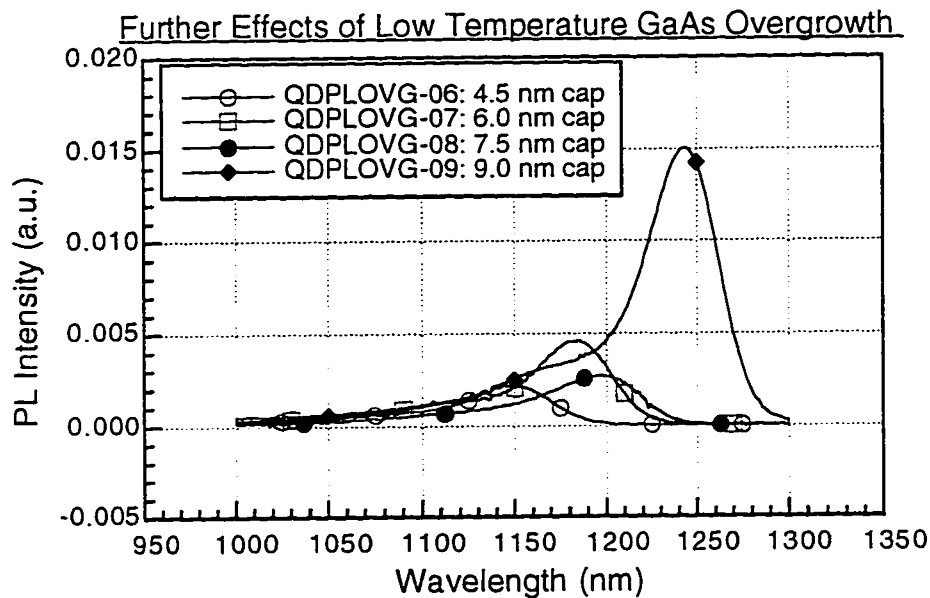

Figure 5-5 RTPL spectra demonstrate the importance of controlling the amount of GaAs grown at low temperature. Using too thin a layer causes the InGaAs islands to partially evaporate, as indicated by the shorter emission wavelengths from the samples with the thinner overgrowth layers.

5.2.4 Summary

The results of the preceding section demonstrate that the GaAs that is grown on top of the InGaAs islands strongly affects the optical properties of the islands. There are benefits to having a growth pause during the capping layer that buries the InGaAs islands, rather than raising the temperature continuously during the growth of the capping layer. The surface is highly nonplanar and strained because of the islands, so the material quality of the overgrowth is affected by these physical parameters. There is an optimum thickness of the GaAs that is grown on top of the InGaAs at the low growth temperature at which the islands are grown. Note that the optimum overgrowth thickness is expected to vary somewhat with the size of the dots. The main reason for this is simply that larger islands require more overgrowth before they are buried. If smaller quantum dots are grown, they may be buried with a thinner layer of GaAs grown at low temperature. So, each set of growth conditions (temperature, InGaAs thickness and composition, As flux and species, etc.) will have an optimum overgrowth thickness, and it would be surprising if that thickness was the same for each island size.

5.3 Barrier Thickness Effects on Multiple Layer Samples

5.3.1 Introduction

Many semiconductor lasers use multiple quantum wells in order to enhance the gain and output power, at the expense of increased threshold current. The most important benefit from having multiple layers of quantum dots is the increase in the density of states (there are strong state-filling effects that occur in the single quantum

dot layers under high excitation (see Chapter 3, Photoluminescence II)). Unlike some of the earlier samples with multiple layers discussed in Chapter 2 (QDPL-01, 04-07), in these samples I would like to have good **layer-to-layer uniformity** so that the peak emission wavelength from each layer is the same. This is a substantially different problem than the layer-to-layer uniformity problems with planar QWs. For the case of multiple QWs, the barrier layer starts out on top of a smooth, two-dimensional surface. For the case of multiple QDs, the surface is strained and three-dimensional, and the barrier layer must bury the islands and smooth the surface before the subsequent layers of islands can be deposited, if good layer-to-layer uniformity is desired. Roughness and residual strain fields can affect the growth of subsequent layers of islands, usually resulting in an earlier transition from two-dimensional growth to three-dimensional growth (see Chapter 2 for more discussion of this).

5.3.2 Structural Properties

In the previous section, the experiments used to optimize the thickness of low temperature GaAs overgrowth for obtaining good optical properties from single layers of InGaAs quantum dots are described. That same thickness of 9.0 nm is also used when growing multiple layers of islands. The first sample grown is QDPLM-01, which has a single layer of InGaAs islands, consisting of 17.7 MLs of $In_{0.3}Ga_{0.7}As$ grown at 515°C by AMBE, followed by 9.0 nm of GaAs grown by conventional MBE at 515°C, and then a growth pause while the substrate temperature ramps up to 570°C for the completion of the capping layers (see Figure 5-1 for a complete layer diagram). QDPLM-02 has two layers of 17.7 MLs $In_{0.3}Ga_{0.7}As$

islands with a 25.0 nm GaAs barrier between the two layers (see Figure 5-6). The first 9.0 nm of the barrier layer are grown at 515°C. The growth is then paused with the As_2 flux incident on the sample while the substrate temperature is increased to 570°C. Then, another 16.0 nm of GaAs are deposited as the substrate temperature is increased from 570°C to about 590°C. The temperature is then decreased again to 515°C to grow the second layer of InGaAs islands. Once again, 9.0 nm of GaAs are deposited at 515°C, followed by a growth pause while the sample temperature is increased to 570°C. The rest of the capping structure is grown as the temperature increases from 570°C to 590°C. QDPLM-03 is identical to QDPLM-02 except an additional 25.0 nm of GaAs are grown as the temperature changes from 570°C to 590°C in the barrier layer. The final barrier thickness is 50.0 nm, compared to the 25.0 nm barrier used for QDPLM-02.

The 2D-3D RHEED transition of the single InGaAs layer of QDPLM-01 occurs between 7.1 MLs and 8.0 MLs of $In_{0.3}Ga_{0.7}As$ deposition. The first $In_{0.3}Ga_{0.7}As$ layer of QDPLM-02 (25.0 nm barrier) has the transition between 7.1 and 8.0 MLs, but the second $In_{0.3}Ga_{0.7}As$ layer has the transition between 6.2 MLs and 7.1 MLs. Both $In_{0.3}Ga_{0.7}As$ layers in QDPLM-03 have the 2D-3D transition between 7.1 MLs and 8.0 MLs.

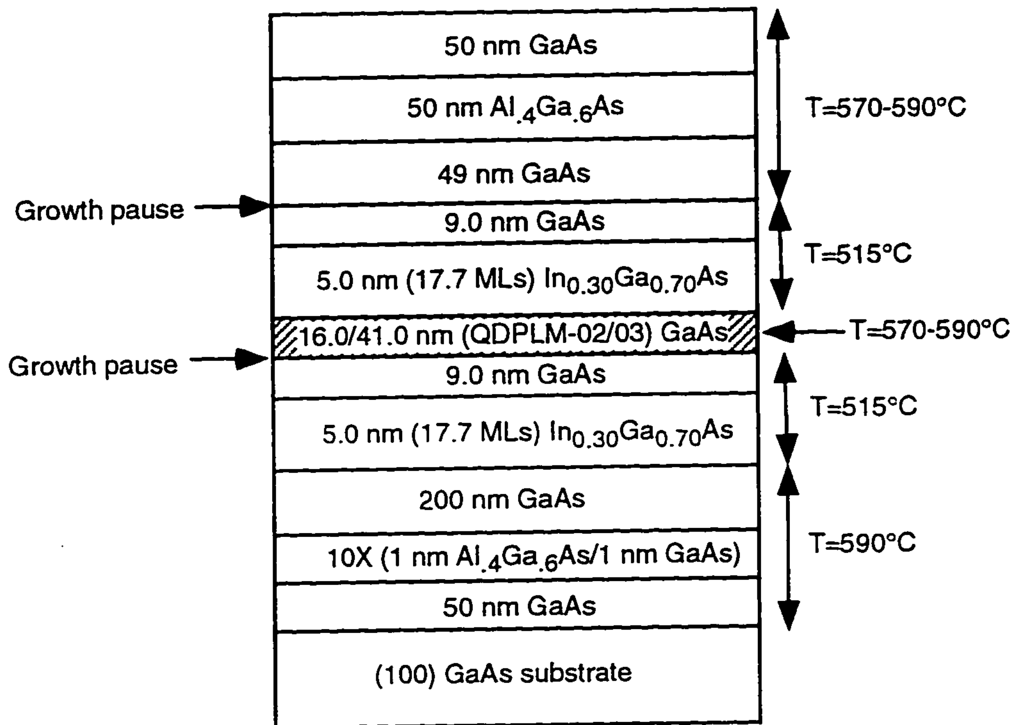

Figure 5-6: Layer diagram for QDPLM-02 and -03. See Appendix A for additional details.

5.3.3 Optical Properties

The RTPL spectra from these three samples are shown in Figure 5-7. Excited state emission is visible in the spectrum from QDPLM-01 (single layer), and the integrated intensity is slightly better than that of either of the two dot layer samples. The peak emission wavelength from QDPLM-01 is around 1245 nm, but for QDPLM-02 the peak emission wavelength is slightly shifted to about 1275 nm. The peak emission wavelength from QDPLM-03 is about 1260 nm, which is still slightly longer than is seen from QDPLM-01 but shorter than that seen from QDPLM-02 with its thinner barrier.

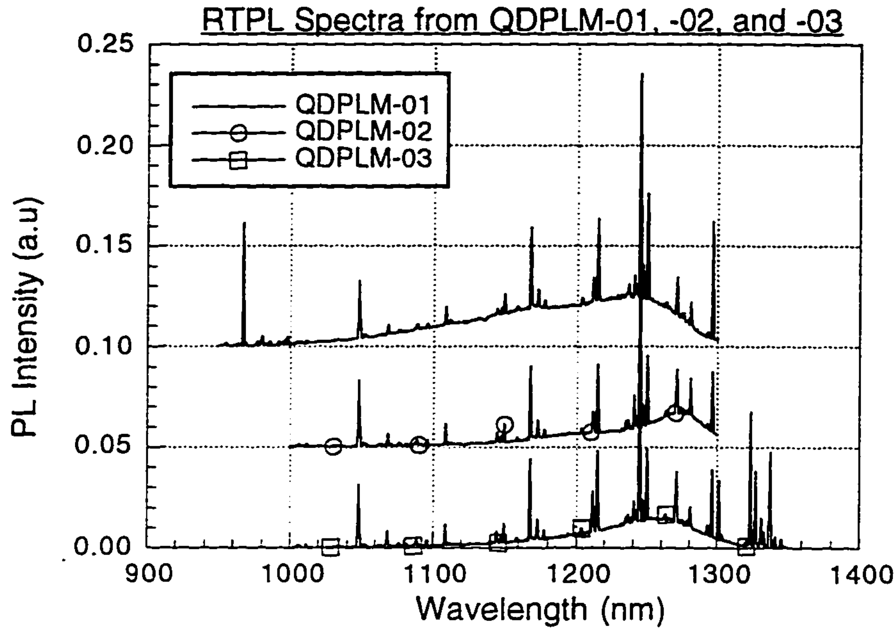

Figure 5-7 RTPL spectra from QDPLM-01, -02, and -03 demonstrate less state-filling in multiple layer samples, but no improvement in integrated intensity.

The peak wavelength difference between QDPLM-01 and -02 can be attributed to the second layer of InGaAs islands. Because the RHEED transition of the second layer occurs sooner than the RHEED transition of the first layer, the islands in the second layer should be slightly taller than the islands in the first layer. Therefore, the quantization energy is lower, and the emission wavelength is longer. This conclusion also agrees with the results of samples QDPL-01 and QDPL-04, -05, -06 and -07 discussed in Chapter 2.

Since the RHEED transition for both layers of QDPLM-03 occurs for the same amount of deposition as for QDPLM-01, it might be expected that the peak emission wavelength for those two samples would be identical. However, the peak emission wavelength is sensitive to the carrier concentration in the quantum dots as

indicated by the pump power dependence seen in Chapter 2 and Chapter 4. Since QDPLM-03 has two layers of quantum dots, the carrier concentration should be lower than in QDPLM-01, which only has a single layer of quantum dots, and therefore the peak emission wavelength should be shorter. Furthermore, the linewidth from QDPLM-03 is better than the linewidth from QDPLM-01, which is attributable to the lower state-filling in the multilayer sample.

5.3.4 Summary

These results indicate that the barrier thickness plays a role in determining the layer-to-layer uniformity in samples with multiple layers of InGaAs QDs, which is important for making devices from these InGaAs islands. The barrier layer thickness must be large enough to ensure that a smooth starting surface is obtained for each subsequent layer of InGaAs, yet thin enough so that multiple layers can be put close together for use in devices. For the samples grown for this experiment, a barrier thickness of 25.0 nm of GaAs is not adequate to ensure a smooth starting surface, but 50.0 nm appears to be enough. The thickness required is expected to vary with the height of the islands as well how efficiently the barrier material can planarize the surface, so growth conditions for the barrier material are very important. No further studies were carried out determine if better growth conditions could be used.

5.4 Optimization of Growth Temperature

5.4.1 Introduction

In addition to composition and thickness, the substrate temperature is another possible parameter to vary in order to change the conditions under which the coherent islands form. Surface diffusion length (SDL), and thus incorporation probability, are directly affected by the substrate temperature. During MBE growth, the surface is very far from being an equilibrium surface, and growth is strongly affected by **kinetic** barriers, rather than thermodynamic limitations. The kinetic barriers are strongly affected by parameters such as substrate temperature, growth rate, V/III flux ratio, and equilibrium step density, i.e., singular or vicinal surface. All of these parameters will change how the islands form because they all affect the same parameter, which is SDL.

In this section, I will discuss how the substrate temperature affects the morphological and optical properties of the quantum dots. There are two physical characteristics that will vary as the substrate temperature is changed. One characteristic is the island formation. The alternating MBE growth sequence that I use to grow these islands ensures that In segregates to the surface. The probability of an In atom segregating will be affected by changing the growth temperature. Therefore, the amount of deposited material required to form the islands may be affected. In addition, by changing the SDL things like island density and size are likely to be affected.

The second physical characteristic that will change as the substrate temperature varies is the quality of the overgrowth layer. As discussed in the previous section, the quality of the overgrowth strongly effects the PL properties such as intensity and linewidth. It is expected that using a growth temperature that is too low will lead to weak PL intensity due to poor quality of the GaAs overgrowth. A growth temperature that is too high will likely cause large amounts of In re-

evaporation, leading to poor control over emission wavelength.

5.4.2 RHEED Observations at Various Substrate Temperatures

Four samples, QDPLT-01, -02, -03, and-04, are grown with identical structures (see Figure 5-8) except for the substrate temperature during the 17.7 ML $In_{0.3}Ga_{0.7}As$ quantum dot layer and the 7.5 nm GaAs overgrowth. The substrate temperature during the InGaAs layer is set to 510°C, 480°C, 450°C, and 420°C for samples QDPLT-01, -02, -03, and -04, respectively. Qualitatively, the 2D-3D RHEED transition occurs after deposition of between 7.1 MLs and 8.0 MLs of $In_{0.3}Ga_{0.7}As$ for the three highest temperatures used. However, when the substrate temperature is reduced to 420°C, the transition does not occur until between 9.7 MLs and 10.6 MLs have been deposited. Since In segregation decreases as the temperature decreases, it is likely that at the lowest temperature more In needs to be deposited in order to build up the required strain for the transition to three-dimensional growth.

Two additional samples are grown to determine the effects of growth temperature on the optical properties of the quantum dots. QDPLT-05 and QDPLT-06 (see Figure 5-8) are grown at temperatures of 515°C and 540°C, respectively. The 2D-3D RHEED pattern transition occurs between 8.0 MLs and 8.8 MLs of deposition for QDPLT-05. For QDPLT-06, it is difficult to see the 2D-3D transition, but it takes more than 9.7 MLs for the transition to occur. It is likely that In is re-evaporating at this temperature (540°C), so additional In needs to be deposited to compensate for the re-evaporated In.

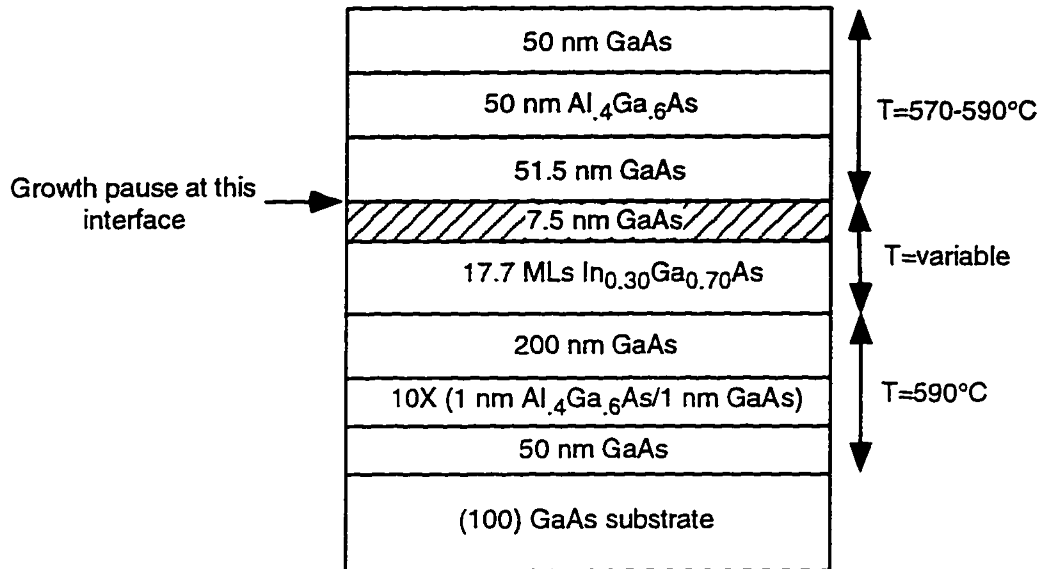

Figure 5-8: Layer diagram for QDPLT-01 to -06. The substrate temperature is varied during the InGaAs epilayer and the adjacent GaAs overgrowth. See Appendix A for detailed descriptions of the InGaAs layers.

5.4.3 Effects of Substrate Temperature on Optical Properties

RTPL spectra from QDPLT-01, -02, -03, and -04 at two different pump powers are shown in Figures 5-9 and 5-10. One important feature is the weak intensity (note the logarithmic vertical scale) of the two samples (QDPLT-03 and QDPLT-04) that are grown at the lowest temperatures of 450°C and 420°C, respectively. The sample grown at 510°C (QDPLT-01) is about a factor of two higher in peak intensity than the sample grown at 480°C (QDPLT-02). These two samples have similarly narrow linewidths; at low pump power, QDPLT-01 has a linewidth of 38.3 meV compared to 38.1 meV for QDPLT-02, and 39.5 meV versus 38.9 meV at high pump power.

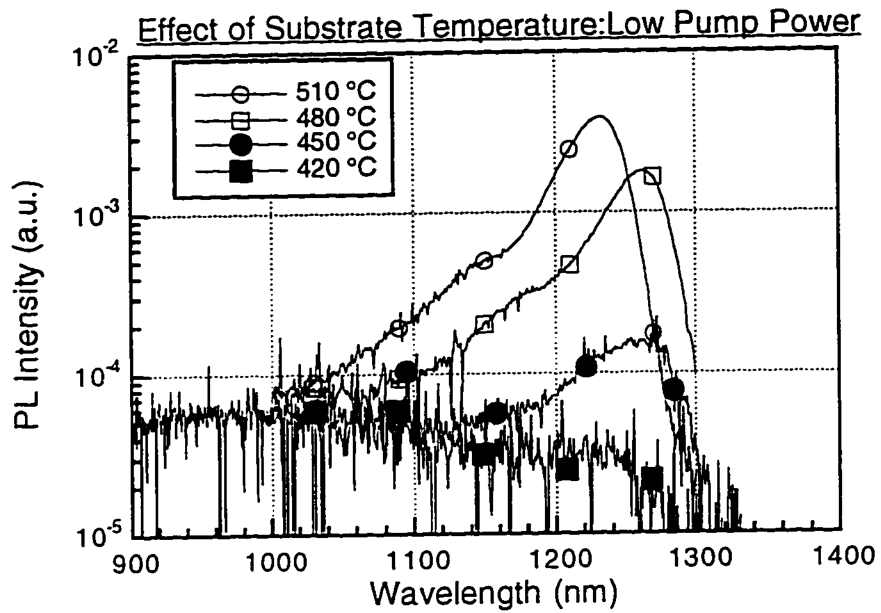

Figure 5-9 RTPL spectra from QDPLT-01, -02, -03, and -04 demonstrate the importance of the growth temperature on the optical quality of the InGaAs islands.

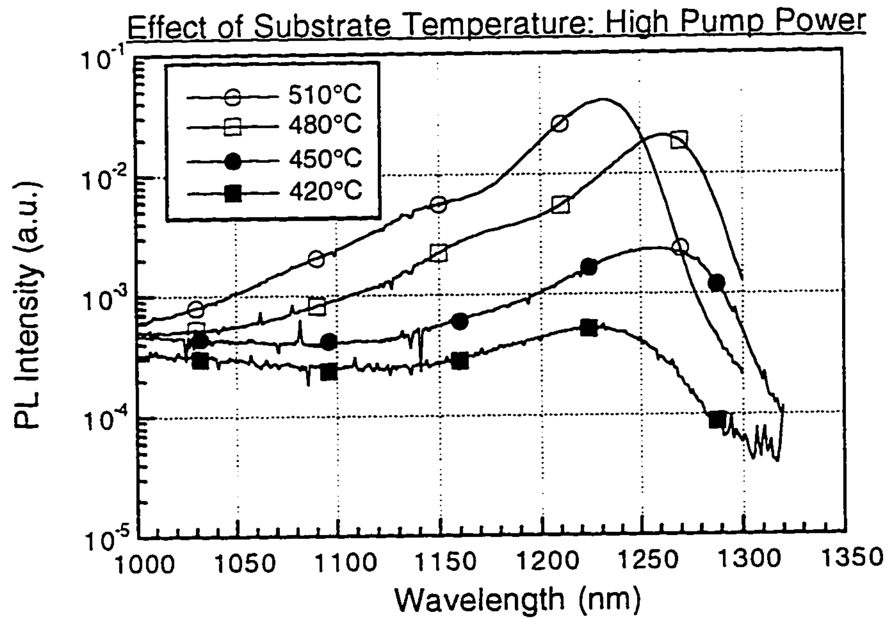

Figure 5-10 RTPL spectra from QDPLT-01, -02, -03, and -04 at high pump power.

The peak emission wavelength of QDPLT-01 (1230 nm) is slightly shorter than that of QDPLT-02 (1260 nm) and QDPLT-03 (1260 nm). This difference is probably due to some In re-evaporation from the surface at the higher growth temperature. This small a wavelength difference is unimportant compared to the benefits of increased efficiency by using the higher growth temperature; if necessary, the wavelength can be increased by growing a thicker epilayer. At the lowest growth temperature of 420°C, the PL peak wavelength is about 1230 nm. As noted earlier, the 2D-3D transition does not occur for this sample until between 9.7 MLs and 10.6 MLs have been deposited, compared to 7.1 MLs to 8.0 MLs for the three samples grown at higher temperatures. Thus, QDPLT-04 is expected to have smaller islands (peak height) and thus a larger quantization energy along the growth direction than the other samples. It is then expected that the peak emission wavelength from QDPLT-04 will be at a shorter wavelength than the previous three samples.

RTPL spectra from QDPLT-05 and -06 are shown in Figure 5-11. The peak emission intensity from QDPLT-06 (the higher temperature sample) is much weaker (about one order of magnitude) than from QDPLT-05. In addition, the peak emission wavelength has shifted from about 1230 nm (QDPLT-05) to about 1080 nm (QDPLT-06). This indicates that a substantial fraction of the deposited In is evaporating before it can be incorporated into the film. This combination of poor intensity and lack of control over emission wavelength indicates that QDPLT-06 has been grown at too hot a substrate temperature.

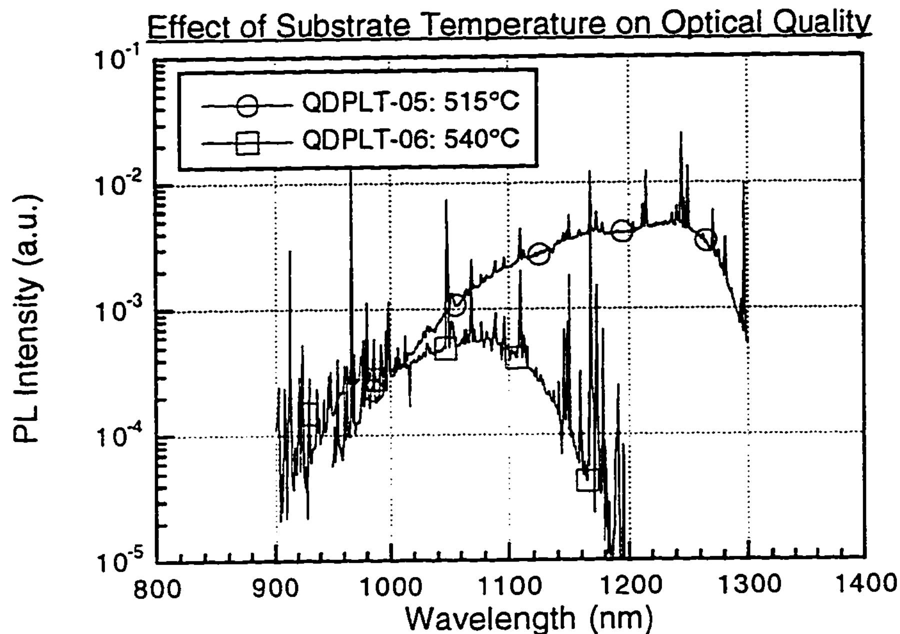

Figure 5-11 RTPL spectra from QDPLT-05 and -06 show that if the growth temperature is too high, the optical quality of the InGaAs islands is poor.

5.4.4 Summary

From these temperature-dependent samples, I conclude that substrate temperatures between 510-515°C give us the best overall optical properties from our quantum dots. Growth at higher temperature leads to excessive In re-evaporation as indicated from the RHEED pattern and the RTPL emission wavelength. Growth at lower temperatures leads to weaker RTPL emission intensity, which can probably be attributed to non-radiative recombination due to the formation of point defects in the either the InGaAs islands or in the GaAs overgrowth layer. Considering the relatively low surface diffusion length of Ga at substrate temperatures less than about

500°C (Ibbetson *et al.*, 1994, Mirin *et al.*, 1994), it is not too surprising that the optical quality of the GaAs grown over the nonplanar surface is degraded.

5.5 Smaller Dots and Multiple Layers of Smaller Dots

5.5.1 Introduction

Most of the samples discussed in this dissertation have been designed to have room temperature emission wavelengths of greater than 1200 nm. This large wavelength is obtained by continuing to deposit strained material long after the surface has undergone the transition to island growth. However, there is some degradation of the integrated PL intensity at room temperature compared to a quantum well, and the degradation is worse as more material is deposited (see Figure 2-16).

The AFM images from Chapter 4 show that the island density is saturated at 2-3 x 10^{10} cm^{-2} after 13.3 MLs of $In_{.3}Ga_{.7}As$ are grown by AMBE (Figure 4-13). Since the base diameter barely changes as more material is deposited, the islands just get progressively taller and more highly strained. In order to better understand the effects of continued deposition beyond the 2D-3D transition, additional samples in which the thickness of the $In_{0.3}Ga_{0.7}As$ epilayer is reduced to 13.3 MLs are grown.

5.5.2 AMBE Growth of Smaller Islands

The layer diagram for QDPLS-01 is shown in Figure 5-12a (also see Appendix A). The thickness of the $In_{0.3}Ga_{0.7}As$ epilayer for QDPLS-01 is only 13.3 MLs. The 2D-3D RHEED transition occurs between 8.8 MLs and 9.7 MLs.

QDPLS-02 has two 13.3 ML-thick layers of $In_{0.3}Ga_{0.7}As$ (see Figure 5-12b) with a 25.0 nm GaAs barrier between the layers. The first 8.0 nm of the barrier are grown at the same temperature as the InGaAs (515°C), and then the temperature is raised to 570°C to grow the remaining 17.0 nm of the barrier. The temperature is again decreased to grow the second layer of InGaAs. The 2D-3D RHEED transition for both InGaAs layers is observed between 8.8 MLs and 9.7 MLs.

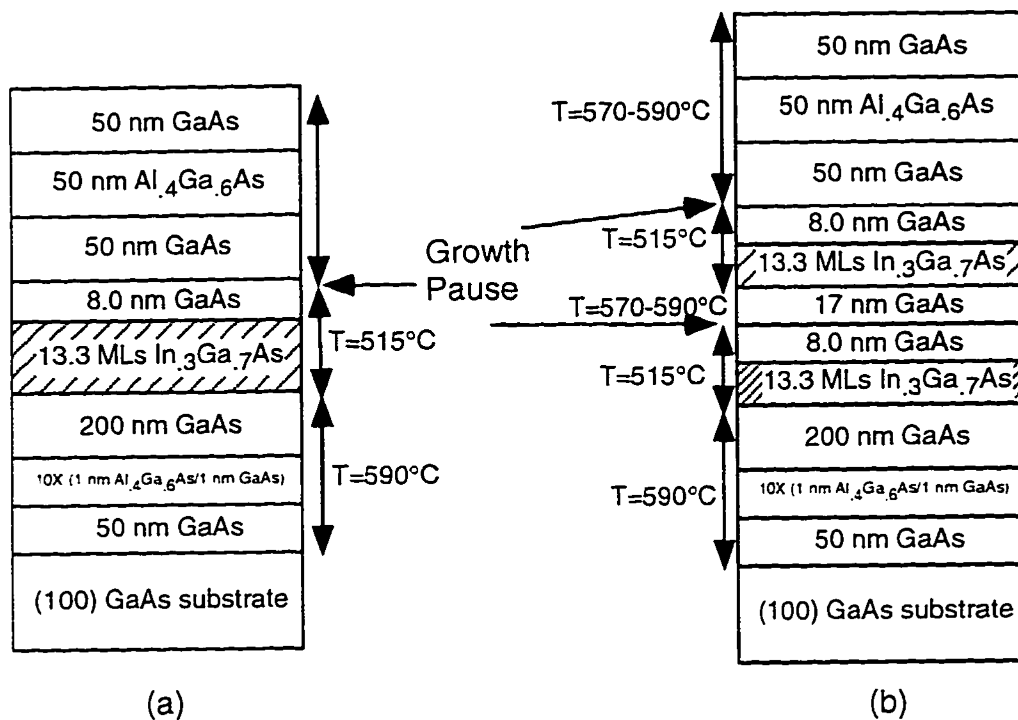

Figure 5-12 (a) Layer diagram for QDPLS-01 and -03. See Appendix A for detailed descriptions of the InGaAs layers. (b) Layer diagram for QDPLS-02, -04, and -05.

5.5.3 Optical Properties of Smaller Islands

RTPL measurements are made on these samples, as well as on QDPLCTRL-

02, which is a reference QW sample. Figures 5-13, 5-14, and 5-15 show RTPL spectra from these three samples at various pump powers. The peak emission wavelength from QDPLS-02 (1175 nm at low pump power, 1166 nm at high pump power), is only 4 nm longer than the peak emission wavelength from QDPLS-01 at all pump powers. This indicates good layer-to-layer uniformity. This is an important consideration when designing multilayer laser structures since nonuniformity between layers will lead to higher threshold currents because all of the radiatively recombining carriers will not be contributing to the lasing mode.

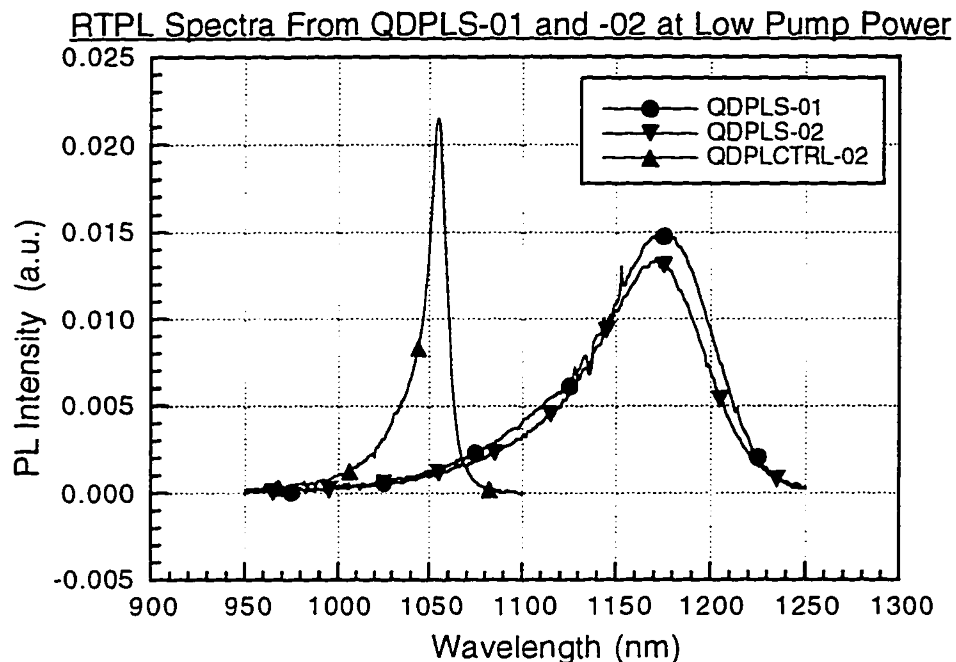

Figure 5-13: RTPL spectra from QDPLS-01 and -02 and QDPLCTRL-02 at low pump power. The integrated intensities are comparable for all three samples.

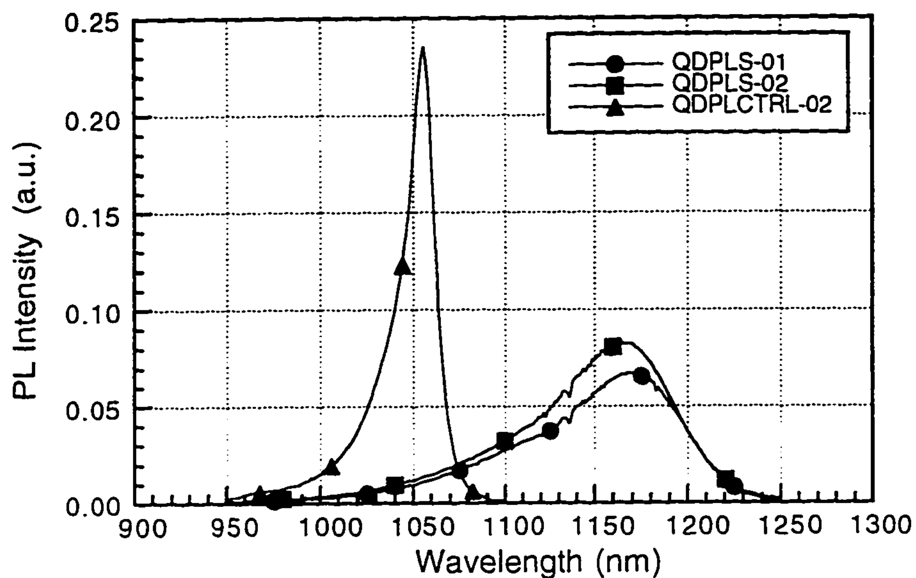

Figure 5-14 RTPL spectra from QDPLS-01 and -02 and QDPLCTRL-02 at intermediate pump power. The intensity is still comparable.

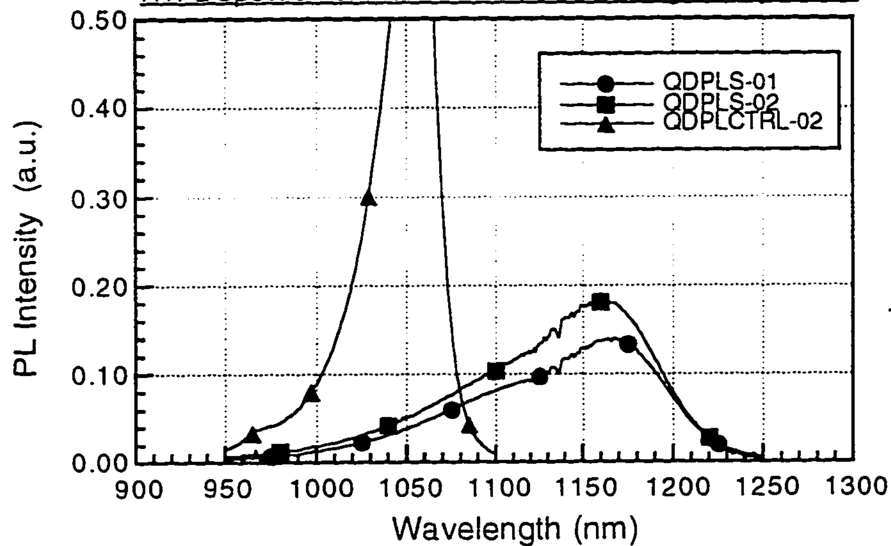

Figure 5-15 RTPL spectra from QDPLS-01 and -02 and QDPLCTRL-02 at high pump power. State filling in QDPLS-01 isvisible as evidenced by the increasing linewidth.

Figure 5-16 shows the integrated intensity as a function of pump power for the three samples. The integrated intensity from the two quantum dot samples is comparable to that of the quantum well sample, although the quantum well is brighter at higher pump powers. There is not much improvement in integrated intensity by changing from one layer of quantum dots to two layers of quantum dots. This may be due to efficient radiative recombination in the single layer sample due to excited state emission. There is a slight improvement in linewidth from the two-layer QD sample as compared to the single QD layer sample, which supports this conclusion.

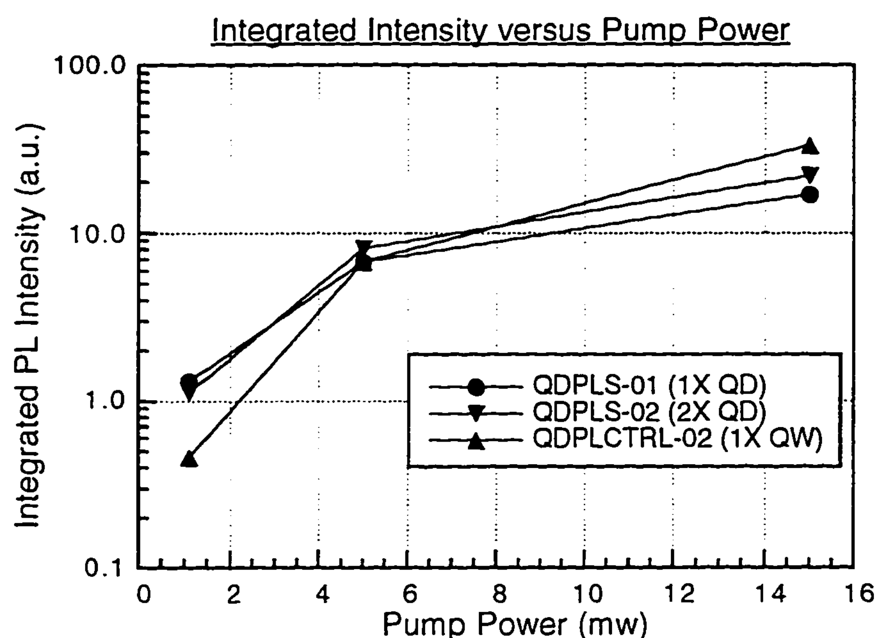

Figure 5-16 The integrated intensity from QDPLS-01 and -02 (quantum dot samples) are comparable to that of QDPLCTRL-02 (QW sample).

5.5.4 Limits to Multiple Layer Samples

In order to investigate the limits to the number of QD layers that can be grown while continuing to see improvements in the optical properties of the samples, three more samples are grown. Samples QDPLS-03, -04, and -05 have one, three, and five layers of 13.3 ML InGaAs islands (see Figure 5-12), respectively. There is a 25.0 nm GaAs barrier between layers; the barrier is grown as described above. Another QW reference sample is also grown (QDPLCTRL-03) that consists of a single 8.5 nm $In_{.2}Ga_{.8}As$ QW (see Figure 5-12a). This reference sample is used to indicate the overall material quality coming from the MBE machine at this point in time.

The 2D-3D RHEED transition occurs between 9.7 MLs and 10.6 MLs of deposition for the first InGaAs and second InGaAs layers. However, the subsequent layers have the RHEED transition slightly sooner, between 8.8 MLs and 9.7 MLs of deposition. This indicates imperfect smoothing by the GaAs barrier, and/or the interaction of the strain field from the underlying islands with the surface.

5.5.5. Optical Properties of Multiple Layers Samples

Figures 5-17, 5-18, and 5-19 show RTPL spectra from these four samples at various pump powers. The peak emission intensity from QDPLS-03 (1 QD layer) is about 20% brighter than from QDPLS-04 (3 QD layers) and about 50% brighter than from QDPLS-05 (5 QD layers). Also, the peak emission wavelength from the multi-QD samples is now 30-40 nm longer than the peak emission wavelength from the single QD layer sample. This is indicative of layer-to-layer nonuniformity caused by insufficient smoothing by the GaAs spacer, or strain-field interaction from the

underlying InGaAs layers, which leads to earlier island formation in the subsequent layers. If the subsequent dot layers nucleate slightly earlier than the initial dot layer, then the latter islands will be taller than the former islands, reducing the quantization energy along the growth direction, and leading to a longer emission wavelength. This agrees qualitatively with what is observed in Figure 5-17. Note that QDPLS-05 (5 QD layers) actually shows a slightly shorter peak emission wavelength than does QDPLS-04 (3 QD layers), but this is probably due to the defects in the uppermost QD layers causing poor efficiency from those layers.

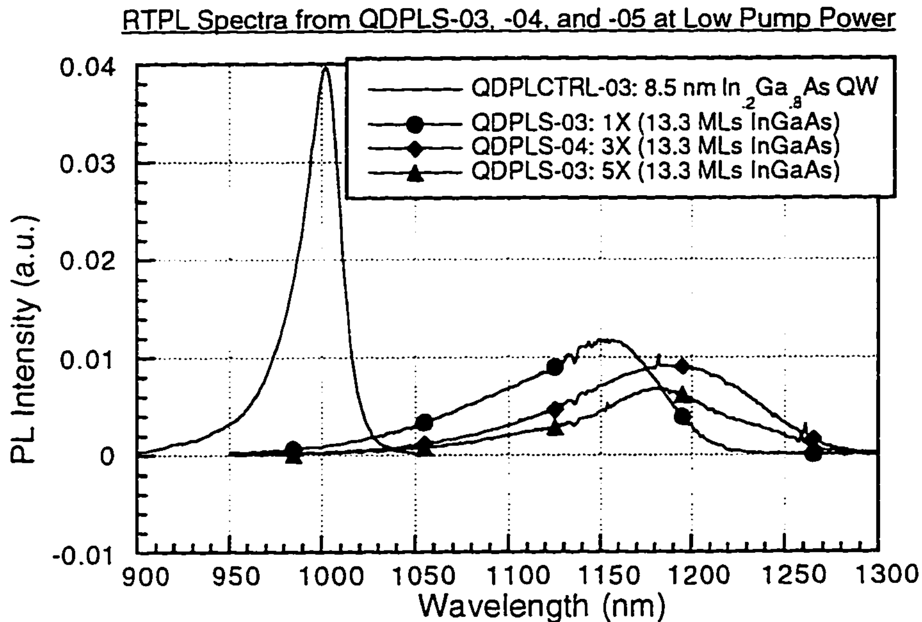

Figure 5-17 RTPL spectra from QDPLS-03, -04, and -05 at low pump power. Note that QDPLS-05 (5 QD layers) has a lower intensity than the 1-QD layer and 3-QD layers samples.

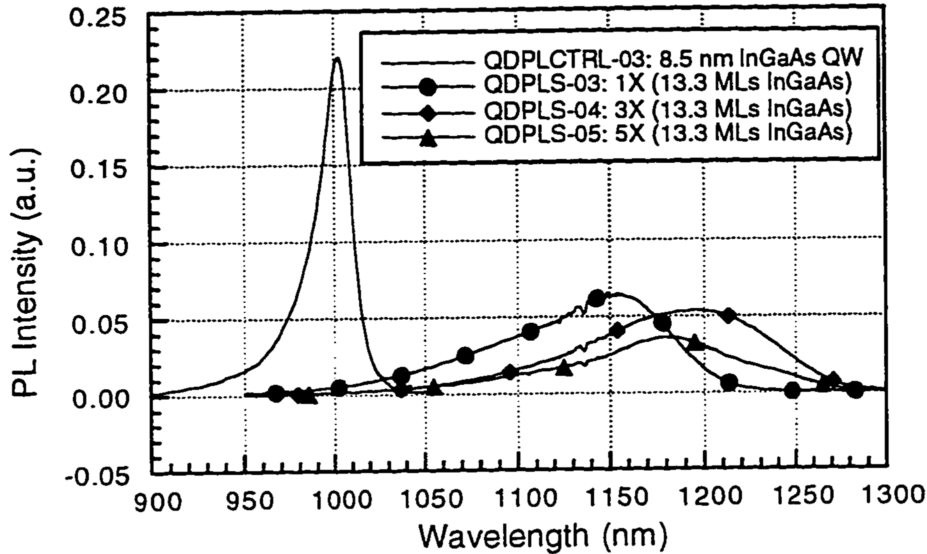

Figure 5-18 RTPL from QDPLS-03, -04, and -05 at intermediate pump power. State-filling effects are noticeable in QDPLS-03, the single layer sample.

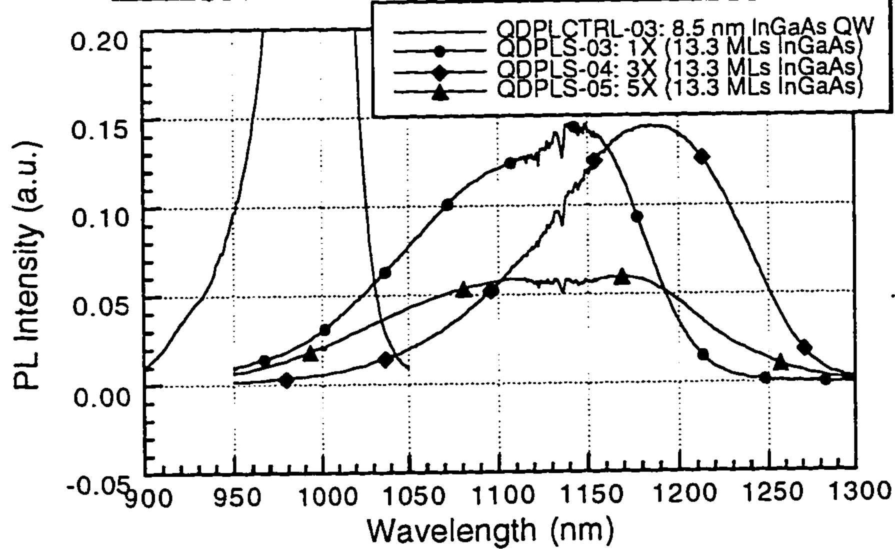

Figure 5-19 RTPL Spectra at high pump power from QDPLS-03, -04, and -05. Strong state-filling effects are apparent in QDPLS-03 (1 QD layer), but not in QDPLS-04 (3 QD layers).

At low pump power (Figure 5-17), the FWHM from QDPLS-04 is larger than the FWHM from QDPLS-03 (103 meV versus 95 meV). This is indicative of layer-to-layer nonuniformity in the multilayer sample. This agrees with the RHEED observations that the latter layers of InGaAs have a slightly earlier transition to three-dimensional growth than do the former layers.

At high pump power (Figure 5-19), the situation is reversed: QDPLS-03 has a FWHM of 139 meV and QDPLS-04 has a FWHM of 112 meV. At high pump power, state-filling effects become important, and QDPLS-04 has a higher density of states due to its three layer structure. The first excited state of QDPLS-03 can clearly be seen in the high pump power spectrum (Figure 5-19), whereas there is only a small amount of broadening in the spectrum of QDPLS-04. Thus, state-filling effects are not as important in the multilayer sample, and this manifests itself as a narrower linewidth at high carrier concentrations.

The peak emission intensity from the QD samples is about a factor of 4 lower than that from QDPLCTRL-03. However, the integrated intensity (Figure 5-20) from the single and triple layer samples are comparable to the integrated intensity from the QW sample. The five QD layer sample has lower integrated intensity than the other samples, which suggests that defects are forming in the subsequent layers due to the large amount of strain in the layers. Also, the integrated intensity from QDPL-21 is included here. This single QD sample has 22.1 MLs of InGaAs, which causes substantially higher strain than in the 13.3 ML samples. QDPL-21 has much lower integrated intensity than any of the other samples, which indicates that defects are causing low efficiency in this sample. This will help explain the performance of some of the lasers shown in Chapter 6 of this dissertation.

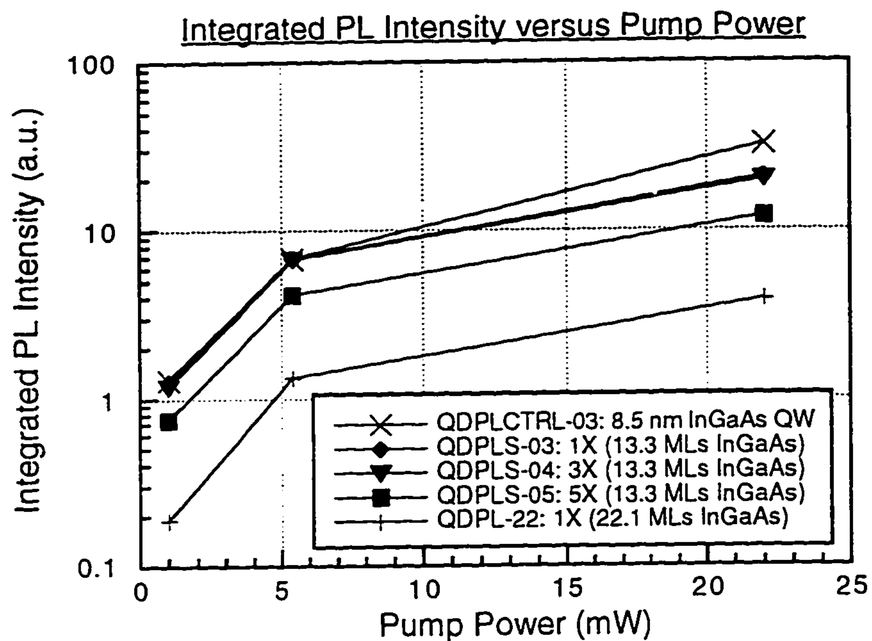

Figure 5-20 Integrated PL intensity as a function of pump power.

5.5.6 *Summary*

This section demonstrates that it is possible to obtain RTPL intensities from quantum dots that are comparable to the intensities obtained from quantum wells. The important thing is to control the amount of strained material that is deposited after the 2D-3D growth transition. It is also possible to use these smaller InGaAs islands to grow multilayer samples that are comparable in optical quality to a single layer sample. However, there are limits to the number of layers that can be grown while still maintaining good optical quality material.

5.6 Summary

This chapter emphasizes some of the important issues that need to be studied in order to obtain the best optical properties from arrays of InGaAs quantum dots. One important, but often neglected, aspect of the growth is the overgrowth, or burial, of the three-dimensional InGaAs islands. There is an optimum thickness of GaAs that must be deposited on top of the InGaAs islands at the low growth temperatures used for depositing the InGaAs islands. If too thick a layer of GaAs is grown at the low substrate temperature, the PL intensity is reduced, probably due to the formation of point defects. If too little GaAs is grown at low temperature, and the substrate temperature is then increased, then the islands can partially evaporate, as indicated by the shift in the ground state transition to higher energy due to the increase in the confinement energy. At some intermediate thickness, it is possible to obtain good control over the peak emission wavelength, as well as highly efficient radiative recombination. This technique for optimizing the optical properties is advantageous compared to the use of MEE-grown overlayers (Xie *et al.*, 1995) since it is simpler to raise the temperature of a sample rather than lower the temperature as must be done for the MEE-grown sample. Additionally, less intermixing of the InGaAs with the GaAs overgrowth is expected when simultaneous molecular beams are used to grow the GaAs overgrowth layer.

This overgrowth optimization leads into the optimization of the growth of multiple layers of InGaAs islands, in which the barrier between layers is equivalent to the overgrowth discussed previously. There is some minimum thickness that must be grown between InGaAs layers in order to get a smooth starting surface for subsequent layers to show good uniformity with previous layers. This is the primary

consideration when growing multiple layer structures for use in diode lasers. There is also a limit on the number of InGaAs layers that can be grown while still seeing improved optical properties, such as brighter PL intensity and reduced state-filling. Beyond a given number of layers, the radiative efficiency is reduced, presumably due to defects that occur due to the buildup of strain.

Chapter 6: Quantum Dot Lasers

6.1 Introduction

The first study of advantages of quantum dot lasers (QD lasers) as compared to bulk lasers and quantum well lasers (QW lasers) came from Arakawa and Sakaki in 1982. In this paper, the authors examined the temperature-dependence of bulk, quantum well, quantum wire, and quantum dot lasers. Their calculations show that quantum dot lasers should have an infinite T_0, where T_0 describes the temperature-sensitivity of the threshold current ($I_{th}=I_{th0}(\exp(T/T_0))$). This paper is often referenced in citing the main advantage for quantum dot lasers versus other types (bulk, quantum well) of lasers. Other predictions for benefits due to the three-dimensional confinement include reduced threshold currents and larger differential gain (Asada, Miyamoto, and Suematsu, 1986).

Once the growth method for quantum dots was well-established, and with the reports of reasonable photoluminescence intensities, several groups set out to investigate quantum dot lasers. At UCSB, an attempt was made to make a quantum dot laser (Leonard, 1995, Thibeault, 1995). Although this device did demonstrate lasing, the emission wavelength of the laser light corresponded to excited state emission from states in the Stranski-Krastanow wetting layer instead of from quantum dot states.

Ledentsov *et al.*, 1994 had the first demonstration of a quantum dot laser. This laser lased very close to the ground state transition at low temperatures. However, the threshold current densitiy was very high. Recent reports from

Bimberg *et al.*, 1996 demonstrate room temperature lasing from the ground state of a multiple layer samples. In this case, the layers of quantum dots are strongly coupled which may mitigate some of the benefits of using quantum dots. Nonetheless, these lasers have low thresholds and high characteristic temperatures.

Other groups have claimed quantum dot lasers, but the evidence for lasing from a quantum dot state is fairly weak. A group at Fujitsu (Shoji *et al.*, 1995) obtains lasing action from an excited state at low temperature (80 K). As proof that the lasing comes from quantum dot states, they show that the wavelength shift of a quantum dot laser is less than that of a quantum well laser under a perpendicular magnetic field. This could be evidence of lateral confinement. However, as will be seen later in this chapter, the lasing wavelength is is a strong function of the threshold current density in quantum dot lasers, but not in quantum well lasers. Therefore, if the magnetic field causes a change in the current density required to reach threshold, the quantum dot laser will be much more strongly affected than the quantum well laser. Another group at USC claims lasing at 80 K from multiple layers of quantum dots (Xie *et al.*, 1996). Although they see an apparent threshold in the device, the spectral widths are much larger than are observed from a laser; this suggests that they only have a superluminescent diode. Finally, Kamath *et al.*, 1996 report room temperature operation of a laser with quantum dots in the active region. However, they offer no evidence that the lasing transition is from quantum dot states.

In this chapter, I will show how the results from the previous chapters can be used to make lasers from these quantum dots. I will describe laser design, crystal growth, and fabrication of the lasers. Then I will present measurements such as spectra and efficiency curves measured on these lasers. Finally, I will discuss inherent limits on QD lasers due to Rayleigh scattering.

6.2 Experimental Procedures

6.2.1 Sample Growth and Processing

The laser diode structure used to test the quantum dots is shown in Figure 6-1. The structure is essentially identical to a quantum well laser diode, except that the active region consists of a layer of quantum dots instead of a quantum well. There is also a quantum well laser grown on the same day as the quantum dot laser as a control sample. This quantum well laser control sample is necessary so that the material quality can be evaluated and any processing or testing abnormalities can be accounted for. The quantum well laser has the identical structure as the quantum dot laser, except that the active region is an InGaAs quantum well.

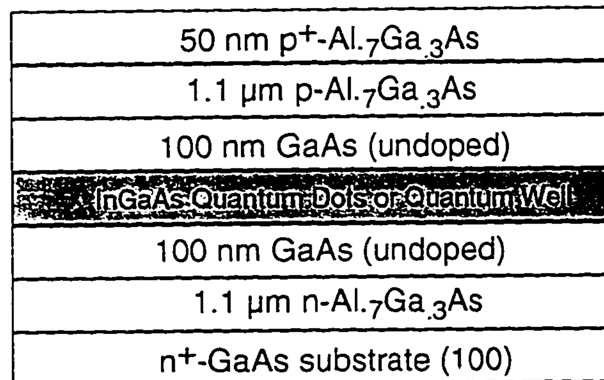

Figure 6-1 Epilayer diagram for the QD and QW lasers.

The QD laser has the structure shown in Figure 6-1. The active region consists of 13.3 MLs of $In_{.3}Ga_{.7}As$ grown by AMBE. This is identical to some of the samples presented in Chapter 5, AMBE Issues and Optimization: Overgrowth and Multiple Layers. The ground state emission is peaked at about 1150 nm at room

temperature. The dot height is around 12 nm and the base diameter is around 30 nm (see Chapter 4, Morphological and Structural Characterization of InGaAs Islands, for more details).

The InGaAs quantum well used in the control sample was grown with the same shutter sequence that was used to grow the quantum dots. The only difference was that the quantum well was terminated after 7.1 monolayers of $In_{.3}Ga_{.7}As$ have been deposited. This is exactly equal to the thickness of the Stranski-Krastanow wetting layer. Thus, any effects in the quantum dot laser that might be attributed to the Stranski-Krastanow wetting layer can be evaluated.

The QW and QD lasers were simultaneously processed into broad-area lasers with a 50 μm wide stripe width. The p-metal contact layer was Ti/Pt/Au (50 Å/ 150 Å/ 2000 Å) which was used as an etch mask for etching the laser stripes. The etchant is H_3PO_4:H_2O_2:H_2O (3:8:50) which etches about 2 μm down, through the active region and into the lower AlGaAs cladding layer. The samples were then mounted with wax on a lapping block and thinned to between 75 and 100 μm. Ni/AuGe/Ni/Au of thickness 50, 1050, 150, and 1500 Å, respectively, were then e-beam evaporated onto the back to make an n-type contact. Finally, the contacts were annealed for 30 seconds at 400°C in a rapid thermal annealer.

6.2.2 Laser Measurements

L-I curves and spectra from both the QD and the QW lasers were measured from 80 K to 304 K. The temperature steps were taken so that k_BT increases 20% per step. All of the measurements were in the pulsed operation mode (≈ 400 ns pulses at a repetition frequency of 1 kHz).

Room temperature L-I curves for an 800 μm long stripe are shown in Figure 6-2. The QW laser has a threshold current density of about 265 A/cm^2, and the QD laser has a threshold current density of about 510 A/cm^2. The reciprocal of external differential efficiency is plotted against (Length/ln(Reflectivity^{-1})) in Figure 6-3 in order to extract the internal differential efficiency, η_i, and the internal loss, α_i, of these lasers. For the QW laser, η_i equals 70% and α_i equals 10 cm^{-1}. For the QD laser, η_i equals 81% and α_i equals 35 cm^{-1}.

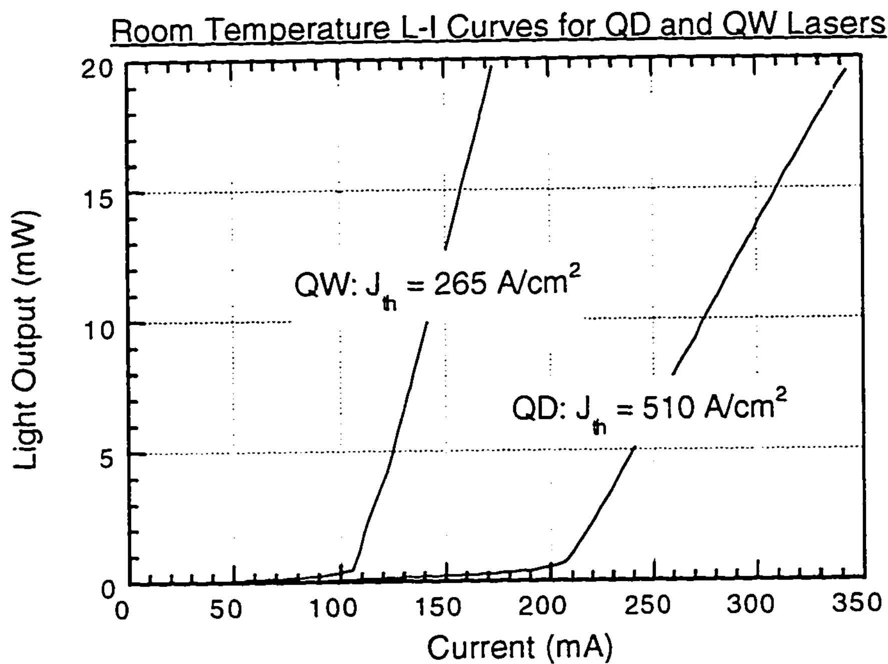

Figure 6-2 Pulsed L-I curves from 50 μm x 800 μm stripe lasers.

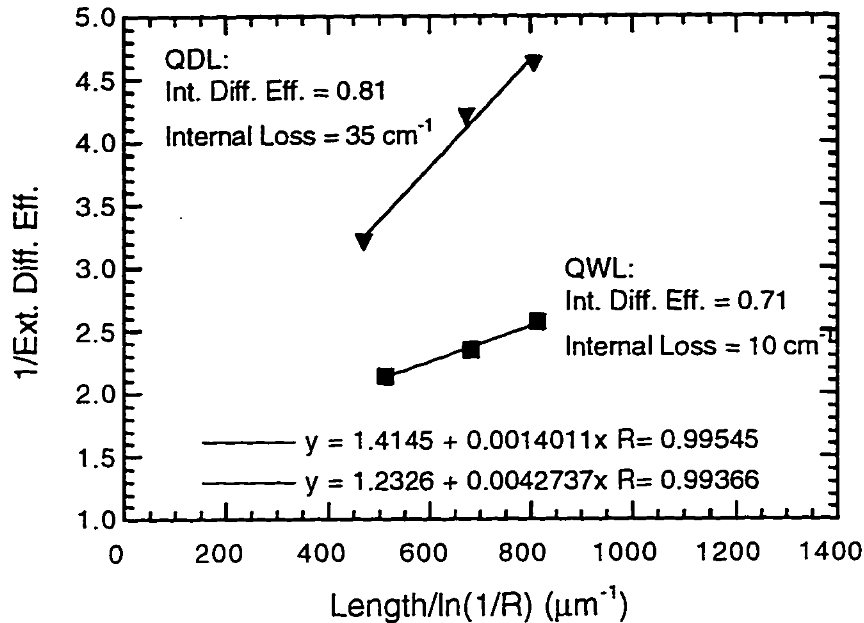

Figure 6-3 Curves for extracting internal loss and internal differential efficiency.

The subthreshold electroluminescence from the QD laser is shown in Figure 6-4. At relatively low current densities, the ground state luminescence at 1150 nm is saturated. Beyond that, any additional current produces emission from an excited state in the dots. As can be seen in Figure 6-4, increasing the current density shifts the peak EL wavelength out to higher and higher energies until lasing is finally achieved at about 1029 nm (see Figure 6-5).

The subthreshold EL from the QW laser is shown in Figure 6-6. There is little or no shift in the peak EL wavelength as the current is increased, and lasing occurs from the ground state of the QW (see Figure 6-7).

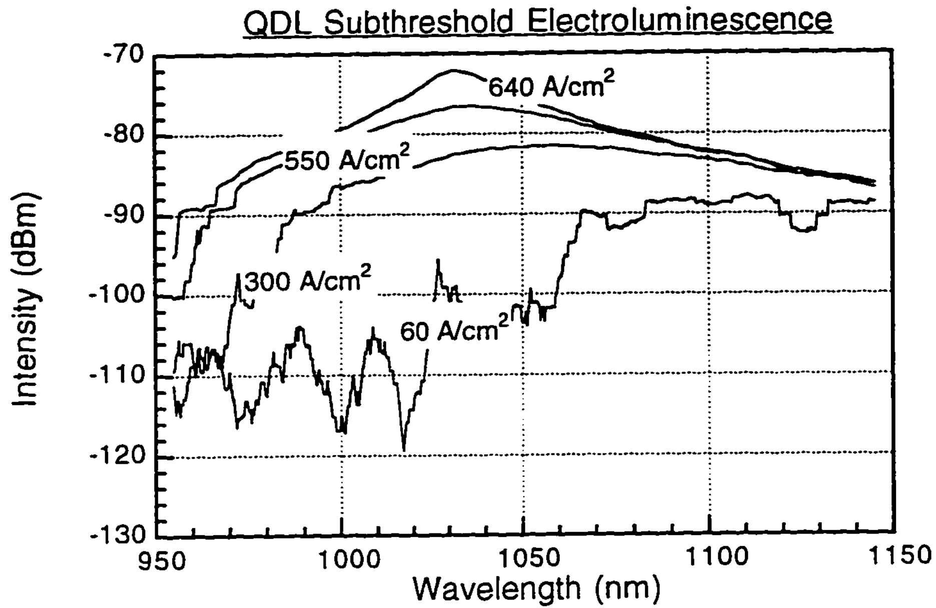

Figure 6-4 Subthreshold EL from the QDL at various current densities with low resolution on the spectrum analyzer. The ground state emission is peaked at 1150 nm.

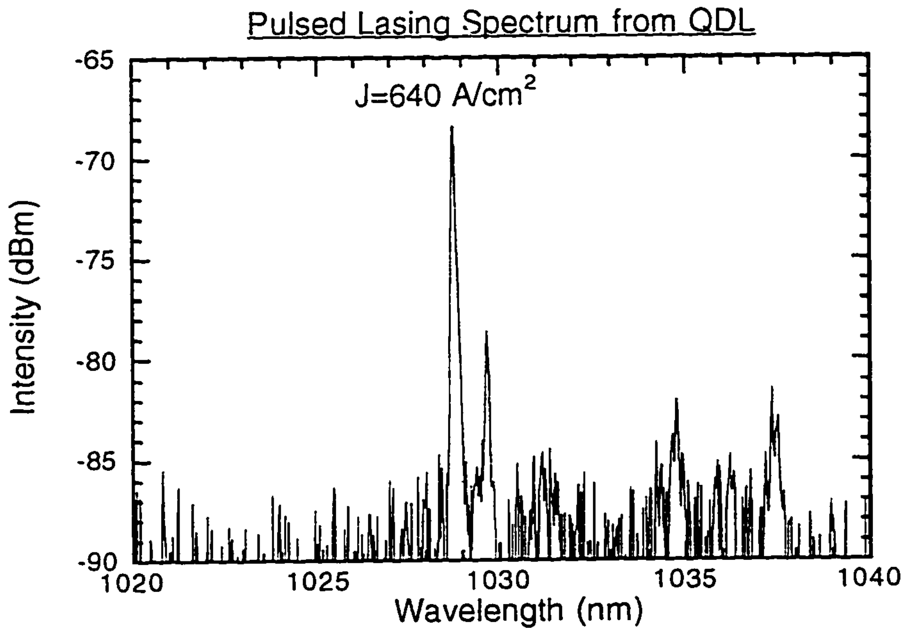

Figure 6-5 Lasing spectrum from the QDL with the spectrum analyzer set on high resolution.

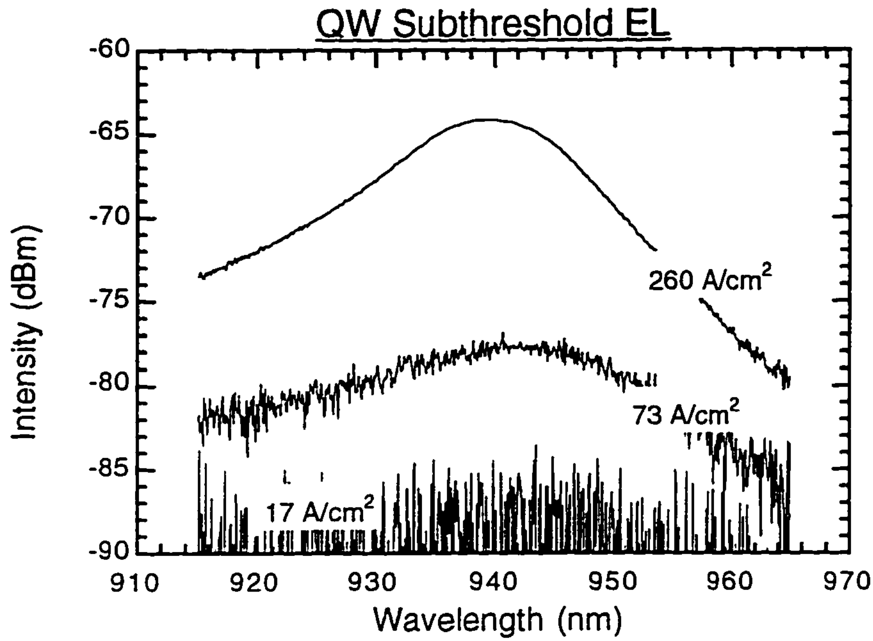

Figure 6-6 Pulsed, subthreshold EL from a 50 x 600 μm QW laser taken at low spectral resolution.

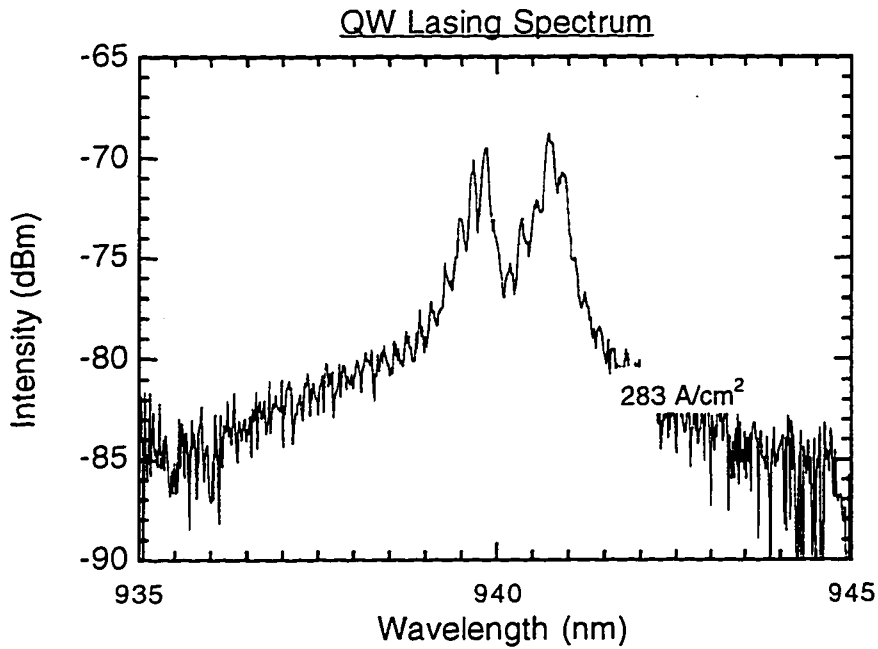

Figure 6-7 Pulsed lasing spectrum from a 50 x 600 μm QW laser.

Temperature-dependent L-I curves for 800 μm long stripes from the QD and the QW lasers are shown in Figures 6-8 (a) and (b), respectively. For both lasers, the threshold current decreases as the temperature is decreased. The threshold current as a function of temperature is plotted in Figure 6-9. The characteristic temperature, T_0, is measured to be 185 K for the QD laser from 80 K to 140 K, and T_0 decreases to 111 K for temperatures from 140 K to 304 K. For the QW laser, T_0 is 173 K from 80 K to 170 K, and it decreases to 95 K from 170 K to 304 K.

6.2.3 Analysis and Discussion

As shown in Figure 6-9, the threshold current decreases as the temperature is decreased for both the QW and the QD lasers. The decrease is due to a reduction in the spread of the Fermi-Dirac distribution of the injected carriers, as well as reduced thermionic emission from the QDs and QWs.

The decrease in threshold current means that there is a corresponding decrease in the state-filling in the QDs that pushes the lasing transition out to higher energies. In Figure 6-10, the lasing wavelength is plotted as a function of temperature for the QD and the QW lasers. The lasing wavelength of the QW laser decreases by about 2.5 Å/°C, which corresponds to the increase in bandgap of the QW. The lasing wavelength of the QD laser decreases by about 0.4 Å/°C, only about 1/6 that of the QW laser.

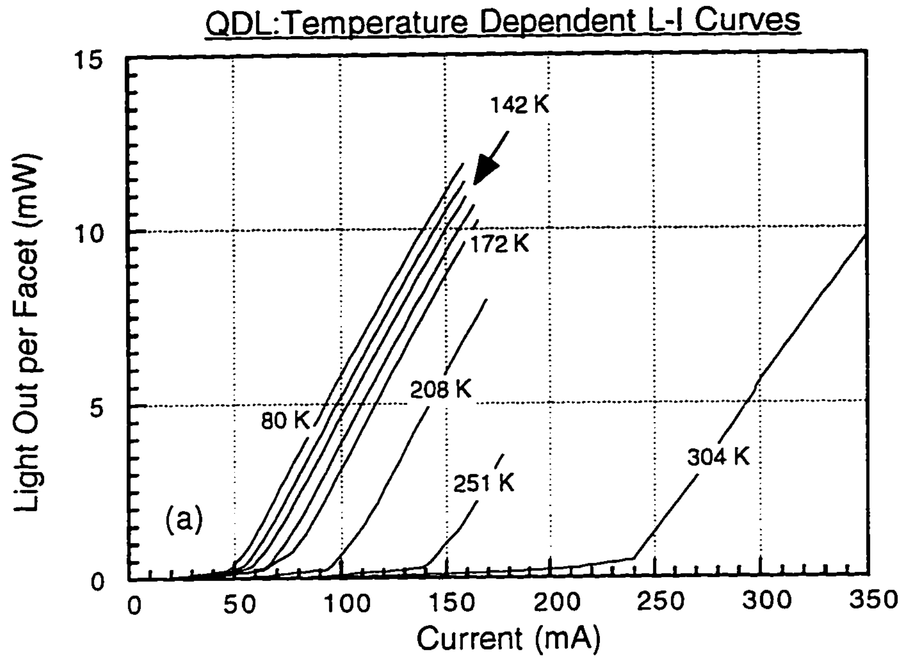

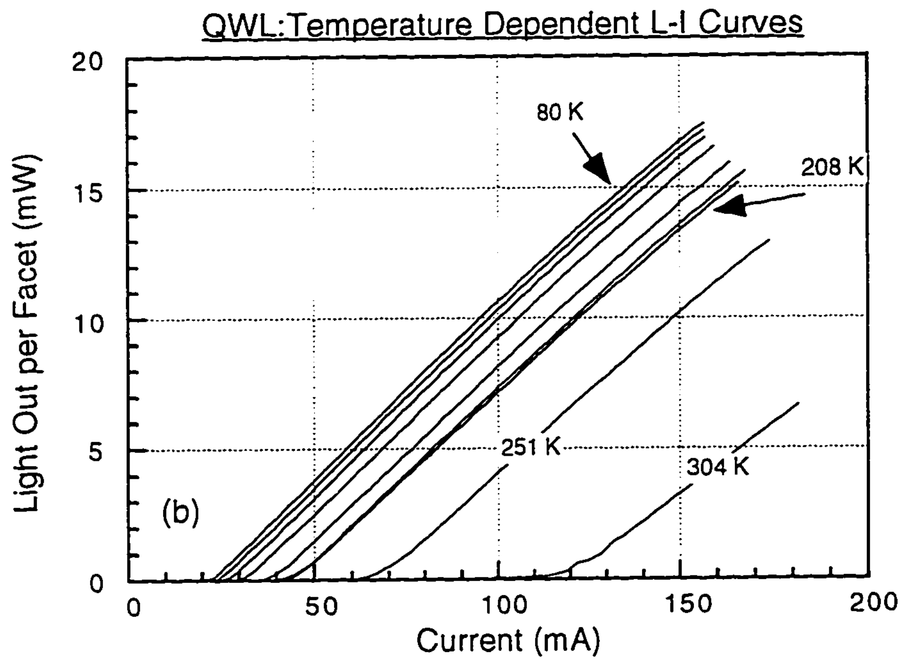

Figure 6-8 (a) L-I curves from an 800 μm long QDL at various temperatures, and (b) L-I curves from an 800 μm long QW laser at various temperatures.

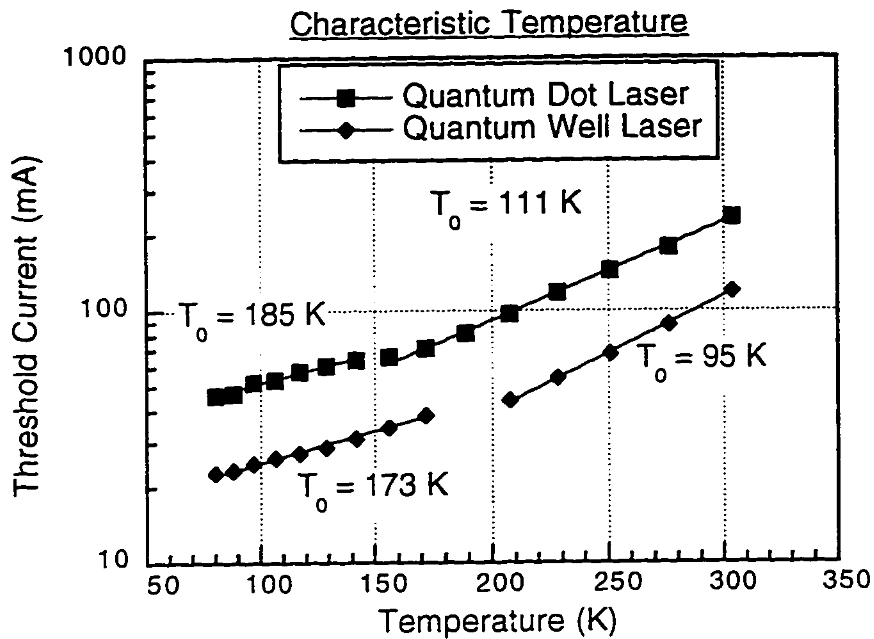

Figure 6-9 A comparison of the characteristic temperature for the QD and QW lasers.

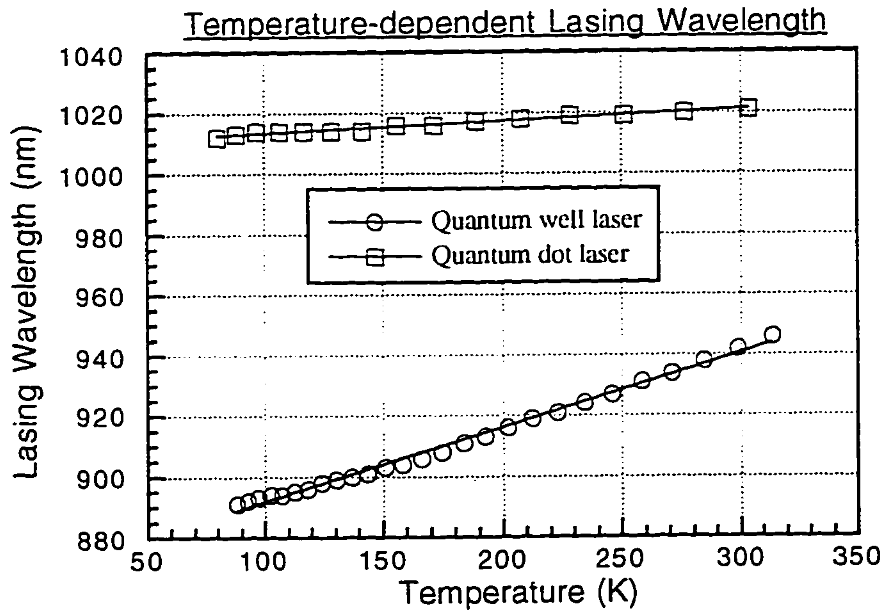

Figure 6-10 Lasing wavelength versus temperature for QD and QW lasers. Note the weak temperature dependence of the lasing wavelength from the QD laser. The solid lines are linear curvefits to the data.

To understand this reduced temperature sensitivity, it is necessary to examine the expression used for gain in semiconductors. I will follow the notation of Coldren and Corzine, 1995 (see Chapter 4 of Coldren and Corzine for detailed derivations of the expressions used here). The maximum material gain at some transition energy E_{21} is given by

$$g_{21} = \frac{\pi q^2 \hbar}{\pi \varepsilon_0 c m_0^2} \frac{1}{h\nu_{21}} |M_T(E_{21})|^2 \rho_r(E_{21})(f_2 - f_1) \qquad (6\text{-}1)$$

where ρ_r is the reduced density of states and $(f_2 - f_1)$ is the Fermi factor. The reduced density of states ρ_r is the most important term for understanding the reduced temperature sensitivity of the lasing wavelength in the QD lasers. As the injected current density is increased, the Fermi factor, $(f_2 - f_1)$, also increases. $\rho_r(E)$ must be increasing as energy increases so that the energy of maximum gain, which corresponds to the highest emission intensity (see Figure 6-4, the subthreshold EL spectra), is increasing since $(f_2 - f_1)$ is always larger for some $E_{21} < E'_{21}$.

If the DOS increases with increasing energy, then the energy of maximum gain will also increase when the quasi-Fermi level separation is increased. This hypothesis can be tested by measuring the length-dependence of the lasing wavelength at some fixed temperature. Shorter lasers have larger distributed mirror loss, α_m=(Length^{-1}*ln(Reflectivity^{-1})), compared to longer lasers. Thus, shorter lasers need higher current densities, and correspondingly higher gain, in order to achieve lasing. Figure 6-11 show a plot of lasing wavelength versus laser length for the QD and the QW lasers. The QW laser lases at approximately the same wavelength for all of the stripe lengths measured. This is typical of strained QW lasers, except

for very short lasers in which bandgap renormalization effects and nonparabolicity effects become important.

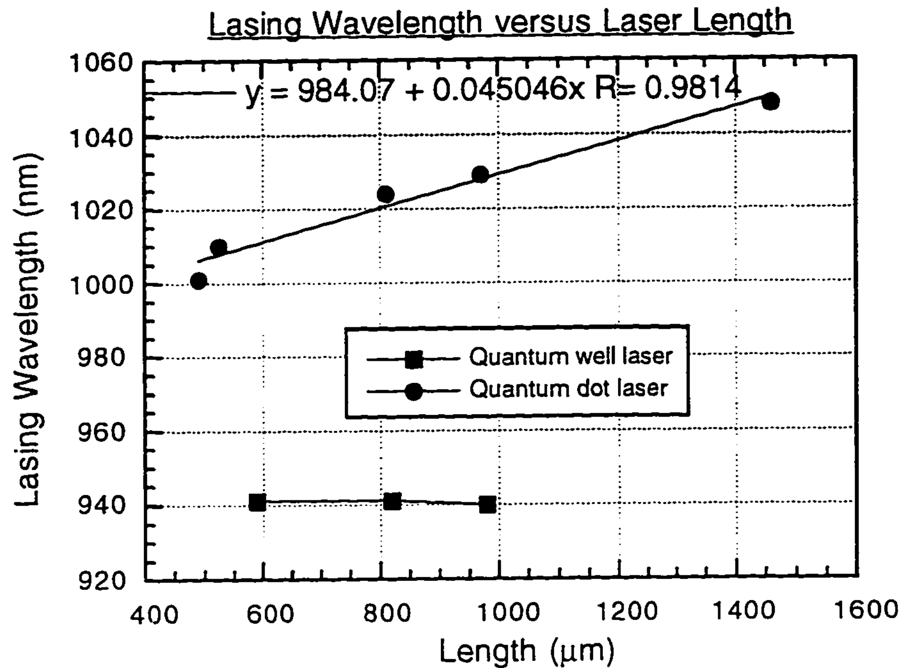

Figure 6-11 The quantum dot lasing wavelength changes dramatically as the laser length changes. The quantum well lasing wavelength barely changes.

The lasing wavelength of the QD laser shows a strong linear dependence on the laser length. Correspondingly, the lasing transition energy varies linearly with the mirror loss, as shown in Figure 6-12. Due to the high level of carrier injection, bandgap renormalization causes a decrease in the bandgap of the active region in typical semiconductor lasers. This bandgap renormalization causes shorter lasers to lase at longer wavelengths compared to longer lasers with the same epilayer structure. Thus, the state-filling effect that shifts the gain to higher energies must also overcome this bandgap renormalization as well.

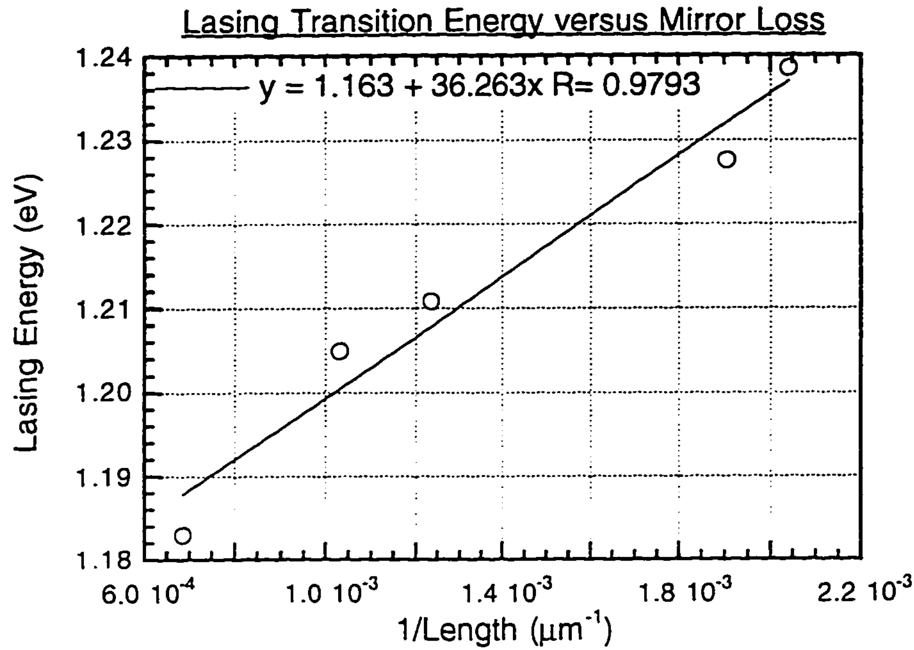

Figure 6-12 Lasing transition energy varies linearly with mirror loss.

6.2.4 Gain Modeling

As shown above, the lasing transition energy varies approximately linearly with the mirror loss for the quantum dot laser. Since the lasing transition energy is the energy at which gain is highest, this implies that the energy of peak gain increases linearly. In order to understand how this can happen we need to examine the expression for gain in more detail.

The expression for gain is given by (Coldren and Corzine, 1995)

$$g(h\upsilon_0) = \frac{\pi q^2 \hbar}{n\varepsilon_0 c m_0^2} \frac{1}{h\upsilon_0} \int |M_T(E_{21})|^2 \rho_r(E_{21})(f_2 - f_1) L(h\upsilon_0 - E_{21}) dE_{21}. \qquad (6\text{-}2)$$

From this expression, it is obvious that the form of the reduced density of states, ρ_r, is the most important variable in determining how the position of the gain peak varies.

Figure 6-13 (a) shows a plot of the gain at various current levels for a reduced density of states (DOS) corresponding to a bulk semiconductor ($\rho_r(E) \propto E^{1/2}$). Figure 6-13 (b) shows a plot of the gain at various current levels for a reduced DOS corresponding to a QW ($\rho_r(E)$ = constant). For the QW, the maximum gain is always at the bandedge. Experimentally, this is what is observed until very short lasers are tested, at which point nonparabolicity and bandgap renormalization (both are neglected in this calculation) become important.

The expected form for the DOS of an ideal array of QDs is a series of delta functions whose heights correspond to the product of the dot density and the degeneracy of the given state. However, the QDs studied here are nonideal; they have a size distribution that leads to a smearing out of the delta function density of states. In order to model this system, we can multiply the delta function DOS by a Gaussian that decribes the energetic linewidth of the ground state transition. Figure 6-13 (c) shows the results of a calculation based on the DOS of a nonideal array of quantum dots. The calculation assumes that there are available states corresponding to the allowed states of an cubic quantum box with dimensions of 13.0 nm on a side; this is the mean dot height as measured by atomic force microscopy and reported in Chapter 4. The DOS at each allowed energy is then convoluted with a Gaussian that describes the linewidth of the ground state transition:

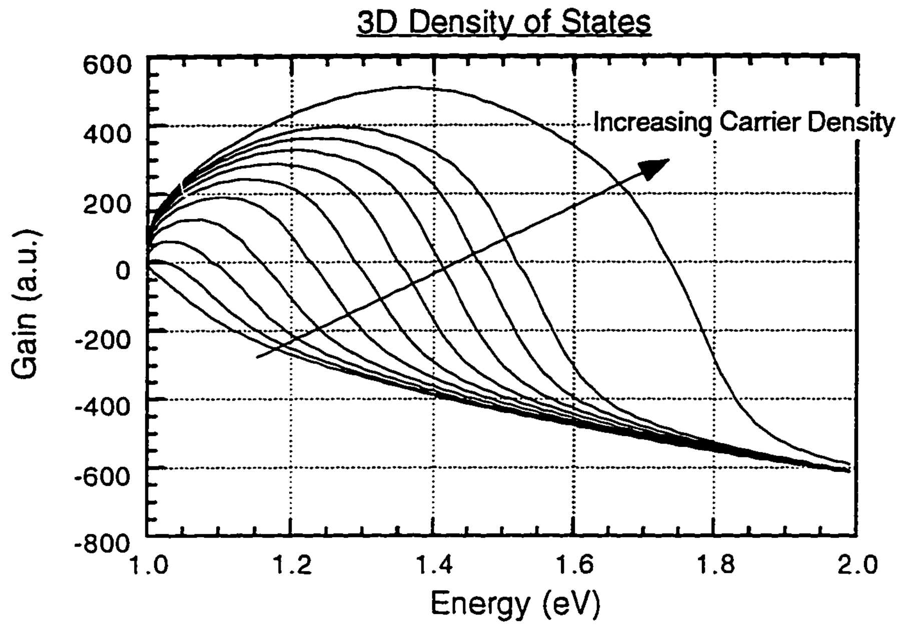

Figure 6-13 (a) Functional form of the gain versus energy for a three-dimensional density of states.

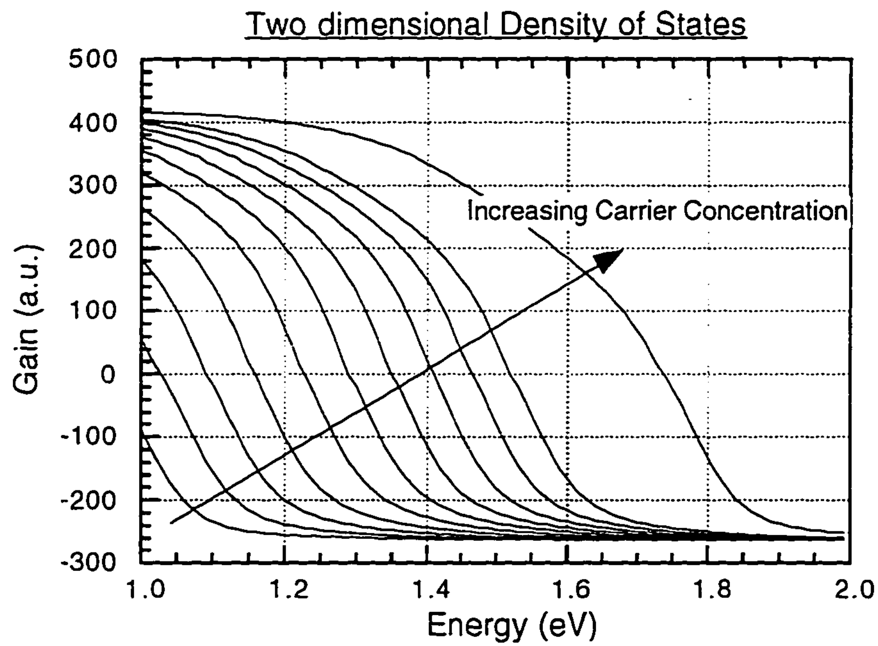

Figure 6-13 (b) Functional form of the gain versus energy for a two-dimensional density of states.

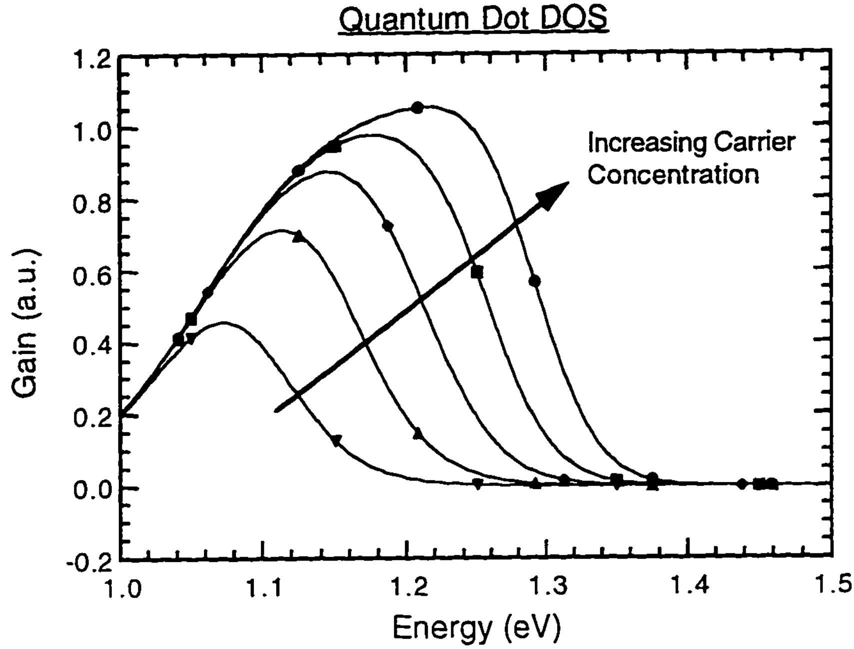

Figure 6-13 (c) Gain versus energy for a quantum dot DOS that includes the energetic distribution of the discrete states due to size fluctuations in the quantum dots.

$$\rho(E) = (\rho_D D)\left(2\pi(\Delta E)^2\right)^{-1/4} \exp\left[-\left(\frac{E - E_Q}{2\Delta E}\right)^2\right], \tag{6-3}$$

where ρ_D is the dot density, D is the degeneracy of the quantum state at energy E_Q, and ΔE is the linewidth of the transition.

Because the linewidth broadening is larger than the separation between energy levels for this system, the DOS is continuous, rather than discete as in an ideal system. As seen in Figure 6-13 (c), the position of the peak gain moves out to higher and higher energies as the carrier density is increased. The reason for this is the increase in the number of available states at higher energies.

Figure 6-14 shows the energetic position of peak gain versus peak gain for the QD DOS. This figure shows that a nonideal array of QDs is expected to have a gain peak position that increases in energy with increasing carrier density. Figure 6-14 shows that the peak position varies parabolically with the maximum gain, whereas experimentally the peak position varies linearly with the maximum gain as seen in Figure 6-12. One likely cause for this discrepancy is that the calculation neglects bandgap renormalization. The bandgap will shrink the most at the highest carrier densities, which means that the energetic position at the highest gain will be reduced. This dampens the parabolic term in Figure 6-14, thus giving better agreement between experiments and theory.

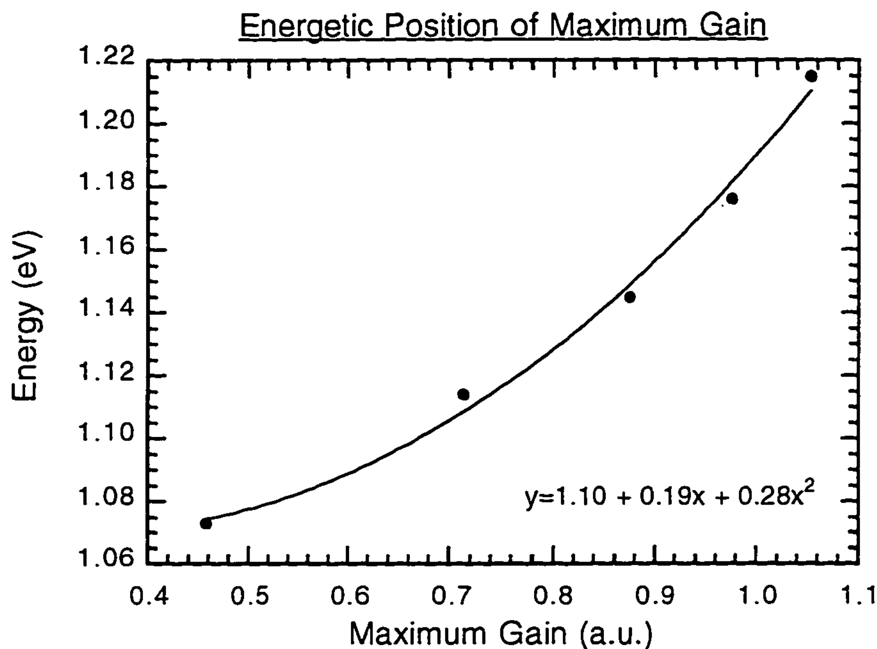

Figure 6-14 Variation of the position of peak gain at different carrier densities for the quantum dot DOS.

6.2.5 *Summary*

Quantum dot lasers have been measured from 80 K to room temperature. By comparing the lasing wavelength from these lasers to quantum well lasers with an active region whose thickness is identical to that of the Stranski-Krastanow wetting layer in the quantum dot laser, I conclude that the lasing action in the QD lasers is coming from QD states, not two-dimensional QW states from the wetting layer. Further evidence of this is in the temperature-dependence of the lasing wavelength and the mirror-loss dependence on lasing wavelength. Both of these quantities indicate that the DOS in the QD laser is a strong function of the energy. The DOS in a QW laser has only a very weak dependence on energy. State-filling effects in the QD lasers are very strong at room temperature and lead to a strong dependence of lasing wavelength on laser length, unlike the QW lasers that lase at about the same wavelength for all stripe lengths. Gain modeling demonstrates that for a nonideal array of quantum dots such as the one used for these lasers, it is expected that the energetic position of the gain maximum will vary as the current density is varied, as is seen experimentally.

6.3 Rayleigh Scattering Limits on Quantum Dot Lasers

6.3.1 *Introduction*

In the active region of a quantum well laser, the optical mode sees a constant refractive index as it propagates in the waveguide. However, in a quantum dot laser the refractive index varies because the layer of quantum dots is not continuous. Any

index discontinuity can cause optical scattering and therefore optical loss. If we assume that the quantum dots behave as small spheres, then we can investiagte Rayleigh scattering as a possible scattering mechanism. Particles are of the proper size for to be Rayleigh scatterers if they meet the criterion that the radius of the particle, a, is less than about 1/10 of the wavelength of light. For the quantum dots that are studied here, the wavelength of light in the semiconductor is about 325 nm (1000 nm/3.2, where 3.2 is the modal refractive index). Thus, in order to be of the proper size for Rayleigh scattering, the QD radius should be less than about 32 nm. The QDs studied in this dissertation meet this condition, and I will show here the limitations imposed on quantum dot lasers due to Rayleigh scattering losses.

6.3.2 Calculations

The derivation of Rayleigh scattering is well-known and only the most important results are reported here. For a more detailed description of Rayleigh scattering the interested reader is referred to Kerker, *The Scattering of Light and Other Electromagnetic Radiation.*

The scattering cross section per particle is given by

$$C_{scat} = \frac{128\pi^5 a^6}{3\lambda^4}\left(\frac{n^2-1}{n^2+2}\right)^2 , \qquad (6\text{-}4)$$

where a is the radius of the Rayleigh scatterer, λ is the wavelength of light in the surrounding medium, and n is the ratio of the refractive indices, n_1/n_2, where n_2 (n_1) is the refractive index of the surrounding medium (scatterer). Note the 6th power

dependence of the scattering strength on the size of the particle.

The total scattering loss due to some density of particles, ρ_v, is usually just given by $C_{scat}*\rho_v$. However, for the special case of a waveguide configuration where the particles are not uniformly dispersed, some slight modification is needed. Only those photons that "see" the QDs can be scattered. Those photons that see the QDs are also the only ones that can give gain. This fraction is the so-called modal confinement factor, Γ, which is given by

$$\Gamma = \frac{\int_{-w}^{w} E^2 dx}{\int_{-\infty}^{+\infty} E^2 dx}. \qquad (6\text{-}5)$$

Thus,

$$\alpha_{RS} = \Gamma C_{scat} \rho_v \qquad (6\text{-}6)$$

gives the net attenuation due to Rayleigh scattering.

6.3.3 Discussion

Let us first examine the limits that Rayleigh scattering imposes on our lasers. Later we will examine the specific case of the laser tested. For these calculations we will assume that n_1, the index of the scatterer, is 3.7 (which is approximately the index of InAs), n_2, the index of the surrounding medium, is 3.2 (which is approximately the index of GaAs), and λ is 325 nm (1000 nm/3.2). For a particle of radius a, the maximum areal density is $(4a^2)^{-1}$. Figure 6-15 shows a plot of Rayleigh

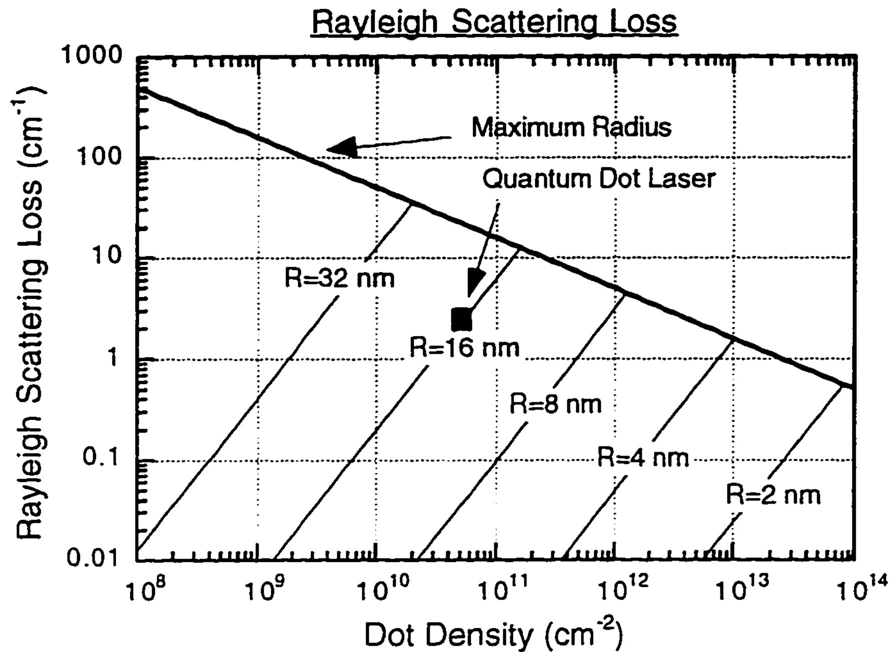

Figure 6-15 Rayleigh scattering loss at a given dot density for InAs dots buried in GaAs.

scattering loss versus dot density for several different dot sizes.

From the AFM sample that is described in Chapter 4 of this dissertation, the QD laser has a dot density of 4-5 x 10^{10} cm^{-2}, and the dot radius is about 16 nm. From Figure 6-15, this corresponds to a scattering loss of 1.5-2.5 cm^{-1}. This is not enough to account for the high loss measured on the QD laser.

Current QD lasers usually have a dot density of between 10^{10} and 10^{11} cm^{-2}. At these densities, the loss due to Rayleigh scattering is on the same order as the other loss mechanisms in semiconductor lasers if the dot size is larger than about 24 nm (10^{10} cm^{-2}) to 12 nm (10^{11} cm^{-2}). If the dots are smaller than these values, then the Rayleigh scattering loss is insignificant compared to the other internal loss mechanisms. If dots with a radius of less than about 8 nm are used, then Rayleigh

scattering will not be an important loss mechanism for QD lasers.

6.3.4 Limitations

The above model for Rayleigh scattering assumes single-particle scattering, which implies that the dot density is such that there is only one or fewer dots per wavelength of light. The dots in the laser described earlier clearly do not satisfy this criterion. If the particle density corresponds to more than one dot per wavelength of light, then the photon may see a lower refractive index difference and thus be scattered less. Therefore, the curves shown in Figure 6-15 must be regarded as the worst case scenario for Rayleigh scattering.

6.3.5 Summary

Rayleigh scattering limitations on QD lasers have been investigated. For QD sizes less than about 8 nm, Rayleigh scattering is unimportant. However, QD lasers with larger size QDs can suffer from Rayleigh scattering losses that are as large as or even larger than the typical values of internal loss. The QD lasers reported in this chapter have only 1-2 cm^{-1} of loss due to Rayleigh scattering.

6.4 Summary

In summary, laser diodes with quantum dot active regions have been grown and measured. These quantum dot lasers have been compared to quantum well lasers that have an active region that consists of a two-dimensional layer whose thickness is

that of the Stranski-Krastanow wetting layer. The lasing wavelength of the QD lasers increases as the length of the laser bars increases, but shows only a very weak dependence on temperature over the range of 80 K to room temperature. Both of these can be explained by state-filling in the QDs. The characteristic temperature of the QD laser is slightly better than that of the QW laser, but it is not substantially improved as predicted by theory. This can be explained by the continuous density of states, rather than a discrete DOS, due to the size fluctuations of the QDs. Better characteristic temperatures from these QD lasers can be expected if ground state lasing is achieved and the excited states cannot be thermally populated.

Rayleigh scattering limits on the performance of QD lasers have been investigated. Rayleigh scattering can only account for a small part of the high loss measured in the QD lasers. If the QDs are kept below about 8 nm in radius then Rayleigh scattering will not be a contributing factor to the loss in QD lasers.

Chapter 7: Conclusions

7.1 Introduction

The previous chapters demonstrated that alternating molecular beam epitaxy (AMBE) can be used to form quantum dots via the Stranski-Krastanow growth transition. During AMBE, In segregation was shown to be very important for quantum dot formation. These quantum dots have been extensively characterized, and optical properties have been correlated with structural properties.

Quantum dot lasers have been fabricated and characterized. Perhaps the most important general result of this dissertation is that quantum dot lasers can be grown almost as easily as can quantum well lasers. The ease of fabrication has led to several different groups investigating the properties of these quantum dot lasers. These quantum dot lasers have threshold current densities that are comparable to the threshold current densities obtained in quantum well lasers, despite the fact that research on quantum dot lasers is only a few years old.

More specific results include the first comparison of a quantum dot laser to a quantum well laser with an active region that is comprised of a single quantum well that has a thickness just equal to the thickness of the Stranski-Krastanow wetting layer. The large difference in lasing transition energies between the quantum dot lasers and this particular quantum well laser provides unambiguous evidence that the lasing in the quantum dots is associated with quantum dot states, as compared to wetting layer states. Finally, the relative temperature-independence of the lasing wavelength and the variation of lasing wavelength with laser length of the quantum

dot laser suggest not only new physics, but also new functionality that is not obtainable with a quantum well laser.

Preliminary calculations of gain in the quantum dots have been performed. These gain calculations are carried out in a similar fashion to quantum well laser gain calculations, where the excited states of the quantum well and the barriers are included in determining the position of the quasi-Fermi level. The excited states of the quantum dots and the degeneracy of these states is used to determine the position of the quasi-Fermi level in the quantum dots. These calculations are the first of their kind for a quantum dot laser.

Limitations on the performance of quantum dot lasers due to Rayleigh scattering by the dots have been analyzed for the first time. Although only a simplified, single particle scattering theory has been applied, clear trends have been established. The high loss in the quantum dot lasers studied in this dissertation cannot be attributed to Rayleigh scattering, but it is likely that Rayleigh scattering losses will become a limit if the quantum dot density gets much larger than is currently available, or if shorter wavelength lasers are fabricated.

7.2 Future Work

The demonstration by others of the three-dimensional confinement of Stranski-Krastanow-grown quantum dots has opened the door to a very simple technique to study the physics of both individual quantum dots and arrays of quantum dots. Extensive research in this area has only been in progress since about 1993 (Leonard *et al.*, 1993, Moison *et al.*, 1994) but already quantum dot devices, especially lasers, have been demonstrated that are approaching the best results

obtained by quantum well devices, which have been investigated for about 20 years.

In the area of crystal growth, the uniformity issue still needs more extensive research. The quantum dots demonstrated in this dissertation, as well as in the research of all others in this area, show variations of about +/- 10% in height. This is not nearly as good as can be achieved with a quantum well. This size distribution is the cause of the inhomogeneously broadened PL linewidths at low temperatures. Improvements in the size distribution should lead quantum dot lasers with improved performance compared to quantum well lasers.

The electronic structure of the quantum dots needs to be computed in order to better understand the optical properties of these quantum dots. This involves using the RHEED, AFM, and TEM information to calculate the band structure of the dots, and using finite element modeling to compute the strain distribution in the quantum dot and the surrounding barrier material. This information can then be used to calculate more detailed information about the gain in the quantum dot lasers.

The area of quantum dot lasers is very promising. Although the threshold currents are still higher than quantum well lasers, quantum dot lasers are only a couple of years old right now. As refinements in the growth of the dots occur, new lasers will benefit.

Early work in this dissertation was devoted to obtaining 1.3 μm room temperature emission from the quantum dots. Although not discussed in this dissertation, room temperature-operating lasers were fabricated using these quantum dots as the active region. However, the threshold currents were higher than those obtained using the smaller dots, and the lasing emission was also from excited states. Nonetheless, this is such an important practical application for quantum dots lasers that more research should be devoted to this area. Current state-of-the art 1.3 μm

lasers are all grown on InP substrates. However, there are several reasons why it would be advantageous to use GaAs substrates instead of InP substrates. First of all, the conduction band offset in the InGaAsP/InP system is small compared to InGaAs/GaAs; the result is that InP-based lasers have characteristic temperatures of 60-70 K, whereas GaAs-based lasers have characteristic temperatures of 150-250 K. Second, production quantities of 4 inch GaAs wafers are currently available, and 6 inch wafers are available in small quantities, with production quantities available in 1997. InP is only available in 3 inch wafers, so it requires many more wafers of InP to yield the same quantity of devices as compared to GaAs. And third, InP is much more fragile than GaAs, which translates into lower yields because of breakage, as well as increased sensitivity to defects.

One area that was not explored in this dissertation but has recently been investigated by others (Bimberg *et al.*, 1996, Xie *et al.*, 1996, Saito, Nishi, and Suguo, 1996) is that of quantum dot lasers with multiple layers of quantum dots as the active region. The results from these lasers are very interesting, although it is not clear in all cases if the dot layers are coupled, or even completely buried by the overlying GaAs.

Another interesting area for research is in QD vertical cavity lasers (QDVCLs) (Saito, Nishi, and Suguo, 1996). In the case of a VCL, the cavity mode spacing is very large compared to in-plane lasers. If the cavity resonance is chosen to line up with the ground state transition in the quantum dots, but there is not enough gain at the ground state transition to overcome all the losses, then this device will probably never lase. Driving additional current just serves to populate excited states that are not aligned to the cavity mode. If the cavity is short (just a few λ or less), then the device will never lase.

For example, suppose the cavity is chosen to be a 1 λ cavity at 1000 nm. If the gain from the quantum dots at 1000 nm saturates before lasing is achieved, then the next available state in the cavity is at 500 nm (a 2 λcavity). However, if the cavity is chosen to be 10 λat 1000 nm, then it is 11 λat 909 nm. Given the range of emission seen from the quantum dots so far, it is reasonable to assume that there will be enough gain to get lasing emission at both these wavelengths, given a properly designed active region.

As far as the quantum dot lasers described in this dissertation are concerned, it would be interesting to study the spectral properties of these lasers in a single-mode waveguide configuration, with CW operation. This will further our understanding of the unusual spectral characteristics that are observed from the broad-area lasers. One area that is particularly interesting here is to measure the mode-suppression ratio (MSR) of these lasers. Kirstaedter *et al.*, 1994 reported single longitudinal mode operation with a MSR of 6 dB at 77 K. However, this device had a multimode waveguide (20 μm wide), and no other reports have followed this initial one.

7.3 Summary

Several new results on the growth and characterization of InGaAs quantum dots and quantum dot lasers have been presented in this dissertation. Many of these results, particularly the 1.3 μm emission and the temperature-dependence and length-dependence of the lasing wavelength, are likely to lead to technological breakthroughs in the next few years. The ease of fabrication of these quantum dot lasers suggests that they can compete with quantum well lasers if the performance improves. Additionally, the quantum dot lasers offer new functionality that is unobtainable with

quantum well lasers. There is plenty of future work to be done in this area, and quantum dot lasers are going to have a very bright future.

Appendix A: Growth Log

A.1 Introduction

This appendix contains detailed descriptions of the molecular beam epitaxy (MBE) growth conditions used for each sample described in this dissertation. Samples are grouped according to the various purposes for which they are grown, i.e., photoluminescence, atomic force microscopy, X-ray, lasers, etc. The tables contain lists of similar samples, with relevant differences between samples also given in the table. Similarities between the samples are given in the text accompanying each table.

All of the samples described here are grown in a Varian Modular Gen II MBE machine. This MBE machine is commercially available, and no important major modifications have been done to it. The substrate temperature is measured with an infrared pyrometer. The arsenic source is a valved cracking cell capable of producing As_4 or As_2. All samples are grown with As_2. The valve can be used to accurately control the amount of As_2 delivered to the sample.

The growth rate of GaAs and InAs is measured with reflection high energy electron diffraction (RHEED) oscillations. The InAs growth rate is measured on an InAs sample, and the growth rate is then converted to the growth rate on GaAs.

The As_2 flux is measured two ways. The first is by a nude ion gauge in the growth position. This gives a value called the beam equivalent pressure (BEP). In addition, arsenic uptake oscillations are on a Ga-saturated GaAs surface at ~500°C (Neave, Joyce, and Dobson, 1984). First, GaAs is grown at about 580°C and annealed in an As_2 flux to ensure a smooth starting surface. Then the substrate is

cooled to ~500°C in an As_2 flux. The arsenic shutter is then closed, and the Ga shutter is opened. The RHEED specular spot intensity immediately begins to decrease, and the surface reconstruction also changes. After about 6 monolayers (MLs) of Ga have been deposited, the arsenic shutter is once again opened; the Ga shutter remains open the entire time. The intensity of the specular spot oscillates, similar what is observed during the more-familiar Ga-induced RHEED oscillations. Once the excess Ga has been consumed, the period of the oscillations changes to correspond to the Ga arrival rate at the surface.

A.2 Photoluminescence Samples

The layer diagram for QDPL-02, -03, and -08 to -22 (the single InGaAs epilayer samples) is shown in Figure A-1, and the layer diagram for QDPL-01, -04 to -07 (the multiple InGaAs epilayer samples) is shown in Figure A-2. The GaAs buffer layers and the $Al_{.4}Ga_{.6}As$/GaAs superlattice are grown at a substrate temperature of 590-600°C. The InGaAs epilayers are all grown at 515°C, except for QDPL-03, which is grown at 485°C. The arsenic species is As_2 with a BEP of about 9.0×10^{-6} Torr, which corresponds to an As arrival rate of about 2.0 MLs/second. The growth rates of GaAs and InAs for each sample are given in Table A-1.

The $In_xGa_{1-x}As$ epilayers are grown by alternating molecular beams of In, As_2, Ga, and As_2. The amount of In and Ga deposited during each cycle is given in Table A-1. The amount of As deposited is 2.0 monolayers after the In deposition and 6.0 monolayers after the Ga deposition. There is also a three second growth pause, without an arsenic flux incident on the surface, after the Ga is deposited but before the 6.0 monolayers of arsenic are deposited. This cycle is repeated in order to obtain

the desired thickness. The number of repetitions for each sample is given in Table A-1.

Table A-1

Sample Name	Sample Number	Nominal Structure	Sequence	GaAs Growth Rate (MLs/sec)	InAs Growth Rate (MLs/sec)
QDPL-01	940715D	4X (6.3 nm $In_{.15}Ga_{.85}As$)	22X (.15 MLs In/.85 MLs Ga)	0.62	0.23
QDPL-02	940727A	5.5 nm $In_{.17}Ga_{.83}As$	22X (.15 MLs In/.74 MLs Ga)	0.54	0.21
QDPL-03*	940727B	5.5 nm $In_{.17}Ga_{.83}As$	22X (.15 MLs In/.74 MLs Ga)	0.54	0.21
QDPL-04	940808A	2X (6.2 nm $In_{.15}Ga_{.85}As$)	22X (.15 MLs In/.85 MLs Ga)	0.54	0.24
QDPL-05	940808E	3X (6.2 nm $In_{.19}Ga_{.81}As$)	22X (.17 MLs In/.74 MLs Ga)	0.54	0.24
QDPL-06	940808G	2X (6.2 nm $In_{.19}Ga_{.81}As$)	22X (.17 MLs In/.74 MLs Ga)	0.54	0.24
QDPL-07	940808H	5X (6.2 nm $In_{.19}Ga_{.81}As$)	22X (.17 MLs In/.74 MLs Ga)	0.54	0.24
QDPL-08	940819B	12.7 nm $In_{.15}Ga_{.85}As$	45X (.15 MLs In/.85 MLs Ga)	0.51	0.22
QDPL-09	940819C	14.1 nm $In_{.15}Ga_{.85}As$	50X (.15 MLs In/.85 MLs Ga)	0.51	0.22
QDPL-10	940821A	17.0 nm $In_{.15}Ga_{.85}As$	60X (.15 MLs In/.85 MLs Ga)	0.51	0.22
QDPL-11	940821B	19.8 nm $In_{.15}Ga_{.85}As$	70X (.15 MLs In/.85 MLs Ga)	0.51	0.22
QDPL-12	940821C	22.6 nm $In_{.15}Ga_{.85}As$	80X (.15 MLs In/.85 MLs Ga)	0.51	0.22
QDPL-13	940821D	11.6 nm $In_{.19}Ga_{.81}As$	45X (.17 MLs In/.74 MLs Ga)	0.51	0.22
QDPL-14	940823D	14.2 nm $In_{.19}Ga_{.81}As$	55X (.17 MLs In/.74 MLs Ga)	0.52	0.22
QDPL-15	940823E	16.7 nm $In_{.19}Ga_{.81}As$	65X (.17 MLs In/.74 MLs Ga)	0.52	0.22
QDPL-16	940823F	12.1 nm $In_{.22}Ga_{.78}As$	45X (.21 MLs In/.74 MLs Ga)	0.52	0.22
QDPL-17	940829A	10.8 nm $In_{.22}Ga_{.78}As$	40X (.21 MLs In/.74 MLs Ga)	0.62	0.22
QDPL-18	940829B	9.4 nm $In_{.22}Ga_{.78}As$	35X (.21 MLs In/.74 MLs Ga)	0.62	0.22
QDPL-19	940829D	8.8 nm $In_{.30}Ga_{.70}As$	35X (.265 MLs In/.62 MLs Ga)	0.62	0.22

QDPL-20	940901D	6.3 nm $In_{.30}Ga_{.70}As$	25X (.265 MLs In/.62 MLs Ga)	0.62	0.22
QDPL-21	941011B	6.3 nm $In_{.30}Ga_{.70}As$	25X (.265 MLs In/.62 MLs Ga)	0.62	0.21
QDPL-22	941011D	5.0 nm $In_{.30}Ga_{.70}As$	20X (.265 MLs In/.62 MLs Ga)	0.62	0.21
QDPL-23	950912C	5.0 nm $In_{.30}Ga_{.70}As$	20X (.265 MLs In/.62 MLs Ga)	0.62	0.21

*This sample was grown at 490°C.

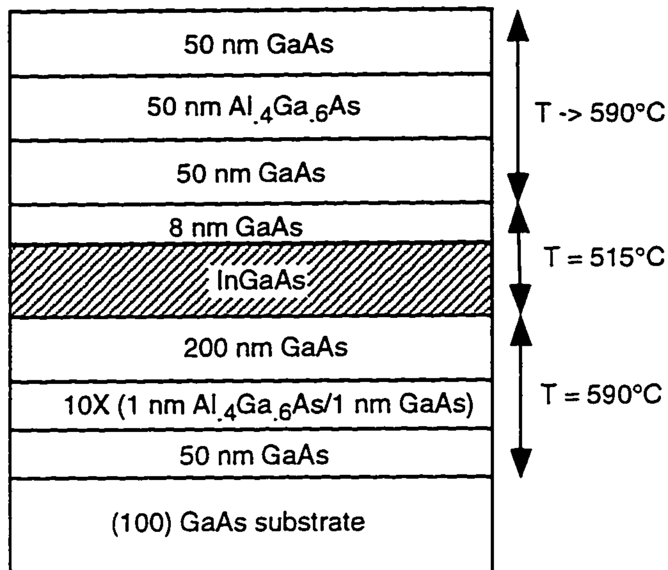

Figure A-1: Layer diagram for QDPL-02, -03, and -08 to -22. The nominal InGaAs composition and thickness for each sample is given in Table A-1. The substrate temperature is ramped to 590°C during the deposition of the 50 nm GaAs epilayer that is adjacent to the 8 nm GaAs epilayer grown at 515°C.

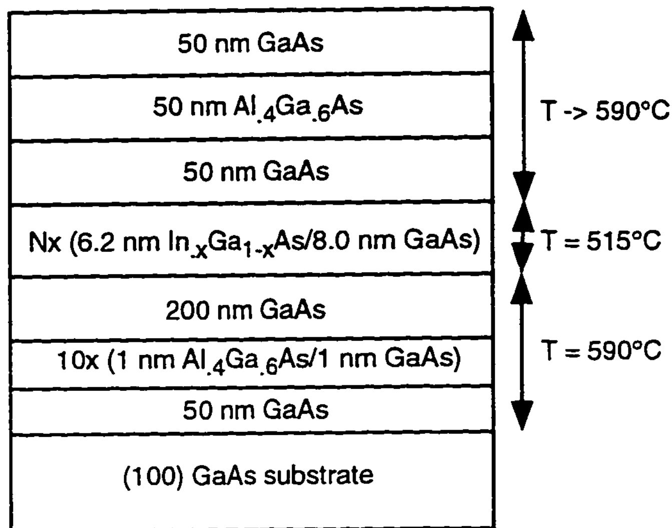

Figure A-2 Layer diagram for QDPL-01, 04, -05, -06, and -07. The composition and number of InGaAs layers varies. The values for each sample are given in Table A-1.

A.3 Photoluminescence Reference Samples

Table A-2 describes the quantum well reference samples grown to check the material quality and give standards to compare to the quantum dots samples. The quantum well samples have the same epilayer design as the quantum dot samples (see Figure A-1).

Table A-2

Sample Name	Sample Number	Quantum Well
QDPLCTRL-01	940829C	9.3 nm $In_{.26}Ga_{.74}As$
QDPLCTRL-02	941011A	9.3 nm $In_{.25}Ga_{.75}As$
QDPLCTRL-03	950921C	6.5 nm $In_{.21}Ga_{.79}As$

A.4 Overgrowth Samples

Table A-3 describes the samples grown to optimize the thickness of GaAs grown at the low temperature at which the InGaAs islands are formed. The layer diagram for the samples is shown in Figure A-3. The GaAs and InAs growth rates are about 0.93 MLs/second and 0.22 MLs/sec. The substrate temperature during the growth of the InGaAs epilayer is 515°C. The As_2 BEP is 9.0 x 10^{-6} Torr, equivalent to a growth rate of 2.0 MLs/second.

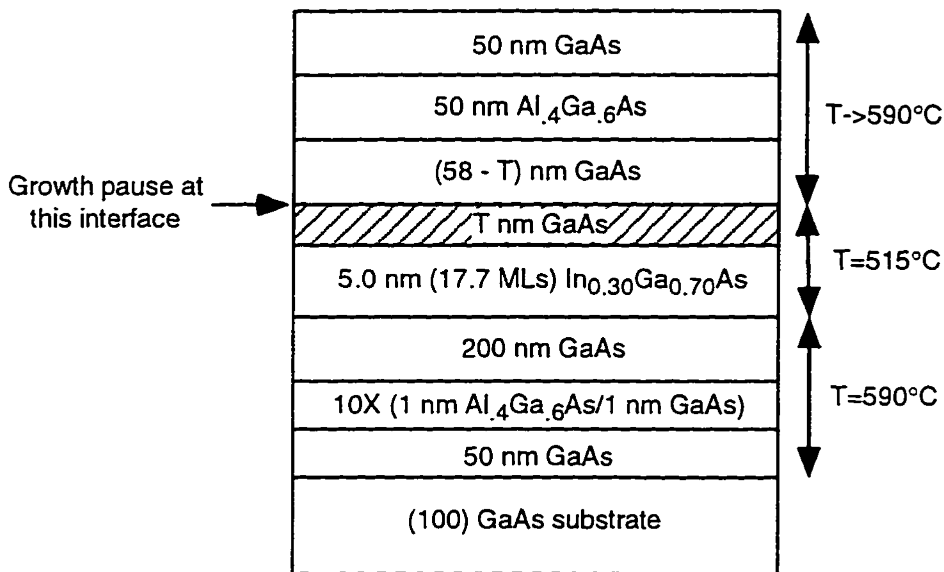

Figure A-3: Layer diagram for QDPLOVG-X. The value of T for each sample is given in Table A-3. After the growth pause, deposition is continued after the temperature reaches 570°C.

Table A-3

Sample Name	Sample Number	Nominal Structure	Sequence	Low Temp. Overgrowth (nm)
QDPLOVG-01*	950630B	5.0 nm $In_{.3}Ga_{.7}As$	20X (.265 MLs In/.62 MLs Ga)	8.0
QDPLOVG-02	950702B	5.0 nm $In_{.3}Ga_{.7}As$	20X (.265 MLs In/.62 MLs Ga)	8.0
QDPLOVG-03*	950807A	6.3 nm $In_{.3}Ga_{.7}As$	25X (.265 MLs In/.62 MLs Ga)	8.0
QDPLOVG-04	950807B	6.3 nm $In_{.3}Ga_{.7}As$	25X (.265 MLs In/.62 MLs Ga)	8.0
QDPLOVG-05	950807C	2X (6.3 nm $In_{.3}Ga_{.7}As$)	25X (.265 MLs In/.62 MLs Ga)	8.0
QDPLOVG-06	950817A	5.0 nm $In_{.3}Ga_{.7}As$	20X (.265 MLs In/.62 MLs Ga)	12.0
QDPLOVG-07	950817C	5.0 nm $In_{.3}Ga_{.7}As$	20X (.265 MLs In/.62 MLs Ga)	6.0
QDPLOVG-08	950817D	5.0 nm $In_{.3}Ga_{.7}As$	20X (.265 MLs In/.62 MLs Ga)	3.0
QDPLOVG-09	950823C	5.0 nm $In_{.3}Ga_{.7}As$	20X (.265 MLs In/.62 MLs Ga)	4.5
QDPLOVG-10	950823D	5.0 nm $In_{.3}Ga_{.7}As$	20X (.265 MLs In/.62 MLs Ga)	6.0
QDPLOVG-11	950823E	5.0 nm $In_{.3}Ga_{.7}As$	20X (.265 MLs In/.62 MLs Ga)	7.5
QDPLOVG-12	950823F	5.0 nm $In_{.3}Ga_{.7}As$	20X (.265 MLs In/.62 MLs Ga)	9.0

*Continuous growth of GaAs overgrowth layer

A-5 Smaller Dots

Table A-4 describes all samples that are grown for investigating the smaller dots, with shorter wavelength emission. The arsenic species is As_2 with a BEP of 9.0×10^{-6} Torr, equivalent to a growth rate of about 2.0 monolayers/second. The growth rate of Ga and In are about 0.96 and 0.25 MLs/second, respectively. The substrate temperature during the growth of the InGaAs epilayer is 515°C. The subsequent 8.0 nm of GaAs are also deposited at 515°C. The sample temperature is then raised to 570°C and the growth is continued as the temperature is increased to 590°C. For the samples with multiple layers of InGaAs, the temperature is decreased to 515°C for the growth of each InGaAs layer, and then the cycle is repeated.

The deposition cycle of the InGaAs is as follows: 0.265 MLs of In, 2.0 MLs

of As, 0.62 MLs of Ga, 3.0 second growth pause, and 6.0 MLs of As. This cycle is repeated 15 times, for a total deposited thickness of 13.3 MLs of $In_{0.3}Ga_{0.7}As$. Samples QDPLS-01 and -03 have only a single layer of InGaAs (Figure A-4), and QDPLS-02, -04, and -05 have 2, 3, and 5 layers of InGaAs (Figure A-5), respectively.

Table A-4

Sample Name	Sample Number	Nominal Structure
QDPLS-01	960122C	3.8 nm $In_{.3}Ga_{.7}As$
QDPLS-02	960122D	2X (3.8 nm $In_{.3}Ga_{.7}As$/25 nm GaAs)
QDPLS-03	960201C	3.8 nm $In_{.3}Ga_{.7}As$
QDPLS-04	960201D	3X (3.8 nm $In_{.3}Ga_{.7}As$/25 nm GaAs)
QDPLS-05	960201E	5X (3.8 nm $In_{.3}Ga_{.7}As$/25 nm GaAs)

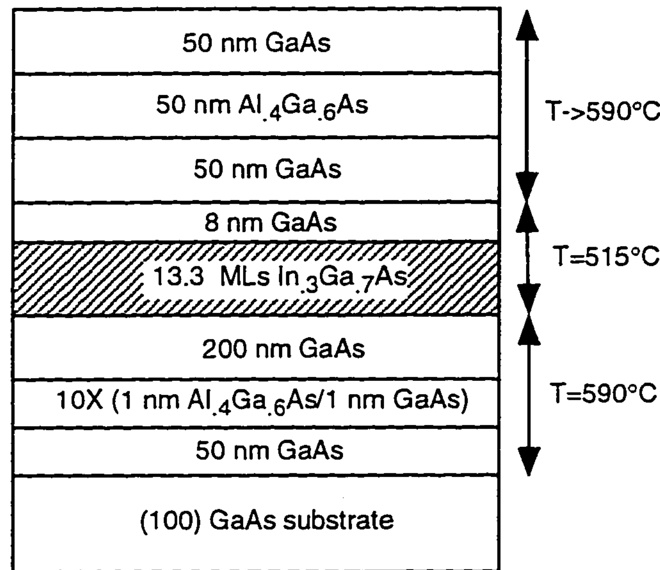

Figure A-4: Layer diagram for QDPLS-01 and -03.

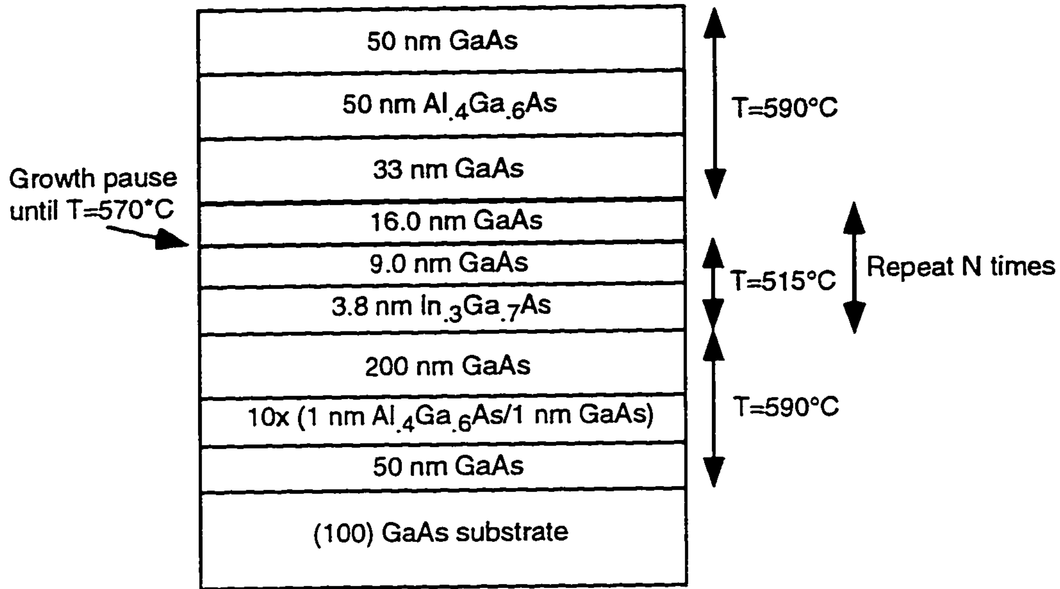

Figure A-5 Layer diagram for QDPLS-02, -04, and -05. N is 2, 3, and 5 for the three samples, respectively.

A.6 Growth Temperature Optimization Samples

Table A-5 describes all of the samples grown for optimization of the substrate temperature during growth (QDPLT-0X). All of the samples have the layer sequence shown in Figure A-6. The substrate temperature is 590-600°C for the growth of the GaAs buffer layer. The arsenic species is As_2 with a growth rate of about 2.0 monolayers/second. The growth rate of Ga and In are about 0.87 and 0.24 MLs/second, respectively. The deposition cycle is as follows: 0.265 MLs of In, 2.0 MLs of As, 0.62 MLs of Ga, 3.0 second growth pause, and 6.0 MLs of As. This cycle is repeated 20 times, for a total deposited thickness of 17.7 MLs of $In_{0.3}Ga_{0.7}As$. The first 7.5 nm of the GaAs overgrowth are deposited at the same temperature at which the $In_{0.3}Ga_{0.7}As$ is deposited. Then there is a growth pause under As_2 flux while the temperature is raised to 570°C. The remaining capping

layers are then deposited as the temperature is raised from 570°C to 590°C.

Table A-5

Sample Name	Sample Number	Substrate Temperature (°C)
QDPLT-01	950828A	510
QDPLT-02	950828B	480
QDPLT-03	950828C	450
QDPLT-04	950828D	420
QDPLT-05	950912C	515
QDPLT-05	950912D	540

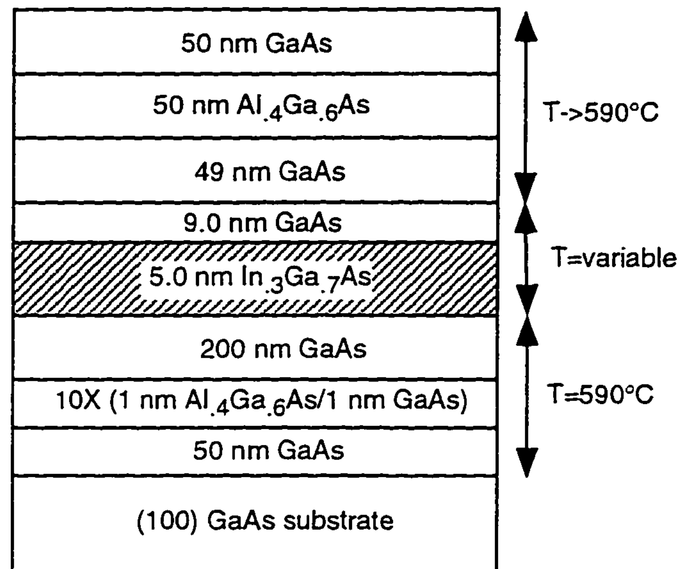

Figure A-6 Layer diagram for QDPLT-01 to -06.

A.7 X-ray Samples

The layer diagram for the samples grown for high resolution X-ray diffraction (HRXRD) is shown in Figure A-7. These samples are very simple so that X-ray simulations can be matched to the experimental results. The GaAs growth rate is

0.925 MLs/s, and the InAs growth rate is 0.182 MLs/s. The As_2 BEP is 9.0 x 10^{-6} Torr. The GaAs buffer layer is grown at a substrate temperature of about 600°C, and then the substrate temperature is lowered to 515°C for the growth of the InGaAs layer and the first 8.0 nm of the GaAs cap layer. Next, there is a growth pause while the substrate temperature is ramped to 570°C. The remaining 50.0 nm of the GaAs cap layer are then deposited as the temperature is increased from 570°C to about 600°C. All of the GaAs layers are grown with conventional MBE, and the InGaAs layers are grown with AMBE, using the same shutter sequence described in section A.6. See Table A-6 below for the nominal InGaAs epilayer thicknesses.

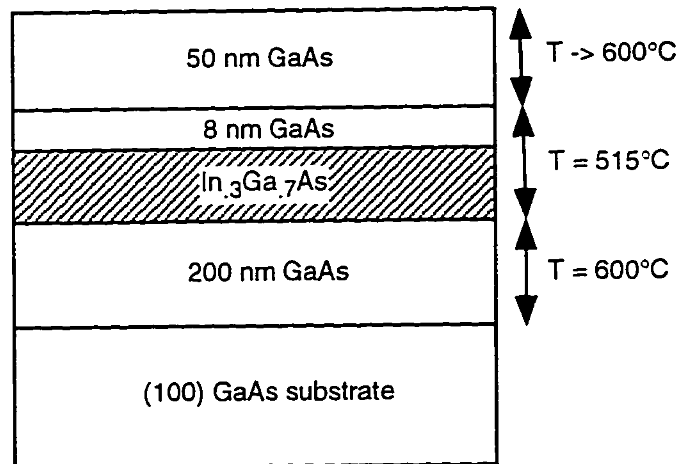

Figure A-7 Layer diagram for QDXRAY-01, -02, and -03.

Table A-6

Sample Name	Sample Number	Nominal InGaAs Thickness (MLs)
QDXRAY-01	960306A	13.3
QDXRAY-02	960306B	17.7
QDXRAY-03	960306C	7.1

A.8 Atomic Force Microscopy Samples

The samples grown for characterization by atomic force microscopy (AFM) are described in Table A-7 and Figure A-8. The GaAs growth rate is around 0.95 MLs/s, and the InAs growth rate is about 0.20 MLs/s. The As_2 BEP is 9.0 x 10^{-6} Torr. The InGaAs is grown with the same AMBE shutter sequence described in section A.6.

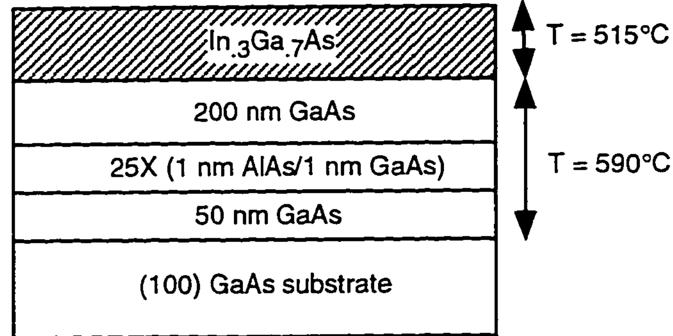

Figure A-8 Layer diagram for QDAFM-01 to -08.

Table A-7

Sample Name	Sample Number	Nominal InGaAs Thickness (MLs)
QDAFM-01	941011C	22.1
QDAFM-02	950629A	0.0
QDAFM-03	950629E	3.5
QDAFM-04	950629B	6.2
QDAFM-05	950526A	7.1
QDAFM-06	950526B	8.0
QDAFM-07	950629C	13.3
QDAFM-08	950629E	17.7

Appendix B: AFM Analysis

This appendix contains the computer program used to analyze the atomic force microscope (AFM) images that are shown in Chapter 4 of this dissertation. The input file format is a Digital Instruments AFM image file. This includes an 8192 byte header that contains information needed for computing heights and widths. The remainder of the input file is 16 bit, 2's complement data for each pixel.

```
/* Richard Mirin 11/29/94
   UC Santa Barbara
   Santa Barbra, CA 93106
   (805) 893-4883
   mirin@nemesis.ece.ucsb.edu

   Image Processing for Quantum Dots
   last modified 1/10/96
                                  */


#include <stdio.h>
#include <string.h>     /* need this to use strcpy() */
#include <fcntl.h>      /* need this for read,write,creat and open */

/* Define external variables */

int SIZE;               /* image size, as read from header */
char text[8192];        /* contains the image file header */
short int *newimage;    /* contains the image after the low pass filter, 16 bit signed */
struct pxl{             /* contains the locations of all maxima */
        struct pxl *next;
        int x;
        int y;
}*pixel;
short int *deltax,*deltay,*laplacex,*laplacey;
double zsens,zmax;              /* zsens,zmax,zscale, and zatten are AFM parameters
needed to compute the height */
int zscale,zatten;
int SCAN;               /* Scan size read from header, needed for area computation */

int readHeader();
void lowpass();
int findmax();
void histogram();
double afm_height();
double ref_level();

main(argc, argv)
int argc;               /* number of command line arguments */
char *argv[];           /* name of command line arguments */

{
        char outputname[20]; /* output file name */
        char inputname[20];  /* input file name */

        extern int SIZE;        /* AFM image is SIZE x SIZE */
        extern char text[];     /* contains the image file header */
        extern short int *newimage;   /* the low pass filtered image */
```

```
	extern struct pxl *pixel;			/* the location in newimage of each
local maximum */
	extern short int *deltax, *deltay,		/* height difference between
adjacent pixels */
	   *laplacex, *laplacey;		/* difference in derivatives */

	int i,j;		/* counters */

	/*
&&&&&&&&&&&&&&&&&&&&&&&&&&&&&&&&&&&&&&&&&&&&&&&&
&&&&&&&&&&&&&&&&&&&&&&&& */

	if (argc != 3){
		printf("usage: process inputfile outputfile\n");
		exit (1);
	}
	else{
		strcpy(inputname,argv[1]);
		strcpy(outputname,argv[2]);
	}

	/* Read in header and assign image size to SIZE */
	printf("Image size is %i\n",SIZE=readHeader(inputname));

	/* Allocate memory for external arrays */
	if ( (newimage = calloc(SIZE*SIZE,sizeof(short int))) ==NULL){
		printf("Can't allocate memory for newimage!\n");
		exit(1);
	}
	if ( (deltax = calloc((SIZE-1)*(SIZE-1),sizeof(short int))) ==NULL){
		printf("Can't allocate memory for deltax!\n");
		exit(1);
	}
	if ( (deltay = calloc((SIZE-1)*(SIZE-1),sizeof(short int))) ==NULL){
		printf("Can't allocate memory for deltay!\n");
		exit(1);
	}
	if ( (laplacex = calloc((SIZE-1)*(SIZE-1),sizeof(short int))) ==NULL){
		printf("Can't allocate memory for laplacex!\n");
		exit(1);
	}
	if ( (laplacey = calloc((SIZE-1)*(SIZE-1),sizeof(short int))) ==NULL){
		printf("Can't allocate memory for laplacey!\n");
		exit(1);
	}

	lowpass(inputname,outputname);
	printf("%i dots found\n",findmax(outputname));
	histogram(outputname);
```

```
}

****************************************

#include <stdio.h>
#include <math.h>      /* need this for pow(i,j) */
#include <string.h>    /* need this to use strcpy() */
#include <fcntl.h>     /* need this for read,write,creat and open */


/* Modified on 2/10/96 by Rich Mirin */


int readHeader (inputname) /* Read in the header from the file-it is 8192 bytes  */
char inputname[20];
{
        FILE *fp;
        extern char text[]; /* the array text[] stores the 8 kbyte header */
        int i=0;
        int j=0;
        int k=0;
        int temp;
        int slash=0;
        int decimal=0;             /* boolean to indicate whether a number contains a
decimal point */
        extern double zsens,zmax,SCAN,zscale;
        extern int zatten;

        zsens=0.0;zmax=0.0;zscale=0.0;zatten=0;
        fp = fopen(inputname, "r");

        /* Read all header info into text[] */
        for (i=0; i<8192; i++)
                text[i]=fgetc(fp);
        fclose (fp);

        /* get parameters for height computation */
        while (slash!=19){  /* Z attenuation is the 19th line (TMAFM/Matls), 20th
line for contact mode */
                if (text[i] == '\\') slash++;
                i++;
        } /* i is the position in the header of the 'Z' */
        if ((text[i]=='Z') && (text[i+1]==' ') && (text[i+2]=='a')){ /* Z attenuation
*/
```

```
		while (text[i+10+j] != 0x0a){ /* find the end of the number and mark
the decimal point*/
			if (text[i+10+j] == ".")
				decimal=1;
			else
				zatten+=(int) ((text[i+10+j]-'0')*pow(10.0,(double) 4-
j+decimal));
			j++;
		}
		printf("Z attenuation=%i\n",zatten);
		if ((zatten > 65536.0) || (zatten < 16384.0)){ /* bad value for zatten
read in */
			printf("Z attenuation is out of range!\n");
			exit(1);
		}
	}
	else {printf("Can't find Z attenuation!\n");exit(1);}

/*Z sensitivity */
	slash=0;i=0;j=0;decimal=0;
	while (slash != 3){ /* Find the 3rd occurence of '\*' */
		if ((text[i] == '\\') && (text[i+1] == '*')) slash++;
		i++;
	}
	while (!((text[i]=='Z') && (text[i+1]==' ') && (text[i+2]=='s') &&
(text[i+3]=='e') && (i<8192))){ /* Z sensitivity */
		i++;
	}
	if (i==8192){ /* Unable to find Z sensitivity in parameter list */
		printf("Can't find Z sensitivity!\n");
		exit(1);
	}

	while (text[i+15+j] != 0x0a){ /* find the end of the number and mark the
decimal point*/
			if (text[i+15+j] == 0x2e){ /* decimal point */
				decimal=j;
				j++;
			}
			else
				j++;
		}
		if (decimal==0) decimal=j;
		j--;
		while (j>=0) { /* add up the number */
			if (j>decimal) /* then the number is to the right of the decimal
point */
				zsens += pow(10.0,(double) (decimal-j)) *
(text[i+15+j] - '0');
```

```
                    else if (j<decimal) /* to the left of the decimal point */
                            zsens += pow(10.0,(double) (decimal-j-1)) *
(text[i+15+j] - '0');
                    j--;
            }
            printf("Z sensitivity=%f\n",zsens);
/* Z sensitivity */

/* Z max*/
        slash=0;i=0;j=0;decimal=0;
        while (slash != 4){ /* Find the 4th occurence of '\*' */
                if ((text[i] == '\\') && (text[i+1] == '*')) slash++;
                i++;
        }
        while (!((text[i]=='Z') && (text[i+4]=='x') && (i<8192))){ /* Z max */
                i++;
        }
        if (i==8192){ /* Unable to find Z max in parameter list */
                printf("Can't find Z max!\n");
                exit(1);
        }
        while (text[i+7+j] != 0x0a){ /* find the end of the number and mark the
decimal point*/
                if (text[i+7+j] == 0x2e){ /* decimal point */
                        decimal=j;
                        j++;
                }
                else
                        j++;
        }
        if (decimal==0) decimal=j;
        j--;
        while (j>=0) { /* add up the number */
                if (j>decimal) /* then the number is to the right of the decimal point */
                        zmax += pow(10.0,(double) (decimal-j)) * (text[i+7+j] - '0');
                else if (j<decimal) /* to the left of the decimal point */
                        zmax += pow(10.0,(double) (decimal-j-1)) * (text[i+7+j] -
'0');
                j--;
        }
        printf("Z max=%f\n",zmax);
/* Z max */

/* Z scale height */
        slash=0;i=0;j=0;k=0;decimal=0;
        while (slash!=109){  /* Z scale height is the 115th (cleanroom AFM) or 120th
(Materials AFM) or 109th (TM) line */
                if (text[i] == '\\') slash++;
                i++;
```

```
	} /* i is the position in the header of the 'Z' */
	if ((text[i]=='Z') && (text[i+1]==' ') && (text[i+2]=='s') &&
(text[i+3]=='c')){ /* Z scale height */
		while (text[i+16+j] != 0x0a){ /* find the end of the number and mark
the decimal point*/
			if (text[i+16+j] == 0x2e){ /* decimal point */
				decimal=j;
				j++;
			}
			else
				j++;
		}
		if (decimal==0) decimal=j;
		j--;
		while (j>=0) { /* add up the number */
			if (j>decimal) /* then the number is to the right of the decimal
point */
				zscale += pow(10.0,(double) (decimal-j)) *
(text[i+16+j] - '0');
			else if (j<decimal) /* to the left of the decimal point */
				zscale += pow(10.0,(double) (decimal-j-1)) *
(text[i+16+j] - '0');
			j--;
		}
		printf("Z scale height=%f\n",zscale);
	}
	else {printf("Can't find Z scale height!\n");exit(1);}
/* Z scale height */

/* Scan size*/
	slash=0;i=0;j=0;k=0;temp=0;SCAN=0;decimal=0;
	while (slash!=105){ /* Scan size is the 111th (cleanroom AFM) or
116th(Materials AFM) or 105th(TM) line */
		if (text[i] == '\\') slash++;
		i++;
	} /* i is the position in the header of the 'S' */
	if ((text[i]=='S') && (text[i+1]=='c') && (text[i+2]=='a') &&
(text[i+3]=='n')){ /* Scan size */
		while (text[i+11+j] != ' '){ /* find the end of the number and mark the
decimal point*/
			if (text[i+11+j] == 0x2e){ /* decimal point */
				decimal=j;
				j++;
			}
			else
				j++;
		}
		if (decimal==0) decimal=j;
		j--;
```

```
		while (j>=0) { /* add up the number */
			if (j>decimal) /* then the number is to the right of the decimal
point */
				SCAN += pow(10.0,(double) (decimal-j)) *
(text[i+11+j] - '0');
			else if (j<decimal) /* to the left of the decimal point */
				SCAN += pow(10.0,(double) (decimal-j-1)) *
(text[i+11+j] - '0');
			j--;
		}
		printf("Scan size= %f nm\n",SCAN);
	}
	else {printf("Can't find Scan size!\n");exit(1);}
/* Scan size*/

	i=0x8a0;
	j=0;
	while ((i<0xb00) && (j==0)){
		if ((text[i]=='S') && (text[i+4]=='s')) /* Matches "Samps/line"
uniquely */
			j=i;
		else i++;
	}
	if (j==0) {printf("Can't find the image size in header!\n");exit(1);}
	switch (text[j+12]){ /* This header byte contains the first number
				of the size of the image */
		case '5':i=512;break;
		case '2':i=256;break;
		case '1':i=128;break;
		default:
			printf("Image size in header is wrong!\n");
			exit(1);
	}
	return(i);
}


****************************************
#include <stdio.h>
#include <string.h>	/* need this to use strcpy() */
#include <fcntl.h>	/* need this for read,write,creat and open */


void lowpass (inputname,outputname) /* Read in the image file, low pass filter it,
and save the filtered image */
char inputname[20],outputname[20];

{
```

```
	FILE *fd;	/* file descriptor for data file */
	int i,j;  /* counters */
	short int *image;	/* the unfiltered raw image (binary) */
	extern short int *newimage;	/* the low pass filtered image, 16 bit signed */
	extern char text[];
	extern int SIZE;
	unsigned char temp;
	float tmp;

	if ( (image = calloc(SIZE*SIZE,sizeof(short int))) == NULL){
		printf("Can't allocate memory for image!\n");
		exit(1);
	}

	/* Header read in, now read in the data (16 bit binary,
	   2's complement	*/
	fd = fopen(inputname,"r");		/* open for read */
	fseek(fd,8192,0);			/* skip the header */
	printf("%i\n",fread(image,sizeof(short int),(SIZE*SIZE),fd));		/* read in
the data as short int */
	fclose (fd);						/* even though MSB
and LSB are reversed */

	/* convert from AFM(LSB*256+MSB) to short int */

	for (i=0; i<SIZE; i++){
		for (j=0; j<SIZE; j++){
			temp = image[SIZE*i+j] & 0xff;		/* temp =s RHByte
(Most Significant on AFM) */
			if (temp >= 128)	/* MSB is set */
				image[SIZE*i+j] = ((image[SIZE*i+j] >> 8) & 0xff) +
((temp-128)*256) - 32768;
			else
				image[SIZE*i+j] = ((image[SIZE*i+j] >> 8) & 0xff) +
(temp*256);
		}
	}

	/* Now low pass filter the image by summing half the value at
	   each pixel with 1/16 the value of each of the 8 adjacent pixels
	   (1st and 2nd nearest neighbors) */

	for (i=1; i<(SIZE-1); i++){				/* ignore the outermost */
		for (j=1; j<(SIZE-1); j++){		/* pixels */
			newimage[SIZE*i+j] = ((0.5*image[SIZE*i+j]) +
(tmp=(0.0625 * (image[SIZE*(i-1)+(j-1)]
				+ image[SIZE*(i-1)+j] + image[SIZE*(i-1)+(j+1)] +
image[SIZE*i+(j-1)]
```

```
                              + image[SIZE*i+(j+1)] + image[SIZE*(i+1)+(j-1)] +
image[(i*SIZE+SIZE)+j]
                              + image[SIZE*(i+1)+(j+1)]))));
                }
        }

        for (i=0; i<SIZE; i++){                              /* deal with the
outermost pixels */
                newimage[i]=image[i];
                newimage[(SIZE-1)*(SIZE)+i]=image[(SIZE-1)*(SIZE)+i];

                newimage[i*(SIZE-1)]=image[i*(SIZE-1)];
                newimage[(i+1)*SIZE-1]=image[(i+1)*SIZE-1];
        }

        /* now convert back to AFM format */
        /* manipulate image instead of newimage to preserve contents of newimage
for */
        /* the rest of code to use */

        for (i=0; i<SIZE; i++){
                for (j=0; j<SIZE; j++){
                        temp = newimage[i*SIZE+j] & 0xff;  /* temp =s RHByte
(Most Significant on AFM) */
                        if (temp >= 128)        /* MSB is set */
                                image[i*SIZE+j] = ((newimage[i*SIZE+j] >> 8) &
0xff) + ((temp-128)*256) - 32768;
                        else
                                image[i*SIZE+j] = ((newimage[i*SIZE+j] >> 8) &
0xff) + (temp*256);
                }
        }

        /* Write the new image to the output file name specified */
        /*
        fd=creat(outputname,0666);          read,write for owner,group,others
        write(fd,text,8192);                put in the old AFM header
        write(fd,image,sizeof(image));
        close(fd);*/

        fd=fopen(outputname,"w");
        for (i=0;i<8192;i++)
                fputc(text[i],fd);
        fwrite(image,sizeof(short int),(SIZE*SIZE),fd);
        fclose(fd);

}
```

****

```
#include <stdio.h>
#include <math.h>
#include <string.h>   /* need this to use strcpy() */
#include <fcntl.h>    /* need this for read,write,creat and open */
#define DELTA 8192  /* derivative must be less than this value to be a possible
maximum */
#define SQUARE 9    /* search an area that is SQAURE x SQUARE around a given
possible maximum*/
                    /* SQUARE should NEVER be less than three and should
ALWAYS be odd */
#define THRESHOLD 8192  /* maximum must be greater THRESHOLD to be a
maximum; this prevents noise
                        from appearing as dots; set THRESHOLD = 0 to have no
threshold condition;
                        acceptable values are -32767 to +32768 (NO ERROR
CHECKING) */
int findmax (outputname)       /* find and store all maxima */

char outputname[20];


/* This subroutine checks a SQUARE x SQUARE array of pixels to ensure only one
local maxima */
/* is found per dot.  oldfindmax.c checks a 5x5 array.  oldestfindmax.c only checks a
3x3 */
{
        int i,j,ii,jj;       /* counters */
        double d1,d2; /* dummy variables needed for use with fabs() */
        unsigned char garbage;          /* a non-zero character, chosen arbitrarily.  do
not set too close to */
                                /* zero or you won't be able to see the difference in the
image */
        extern int SIZE;
        extern short int *newimage;   /* contains 16 bit unsigned low pass filtered
image */
        extern short int *deltax, *deltay,       /* height difference between adjacent
pixels */
                        *laplacex,*laplacey;   /* difference in derivatives */

        int maxima;     /* Boolean which determines if a point MAY BE a local
maxima */
                        /* maxima is true if the derivatives are small (but not
necessarily zero) */
                        /* and the second derivatives are negative */
        int dots=0;     /* the number of dots found */
        char out[50];   /* output file name */
        FILE *fp;
```

```
	for (i=0; i<(SIZE-1); i++){		/* deltax(deltay) are undefinable for
rightmost(bottommost) column(row) */
		for (j=0; j<(SIZE-1); j++){	/* pixels */
			deltax[SIZE*i+j]=newimage[SIZE*i+j]-
newimage[SIZE*i+(j+1)];
			deltay[SIZE*i+j]=newimage[SIZE*i+j]-
newimage[SIZE*(i+1)+j];
			/* Laplacian using  RWVD, p. 321  */
			laplacex[SIZE*i+j]=newimage[SIZE*i+(j+1)] - (2 *
newimage[SIZE*i+j]) + newimage[SIZE*i+(j-1)];
			laplacey[SIZE*i+j]=newimage[SIZE*(i+1)+j] - (2 *
newimage[SIZE*i+j]) + newimage[SIZE*(i-1)+j];
		}
	}

	/* file stuff for PGM file */
	garbage="c";
	strcpy(out,outputname);
	strcat(out,".dots");
	fp = fopen(out,"w");
	fprintf(fp, "P5 %d %d 255\n", SIZE, SIZE);
	for (i=0; i < (SIZE*SIZE); i++)
		fwrite(0, 1, 1, fp);

	/* start the search for maxima */
	for (i=(SQUARE/2); i<(SIZE-(SQUARE/2)); i++){
		for (j=(SQUARE/2); j<(SIZE-(SQUARE/2)); j++){
			if ( (fabs(d1=deltax[SIZE*i+j]) < DELTA) &&
(fabs(d2=deltay[SIZE*i+j]) < DELTA)  /* &&
				(laplacex[SIZE*i+j] < 0) && (laplacey[SIZE*i+j] <
0)*/ ){

		/* it's a possible maximum, now check to see if it is THE maximum
by */
		/* checking a SQUARE x SQUARE area to see if this is a local
maximum */

				maxima = 1; /* need this for exit conditions */
				for (ii=i-(SQUARE/2); ii<=(i+(SQUARE/2)); ii++){
					if (maxima==0) break;		/* exit the ii
loop; should only do this if jj break was executed first */

					for (jj=j-(SQUARE/2); jj<=(j+(SQUARE/2));
jj++){
					/* first check if it's larger */
					/* Then if it's equal, arbitrarily make the first
one found the local maximum */
```

```
                                        /* This ensures no double counting if equal,
but still count it */
                                                if (!(i==ii && j==jj)) maxima =
(newimage[SIZE*i+j]>newimage[SIZE*ii+jj]);
                                                if ((!(i==ii && j==jj)) &&
(newimage[SIZE*i+j]==newimage[SIZE*ii+jj])) maxima =
((SIZE*i+j)>(SIZE*ii+jj));
                                                if (maxima==0) break; /* exit the jj
loop; ii loop will be exited by a separate break */
                                        } /* for jj */
                                } /* for ii */

                                if ((maxima) &&
(newimage[SIZE*i+j]>THRESHOLD)){
                                        dots++;                 /* add one to the number
of dots */
                                        fseek(fp,(SIZE*i+j+15),0); /* 15 is the length
of the header */
                                        fwrite(&garbage, 1, 1, fp);
                                }
                        } /* if possible maximum */
                } /* for j */
        } /* for i */
        fclose(fp);
        return dots;

}
```

```
*****************************************

#include <stdio.h>
#include <string.h>    /* need this to use strcpy() */
#include <fcntl.h>     /* need this for read,write,creat and open */
#include <limits.h>
#include <assert.h>
#define THRESHOLD 46       /* This value is the maximum difference allowed
between the peak value of the
                        dot and a given pixel for that pixel to be included as part of
the dot.
                        Set THRESHOLD equal to 255 to have no threshold
condition, and 0 to eliminate
                        all pixels immediately (a trivial and stupid thing to do)  */
#define NOISE 1024  /* allowable noise in the slope, taken from original 16 bit data.
A value of 0
                        means that no noise is allowed, and the sign of the slope
must change to
                        signify the edge of the dot.  A positive value of NOISE will
allow us to detect
```

```
                        the edge of the dot even though the slope might not change
*/

#define OVERWRITE -512    /* slope noise specifically for checking if a pixel down
the centerline
                        is part of the dot. this is needed because NOISE is used to
contain smaller
                        dot from being viewed as bigger (THRESHOLD doesn't
contain the size of the
                        smaller dots). OVERWRITE should be less than zero */
double ref_level();
double afm_height();

void histogram(outputname) /* compute a histogram of dot area and height */

char outputname[];

{ /* function */

        int i,j,q=1,        /* counters */
        top,                /* the y position of the top edge of the dot */
        n=0,                /* n determines the color for each dot */
        x=0,                /* temporary value for loop control */
        perimeter,          /* the number of pixels on the perimeter of each dot */
        total,              /* the sum of the heights of the dots on the perimeter */
        interior,           /* the number of interior pixels */
        complete,           /* Boolean: 1 if the entire dot was in the image, 0 if incomplete
*/
        numcomplete=0,           /* number of complete dots */
        incomplete=0,            /* number of incomplete dots */
        color;              /* color of a given dot */

        double major_axis,       /* length of the major axis of the dot, in nm */
        minor_axis,              /* length of the minor axis of the dot, in nm */
        length_pixel,  /* the length of a single pixel, in nm (equal to (SCAN/SIZE) */
        area_pixel,         /* the area of a single pixel, in nm^2 (equal to
(SCAN*SCAN)/(SIZE*SIZE) */
        area;               /* area of a dot, in nm^2 */

        int t=0,r=0,l=0,b=0; /* number of incomplete dots by top,right,left, and
bottom */

        extern short int *newimage;    /* the low pass filtered image */
        extern short int *deltax,*deltay,         /* height difference between adjacent
pixels */
                    *laplacex,*laplacey;     /* difference in derivatives */

        extern int SIZE;           /* image file is SIZE x SIZE pixels */
```

```
	extern double SCAN;			/* scan size of image is SCAN x SCAN
*/

	char *dots;
	FILE *fp;
	char out[30];
	char *image;
	unsigned char *another;			/* an 8-bit version of newimage */
	double level;	/* reference level, in nm */
	double height;	/* height of a dot, in nm */
	unsigned char thresh;	/* another[SIZE*i+j]-THRESHOLD; if THRESHOLD
> another[SIZE*i+j]
					then set thresh=0 */

	struct hstgrm{
		int x,y;
		double height;
		double area;
		double major_axis;
		double minor_axis;
		struct hstgrm *next;
	};
	struct hstgrm *qd=NULL,*temp_qd=NULL;

/* Search algorithm: 1) Start at the center of each dot (known location)
		2) Move up 1 pixel at a time until the edge of the
		  dot is found, as indicated by a change in the sign
		  of the slope
		3) Move down 1 row at a time, moving outward from the
		  center column, locating the edges by slope change
		4) Terminate when width is one
		*/

	dots = calloc(SIZE*SIZE,sizeof(char));
	another = calloc(SIZE*SIZE,sizeof(char));
	image = calloc(SIZE*SIZE,sizeof(char));

	level = afm_height(ref_level());
	length_pixel = (double) (1.0*SCAN/SIZE);
	printf("Reference level is %f nm\n",level);
	printf("Length = %f\n",length_pixel);
	area_pixel = (double) (1.0*SCAN*SCAN)/(1.0*SIZE*SIZE);

	for (i=0; i<SIZE; i++){
		for (j=0; j<SIZE; j++){
			image[SIZE*i+j]=0; /* initialize to all zeroes */
			another[SIZE*i+j] = (((newimage[SIZE*i+j] >> 8) & 0xff) ^
0x80);
```

```
                        image[SIZE*i+j]=another[SIZE*i+j];          /* convert to 8
bit */
                }                                           /* ^ 0x80 is EOR
(decimal 128) */
        }                                           /* which converts a signed char
to an unsigned char */


        /* Read the location of the dot maxima into the array "dots" */
        /* The file outputname.dots is generated by findmax() */
        strcpy(out,outputname);
        strcat(out,".dots");
        fp = fopen(out,"r");
        fseek(fp,15,0);
        fread (dots,sizeof(char),SIZE*SIZE,fp);
        fclose (fp);

        /* Create a new file in which to store height data */
        strcpy(out,outputname);
        strcat(out,".height");
        fp = fopen(out,"w");
        fprintf(fp. "Height (nm)\tArea (nm^2)\tMajor Axis (nm)\tMinor Axis
(nm)\n");


        for (i=0; i<(SIZE-1); i++){
                for (j=0; j<(SIZE-1); j++){
                        if (dots[SIZE*i+j] != 0) { /* then we're at the center of a dot */

                                perimeter = 0;  /* reset */
                                area = 0.0;
                                major_axis = 0.0;
                                minor_axis = 0.0;
                                color =(((n%8)+1)*32)-1;
                                image[SIZE*i+j]=color;
                                n++;
                                x=0;
                                interior=0;
                                top=i;
                                complete=1;    /* search until false */
                                if (THRESHOLD >= another[SIZE*i+j])
                                        thresh = 0;
                                else
                                        thresh = another[SIZE*i+j] - THRESHOLD;

                                while ((deltay[SIZE*(top-1)+j] < NOISE) &&
(another[SIZE*top+j] >= thresh)  && (top > 0)){
                                        top--; /* find the top edge of the dot */
                                }
```

```
                    if (top != 0){
                            image[SIZE*top+j]=color;
                            total=newimage[SIZE*top+j];
                            area+=area_pixel;
                            major_axis+=length_pixel;
                            perimeter++;
                    }else {complete = 0;t++;}       /* never found the top
edge */

            /* 1 */  while ( (x!=(j+1)) && (complete) && (top<(SIZE-
2))){ /* first condition means we have found the bottom edge of the dot */
                            top++;
                            if ( (top > (i+1)) && (deltay[SIZE*top+j] <=
OVERWRITE) ){printf("i,j=%i,%i\n",i,j); x=j+1;} /* To avoid overwriting other
dots, check to see if the slope is correct */
                            else{
                            major_axis+=length_pixel;
                            area+=area_pixel;
                            image[SIZE*top+j]=color; /* down the center
path */
                            x=j-1;

                    /* 2 */  while ((deltax[SIZE*top+x] <= NOISE) &&
(deltax[SIZE*top+(x-1)] <= NOISE ) && (another[SIZE*top+x] >= thresh) &&
(x>-1)){ /* this pixel is part of the dot */
                                    image[SIZE*top+x]=color;
                                    area+=area_pixel;
                                    if (top==i) minor_axis+=length_pixel;
                                    x--;
                    /* 2 */  }
                            if (x==-1){ complete=0;l++;}
                            interior=interior + (j-1-x);
                            if (x != j-1){ /* found a perimeter pixel */
                                    total = total +
newimage[SIZE*top+(x+1)];
                                    perimeter++;
                                    interior--;      /* this takes care of extra
pixel added to interior */
                            }

                            x=j+1;
                    /* 3 */  while ( (deltax[SIZE*top+x] >= (-NOISE))
&& (deltax[SIZE*top+(x+1)]>=(-NOISE)) && (another[SIZE*top+x] >= thresh)){
/* this pixel is part of the dot */
                                    image[SIZE*top+x]=color;
                                    area+=area_pixel;
                                    if (top==i) minor_axis+=length_pixel;
                                    x++;
                    /* 3*/   }
```

```
					if (x==(SIZE-1)) {complete=0;r++;}
					interior=interior + (x-(j+1));
					if (x != j+1){ /* found a perimeter pixel */
						total = total +
newimage[SIZE*top+(x+1)];
						perimeter++;
						interior--;
					}else if (top<i) x=j;  /* gotta set it equal to
something other than (j+1) IF it's the top half of the dot */
					} /* else */
			/* 1 */  }

				if (top==(SIZE-2)) {complete=0;b++;}
				if (complete){
					numcomplete++;
					height = afm_height((double)
(newimage[SIZE*i+j])) - level;
					/* printf("Height = %f nm
\n",afm_height((double) (newimage[SIZE*i+j])) - level); */
					/* printf("Area = %f nm^2\n",area); */

	fprintf(fp,"%f\t%f\t%f\t%f\n",height,area,major_axis,minor_axis);
					if (qd == NULL){  /* first dot found */
						qd = (struct hstgrm *)
malloc(sizeof(struct hstgrm));		/* allocate memory */
						qd->x=j;
						qd->y=i;
						qd->height=height;
						qd->area=area;
						qd->major_axis=major_axis;
						qd->minor_axis=minor_axis;
						qd->next=NULL;
					}
					else{  /* not the first dot so search list 'til we
find the end */
						temp_qd = qd;
						while (temp_qd->next != NULL)
						temp_qd = temp_qd->next;
						temp_qd->next = (struct hstgrm *)
malloc(sizeof(struct hstgrm));		/* allocate memory */
						temp_qd->next->x=i;
						temp_qd->next->y=j;
						temp_qd->next->height=height;
						temp_qd->next->area=area;
						temp_qd->next-
>major_axis=major_axis;
						temp_qd->next-
>minor_axis=minor_axis;
						temp_qd->next->next=NULL;
```

```
                                        }
                                } /* if complete */
                                else {
                                printf("%i,%i\n",j,i);
                                incomplete++;
                                }
                        } /* if pixel[SIZE*i+j] */
                } /* for j */
        } /* for i */

        fclose(fp);

        strcpy(out,outputname);
        strcat(out,".hst");
        fp = fopen(out,"w");
        fprintf(fp, "P5 %d %d 255\n",SIZE,SIZE);
        fwrite(image,sizeof(char),SIZE*SIZE,fp);
        fclose (fp);
        printf("Complete dots=%i\n",numcomplete);
        printf("Incomplete dots=%i\n",incomplete);
        printf("top=%d  bottom=%d  right=%d  left=%d  \n",t,b,r,l);
        free(dots);
        free(another);
        free(image);

        printf("Reference level is %f nm\n",level);

} /* function */
```

****

```
/* converts binary height into a numerical value using the formula
given on page 85 of the Nanoscope III Version 3.0 software manual */

#include <stdio.h>

double afm_height(height)

double height;

{
        extern double zsens,zmax,zscale;                /* zsens,zmax,zscale, and zatten
are */
        extern int zatten;        /* AFM parameters needed to compute the height */
```

```
        return ( (height/65536.0)*(zscale*(zatten/65536.0)*
          ((zmax*2)/65536.0)*zsens) );
}


****************************************
#include <stdio.h>
#include <math.h>
#define percent 10

double ref_level()

{
        extern int SIZE;
        extern short int *newimage;
        int i,j,k,l;
        short int *image;
        int total=0;
        short int temp;
        int PIXELS;   /* number of pixels needed */
        short int *small;         /* small[0] will be the biggest of the small numbers */

        PIXELS = (int) floor((double) ((percent/100.0) * (SIZE*SIZE))); /* number
of pixels to be included */
        small = calloc (PIXELS,sizeof(short int));
        image = calloc (SIZE*SIZE, sizeof(short int));
        printf("PIXELS=%i\n",PIXELS);

        for (i=0; i<SIZE; i++){
                for (j=0; j<SIZE; j++){
                        image[SIZE*i+j] = newimage[SIZE*i+j];
                        /* printf("Data = %X\n",newimage[SIZE*i+j]);
                        temp = newimage[SIZE*i+j] & 0xff; */        /* temp =s
RHByte (Most Significant on AFM) */
                        /*printf("temp = %X (%i)\n",temp,temp);*/
                        /*if (temp >= 128)*/   /* MSB is set */
                        /*        image[SIZE*i+j] = ((newimage[SIZE*i+j] >> 8) &
0xff) + ((temp-128)*256);
                        else
                                image[SIZE*i+j] = ((newimage[SIZE*i+j] >> 8) &
0xff) + (temp*256);
                         if (temp >= 128)        MSB is set
                                image[SIZE*i+j] = ((newimage[SIZE*i+j] >> 8) &
0xff) + ((temp-128)*256) - 32768;
                        else
                                image[SIZE*i+j] = ((newimage[SIZE*i+j] >> 8) &
0xff) + (temp*256);
                        if ((i==14) && (j==31)){
```

```
                        printf("%i\n",temp);
                        printf("%x\n",newimage[SIZE*14+31]);
                        printf("%i\n",image[SIZE*14+31]);
                        exit(1);
                } */
        }
    }

    for (i=0; i<PIXELS; i++)
        small[i]=32767;

    for (i=(PIXELS-1); i>=0; i--){ /* put the first PIXELS data points in
numerical order */
        j=(PIXELS-1);
        while ((image[i] > small[j]) && (j>0))
            j--;
        for (k=0; k<j; k++)
            small[k]=small[k+1];
        small[j]=image[i];
    } .

    for (i=0; i<SIZE; i++){
        for (j=0; j<SIZE; j++){
            if ((image[SIZE*i+j] < small[0]) && ((SIZE*i+j)>PIXELS)){
/* then this number goes into the list */
                k=(PIXELS-1);
                while ((image[SIZE*i+j] > small[k]) && (k>0))
                    k--;
                for (l=0;l<k;l++)
                    small[l]=small[l+1];
                small[k] = image[SIZE*i+j];
            }
        } /* for j */
    } /* for i */

    for (i=0; i<PIXELS; i++)
        total += small[i];
    /* printf ("Total = %i\n", total);
    printf ("Pixels = %i\n", PIXELS); */
    printf ("ref_level = %f\n",(double)(total/PIXELS));

    return((double)(total/PIXELS));
}
```

Bibliography

Anand, S., Carlsson, N., Pistol, M-E., Samuelson, L., and Seifert, W. "Deep level transient spectroscopy of InP quantum dots", *Applied Physics Letters* **67** (20), 3016-3018 (1995).

Asada, M., Miyamoto, Y., and Suematsu, Y. "Gain and the threshold of three-dimensional quantum-box lasers", *IEEE Journal of Quantum Electronics* **QE-22** (9), 1915-1921 (1986).

Bacher, G., Scheizer, H., Kovac, J., Forchel, A., Nickel, H., Schlapp, W., and Losch, R. "Influence of barrier height on carrier dynamics in strained In_xGa_{1-x}/GaAs quantum wells", *Physical Review B* **43** (11), 9312-9315 (1991).

Bacher, G., Hartmann, C., Schweizer, H., Held, T., Mahler, G., and Nickel, H. "Exciton dynamics in $In_xGa_{1-x}As$ quantum-well heterostructures: Competition between capture and thermal emission", *Physical Review B* **47** (15), 9545-9555 (1993).

Benisty, H., Sotomayor-Torres, C.M., and Weisbuch, C. "Intrinsic mechanism for the poor luminescence properties of quantum-box systems", *Physical Review B* **44** (19), 10945-10948 (1991).

Bimberg, D., Ledentsov, N., Grundmann, M., Kirstaedter, N., Schmidt, O., Mao, M., Ustinov, V., Egorov, A., Zhukov, A., Kopev, P., Alferov, Zh., Ruvimov, S., Gosele, U., and Heydenreich, J. "InAs-GaAs quantum pyramid lasers - *in situ* growth, radiative lifetimes, and polarization properties", *Japanese Journal of Applied Physics* **35** 1311-1319 (1996).

Brandt, O., Tapfer, L., Ploog, K., Bierwolf, R., and Hohenstein, M. "Effect of In

segregation on the structural and optical properties of ultrathin InAs films in GaAs", *Journal of Crystal Growth* **127** 513-514 (1993).

Casey, H., and Panish, M. *Heterostructure Lasers: Part B, Materials and Operating Characteristics* 1-330 (Academic Press, New York, 1978).

Castrillo, P., Hessman, D., Pistol, M.-E., Anand, S., Carlsson, N., Seifert, W., and Samuelson, L. "Band filling at low optical power density in semiconductor dots", *Applied Physics Letters* **67** (13), 1905-1907 (1995).

Chadi, D.J. "Theoretical study of the atomic structure of silicon (211), (311), and (331) surfaces", *Physical Review B* **29** (2), 785-792 (1984).

Cho, A. (eds. Cho, A.) 570 (American Institute of Physics, Woodbury, NY, 1994).

Cingolani, R., and Ploog, K. "Frequency and density dependent radiative recombination processes in III-V semiconductor quantum wells and superlattices", *Advances in Physics* **40** (5), 535-623 (1991).

Coldren, L.A., and Corzine, S. *Diode Lasers and Photonic Integrated Circuits*, 1-593 (Wiley-Interscience, New York, 1995).

Dingle, R., Wiegmann, W., and Henry, C.H. "Quantum states of confined carriers in very thin $Al_xGa_{1-x}As$-GaAs-$Al_xGa_{1-x}As$ heterostructures", *Physical Review Letters* **33** (14), 827-830 (1974).

Ebner, J.T., and Arthur, J.R. "The effect of lattice mismatch on the dynamical microstructure of III-V compound surfaces", *Journal of Vacuum Science and Technology A* **5** (4), 2007-2010 (1987).

Esaki, L., and Chang, L.L. "New transport phenomenon in a semiconductor "superlattice"", *Physical Review Letters* **33** (8), 495-498 (1974).

Georgsson, K., Carlsson, N., Samuelsonn, L., Seifert, W., and Wallenberg, L. "Transmission electron microscopy investigation of the morphology of InP

Stranski-Krastanow islands grown by metalorganic chemical vapor deposition", *Applied Physics Letters* **67** (20), 2981-2983 (1995).

Gerard, J., d'Anterroches, C., and Marzin, J. "Monolayer scale study of segregation effects in InAs/GaAs heterostructures", *Journal of Crystal Growth* **127** 536-540 (1993).

Goldstein, L., Glas, F., Marzin, J., Charasse, M., and LeRoux, G. "Growth by molecular beam epitaxy and characterization of InAs/GaAs strained-layer superlattices", *Applied Physics Letters* **47** (10), 1099-1101 (1985).

Hatami, F., Ledentsov, N., Grundmann,H., Böhrer, J., Heinrichsdorff, F., Beer, M., Bimberg, D., Ruvimov, S., Werner, P., Gösele, U., Heydenreich, J., Richter, U., Ivanov, S., Meltser, B., Kop'ev, P., and Alferov, Z. "Radiative recombination in type-II GaSb/GaAs quantum dots", *Applied Physics Letters* **67** (5), 656-658 (1995).

Hayakawa, T., Nagai, M., Horie, H., and Niwata, Y. "Effects of growth temperature and substrate misorientation in InGaAs/GaAs strained quantum wells grown by MBE", *Journal of Crystal Growth* 532-535 (1993).

Herman, M.A., Bimberg, D., and Christen, J. "Heterointerfaces in quantum wells and epitaxial growth processes", *Journal of Applied Physics* **70** (2), R1-R52 (1991).

Hirayama, H., Matsunaga, K., Asada, M., and Suematsu, Y. "Lasing Action of $Ga_{0.67}In_{0.33}As$/GaInAsP/InP tensile-strained quantum-box laser", *Electronics Letters* **30** (2), 142-143 (1994).

Holloway, H. "X-ray interferometry and its application to determination of layer thickness and strain in quantum-well structures", *Journal of Applied Physics* **67** (10), 6229-6236 (1990).

Horikoshi, Y., Kawashima, M., and Yamaguchi, H. "Migration-enhanced epitaxy of GaAs and AlGaAs", *Japanese Journal of Applied Physics* **27** (2), 169-179 (1988).

Houzay, F., Moison, J., Guille, C., Barthe, F., and van Rompay, M. "Surface segregation of third-column atoms in III-V ternary arsenides", *Journal of Crystal Growth* **95** 35-37 (1989).

Ibbetson, J.P., Mirin, R.P., Mishra, U.K., and Gossard, A.C. "Effects of As_4 flux on RHEED oscillations during growth of GaAs at low temperatures", *Journal of Vacuum Science and Technology B* **12** (2), 1050-1052 (1993).

Ilg, M., Alonso, M.I., Lehmann, A., Ploog, K.H., Hohenstein, M. "Investigation of InAs submonolayer and monolayer structures on GaAs (100) and (311) substrates", *Journal of Applied Physics* **74** (12), 7188-7197 (1993).

Kamath, K., Bhattacharya, P., Sosnowski, T., Norris, T., and Phillips, J. "Room temperature operation of $In_{0.4}Ga_{0.6}As$/GaAs self-organized quantum dot lasers", *Electronics Letters* **32** (15), 1374-1375 (1996).

Kapon, E. in *Epitaxial Microstructures* (eds. Gossard, A.C.) (259-336, 1994).

Kash, K., Mahoney, D.D., Van der Gaag, B.P., Gozdz, A.S., Harbison, J.P., and Florez, L.T. "Observation of quantum dot levels produced by strain modulation of GaAs-AlGaAs quantum wells", *Journal of Vacuum Science and Technology B* **10** (4), 2030-2033 (1992).

Kitamura, M., Nishioka, M., Oshinowo, J., and Arakawa, Y. "In situ fabrication of self-aligned InGaAs quantum dots on GaAs multiatomic steps by metalorganic chemical vapor deposition", *Applied Physics Letters* **66** (26), 3663-3665 (1995).

Krost, A., Heinrichsdorff, Bimberg, D., Darhuber, A., and Bauer, G. "High-

resolution X-ray diffraction of self-organized InGaAs/GaAs quantum dot structures", *Applied Physics Letters* **68** (6), 785-787 (1996).

Leonard, D., Pond, K., and Petroff, P. "Critical layer thickness for self-assembled InAs islands on GaAs", *Physical Review B* **50** (16), 11687-11692 (1994).

Leonard, D. *PhD Dissertation* (1995).

Lide, D.R. *Handbook of Chemistry and Physics* (CRC Press, Inc., West Palm Beach, Florida, 1990).

Lin, X.W., Washburn, J., Liliental-Weber, Z., and Weber, E.R. "Morphological transition of InAs islands on GaAs (001) upon deposition of a GaAs capping layer", *Applied Physics Letters* **65** (13), 1677-1679 (1994).

Marzin, J.-Y., Gerard, J.-M., Izrael, A., and Barrier, D. "Photoluminescence of single InAs quantum dots obtained by self-organized growth on GaAs", *Physical Review Letters* **73** (5), 716-719 (1994).

Michler, P., Hangleiter, A., Moser, M., Geiger, M., and Scholz, F. "Influence of barrier height on carrier lifetime in Ga(1-y)In(y)P/(AlGa)InP single quantum wells", *Physical Review B* **46** (11), 7280-7283 (1992).

Miller, R.C., Kleinman, D.A., Nordland, Jr., W.A., and Gossard, A.C. "Luminsecence studies of optically pumped quantum wells in GaAs-Al(x)Ga(1-x)As multilayer structures", *Physical Review B* **22** (2), 863-871 (1980).

Mirin, R., Tan, I-H., Weman, H., Leonard, M., Yasuda, T., Bowers, J., and Hu, E. "InGaAs quantum well wires grown on patterned GaAs substrates", *Journal of Vacuum Science and Technology A* **10** (4), 697-700 (1992).

Mirin, R., Krishnamurthy, Tan, I-H., Bowers, J., Gossard, A., and Hu, E. "Morphology and optical properties of strained InGaAs quantum wires",

Journal of Crystal Growth **127** 881-886 (1993).

Mirin, R.P., Ibbetson, J.P., Mishra, U.K., and Gossard, A.C. "Low temperature limits to molecular beam epitaxy of GaAs", *Applied Physics Letters* **65** (18), 2335-2337 (1994).

Mirin, R., Ibbetson, J., Nishi,K., Gossard, A., and Bowers, J. "1.3 μm photoluminescence from InGaAs quantum dots on GaAs", *Applied Physics Letters* **67** (25), 3795-3797 (1995).

Moison, J.M., Houzay, F., Barthe, F., Leprince, L., Andre, E., and Vatel, O. "Self-organized growth of regular nanometer-scale InAs dots on GaAs", *Applied Physics Letters* **64** (2), 196-198 (1994).

Muraki, K., Fukatsu, S., Shiraki, Y., and Ito, R. "Surface segregation of In atoms and its influence on the quantized levels in InGaAs/GaAs quantum wells", *Journal of Crystal Growth* **127** 546-549 (1993).

Nagle, J., Landesman, J., Larive, M., Mottet, C., and Bois, P. "Indium surface segregation in strained GaInAs quantum wells grown on GaAs by MBE", (1993).

Nambu, Y., and Arakawa, K. "Theoretical analysis of optimal conditions in quantum structure semiconductor lasers for low threshold current", *Applied Physics Letters* **67** (11), 1509-1511 (1995).

Neave, J.H., Joyce, B.A., and Dobson, P.J. "Dynamic RHEED observations of the MBE growth of GaAs", *Applied Physics A* **34** 179-184 (1984).

Nötzel, R., Ledentsov, N.N., Däweritz, L., Hohenstein, M., and Ploog, K. "Direct synthesis of corrugated superlattices on non-(100)-oriented surfaces", *Physical Review Letters* **67** (27), 3812-3815 (1991).

Pankove, J.I. *Optical Processes in Semiconductors* 1-422 (Prentice-Hall,

Englewood Cliffs, NJ, 1971).

Parker, E.H.C. *The Technology and Physics of Molecular Beam Epitaxy* 686 (Plenum Press, New York, 1985).

Ponchet, A., Le Corre, A., L'Haridon, H., Lambert, B., and Salaün, S. "Relationship between self-organization and size of InAs islands on InP(001) grown by gas-source molecular beam epitaxy", *Applied Physics Letters* **67** (13), 1850-1852 (1995).

Roan, E., and Cheng, K. "Long-wavelength (1.3 µm) luminescence in InGaAs strained quantum-well structures grown on GaAs", *Applied Physics Letters* **59** (21), 2688-2690 (1991).

Rodden, W., Sotomayor-Torres, C., and Ironside, C. "Three-dimensional phonon confinement in CdSe microcrystallites in glass", *Semiconductor Science and Technology* **10** (6), 807-812 (1995).

Saito, H., Nishi, K., and Sugou, S. in Proceedings of *IEICE General Conference* (1996)

Schwoebel, R.L., and Shipsey, E.J. *Journal of Applied Physics* **37** 3682 (1966).

Shoji, H., Mukai, K., Ohtsuka, N., Sugawara, M., Uchida, T., and Ishikawa, H. "Lasing at three-dimensionally quantum confined sublevel of self-organized $In_{.5}Ga_{.5}As$ quantum dots by current injection", *Photonics Technology Letters* **7** (12), 1385-1387 (1995).

Simmons, G.W., Mitchell, D.F., and Lawless, K.R. "LEED and HEED studies of the interaction of oxygen with single crystal surfaces of copper", *Surface Science* **8** 130-164 (1967).

Solomon, G.S., Trezza, J.A., Marshall, A.F., and Harris, J.S. "Vertically aligned and electronically couples growth induced InAs islands in GaAs", *Physical*

Review Letters **76** (6), 952-955 (1996).

Sopanen, M., Lipsanen, H., and Ahopelto, J. "Strain-induced quantum dots by self-organized stressors", *Applied Physics Letters* **66** (18), 2364-2366 (1995).

Tan, I.-H., Lishan, D., Mirin, R., Jayaraman, V., Yasuda, T., Hu, E.L., and Boers, J. "Systematic observation of strain-induced lateral quantum confinement in GaAs quantum well wires prepared by chemical dry etching", *Applied Physics Letters* **59** (15), 1875-1877 (1991).

Tapfer, L., Ospelt, M., and von Kanel, H. "Monolayer resolution by means of x-ray interference in semiconductor heterostructures", *Journal of Applied Physics* **67** (3), 1298-1301 (1990).

Thibeault, B., Personal Communication, (1995).

Tsao, J.Y. *Materials Fundamentals of Molecular Beam Epitaxy* 1-301 (Academic Press, Boston, 1993).

Vening, M., Dunstan, D.J., and Homewood, K.P. "Thermal quenching and retrapping effects in the photoluminescence of $In_yGa_{1-y}As/GaAs/Al_xGa_{1-x}As$ multiple-quantum-well structures", *Physical Review B* **48** (4), 2412-2417 (1993).

Wharam, D.A., Heinzel, T., Manus, S., Kotthaus, J. "High magnetic field investigations of quantum dots", *Superlattices and Microstructures* **15** (1), 37-40 (1994).

Wie, C.R., Chen, J.C., Kim, H.M., Liu, P.L., Choi, Y.-W., and Hwang, D.M. "X-ray interference measurement of ultrathin semiconductor layers", *Applied Physics Letters* **55** (17), 1774-1776 (1989).

Xie, Q., Chen, P., Kalburge, A., Ramachandran, T., Nayfonov, A., Konkar, A., and Madhukar, A. "Realization of optically active strained InAs island

quantum boxes on GaAs (100) via molecular beam epitaxy and the role of island induced strain fields", *Journal of Crystal Growth* **150** 357- (1995).

Xie, Q., Kalburge, A., Chen, P., and Madhukar, A. "Observation of Lasing from Vertically Self-Organized InAs Three-dimensional Island Quantum Boxes on GaAs (100)", *Photonics Technology Letters* **8** (8), 965-967 (1996).

Yamaguchi, H., and Horikoshi, Y. "Anomalous distribution of In atoms in GaAs during migration-enhanced epitaxy", *Japanese Journal of Applied Physics* **28** (11), L2010-L2012 (1989).

Yamaguchi, H., and Horikoshi, Y. "Replacement of group-III atoms on the growing surface during migration-enhanced epitaxy", *Journal of Applied Physics* **68** (4), 1610-1615 (1990).

Yao, J.Y., Andersson, T.G., and Dunlop, G.L. "The interfacial morphology of strained epitaxial $In_xGa_{1-x}As/GaAs$", *Journal of Applied Physics* **69** (4), 2224-2230 (1991).